Compensation for Distortion in the Imaging Process for 3-D Surfaces

Kok Hoe WONG
March 2002

A thesis submitted to The Nottingham Trent University
in partial fulfilment of the requirements for the degree
of Doctor of Philosophy

The Nottingham Trent University
in collaboration with
Axiomatic Technology (UK) Ltd

Abstract

Digital models play a crucial role in today's numerous industries, ranging from rapid-prototyping in manufacturing to digital animation in the entertainment industry. In CNC manufacturing, digital models, obtained via reverse engineering of existing objects, help reduce the time to production. After the data has been captured, it can be refined or manipulated to create either a replica or a modified version of the original object. This reduces the cost and time in reproducing a blueprint and physical prototype of the object. There are many methods used to obtain 3-D images of an object, including laser triangulation (non-tactile) and touch-trigger probe (tactile). Different methods are appropriate for different purposes but ultimately each provides a set of points in 3-D space, representing the surface of the object of interest. These digital models, known as range images, often suffer from distortions, depending on the type of sensor used and also the physical attributes of the object. Before such an object can be physically reproduced, these distortions need to be compensated.

The size and nature of the distortions in the measurements depend on the type of sensor used. Significant distortions can be generated by a single-perspective active triangulation laser sensor (non-tactile), also known as a point sensor, in which a beam of laser light is projected towards the diffusely reflective surface of an object. The spot image produced on the surface of the object is sampled by a single position-sensitive photodetector in the sensor and the distance of this spot is computed using triangulation. This method of 3-D imaging is fast gaining ground in industries requiring reverse engineering, for it provides a rapid, cost-effective and non-destructive alternative to tactile imaging. However, when these optical sensors are used for scanning objects, significant distortions may occur.

A detailed investigation has been conducted into distortions obtained from a single-perspective point sensor. Small distortions are encountered due to noise and simple algorithms have been developed for smoothing. More significant systematic distortions have been found close to high curvature regions of an object, especially where there are inclined or near-vertical faces. This systematic behaviour can be classified into two types. One type is caused by secondary reflections from other parts of the object while the other results from occlusion of the returning beam by the object. However, it has also been found that incidence of such distortions depends on the orientation of the sensor with respect to the geometry of the object, whereas it is independent of the scanning direction. Another contributory factor to distortions is the quality of the surface of the object.

Compensation algorithms have been developed to correlate multiple range images, taken with different orientations of the sensor, and yield a complete image with minimal distortions. Error regions are identified based on the disparities between the different range images. Edge detection algorithms have been developed to recognise inclined faces of an object based on its geometry adjacent to the error regions. The detected edges are then used to combine those range images with the smallest distortions within the error regions. The algorithms developed have been evaluated on both simple objects and more complex freeform objects.

The work described in this Thesis is the Author's own, unless otherwise stated, and it is, as far as he is aware, original.

To my grandma, my dad, my mum, my brothers and my little sister for their love, support and encouragement. No words can express my deepest gratitude to them.

僅以此文，獻給我的父母，
以及愛護，關心我的人們。

Acknowledgments

I would like to pay tribute and extend my sincere gratitude to several people who have helped and motivated me through the course of my research work with the university.

My first supervisor, Dr. Janet Poliakoff, who has helped me tremendously by guiding me throughout my research, and has spent countless hours reading my documents, which include conference papers, transfer report and especially this thesis.

My second supervisor, Professor Peter Thomas, who has provided me with the opportunity to undertake this research with the group.

The staff of Axiomatic Technology (UK) Limited for their technical support and for providing me with the tools I need for my research.

Dr. Alf Linney of University College London and Dr. Heather Powell of The Nottingham Trent University for being the best examiners one could ever hoped for.

My group of friends in UK and in Malaysia, whom I have the privilege to share many happy moments with, cheering and lifting my spirit when I am feeling beside myself.

And of course my dear grandma, dad and mum, two younger brothers and sister of mine, who have been my pillars of strength and encouragement, and for believing in me always.

Table of Contents

Glossary of Terms

a priori	Information based on conjecture or hypothesis rather than experimental evidence.
active sensing	Imaging process where an artificial source of light is used for illumination.
bow wave	A collection of 3-D points that is above the object's true surface, which usually occurs near the edge of an object due to secondary reflection and diffusion of the spot image.
CAD	Computer Aided Design
CAM	Computer Aided Manufacture
CCD	Charge-Coupled Device
centroid	Weighted centre of the laser beam spot reflected on the detector.
CNC	Computer Numerical Control
cooperative target	A target with specular reflective properties similar to a mirror, in which it reflects most, if not all, of the light to the sensor's detector. Besides mirrors, cooperative targets include highly polished metals.
crest	Rising occlusion spikes where 3-D points are above the true surface of an object due to detection of traces of light reflected and diffused from the spot image.
digital photogrammetry	A method of 3-D imaging that utilises digital images to derive geometrical parameters of remote objects.
edge	The tangent of the curvature of an object's inclined face.
edge detection	A compensation process for significant distortions where edges of an object are identified and then used in selection of the best scan points from multiple range images that closely conform to the actual shape of the object.
error map	A map of the size of distortions found when comparing differences between multiple range images of an object.
focus point (FP)	The scan point that is processed in a particular instance.
forward engineering	Traditional engineering approach that begins with a logical description of a design to its physical implementation.
freeform object	An object that has more varied geometrical structures and curvatures.
imaging direction	The direction of the sensor's motion in which it captures a single scanline.

mesh	A latticework of connected 3-D coordinates, forming a polyhedral surface description.
microtopology	Microscopic topology of a surface.
noise level	The computed standard deviation of points from the true surface of an object.
noisy data	Data that is notably affected by measurement errors.
occlusion	Illuminated spot is hidden from the detector's field-of-view.
occlusion spike	Distorted 3-D point that is incorrectly measured by the detector due to total or partial occlusion of the spot image.
origin	A selected position on the testbed where the projected spot image is positioned and registered initially before commencement of the scanning process.
parametric equation	A continuous mapping of the form $f(u,v) = (x(u,v), y(u,v), z(u,v))$ where $f: \Delta \rightarrow \Re^3$ and $\Delta \subseteq \Re^2$ is a connected domain.
passive sensing	Imaging process where source of illumination is natural ambient lighting.
phantom spot	An incorrect position of the spot image from the true surface of an object due to detection of other dispersed traces of light.
point cloud	A set of 3-D coordinates in Euclidean space, which represents the digitised version of an object.
range image	Digitised image of an object which has spatial information, usually depth values, of its position in a 3-D environment.
registration	The alignment of two or more range images into a common coordinate system.
reverse engineering	Engineering process that begins with an existing physical implementation of design and results in a digital representation of it.
scanline	A sequence of 3-D points captured along the scanning direction of the sensor.
sensor orientation	The positioning of the detector relative to the emitter.
separation	Horizontal distance between 3-D points, usually defined by the user prior to a scanning process along x- and y-axis.
shading	Another term for describing the occlusion of the spot image.
speckle	A scattered ill-defined light source.
spike	Distorted point that a sudden rise or fall from the object's true surface.
spot diameter	Diameter of the laser spot at standoff distance.
square grid	A square matrix of scan points used in compensation for noise.
standoff distance	Distance from the sensor's housing to the centre of the measurable range.

surface reconstruction Producing a digital representation of 3-D surfaces that can be used for purposes of modelling, simulation, analysis, inspection and/or reproduction.

target The surface that is illuminated by a light source, from which the light is reflected to the detector in an optical sensor. This may refer to a specific object or material designed to reflect light, or to any type of surface or material at which a sensor is pointed. Target's reflectivity is the most important factor in determining the maximum range of a sensor.

theodolite A 3-D measurement device that measures horizontal and vertical angles of its position from a remote object.

transitional spike Distorted 3-D point that rises above or falls below an object's true surface due to sudden transition between two contrasting regions of the object.

triangulation angle Angle between direction of illumination and direction of detection of a sensor – which changes as the height between sensor and object changes.

triangulation principles The theory behind a 3-D imaging method where depth measurement is computed spatially based on the observation of an illuminated target.

trough Falling occlusion spikes that are below the true surface of an object due to total occlusion of the spot image from the detector's field-of-view.

uncooperative target Uncooperative targets include any surfaces or materials being measured that diffusely reflect light to the sensor's detector. This includes anodized metal or painted surfaces and loose or granular solid substances.

Chapter 1

Introduction

1 Introduction

Engineering can be described as the tangible realisation of ideas and principles, be they scientific or mathematical. Engineering is the profession involved in designing, manufacturing, constructing, and maintaining products, systems, and structures. Without a doubt, engineering is pervasive in our modern society. In the more traditional engineering process, an idea or design is first conceptualised and then modified, using either technical drawings on paper or a digital representation on a Computer Aided Design (CAD) system before production of a real physical system or tangible prototype. For example, in manufacturing a piece of furniture, in the past the designer would first sketch an idea on a piece of paper, with proper dimensioning. However, in this day and age, the designer would most probably use the computer and any appropriate software to better illustrate the design. This design would then be realised by either handcrafting the piece of furniture or feeding its digital representation into a highly precise cutting machine, such as a Computer Numerical Control (CNC) machine. The finished physical product should closely resemble the original design.

1.1 Reverse Engineering

In its most fundamental description, engineering can be divided into two types: *forward engineering* and *reverse engineering* (see Fig. 1-1). Forward engineering is a more common practice and was described previously for the example of a piece of furniture. Reverse engineering, meanwhile, takes the opposite route, starting with an existing physical model from which a qualitative analysis then leads to its logical representation [1]. This logical representation can then be re-engineered to produce a modified physical model or a replica of the original one. Reverse engineering is the analysis of an object or system to see how it functions in order to duplicate or enhance the object or system.

Reverse engineering can be viewed as the process of analysing an existing system to:

1. Identify the system's components and their inter-relationships;
2. Establish other forms of representation of the system or a higher level of abstraction;
3. Produce or replicate that system.

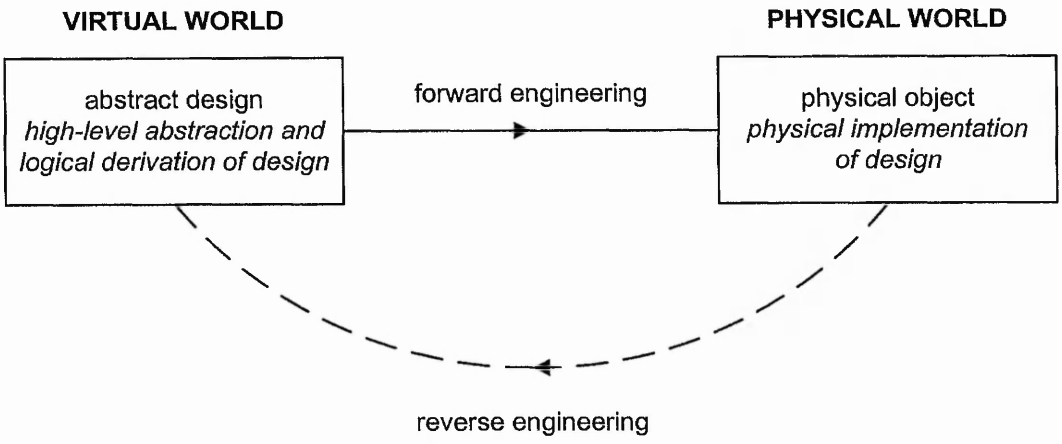

Fig. 1-1: Contemporary engineering practices.

Reverse engineering has permeated and influenced a multitude of industries, which include software engineering, entertainment, automotive, consumer products, microchips, chemicals, electronics and mechanical designs. For example, in civil engineering, bridge and building designs are copied from past successes and are reinvented to fit the new environments so there will be less chance of catastrophic failures.

In some situations, designers give a shape to their ideas by using clay, plaster, wood or foam rubber but a CAD model is needed to enable the manufacturing of the part. As products become more organic in shape, designing in CAD may be challenging or impossible. There is no guarantee that the CAD model will be acceptably close to the sculpted model. Reverse engineering provides a solution to this problem because the physical model is the source of information for the CAD model. This is also referred to as the part-to-CAD process.

Also in the intensely competitive global market, manufacturers are constantly seeking new ways to maximize profits by minimizing the time-to-market of new products. There are many instances where existing designs or replacement parts require modifications and technical details, such as drawings, bills-of-material or engineering data, such as thermal and electrical properties, are not available. Not only will reverse engineering shorten the design cycle, it will minimize waste and improve fit and finish of the final product as well. For example, injection-moulding companies must drastically reduce the

tool and die development times. By using reverse engineering, a three-dimensional product or model can be quickly captured in digital form, re-modelled and exported for rapid-prototyping or tooling. These needs, together with advances in computer processing and new mechanical design software applications, show why design techniques like rapid-prototyping and reverse engineering are growing rapidly.

Reverse engineering can be divided into several categories. For software reverse engineering, an existing program is analysed in an effort to create a representation of the program at a higher level of abstraction than source code. This process is known as design recovery [2, 3]. Software reverse engineering is required for many purposes: to retrieve the design of a program when its specification has been lost, to study how the program performs certain operations, to improve the performance of a program, to correct an error in the program, to identify malicious content in a program such as a virus, or to adapt a program written for use with one microprocessor for use with a differently designed microprocessor. Reverse engineering for the sole purpose of copying or duplicating programs constitutes a copyright violation and is illegal, as it impinges on the intellectual property of the inventor [4]. In some cases, the licensed use of software specifically prohibits reverse engineering.

Hardware reverse engineering involves taking apart a device to see how it works. For example, an existing device can be disassembled and then a similar one can be reproduced. However this process is illegal in many countries, if it involves a competitor's device. In general, hardware reverse engineering requires a great deal of expertise and is quite expensive.

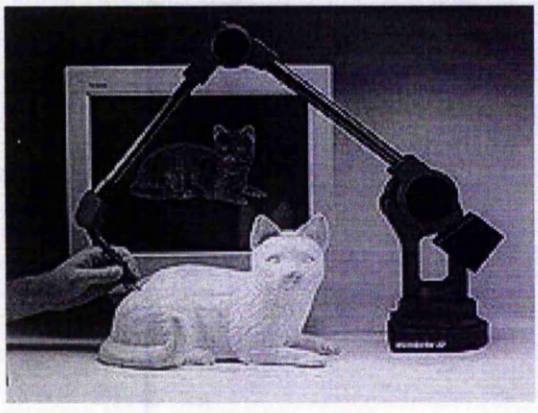

Fig. 1-2: Digitising a cat model using a Coordinate Measuring System.

Fig. 1-3: Digitising a tile object using an optical sensor. The acquired range image is displayed on the monitor to the right.

For manufacturing, reverse engineering involves producing 3-D images of the objects when their blueprints are not available in order to re-engineer them. In the reverse engineering of an object, it is first measured either by a Coordinate Measuring System or an optical sensor, generating a set of 3-D coordinates (see Fig. 1-2 and Fig. 1-3). These coordinates can then be represented with a 3-D wire frame or rendered surfaces and displayed on a monitor as a CAD model [5]. This process is known as 3-D imaging. If more than one set of 3-D coordinates are needed to completely represent the entire object, these results must then be aligned together in a common coordinate system by a process known as *registration*. Further refinements or analysis can be performed on the CAD model before it is exported into a Computer Aided Manufacture (CAM) system to produce the physical object. Many types of object can be reverse engineered using these methods and an example would be the making of moulds for manufacturing tiles. The interest of this research, thus, focuses on the measuring process involved in this type of reverse engineering. In particular it is concerned with the use of optical sensors for 3-D imaging [6].

1.2 3-D Imaging

With the advent of more powerful computers, 3-D imaging has come to the forefront of the engineering world [7]. The domain of 3-D imaging is vast and varied, with many

of today's applications heavily dependent on it, be they industrial, commercial or research applications. Some of these applications include:

1. Visualization and inspection of defects [8], e.g. the detection of dents or ripples on the sheet metal of car bodies;
2. Tool calibration and condition monitoring [9] to measure the slightest variation in radial and axial loads of a device;
3. Geodesy [10], in which to observe, survey and measure the shape and size of parts of the earth;
4. Heritage and archaeology [11], which is for restoration purposes and archiving for posterity;
5. General virtual reality and entertainment, for example the proliferation of 3-D animations [12] in computer graphics and films;
6. Manufacturing with CNC machining [13] to produce replicas of original objects.

1.2.1 3-D Imaging Methods

In order to capture 3-D information, there are broadly two types of method available: tactile and non-tactile (see Fig. 1-4). Tactile imaging, which is mostly used in the field of reverse engineering, involves having a mechanical touch probe moving along the surface of an object while computing the positions of points by establishing their coordinates in 3-D space [14]. This type of imaging produces very accurate representation of the original object, as the probe registers its position each time it comes in contact with the object before moving on. Another advantage is that it does not depend on the optical properties of the object. Unfortunately it is destructive for objects that are very delicate in nature, e.g. ceramics, as the contact will leave depressions on the surface. Moreover accuracy comes with a heavy price: high probing time. It requires a notoriously long period to successfully digitise a complete object. It is also a very costly solution to 3-D imaging as touch probes are very expensive.

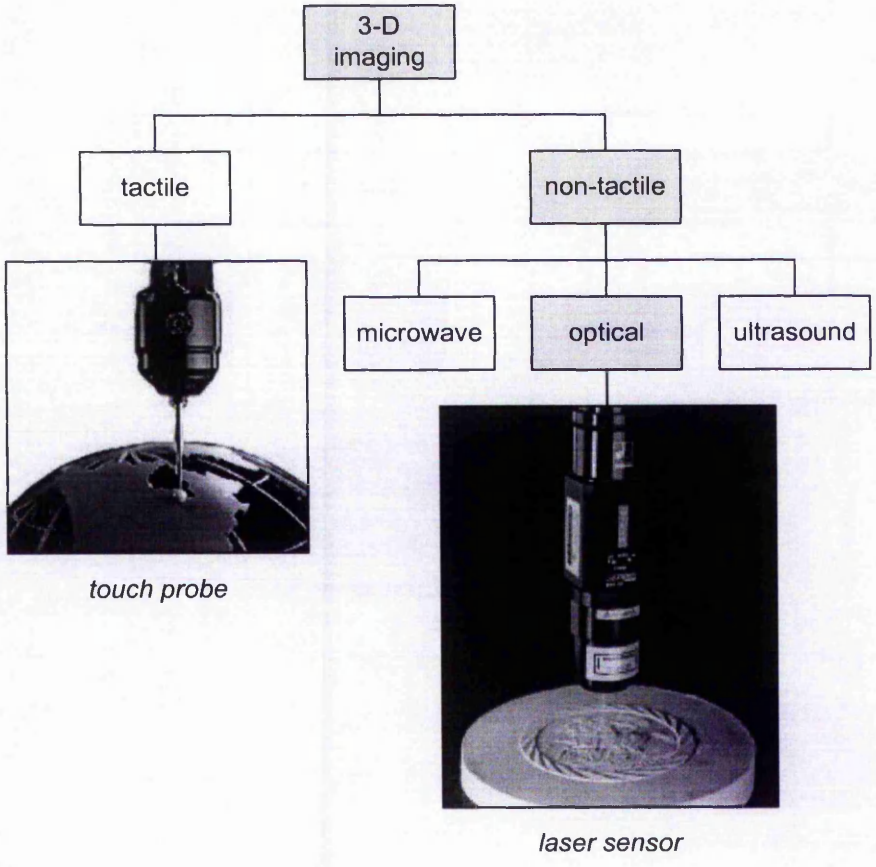

Fig. 1-4: 3-D imaging methods and the focus of this research is shaded.

Non-tactile imaging involves, for example, optical, ultrasound or microwave sensors. Microwave sensors are not appropriate for reverse engineering in industrial production automation, as they do not reach the required angular resolution due to diffraction [15] while ultrasound sensors are highly susceptible to changes in ambient temperature and pressure [16]. They are, however, widely used in the medical field and also for inspection purposes, where image coherence is more important than its resolution. Optical sensors are the preferred choice for 3-D imaging in reverse engineering, as they provide higher lateral and angular resolution [17].

In optical sensors, there are three fundamental measurement techniques: triangulation, phase-shift interferometry and continuous-wave or pulse time-of-flight [18]. These can be further classified into passive or active sensing, depending on the need for a source of illumination. Determining which technique to use depends on the application. More details of these measurement techniques will be presented in Chapter 2. Given a particular object or environment, each of these methods generates depth information,

also known as *range image*, either by means of spatial or temporal periodicity (see accompanying range images from imaging a cat model in Fig. 1-2 and a tile object in Fig. 1-3).

In the field of reverse engineering, the advantages of using optical sensors compared to tactile methods are that they are non-destructive to the object of interest and allow accelerated acquisition of range images with little compromise in imaging precision. It is non-destructive because each detail is traced by means of observing the illuminated surface of an object, unless of course the object's material is photosensitive in nature. Therefore no physical contact is established between the sensor and its designated target, forgoing the need to carefully reposition any mechanical touch probe before taking the next reading, and as such reducing the acquisition time to capture a complete range image. Also without the limitation of reach of tactile sensors, optical sensors can have far greater ranges.

For most optical sensors, uncooperative targets with high reflectivity provide better results than cooperative targets. This is due to the fact that diffuse reflections of an uncooperative target's illuminated region are multi-directional, thus can be consistently detected by the sensor's detecting element, or detector. Reflections of specular surfaces, however, are uni-directional. Therefore for consistent detection of such reflections, a dynamically adjusting detector is required, which will be difficult to realise, given the unknown contour of an object. Consequently cooperative targets, such as polished metal or mirrors, are best treated with a layer of matt paint before commencing the imaging process. Outliers, noise and aliasing are common problems due to the sensitivity of the sensor's detector to ambient illumination and mechanical vibration of its mount. Multiple reflections and occlusion contribute to unreliable readings as well. Therefore several range images may be needed to construct a complete profile of an object.

1.2.2 3-D Imaging with Optical Sensors

Imaging with optical sensors requires two principal components: an illuminated target and a detecting element. The target must be sufficiently illuminated for it to be detected by a detecting element. Illumination can either be natural ambient light or simulated sources. The latter includes laser diodes that emit a collimated beam of light onto the

surface of an object before being traced by the detector. Structured lighting, another form of simulated illumination, is also a popular option in stereoscopic profiling whereby Moiré fringe patterns of two or more contrasting lights are projected onto the surface of an object [19, 20]. Profilometry or interferometry can then be applied to measure depth from the topologically distorted patterns when compared to an adapted reference grating. Lu [21] presented an interesting method of modulation projection by introducing patterns with progressive intensity gradients.

Depending on the requirements of each application, different types of optical sensors are utilized. Several key parameters to consider when determining which type is to be used for a specific 3-D imaging task are:

1. Measurable range from sensor to target;

   Depending on the measurable range, the method of measuring distance fits into one of three categories:

   i. For short-range, an optical triangulation system [22], which measures the position of an illuminated part of an object within the field-of-view of the detector, is appropriate because of its high spatial accuracy and has resolution in terms of microns-millimetres;

   ii. For medium-range, a phase-shift or modulated beam system [23], which compares the phase difference between projected and reflected signals, yields fairly accurate profiles at high speed with resolutions in terms of millimetres-centimetres;

   iii. For long-range, the most appropriate method is pulse time-of-flight system [24], which measures depth information based on temporal periodicity. It calculates the time delay for an intense pulse of light to reach its target and return. This provides photogrammetry and remote sensing results with resolutions in terms of centimetres-metres.

2. Size of illumination and its divergence;

   Some applications require a small but focused light source for high-resolution measurement while others require a larger spread of light source for averaging rough surfaces or for eye safety concerns.

3. Accuracy, resolution and repeatability of optical sensor;

   The accuracy of a sensor is a measurement of the difference that can be expected between a sensor's reading and the actual distance to be measured.

The resolution is the smallest change in distance that a sensor can detect, and is typically a smaller value than the accuracy error. Accuracy may be affected by vibration, temperature, target reflectivity or ambient light, which generally will not affect the resolution. For many applications, resolution is more important than absolute accuracy. Repeatability is a measure of sensor stability over time. Typically, sample-to-sample repeatability will be lower for very fast sample rates, since less time is used to average the measurement. As the sample rate is lowered, repeatability will improve, but this does not continue indefinitely. Beyond a certain point, repeatability will start to worsen as long term drift in the components and temperature changes cause changes in the sensor's output.

4. Sensitivity of the detector;

   All detectors require some light to return to them from the target surface in order to function. The amount of light needed is a measure of the sensitivity of the device. In general, the most sensitive devices are the most costly, and accurate measurements at high sample rates require stronger reflection than for lower sample rates.

5. Surface properties, i.e. reflectivity and specularity, of target and its surrounding ambience.

   The higher the reflectivity of an uncooperative target, the better a sensor's performance will be. High diffusely reflective materials, such as paper or white painted surfaces, work well at all distances. Low diffusely reflective materials, such as black coals or dark painted surfaces, located far from a sensor, may return only a small amount of light to the detector, thus yielding unreliable results. In addition to the amount of light a surface reflects, the way in which light is reflected can affect an optical sensor's performance. Many surfaces are partially specular and partially diffuse. These can be difficult to measure, and the amount of light returning to a sensor's detector may vary greatly with the angle of the target surface.

1.2.3 Optical Imaging in Reverse Engineering

As explained above, there are many applications for optical sensors, ranging from medicine to geodesy. The types of sensor employed also vary with the application. Due to the extensiveness of available optical sensors, it is beyond the scope of this research to cover each and every one of them. Therefore the focus of this research is on optical

sensors that employ triangulation principles and are used in reverse engineering, especially in the manufacturing industries. In such a scenario, the shape of a physical object, preferably an uncooperative target, is first digitally sampled, or scanned, with a selected optical triangulation sensor, yielding a range image in the form of a *point cloud*, which is a collection of 3-D coordinates in Euclidean space. Fig. 1-5 shows an example of a tile object. Fig. 1-6 shows the range image obtained by scanning that tile object with orientation of the sensor at 90° (see Chapter 3 for more details on orientation of the sensor). In most circumstances, a single range image will not be sufficient to fully represent the object of interest. Therefore multiple range images, acquired from different viewpoints, are needed for a complete surface description. These range images will often contain distortions, such as noise and outliers. Current practice involves manual identification and selection of portions, or data sets, of the range image with minimal distortions. These data sets are then aligned and merged under a common coordinate system – a process known as *registration* – to form a complete surface description.

Fig. 1-5: Tile object with flowery motif.

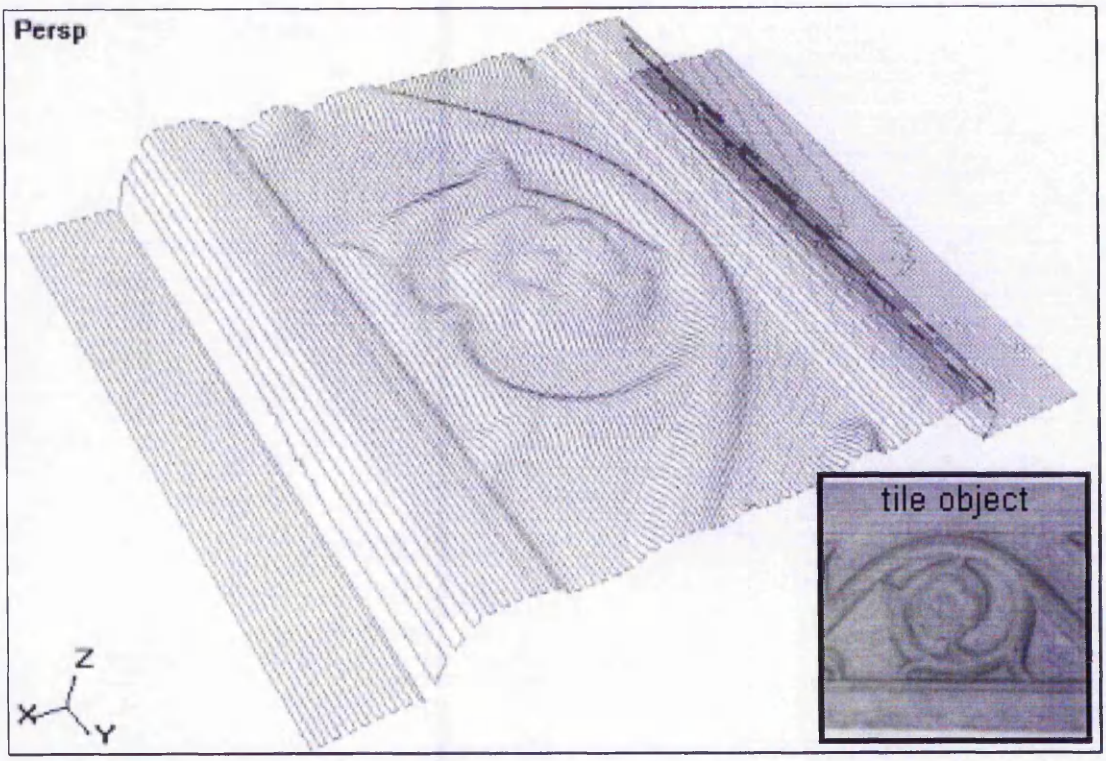

Fig. 1-6: Range image in scanline form from imaging tile object (inset) with orientation of the sensor at 90° (see Chapter 3 for more details on orientation of the sensor).

If there is working knowledge on the position and movement of the sensor with respect to the object of interest, registration can be carried out accordingly. Without this knowledge, registration can only be carried out when the acquired data sets overlap sufficiently. Registration can be performed either interactively or intuitively. Interactive registration usually involves a user who has prior knowledge of the object's description, thus the final registered description has higher compatibility. However many researchers are now focused on intuitive registration of multiple scans. The most common method used in intuitive registration is the Iterative Closest Point (ICP) method, proposed by Besl and McKay [25], in which data sets are iteratively matched point-by-point until they have minimal deviations. This method can be extended using the pairwise local matching and global alignment strategy [26]. Another strategy is iterative matching patches of low curvature on the data sets [27]. A proper registration will yield a digital model with points closely matched to their actual location on the object of interest.

Automated or interactive *surface reconstruction* can then be applied to produce a parametric description, e.g. Non-Uniform Rational B-Splines (NURBS) or featured lines, of the

object [28, 29, 30], rendering it viable for display and manipulation on a CAD system [31]. One of the simplest and most accurate ways is to generate a polyhedral surface, otherwise known as *mesh generation* [32, 33, 34] by connecting neighbouring points to form polygons, e.g. triangular patches. Mesh optimisation and smoothing can then be applied to produce a more faithful description of the surface by reducing, if not eliminating measurement errors. One approach to mesh optimisation is to perform finite element analysis using Genetic Algorithms [35] and another is transformation of surfaces between real space and parametric plane [36]. Hoppe [37] used an energy function to optimise unorganised points. Besides parametric or mesh generation, other methods of 3-D representation include graph theory [38] and volumetric description using voxels [39, 40]. The latter is based on well-established algorithms of computer tomography like marching cubes [41].

The reconstructed model can then be used for visualisation or rapid-prototyping. For the latter, the model is vectorised with a computer system and an accurate or modified replica can thus be fabricated using a CNC milling machine or by means of stereolithography [42].

Fig. 1-7 illustrates the fundamental process in 3-D imaging, from the initial stage of capturing point clouds to replicating the object on a CNC milling machine in the final stage. In between, post-processing, such as generation and optimisation of polygonal mesh, and surface rendering may be involved.

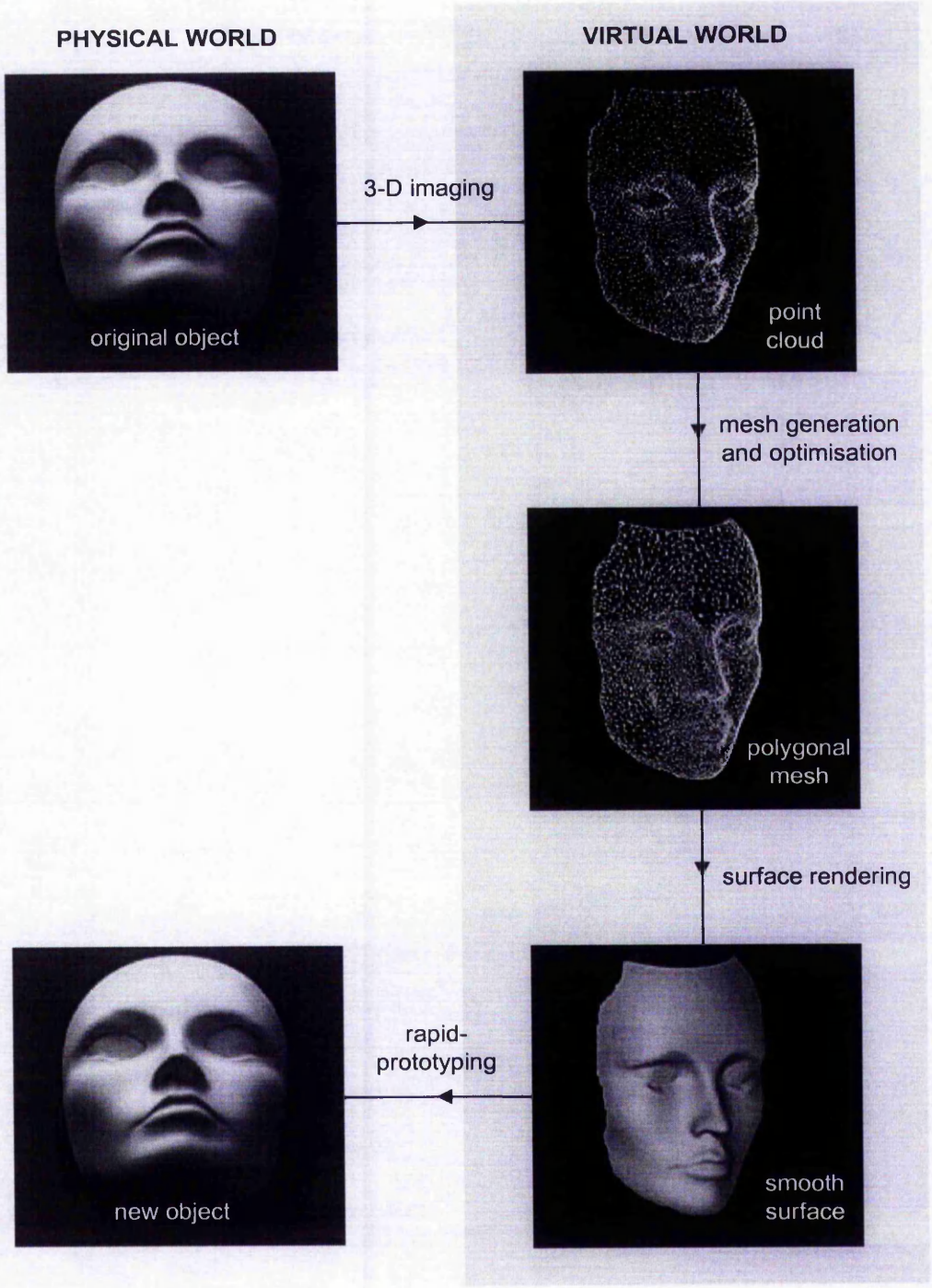

Fig. 1-7: Complete process of 3-D imaging in reverse engineering.

For reverse engineering applications, the following characteristics and properties of optical triangulation systems used in 3-D imaging are desirable:

1. high spatial sampling rate, that is, acquisition of dense coordinate point clouds, especially for complex surfaces;
2. high signal-to-noise ratio, that is, robust against mechanical vibration, surface slopes and discontinuities;
3. high imaging speed, that is, the ability to quickly and accurately profile an object;
4. low costs, dependent on the application;
5. ease of use, that is, the user is able to calibrate and operate the system without much difficulty;
6. automated or highly intuitive tools for fast range image analysis and post-processing of the measured point clouds.

Hence, for reverse engineering, a 3-D imaging system is deemed ideal when it is cost effective, efficient and expeditious in capturing dense and accurate point clouds of varied surfaces.

1.3 Distortions from Optical Sensors

Regardless of which type of sensor is used in 3-D imaging, the raw data or range image acquired is rarely ready for reproduction. There are distortions that need to be dealt with. With optical sensors, distortions can be caused by the detector's high sensitivity to light. The types of distortion depend on the kind of sensors used, e.g. active stereovision sensors using structured lighting generate measurement errors known as waviness – noise due to surface topography – in the fringe pattern [43]. However the work described in this thesis involves the distortions produced by optical triangulation point sensors. A collimated beam emitted from a laser diode is used as the source of illumination and the detector is either a Position-Sensitive Photodetector (PSD) or Charge-Coupled Device (CCD). The measuring principle employed is active triangulation (see Chapter 2). There are several drawbacks to using triangulation-based laser sensors but these are outweighed by the benefits, such as being one of the most cost effective approaches to 3-D imaging. Additionally it is non-destructive to objects because it is non-tactile, a relatively quick imaging process and highly robust against

ambient lighting, temperature and pressure. The properties and characteristics of triangulation will be further examined in Chapter 2.

Before surface registration and reconstruction, existing problems of data loss or distortions in range images (see Fig. 1-8) need to be identified and compensated. Contributory factors include:

1. Vibration of the mounting causes surface noise;
2. Errors in signal processing and calibration of imaging system causes systematic distortions;
3. Shadowing or occlusion of spot image from detector, which can yield systematic detrimental outliers, which are referred to in this thesis as "spikes";
4. Surface properties of the object, such as specularity, translucency and reflectivity, which affect the light received by the detector, and contribute to the emergence of surface noise and more systematic distortions, which are referred to in this thesis as "bow waves". Variations in surface reflectivity of the object can also give rise to another type of systematic distortion, which is referred to in this thesis as "transitional spikes".

Overcoming such distortions in range images is one of many fundamental challenges in 3-D imaging. Some approaches to circumvent this problem are based on a specially trained operator performing interactive manipulation of several range images, which include cropping, merging, segmenting and smoothing. However few researchers have scrutinized the causes of these systematic distortions in range images. A more comprehensive study of the behaviour of triangulation-based laser sensors needs to be carried out to determine the variables that lead to the generation of distortions, particularly in regions of high curvature on the object. This will in turn facilitate the derivation of an efficient algorithm to optimise the imaging process. The optimised range images can then be vectorised and fed into a CNC milling machine for reproduction without the need for manipulation by the specialised operator.

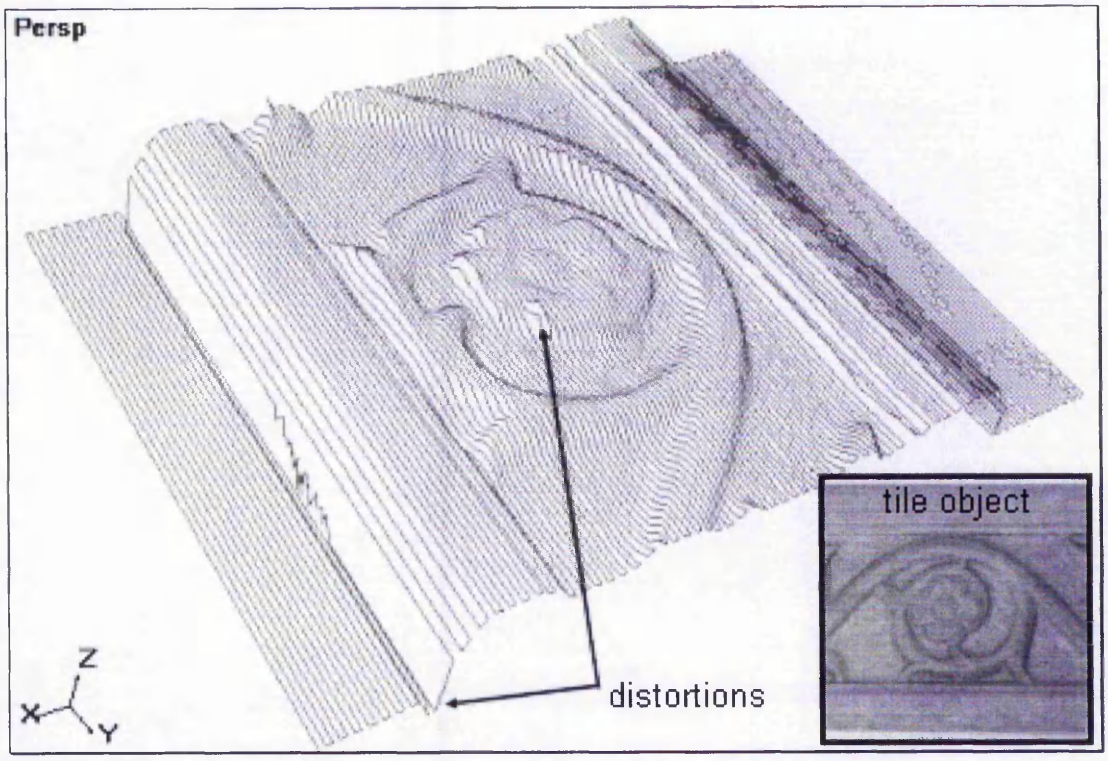

Fig. 1-8: Distortions in range image of tile object (inset) with orientation of the sensor at 180°(see Chapter 3 for more details on orientation of the sensor).

1.4 Aims and Objectives

The work described in this thesis is aimed at investigating distortions generated by a single-perspective optical triangulation sensor, and, using that understanding of the process, develops new compensation algorithms that tackle distorted range images before surface reconstruction.

In order to develop such compensation algorithms, it will be necessary to:

1. Define a precise problem specification;
2. Develop an understanding of the operation of optical triangulation sensors and their interaction with different objects;
3. Develop an understanding of distortions in optical triangulation sensors;
4. Establish the relationship between these distortions and their possible sources;
5. Develop new automated compensation algorithms to reduce these distortions;
6. Evaluate the developed algorithms for multiple objects including a comparison of different strategies.

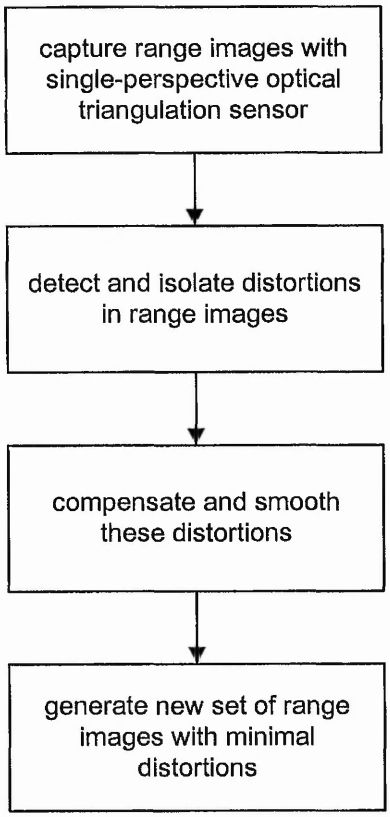

Fig. 1-9: Breakdown of stages of processing involved in this research.

Since there is little research that focuses on the understanding of the systematic distortions caused by optical triangulation sensors, particularly single-perspective sensors, the primary objective of this work is to offer a practical solution to this problem. Therefore the framework of this research includes the fulfilment of the following objectives:

1. Empirical study of range images, collected with triangulation-based collimated beam laser sensors from selected objects;
2. Investigation of the behaviour of data loss and distortion in these range images;
3. Establishment of a relationship between curvatures and properties of objects to data loss and distortions;
4. Establishment of possible strategies for new compensation algorithms;
5. Development of error region identification algorithms for multiple range images;
6. Development of edge detection algorithms based on the identified error regions;
7. Development of new edge-based algorithms for combination of data sets from different range images;
8. Evaluate effectiveness of the optimisation process on simple objects;

9. Evaluate effectiveness of the optimisation process on freeform objects with varied curvatures.

1.5 Organisation of Thesis

This thesis is structured into seven chapters. Chapter 1 introduces reverse engineering and its application in today's society. It then concentrates on reverse engineering using 3-D imaging and the employment of optical triangulation sensors. It also provides an overview of distortions generated when using optical sensors, in particular single-perspective optical triangulation sensors. Furthermore the framework of the research in analysis of distortions and the formulation of new compensation strategies is established.

Chapter 2 outlines the principles of the methods used by optical sensors. It then focuses on optical triangulation, specifically of the single-perspective variety, together with its physical limitations and distortions, such as spot image variation, secondary reflections and occlusion.

Chapter 3 describes the controlled experimental environment used for this work, including calibration of the single-perspective triangulation sensor. The distortions generated on some selected simple objects are then presented. The basis of these distortions is assessed and a comparison is made with circular-perspective sensors.

Chapter 4 provides an overview of compensation techniques for distortions from single-perspective triangulation sensors. A simple smoothing algorithm to reduce distortion in the form of noise is first presented. New compensation algorithms for multiple range images, developed by the Author, are then presented. These new algorithms use error region identification, followed by edge detection and edge-based combination of data sets. Chapter 5 provides a qualitative evaluation of the developed algorithms.

Chapter 6 discusses the work conducted and the achievements of this research. Ideas for future work are also highlighted. Chapter 7 presents the conclusions of the thesis.

Additionally five appendices are provided with the thesis. Appendix A presents the specifications for the optical sensors that were used in this research while Appendix B

highlights some fundamental theory behind active triangulation. Distortions in range images together with raw and processed range images – after applying compensation algorithms – of several objects are presented in Appendix C. Appendix D summarises the developed algorithms into flowcharts. Finally copies of the Author's two published scientific papers [44, 45], which were presented at conferences in 2001, can be found in Appendix E.

Chapter 2

Optical 3-D Imaging

2 Optical 3-D Imaging

As mentioned in Chapter 1, 3-D imaging can be divided into two categories: tactile and non-tactile. For non-tactile optical imaging, it can be further categorised into *passive* or *active* sensing [46]. An imaging system is said to be passive if its operation involves only a detection to recover depth information – that is no energy is emitted for the purpose of sensing, it is only received. Passive sensing techniques are supposed to reflect the way human vision works. Such a system relies on natural ambient lighting, e.g. the sun's energy, to illuminate the object of interest. Passive techniques include stereovision and monocular "shape-from-" techniques, e.g. shape-from-contour or shape-from-shading [47]. Recovering 3-D information from a single 2-D image is not possible. Thus monocular techniques have to add *a priori* information such as surface smoothness to recover 3-D data – a process known as regularization [48]. Stereovision techniques employ two or more sensors, and thus two or more 2-D images are used to recover 3-D information. To deal with disparity between images, the problem of matching common regions between different views must be solved, in which it has been formulated as an ill-posed problem in a general context and is a task difficult to automate. Photogrammetry has long relied on stereo vision and manual processing to recover 3-D information [49].

For an active system, a source of illumination is purposefully projected onto the target and the reflected light is then measured by the detecting element. With a focused signal established on the surface of the target, the positions of 3-D data points can be calculated from the distance between sensor and target with relative ease as compared with passive sensing. Methods of computing this distance depend on the selected measuring principles (see Section 2.1). Advantages of active systems include the ability to obtain measurements at any time, regardless of the time of day or season. Active systems can be used for examining at wavelengths that are not provided sufficiently by the sun, such as microwaves, or to better control the way a target is illuminated. However as an active system requires a source of illumination, this may increase the cost of its use in 3-D imaging. Volume digitization techniques like computerized tomography, magnetic resonance imaging or ultrasound imaging also fall in this category [50].

2.1 Optical 3-D Imaging Techniques

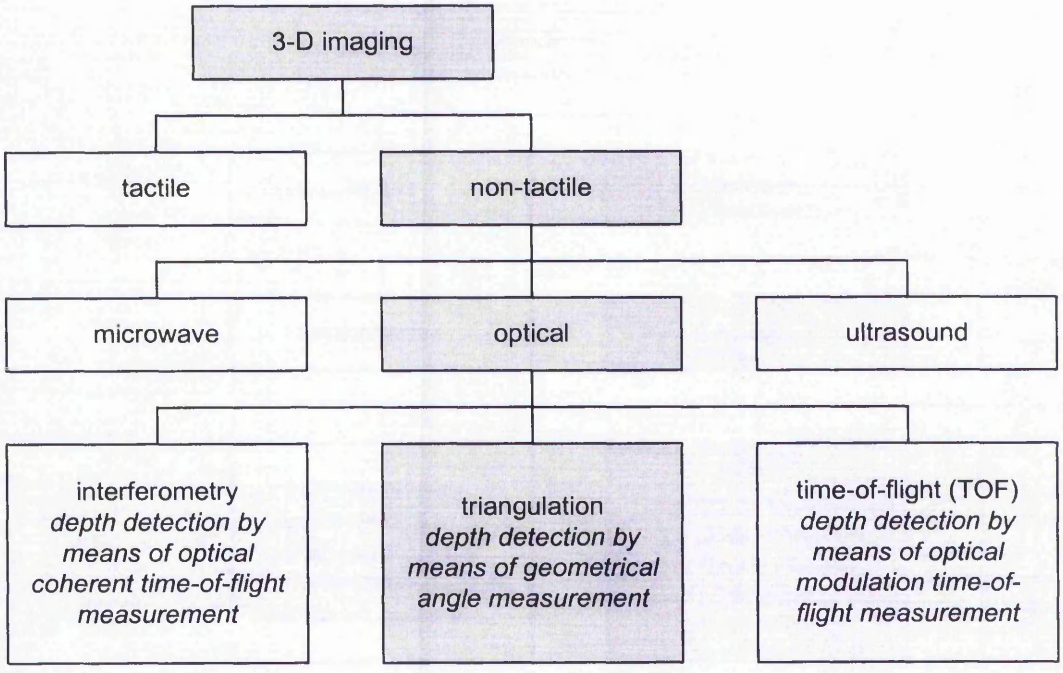

Fig. 2-1: Principles of 3-D imaging and focus of this research.

Fig. 2-1 is an illustration of 3-D imaging methods, with special focus on triangulation as the measuring principle [51].

Interferometry, also known as modulated-beam imaging, works on the principle of deciphering interference patterns in wave propagation. Michelson [52] first demonstrated the practical usage of optical interferometry. Based on the principles that light travels in waves, the phase-shift between the beams of light can be computed when they reach two or more detectors. An interferometer is a device for making such measurements [53]. Though there are many different types and designs of interferometers, virtually all of them operate on the same basic principle. From a beam of light coming from a single source, e.g. laser, lamp, etc., two or more flat mirrors are used to split off different light beams [54]. These beams are then combined so as to interfere with each other, resulting in the formation of the phenomenon known as wave interference. The interference can be constructive or destructive, depending on the phase difference between beams. This interference, or fringe, pattern appears as a series

of bright and dark bands: dark where the two light waves cancel each other out, and bright where they augment each other (see Fig. 2-2).

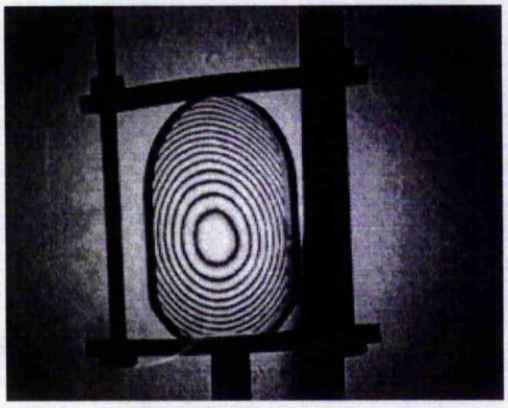

Fig. 2-2: Example of a fringe pattern generated by means of interferometry.

Phase measurement is limited in accuracy by the frequency of modulation and the ability to resolve the phase difference between the beams or signals. As the fringes are only one light-wavelength apart, interferometers are therefore incredibly sensitive – so much so that any vibration, movement, thermal expansion, etc. is picked up as well. Interferometry is typically used in intermediate range applications, for distances from a few centimetres to several metres on uncooperative targets. With cooperative targets, range can be extended to several hundreds or thousands of metres. Therefore these types of system are widely used in astronomy [55] and geodesy.

Another optical measurement technique is the continuous-wave or pulsed time-of-flight [56]. Its operation is not unlike that of RADAR (RAdio Detetecting And Ranging), whereby a radio wave is emitted and a receiver senses the returned energy, which is reflected from the target. Since the speed of radio waves and the time delay between emission and reflection are known, the distance to the target can be determined. LIDAR (LIght Detecting And Ranging) is the optical equivalent or RADAR. LIDARs emit a concentrated light beam onto the target and measure the energy reflected back to the receiver. The intensity or amount of reflected energy measured by the receiver provides the needed information about the target (see Fig. 2-3). With LIDARs, the light source is not a radio wave, but rather it is in the visible and adjacent regions (ultraviolet and infrared) of the electromagnetic spectrum. The light source is generally a laser. Depending on the measuring distance required, there are several types of LIDAR

available [57]. Shorter wavelength LIDARs, or smaller scale laser range finders are effective for much smaller targets. Indeed by scanning the surface of the target, advanced range finders can determine the target's shape and size in addition to its distance [58]. Thus pulse detection systems, directly registering the time-of-flight of a very short laser pulse, are well suited for measuring distances of several metres up to a few hundred metres. They can measure considerably longer distances still, if equipped with appropriate reflectors. Integrated into binoculars, used for velocity measurements in traffic monitoring, for single and multi-dimensional surveying tasks, and for accurately outlining protection areas, these systems are in high demand. The accuracy of these sensors is typically limited by the accuracy with which the time interval can be measured, and the rise time of the laser pulse.

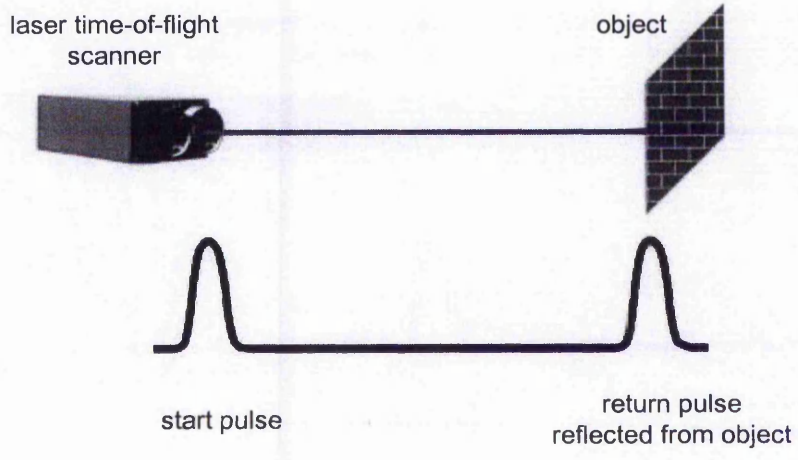

Fig. 2-3: A simple pulsed time-of-flight system.

Among the three fundamental techniques in optical measurement, triangulation is the most widely adopted technique in the field of reverse engineering. It is a fairly simple but effective system for the recovery of depth information, especially in applications that require high precision measurements. A more detailed description of triangulation techniques is presented in Section 2.2.

2.2 Triangulation Principles

The work described in this thesis is based on the use of optical triangulation laser sensor, so the goal of this chapter is thus to provide a better understanding of the theory behind

the system, namely *triangulation principles*. A triangulation sensor may provide the same information as a linear variable differential transformer or tactile probe, but without physical contact with the object to be measured. Triangulation sensors are ideal for measuring the distance to small, fragile parts or soft surfaces susceptible to deformation if touched by a tactile probe. Today, the availability of good components and powerful microcomputers has led to increased industrial use of triangulation sensors. There are two techniques for optical measurement based on triangulation and they are described in the following two sections.

2.2.1 Passive Triangulation

The notion of *passive* in triangulation is similar to the description of passive sensing, in that no man-made artificial light is used for illumination. The object of interest must be sufficiently illuminated by natural or ambient sources, such as sunlight. The sensor's detecting element will then capture the image of the object and compute its depth information. Passive triangulation encompasses *digital photogrammetry*, which is widely used in cartography [59] and industrial inspection. For photogrammetric techniques, at least three different views of a particular point are required to determine its 3-D position. Dynamic processes often require multiple self-calibrating cameras with known relative positions while for static scenes a single camera that takes images from three or more different unknown views is sufficient [60].

Another form of passive triangulation involves the usage of *theodolites*. A theodolite, consisting of a small tripod-mounted telescope, is an instrument for measuring horizontal and vertical angles of its position from an object of interest. It is used for accurate measurements of large-scale objects [61]. A source of illumination, for example, a laser, can be incorporated but such a system would then fall under the second type of triangulation techniques, which is described in the next section.

2.2.2 Active Triangulation

In contrast to passive triangulation, *active* in this context means that the geometrical arrangement of the illumination source is known and can be taken into account in the computation of depth information. The emitted light interacts with the surface of the object and is reflected or scattered towards the sensor's detecting element, or detector.

This detector has an aperture to gather the light and an optical system to detect each part of the surface using a spatially resolving detector. The source of illumination can be structured or diffuse. It can be temporally coherent or broadband. It can be polarized or unpolarized.

Some of the measurement techniques based on active triangulation include focus techniques and shape-from-shading techniques. Focus techniques include confocal microscopy, controlled focusing and defocusing method to determine distance by evaluating the diameter or the intensity of spot image in the focal plane and the Rayleigh depth of focus [62 , 63]. The shape-from-shading technique, also known as photoclinometry, is a method for determining the shape of a surface from its image irradiance and the known position of the camera and the illumination sources [64]. The various types of shape-from-shading techniques include extensions using multiple images with different illuminations or image sequences with moving light sources, known as photometric stereo [65].

The measurement technique used in this research is, however, based on triangulating the distance of a projected laser beam on the surface of an object to a point sensor. The acquisition of a complete range image with a point sensor requires a surface scan of the object of interest. Besides light beam sensors, light sheet or structured light volume sensors can also used [66]. In the case of a light sheet, a 2-D detector is used to detect a reflected light stripe. Therefore only a 1-D scan perpendicular to the light stripe is required for 3-D imaging [67]. Meanwhile light volume triangulation requires no scanning as it illuminates the whole 3-D object to be measured with structured light [68]. The correspondence between directions of projection and of acquisition can then be expressed by means of proper light coding in whole field profilometers such as Moiré technique [69], binary patterns [70], Gray code pattern [71, 72] or phase-shift information [73, 74]. A detailed analysis of the fundamentals of active triangulation techniques using point sensors is presented in Section 2.3.

2.3 Active Triangulation Point Sensors

Consider an optical sensor, commonly known as point sensor, whereby a collimated beam of laser light is projected onto the surface of an object in a certain direction while

the sensor's detector perceives the spot image from a different direction. The angle between these directions is thus known as the *triangulation angle* (see Fig. 2-4). A change in distance of the point on the surface from the sensor will affect the size of this angle (see Fig. 2-5). The distance between the sensor and the object is calculated by determining where the diffusely reflected light falls on a detector. As the spot image on the object moves closer to or further from the sensor, its reflected position on the detector changes accordingly. The sensor electronics then converts this to an analogue signal that can be interpreted as a distance measurement (see Fig. 2-6).

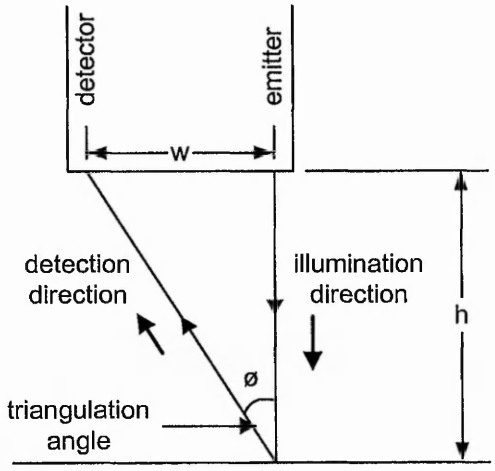

Fig. 2-4: Directions of illumination and detection for a single-perspective sensor.

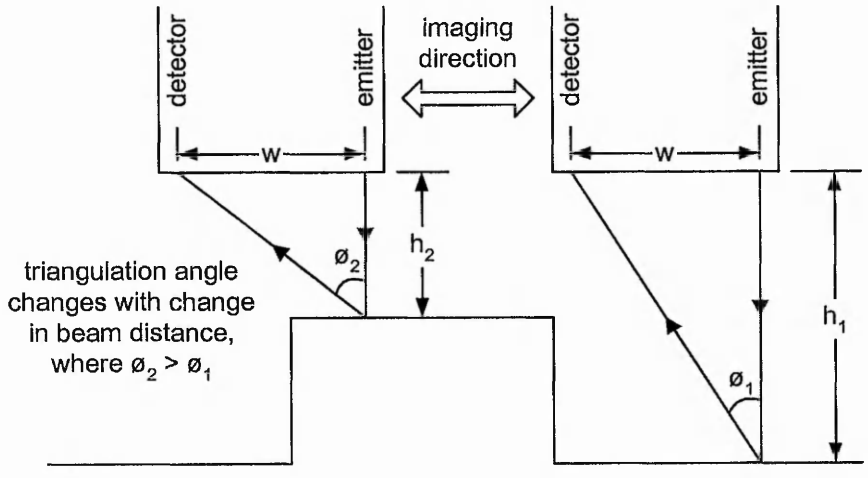

Fig. 2-5: Changes in triangulation angle with changes in distance.

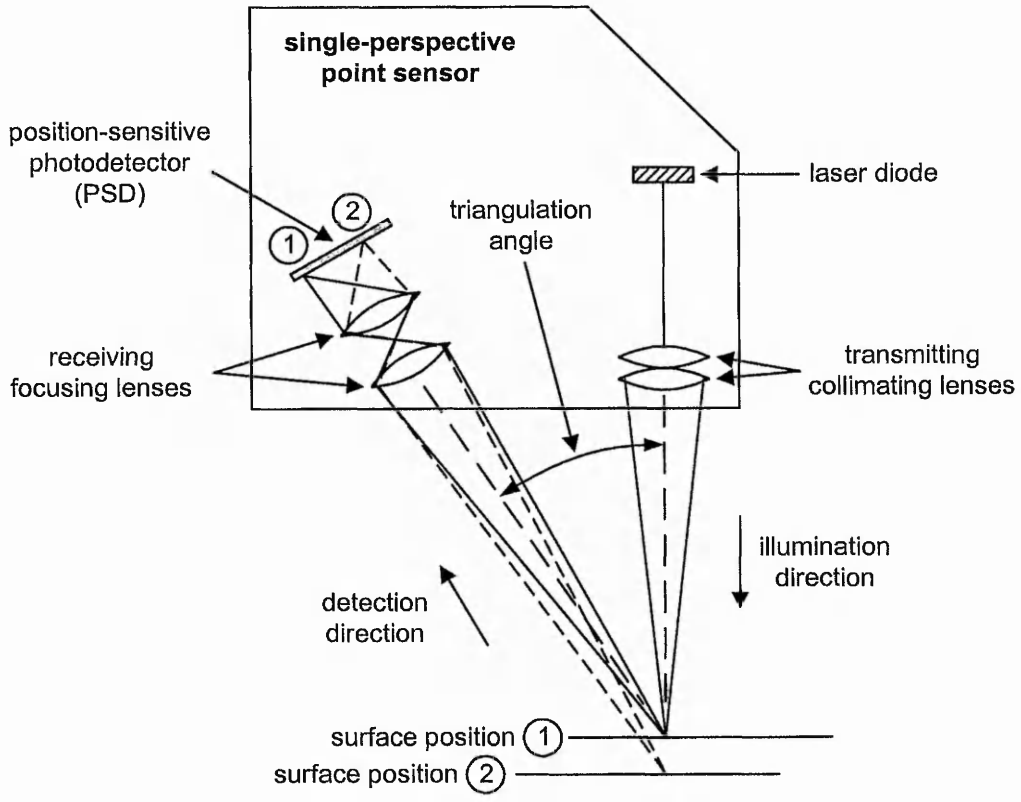

Fig. 2-6: Internal functions of a single-perspective point sensor. The distance measured from reflected light at different points on position-sensitive photodetector as surface position changes.

The formula for distance measurement is thus,

$$h = \frac{w}{\tan\phi} \tag{2-1}$$

where h is the distance of sensor from spot image, ϕ is triangulation angle and w is the distance between emitter and detector.

2.3.1 Specular and Diffuse Reflectivity

Triangulation sensors are either diffuse or specular. The need for two types of sensors arises from differing reflectivity characteristics of materials being examined. Smooth surfaces, such as mirrors or polished metals, are specularly reflective and are classified as *cooperative targets*. Others, such as anodized aluminium or wood, are diffusely reflective and are known as *uncooperative targets* (see Fig. 2-7). Smooth or shiny surfaces typically require a specular sensor whereby the laser illumination hits the target in such a way that

the primary reflected light is reflected into the receiving detector. Steps must be taken to ensure that the laser light does not simply reflect back to the source so the arrangement of emitter and detector is never coaxial. Where it is possible, the position of the light source should be set obliquely to the surface, rather than normal to it. For diffusely reflective surfaces that scatter light, depth measurement is more effective with a diffuse sensor. Therefore the selection of sensor type is dictated by the surface property of the object being examined. A measure of the received signal strength (more = better), or of the amount of time required to achieve the desired signal strength (less = better), is an indication that the right type of sensor has been chosen. However most materials are, optically, a combination of diffuse and specular surfaces. Because triangulation operates by detecting light reflected from the surface, a change in reflectivity affects the level or intensity of light reaching the detector [75]. This in turn affects the measurements obtained, as explained below.

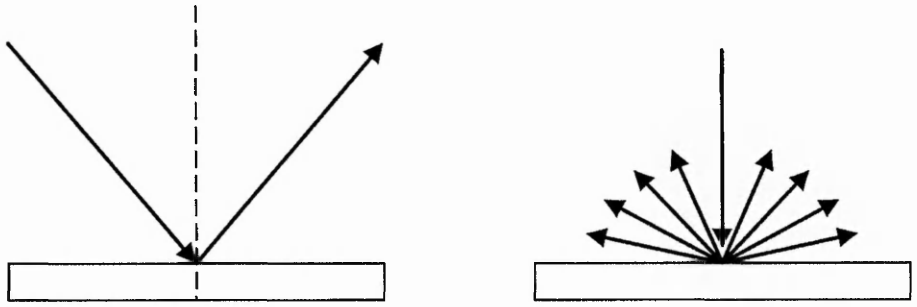

Fig. 2-7: Specular surfaces (a) are mirror like, producing a predictable reflection. Diffuse surfaces (b) are irregular, resulting in scattered reflections.

In cases where the surface reflectivity changes dramatically, such as components with different coloured-regions, the sensor must be able to respond to these changes automatically. Applications where this is a factor require a very fast feedback scheme that controls the laser intensity or some other exposure feature in real time to ensure that stable and reliable data is obtained. This consideration leads to the reason for preferring the small spot size that lasers offer, which is differential reflectivity may shift the *centroid* of the spot image, introducing an error in the measurement. Depth measurement is based on the centroidal position of the reflected spot image on the detector. A sudden change in reflectivity shifts the centroid's position as the spot image

becomes momentarily incoherent (see detector/receiver subsystem in Section 2.3.2 for more details). Another approach, which is commonly adopted in the optical imaging industry, in dealing with varying surface reflectivity is to treat the surface of the object with a layer of diffusely reflecting paint or chemical products. This would ensure uniform reflectivity during the operation of the sensor.

2.3.2 Sensor's Architecture

An active triangulation sensor consists of three subsystems: emitter, detector and electronic processor (see Fig. 2-8). The electronic processor controls the emitter that projects the laser beam. The beam illuminates the object of interest, which reflects light into the detector. The detector transmits data back to the processor, which interprets the data and outputs a measurement.

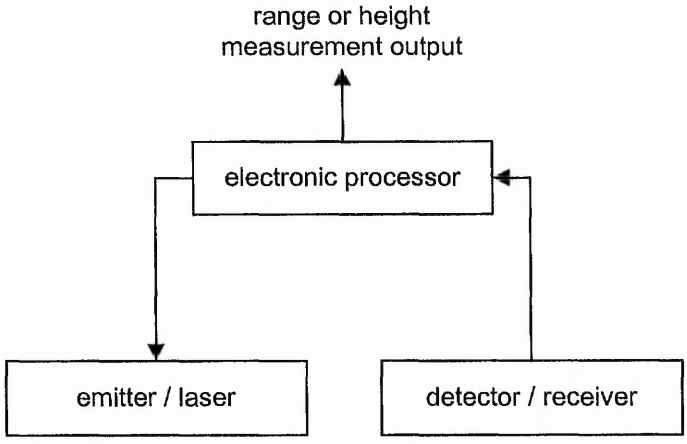

Fig. 2-8: Working subsystems of an active triangulation sensor.

The emitter, typically a laser diode with collimating lenses, projects a beam that illuminates a part of the object of interest. The most popular emitter at present is an inexpensive, low-powered laser diode with a visible beam of wavelength between 670nm – 690nm. The lenses used to manipulate the laser diode output create a small spot image on the surface of the object. The size of the spot is dictated by the optical design, and influences the overall system design by setting a target feature size detection limit. For instance, if the *spot diameter* is 50μm it will be difficult to resolve a lateral feature of less than 50μm in dimension.

It must be remembered that the feature size limitation is the spatial lateral resolution, approximately equal to the spot diameter (see Fig. 2-9). When the beam diameter is smaller than or the same size as the feature, the sensor has sufficient resolution. However when the feature is smaller than the beam diameter, the resolution is inadequate for feature detection and measurement.

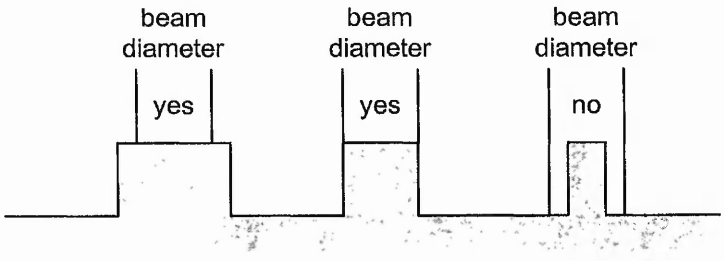

Fig. 2-9: Diameter of beam dictates minimum measurable feature size, or spatial lateral resolution.

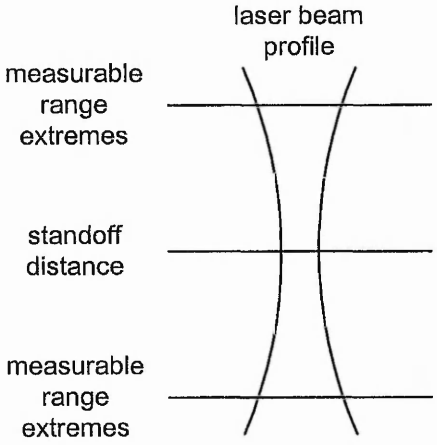

Fig. 2-10: Schematic diagram of a laser beam where its diameter is smallest at standoff distance.

Spot diameter is usually specified in the centre of the measurable range, but the limitations of physical optics dictate that it will not remain at that size throughout the working range. The collimating lenses forms a beam waist at the *standoff distance*; at the extremes of the measurable range the beam diameter is larger (see Fig. 2-10). The same rule of feature size detection holds true at the extremes of the measurable range, but the beam size is larger so the smallest detectable feature size is larger also. The limitation

imposed by the beam diameter on the feature size that can be detected may be an important consideration for some applications.

The detector/receiver subsystem gathers the light reflected from the target and focuses the light onto a detector. The detector then passes the measured spot position to the processor, which calculates the range or height. Of the many types of optical detectors available, two are most commonly used for laser triangulation sensors: position-sensitive photodetector (PSD), and charge-coupled device (CCD). Each type has limitations and capabilities.

PSDs are analogue detectors and are available in one-axis or two-axis forms, with single-axis types generally used in triangulation sensors. The PSD is a single element detector that converts reflected light into continuous position data [76, 77]. The detector chip has outputs at both ends, and the amount of current from each output is proportional to the position of the reflected spot on the detector. If the spot is in the middle of the detector, the two outputs will be equal; as it moves off centre, the two outputs change and spot position can be calculated from the relative change (see Fig. 2-11).

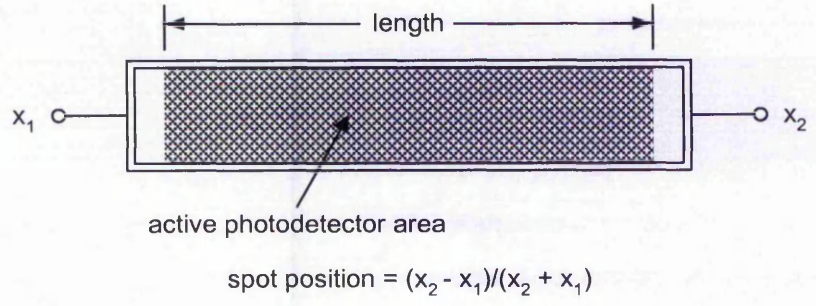

Fig. 2-11: Position-sensitive photodetector produces two electrical current outputs that vary in relation to spot position.

One advantage of PSD-based systems is that they provide the highest data rates, up to 500 kHz. PSDs are efficient and the processing required to get an answer is simple. They also have the fastest rates of gain control – an important consideration when dealing with surfaces of varying texture, colour and reflectivity. Output will be given regardless of the intensity distribution of the spot. To an extent, this removes the effect of laser speckle from the system, albeit in a somewhat questionable manner. Speckle is an optical noise effect that limits the ability to determine true spot position.

One disadvantage of PSDs is that the detector determines the centroid of the spot image. If two spots are present the detector will report a single centroid of both spots. Another drawback is that PSD systems are very sensitive to spot intensity. This is inherent in the detector and can be accommodated by additional circuitry. The effect of this sensitivity is that if the spot intensity changes while the spot position remains the same, the calculated position of the spot may change.

CCD detectors are essentially a form of television camera and come in one-dimension or two-dimension forms. In most simple triangulation sensors, a single-dimensional CCD is used. The detector consists of a single row of discrete photodetectors, often referred to as pixels, and is thus known as a pixelized array detector, sometimes referred to as a digital detector. The term digital is used because their output is composed of discrete voltages representing the amount of light on each element of the detector [78]. A 128-element detector consists of 128 discrete samples that constitute the output signal. The sensor electronics determine the centre of the imaged spot for triangulation processing (see Fig. 2-12).

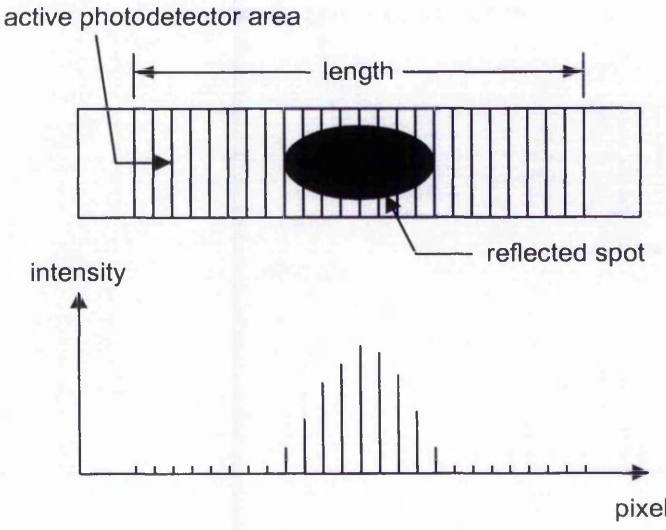

Fig. 2-12: A pixelized array detector produce a series of discrete voltage outputs that vary depending on the amount of light detected by each element of the array.

Pixelized array detectors have several advantages. First, the output of the sensor can be used to obtain light levels as well as show any stray light effects. The discrete intensity distribution of the reflected spot allows the user to truly understand the nature of the

material or part being examined. There are many cases, such as threads or transparent materials, where there will be multiple spots on the detector. Without an array detector the user may be unaware of this. Observing the detector output on an element-by-element basis allows the user to understand the application better. Further, analysts can filter or process the image for their unique needs, such as performing weighted centroid calculation to determine the position of the spot. This can remove unwanted multiple spots, reflections or other light.

The chief disadvantage of the CCD detector, specifically the array detector, is that it is slower than a PSD. Gain control in CCD-based sensors is not as fast as in PSD-based sensors, a drawback in applications where surface reflectivity changes rapidly. Therefore they require more post-processing than do PSDs. Furthermore array detectors are usually larger than PSDs, making for a larger sensor package that may present integration problems.

A sophisticated version of the CCD sensor is available that collects data at multiple points in a single frame, generating contour information along a line of the part being inspected. This sensor projects a line of laser light onto the surface rather than a single point. It uses a two-dimensional CCD as the detector. The image of the laser line on the detector maps out the contour of the surface. Analysing multiple points along the laser line using the triangulation equations generates a profile of the part. The sensor thus generates a 3-D map as the laser line moves across the surface of the object.

The processing electronics varies according to the type of detector used in the sensor. The amount of post-processing that can be performed depends on the amount of information available from the detector. For example, PSDs provide two electrical current outputs that are proportional to the position of the reflected spot on the detector. These currents are first converted into a voltage signal before being quantized into a digital signal by an A/D converter. The only other information that can be derived from the PSD is that the two outputs can be added together to measure the total optical power incident on the detector. But there is no way to determine any of the characteristics of the spot distribution or even the total number of spots on the detector. On the other hand, an array detector provides a large amount of information for post-

processing. The user can observe and manipulate multiple reflections, perform thresholding, and execute specialized digital filtering [79].

2.3.3 Sensors with Different Perspectives

Two types of such sensor were made available for the Author: single-perspective triangulation point sensors of differing range from Matsushita NAIS and a circular-perspective triangulation point sensor from Wolf & Beck Sensorik (see Fig. 2-13). The former detects a projected spot image on the surface of an object from a single viewpoint PSD, encased together with the laser diode emitter. The circular-perspective point sensor, however, does not exactly employ a circular PSD but rather the detector is segmented into eight PSDs placed in a circular configuration surrounding the emitter. Implicit averaging between these detectors is thus used to compute depth information.

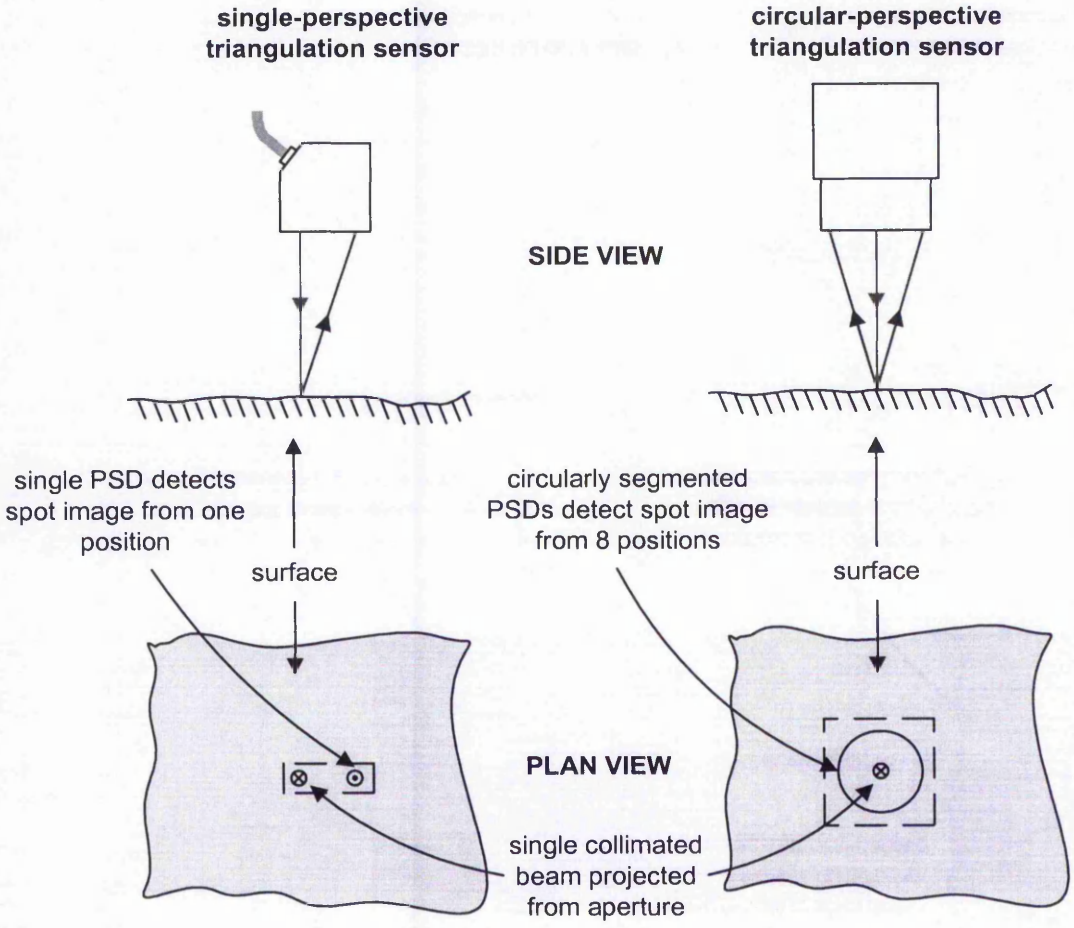

Fig. 2-13: Comparison between single-perspective and circular-perspective laser triangulation point sensors.

2.4 Potentials and Limitations of Active Triangulation Point Sensors

Besides being non-destructive, point sensors are less susceptible to changes in ambient temperature, lighting and pressure due to their collimated beam of light, as compared with structured light methods. They also provide a wide measurement range, dependant on the intensity of the beam and the sensitivity of the detector. As acquisition of depth information is based on spatial instead of temporal periodicity, the electronics for processing are less complicated and as such they are more cost-effective.

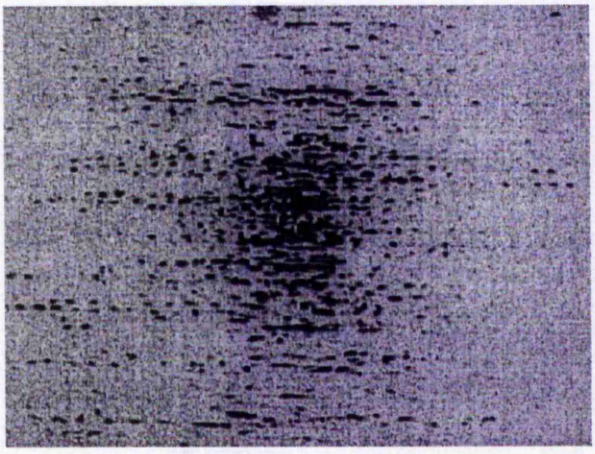

Fig. 2-14: Photograph of spot image after reflection from a rough surface [81].

One of the weaknesses of point triangulation is that it is not robust against spot image variation. There appears to be localization error from a scattered spot image, known as *speckle* on rough surfaces [80]. The shape of the spot image depends on the unknown *microtopology* of the surface [81]. As the spot image is unfocused, the detector would, in most cases, yield an unreliable signal in the form of noise, which is then processed by the sensor's electronics. Therefore depth information of an object acquires some random noise in its readings (see Fig. 2-14).

The influence of the colour of an object, or the material an object is made of, is important in ensuring that uniform depth information is recovered by optical triangulation sensors. Contrasting colours would affect the intensity of the spot image as it moves along the surface of the object. An abrupt change in intensity translates to incorrect readout by the detector. Also specular reflections in cooperative targets may

render the sensor's detector ineffective, as it is not angled correctly for proper readings. Therefore it is preferable if the object of interest has a homogeneously diffused surface, and if that is not the case, it should be treated to be so. Transparency and translucency, whereby the spot image penetrates the surface of an object to a certain depth before reflection, would also yield unreliable depth information [82].

Another drawback of triangulation is that of stray reflections, where the projected spot image on a highly reflective surface results in a small amount of stray light reflected to the detector. The combination of such stray reflections with the primary spot image could cause the detector to give out erroneous signals [83].

In triangulation, illumination and detection are often not coaxial. Hence some part of the object is either not illuminated or the illuminated spot is occluded from the detector's field-of-view. For example, a single-perspective point sensor with a particular orientation can suffer from significant distortions near the steep sides of an object (see Fig. 2-15(a) and Fig. 2-16(a)). With a different orientation of the sensor, however, these distortions cease to exist (see Fig. 2-15(b) and also Chapter 3 for more details on the relationship between orientation of the sensor and significant distortions). The readings, if any, from the sensor during *occlusion* of the spot image by a steep side of an object are unreliable, as will be presented in Chapter 3. For a circular-perspective point sensor, however, the spot image will not, in most cases, be completely occluded due to its extended viewpoints with PSDs located around the emitter (see Fig. 2-16(b)).

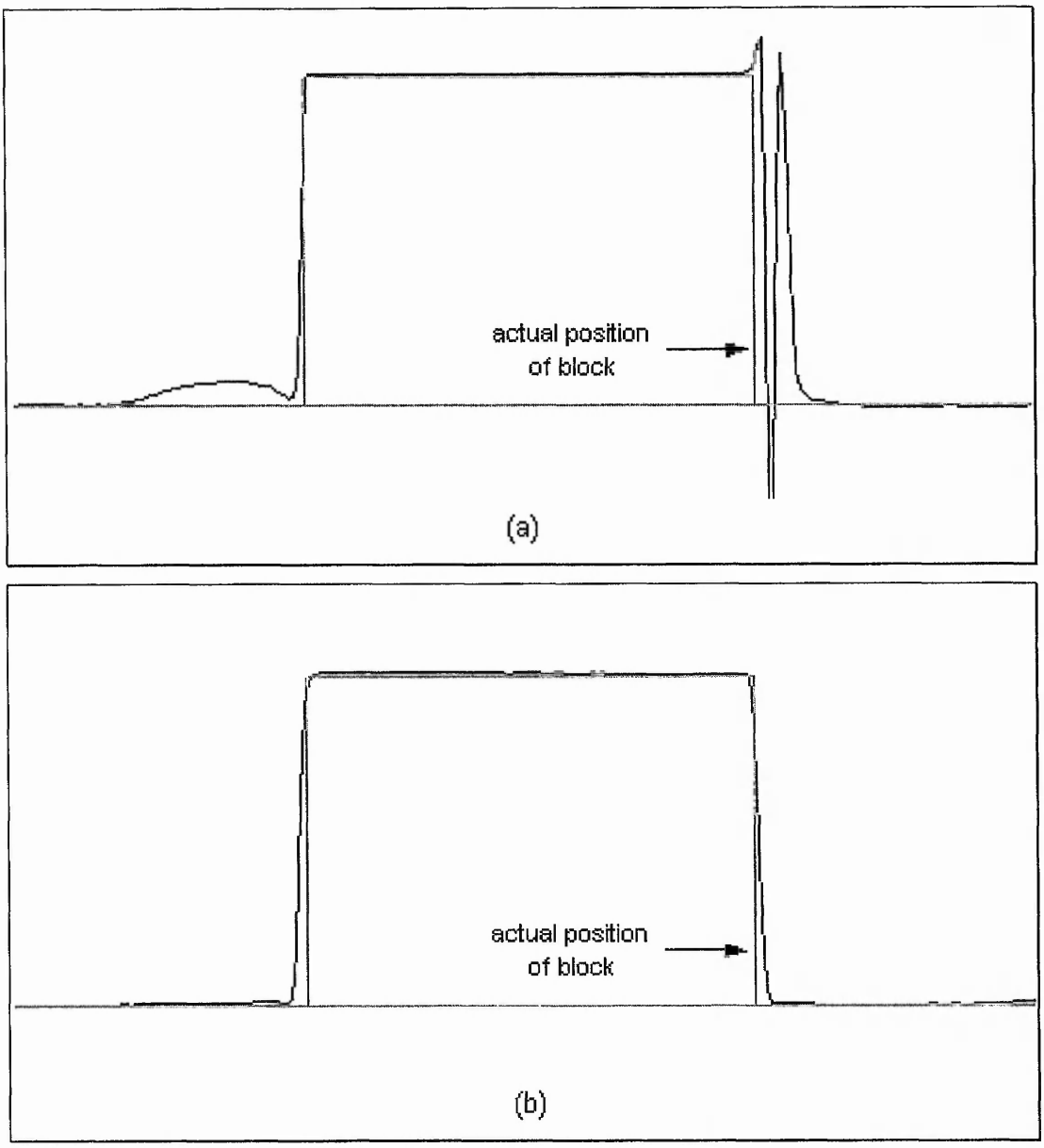

Fig. 2-15: Scanlines of a block (a) with significant distortions where orientation of the sensor is at 0° to scanning direction and (b) without significant distortions where orientation of the sensor is at 90° to scanning direction.

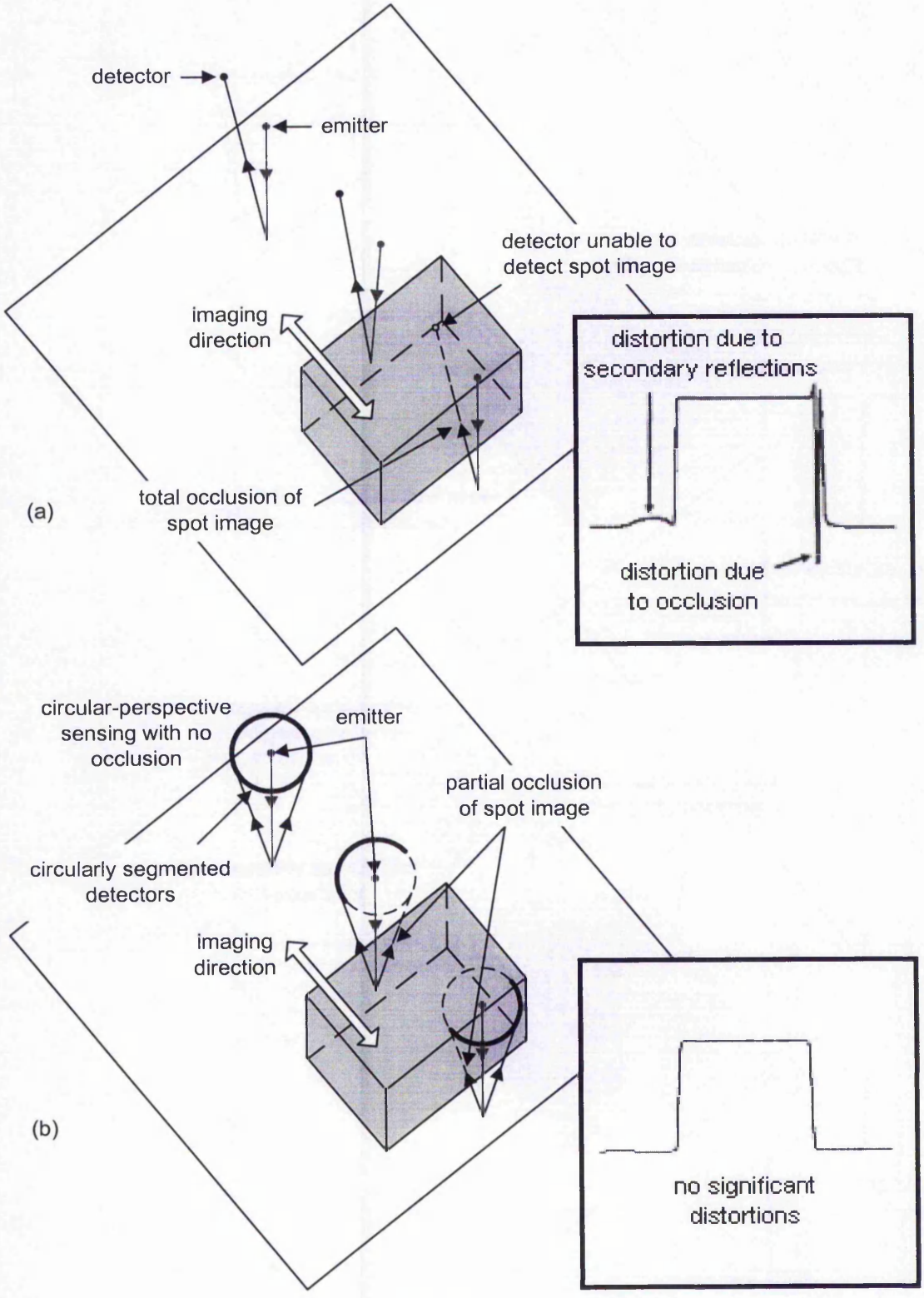

Fig. 2-16: Schematics and their associated output diagrams in the form of scanlines (see insets) of distortions suffered by (a) a single-perspective triangulation point sensor and (b) a circular-perspective triangulation point sensor.

2.5 Previous Approaches to Dealing with Distortions

In order to obtain a good digital representation of an object of interest, the underlying distortions need to be addressed. A digital representation filled with distortions is not of much use for either visualisation or reproduction purposes. Therefore to reduce these distortions, interactive and automated approaches have been explored.

Distortions generated can be categorised as either stochastic or systematic. Stochastic distortions, also known as noise, may appear due to random measurement inaccuracies, such as mechanical vibration of the testbed or weak source of illumination. Ensuring that the system is set up in a conducive experimental environment whereby the optical sensor is mounted on a platform that has sufficient damping can reduce some of this distortion. It is also preferable that minimal stray light is introduced during the imaging process. To further reduce noise, post-processing of the range images can be applied. Methods such as wavelet transform that allows multi-resolution feature selection and extraction [84] or smoothing based on an approximation of a mesh by circular arcs [85] can be employed.

Systematic distortions will occur if there is an error in the calibration of the system. For example, selection of the wrong scaling will lead to consistently false distance measurements. Therefore the setting up of the system must be meticulous to prevent this type of distortion. Surface properties of the object of interest, such as highly contrasting surfaces, also impart systematic distortions, which can be prevented by ensuring homogeneity in surface reflectivity. This can be achieved by treating the object with a non-permanent coating prior to any imaging. Orientation of the sensor with respect to object of interest will produce systematic distortions at certain regions of the scan. This is further discussed in Chapter 3 of this thesis. Strategies to reduce systematic distortions due to sensor's orientation include planning the optimal orientation and path for laser scanning [86] or employing sensors with multiple detectors with intrinsic averaging. Another procedure for removing significant distortions is to simply trim them and replace the discarded values with new interpolated or averaged values. Such an approach, however, will inevitably remove any detail in those trimmed regions as well.

2.6 Summary

Optical imaging is being used increasingly in reverse engineering. Many techniques have been discussed. Interferometry and time-of-flight systems provide good results for medium-range and long-range recovery of depth information. However they have lower resolutions than triangulation systems. This is due to the high sensitivity of detectors used in a triangulation system to detect even small changes in distance.

For imaging purposes, an active triangulation sensor is a simple yet highly functional device, which consists of three parts: emitter, detector and electronic processor. The emitter illuminates a small part of the object of interest. The illumination is then diffusely reflected towards the detector. Changes in elevation or distance between sensor and object affect the position of the reflected image on the detector, which is processed electronically by the internal circuitry of the sensor. The output signals of the detector can either be analogue or discrete, depending on the type of detectors being used. Discrete signal detectors are slower to produce results, as more post-processing is needed to compute and filter out the final output. However they are more accurate than analogue signal detectors because they are less susceptible to misinformation when faced with multiple spot images and varying intensity of the spot image.

The study of triangulation principles, especially that of active triangulation, is critical in the understanding of distortions yielded by such systems. This chapter provides the required background regarding active triangulation point sensors, which have been used in the research described in this thesis. The aforementioned potentials and limitations of triangulations pave the way for a detailed empirical study of distortions in Chapter 3.

Chapter 3

Distortions from Optical Triangulation Sensors

---

3 Distortions from Optical Triangulation Sensors

3.1 Scanning Environment and Calibration

The development of new compensation algorithms for distortions requires a detailed understanding of how optical triangulation sensors are used for collecting range images. Chapter 2 describes the internal functions of an active triangulation point sensor and highlights its potentials and limitations, which give rise to some distortions. The algorithms developed in this research are concerned with 3-D imaging using one type of such sensor, specifically single-perspective point sensor. These sensors are extremely cost effective compared to more complex 3-D imaging methods, such as camera stereovision system. Also when compared to the more expensive circular-perspective triangulation point sensor, the single-perspective version offers more diversity in terms of selective post-processing instead of being limited to intrinsic hardware averaging as employed by the circular-perspective model, which may remove some intricate details from the object of interest. This chapter explains the types of distortion generated when using a single-perspective active triangulation point sensor. By understanding the cause of these distortions, new compensation algorithms can be formulated to reduce their effects, resulting in range images that remain truer to the original object of interest.

3.1.1 Scanner Selection and Scanning Environment

The scanning system used in this research includes laser analogue point sensors from Matsushita NAIS. Two models of different measurable ranges were available for the empirical study of distortions: ANR1115 with range (130 ± 50mm) and ANR1182 with range (80 ± 20mm). Due to the latter's shorter range, and hence higher resolution, it has normally been used, as distortions were discovered to be similar to those when using ANR1115. These two models are single-perspective active triangulation point sensors where a single collimated beam of Class 1 laser – with wavelength 685nm – is projected from an emitter, which is a laser diode. The spot image on the surface of the object is then detected by the detector, which is a PSD, housed in the same casing with the laser

diode. Some samples were also collected using a circular-perspective point sensor, model OTM3-20, which is manufactured by Wolf & Beck Sensorik (see Appendix A for details).

These laser sensors were mounted on a CNC machine, supplied by Pacer Systems (UK) Ltd, with three degrees of freedom (DOF), translating along *xyz* axes (see Fig. 3-1). Soft sponges were used to dampen mechanical vibration, reducing its contribution to stochastic distortions in range images. The whole experimental rig was then placed in a low lighting environment, reducing the possibility of stray light interfering with the readings by the sensor's detector. Ideally the detector should only detect the spot image projected by the emitter onto a surface with high diffuse reflectivity.

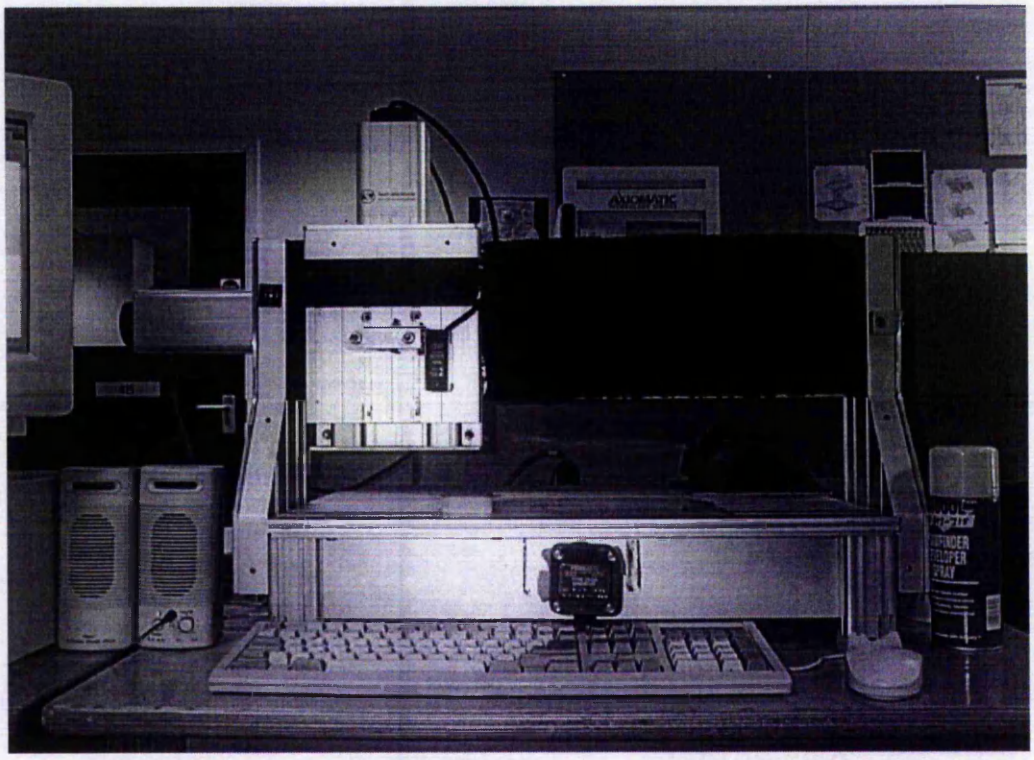

Fig. 3-1: Experimental rig for investigation of distortions in range images.

Axiomatic Technology (UK) Ltd's Scan3D software was used to operate the whole scanning procedure, from calibrating the experimental rig to saving the captured range images. The experimental rig was set up according to the type of sensor that was

mounted. For example, parameters like Scan Height Adjust[1] and Scan Speed[2] were maintained for all scans of a particular object. This is to remove any possible disparity in the scanning, which may contribute to systematic distortions or some perceived errors. Scan3D software was used to produce only raw range images for the analysis (with no prior modification or enhancement). Depending on the details needed from an object, the separation of points to be collected from within the same scanned area can be adjusted along both x and y axes.

The complete scanning process for an object is as follows:

1. The selected laser sensor is mounted securely on the CNC machine;
2. The sensor's starting point, known as the *origin*, is then defined. When collecting multiple range images of an object, the origin will be used for registration because the multiple ranges share this common coordinate;
3. The experimental rig is then set up to determine the density of 3-D points to be collected, scan speed, effective measurable range, scanning direction, and other relevant parameters;
4. The object is placed on a planar surface. Together with the planar surface, it is treated with a non-permanent coating of diffusely reflective spray if it is specular, or is of low reflectivity, or has highly contrasting colours. This is to ensure homogeneity in surface reflectivity, thereby reducing some of the possible stochastic and systematic distortions;
5. A scan region, where 3-D points will be collected, is defined. This scan region would need to cover an area wider than the area occupied by the object for analysis and compensation purposes;
6. The lowest and highest points of the scan are then defined. The former is important in determining the scaling and calibration of the assigned lowest point to zero value upon completion of a scan. The planar surface on which the object lies is assigned the lowest point and hence, upon completion of a scan, the base of the range image, which is the planar surface, is shifted to zero. The highest part of the object is assigned the highest point. The highest point is crucial in ensuring the object is within the sensor's measurable range;

---

[1] Scan Height Adjust ensures the sensor is placed within the measurable range from the object of interest.

[2] Scan Speed determines the CNC's mounting speed translating along the selected axis.

7. The scanning process then begins whereby the sensor will traverse laterally along either x- or y-axis, with z-axis fixed. A *scanline*, which is a line of 3-D points, is recorded by the Scan3D software for every complete translation of the sensor along the chosen direction. This procedure is repeated for other scanlines until the entire defined scan region has been covered;
8. The acquired range image is then saved as a raw point cloud so that further post-processing can be performed;
9. For multiple range images of an object, the sensor is set to a different orientation and then its position is adjusted until the spot image is again on the defined origin;
10. Maintaining the initial set up parameters of the experimental rig, steps 5 – 9 are repeated until all the required range images are acquired.

Upon completion of the scanning process, the collected range images can be used in the analysis of possible distortions. The understanding of the formation of these distortions will thus aid the development of new compensation algorithms. However it is difficult to study the causes of distortions when objects to be scanned have complex details. Therefore initially simple objects with primitive geometry, e.g. rectangular blocks (sometimes with rounded corners) or circular blocks, were used. Objects with more complex geometry, also known as *freeform objects*, were used to evaluate the algorithms developed.

Before commencement of the scanning process, it is essential to ensure the experimental rig and the mounted sensor are set up and calibrated appropriately. This is to remove their contributions of processing error by introducing artefacts, which may be perceived as systematic distortions, in the acquired range image. The following section highlights one such error and its generated artefact.

3.1.2 Scan Height Calibration

When a spot image is detected by the sensor's PSD, its distance is calculated based on output voltage of the PSD (see Chapter 2). This voltage is then quantized into discrete values with an A/D converter. Each of these values is then scaled according to the sensor's measurable range. An empirical study was thus conducted with objects of varying heights in order to check for correct scales in the calibration of scan height measurement.

For an initial experiment, pieces of Perspex, painted maroon, with a thickness of 5mm, were stacked together on a piece of white A4 paper. A scan region was then defined to cover the required heights for this initial analysis (see Fig. 3-2). Upon completion of the scanning process, a scanline, extracted from the acquired range image, was plotted. With increasing height, it can be seen that there is a systematic increase in the discrepancy between measured height and true height (see Fig. 3-3).

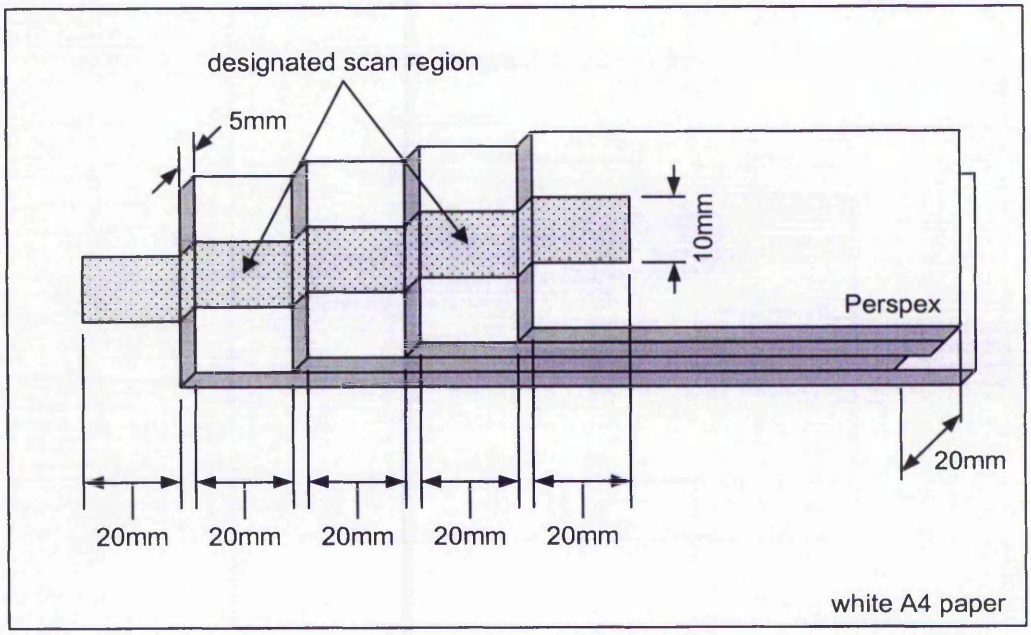

Fig. 3-2: Layout of Perspex pieces for analysis of scan height calibration.

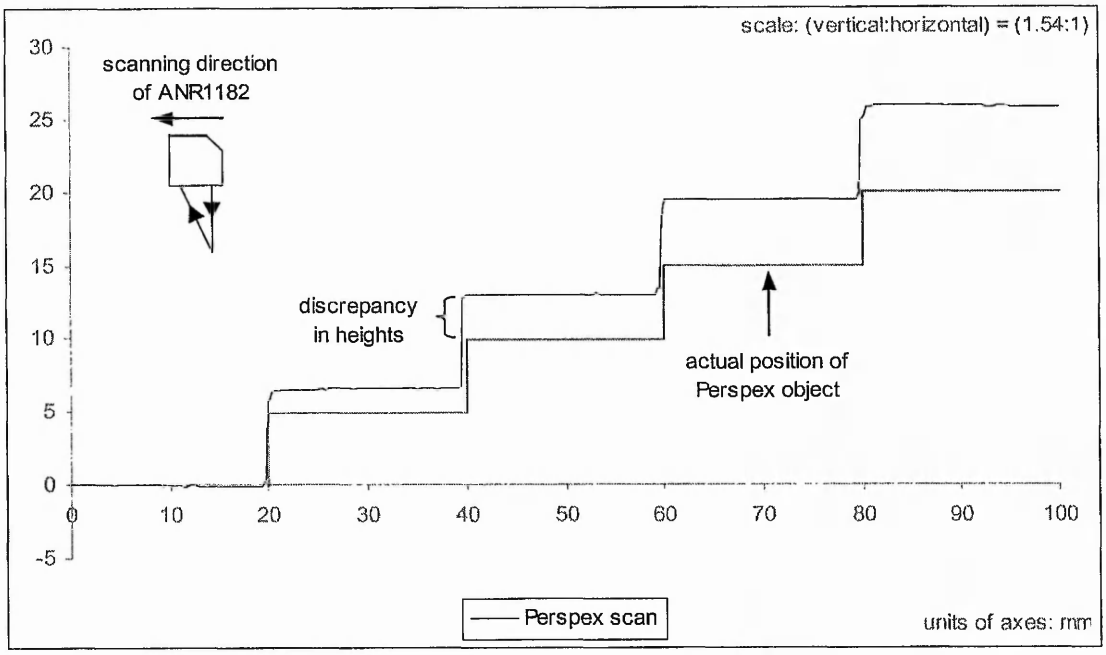

Fig. 3-3: Discrepancy in height between scanline and actual position of Perspex object (scale is increased for greater clarity).

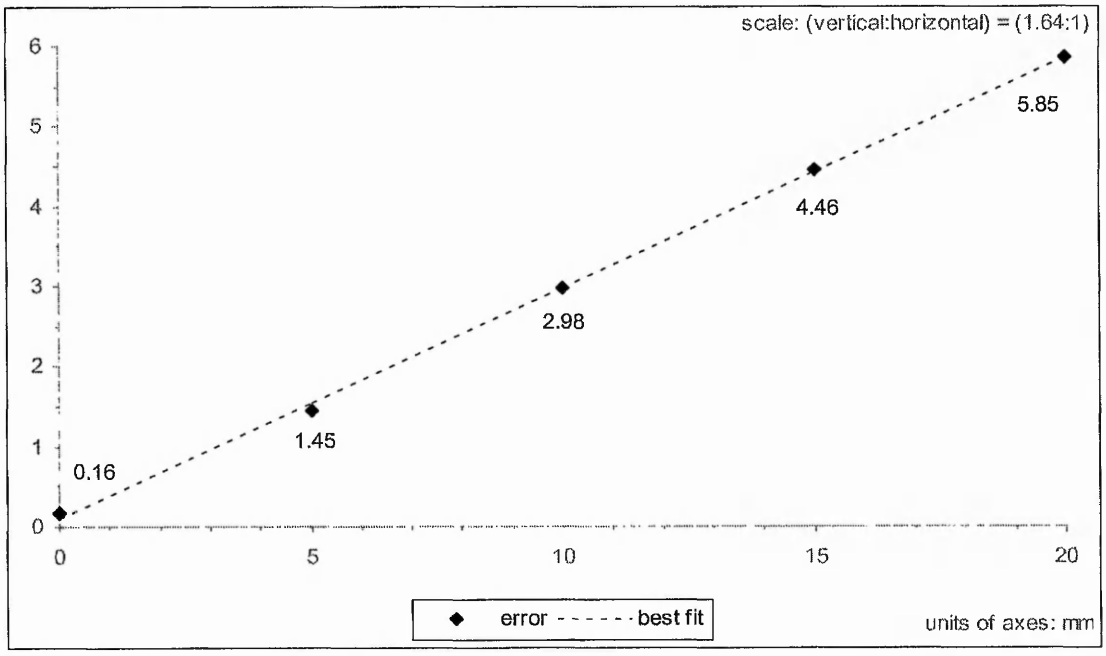

Fig. 3-4: The averaged offset of height for a scanline has been plotted against actual height. A least squares fit shows that the effect is proportional to the actual height.

In Fig. 3-4 each error point represents the mean value of differences in height for each elevated piece of Perspex. A straight line can then be fitted using the least squares method. Therefore it can be deduced that the error in height from the scan is proportional to the height being measured. This systematic distortion is attributed to an error in calibration of the sensor, which can be corrected by adjusting the scaling prior to any scanning.

After proper calibration, a single piece of Perspex was scanned. Then another piece of Perspex was stacked on top of the first and scanned. This process was repeated until there were four stacked pieces of Perspex. Plots of scanlines of these four processes illustrate their close fit to the actual positions of the Perspex object (see Fig. 3-5). However the scanlines in Fig. 3-5 have more noticeable surface noise than the scanline in Fig. 3-3. This is because for Fig. 3-3, the Perspex object, which was painted maroon, was treated with a non-permanent high reflectivity coating while those in Fig. 3-5 were not (as it was not expected to affect the observation of discrepancies in scan height measurement). As discussed in Chapter 2 on the structure of a PSD, its high sensitivity to changes in intensity of the spot image results in noisy data, especially when the spot image is less coherent on surfaces of low reflectivity, as in the case of Fig. 3-5.

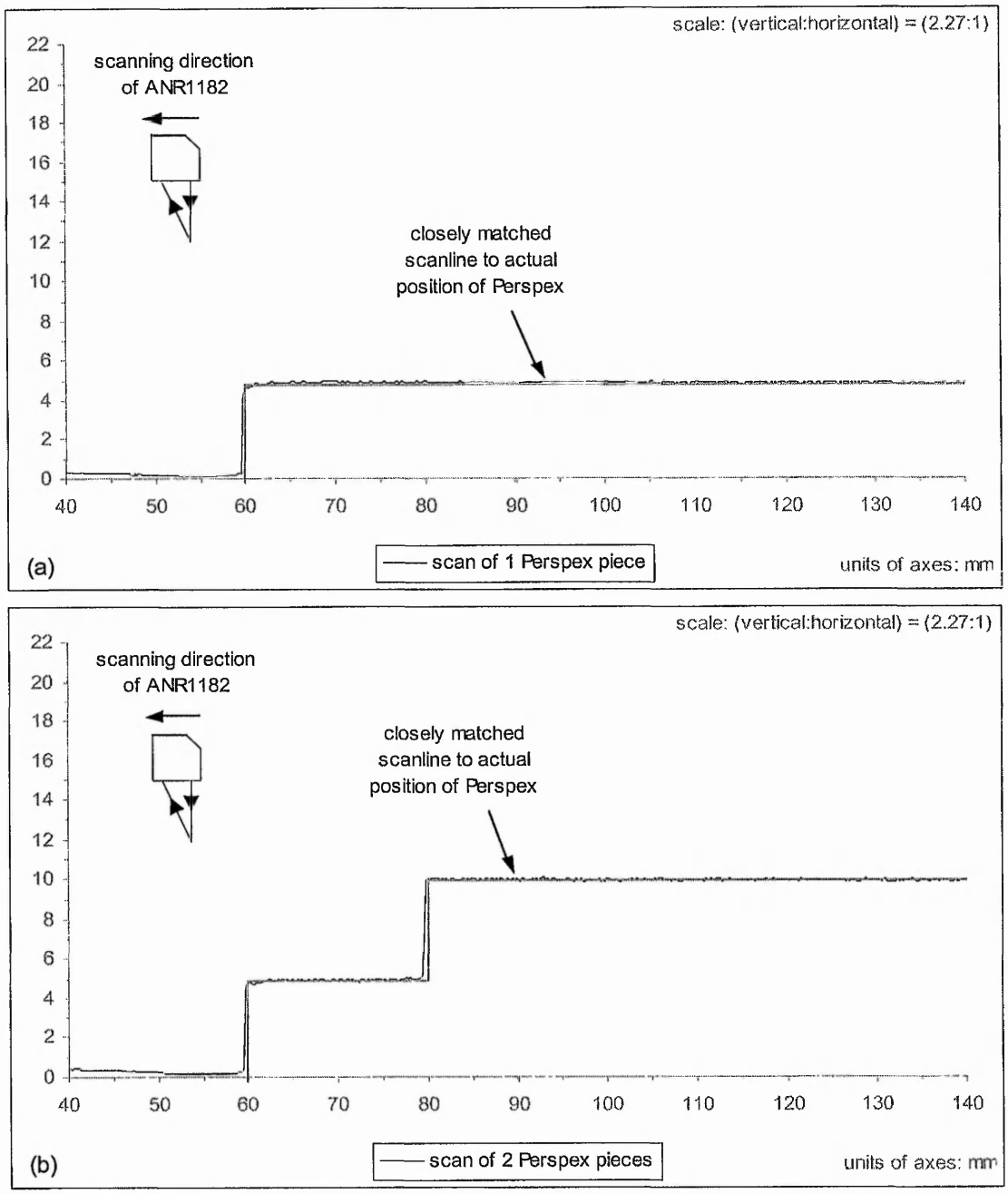

Fig. 3-5: No discrepancies in scan height after proper calibration for (a) one Perspex piece and (b) two Perspex pieces ((c) and (d) on following page – scale is increased for greater clarity).

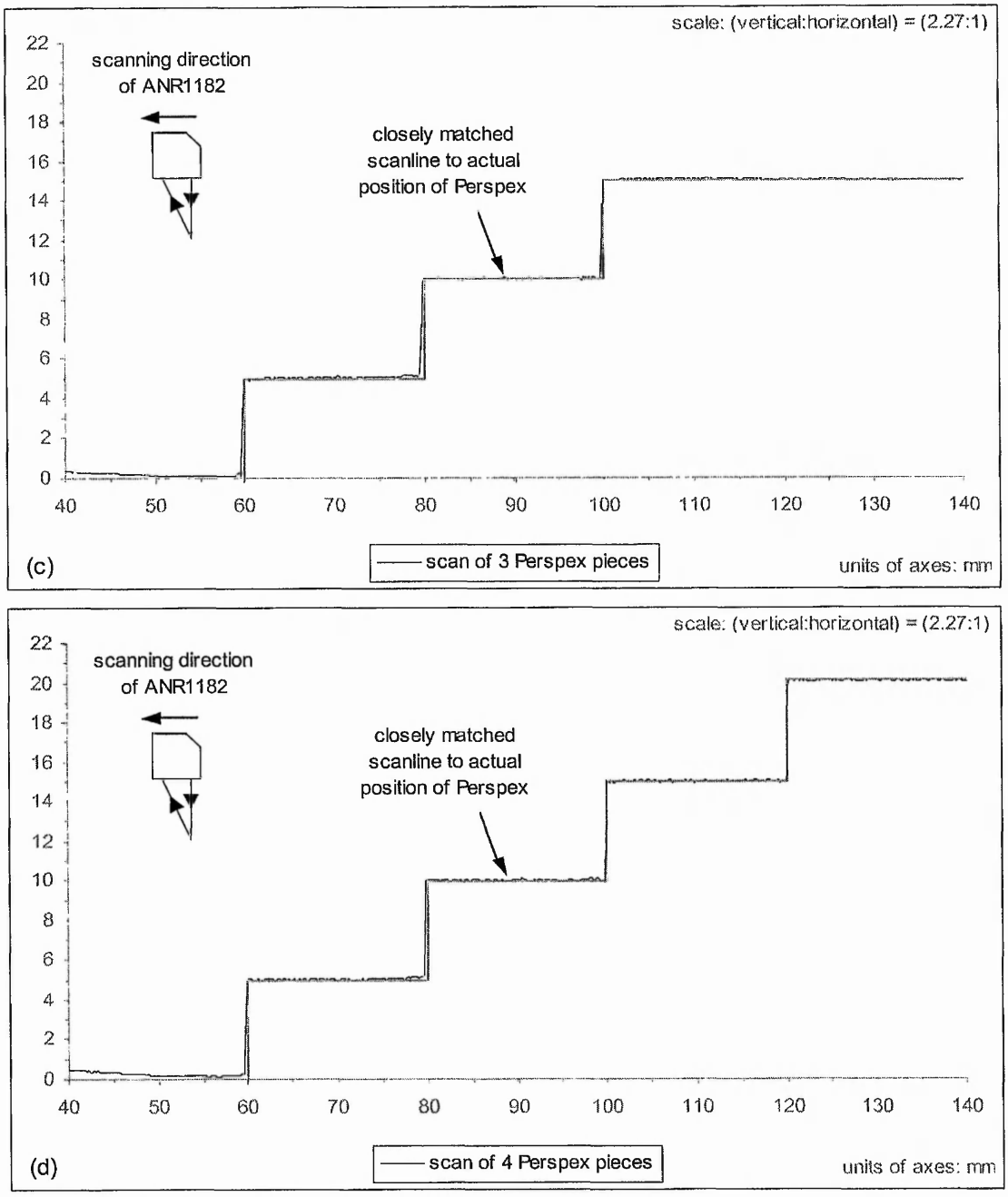

Fig. 3-5: No discrepancies in scan height after proper calibration for (c) three Perspex pieces and (d) four Perspex pieces (scale is increased for greater clarity).

3.2 Overview of Distortions

Ensuring the system's parameters and settings are in place prior to commencing the scanning process can prevent artefacts or distortions due to calibration errors. However there are other types of distortion, which are more difficult to resolve. They include noise and outliers caused by interactions between sensor and object. The types of distortion focused on by this research are systematic, depending on the surface properties and geometry of an object, and the positioning of the sensor. In order to investigate the causes of these distortions, simple geometrical objects were used in the analysis. Once established, their occurrences in more complex geometrical objects can be deduced.

This research has mainly involved the types of distortion caused by objects with regions of high curvature. These are commonly known as outliers but they are referred to in this thesis as *bow waves* and *spikes* due to their systematic behaviours. Their occurrence depends on the orientation of the sensor with respect to the region of high curvature. Besides studying these distortions, the Author has also investigated situations where objects have highly contrasting surfaces. In such situations, there can be distortions, known as *transitional spikes* in this thesis.

Distortions generated by a circular-perspective point sensor have also been analysed. This sensor has more than one detector (in fact eight are placed with equal spacing around the emitter) whereas the single-perspective point sensor has only one. However it still yields distortions such as noise and bow waves although the effects are much smaller. The following sections will highlight the above distortions in greater detail.

3.3 Distortions from Single-Perspective Point Sensor

Single-perspective point sensors are the focus of this research in 3-D imaging methods. They have the advantage of low cost, expedient depth measurements with little compromise in data accuracy, compact design, portability and a non-destructive scanning process. A detailed study of distortions from this type of sensor has been conducted in order to facilitate the development of new compensation algorithms. By reducing these distortions, a replica of improved quality can be reproduced, either

visually or physically. Moreover knowledge of the causes of these distortions will aid the understanding of the limitations of triangulation. This, in turn, may enable compensation for distortions in multi-perspective point sensors.

3.3.1 Nomenclature for 3-D Scanning using Point Sensor

Before proceeding with detailed analysis of distortions in range images, orientation of the sensor with respect to placement of the object needs to be defined. Since the point sensor is single-perspective, its orientation can affect the results and has been found to be vital in determining the types of distortion that will be produced when scanning an object. Therefore it is proposed that the orientation of the sensor is represented by an arrow in the direction from emitter to detector. When placement of the detector is further away from a region of high curvature than the emitter, the sensor is said to be oriented "down" the edge. However when the placement of the detector is closer to a region of high curvature than the emitter, the sensor is said to be oriented "up" the edge (see Fig. 3-6).

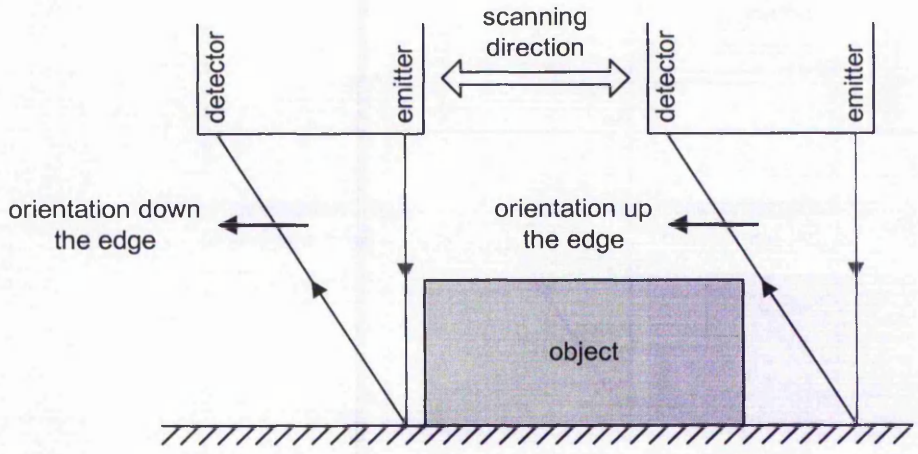

Fig. 3-6: Position of the sensor with respect to regions of high curvature.

Also in order to better identify orientation of the sensor and its scanning direction, a convention has been established, thus reducing the need for their repetitive descriptions in diagrams illustrating layouts of experiments (see Fig. 3-7). To reduce the time to scan an object, scanning alternates in direction along the selected axis. This does not affect the result of distortions in the range image because it is only the orientation of the sensor with respect to the geometry of the object that affects the results. The

orientation of the sensor is given as the angle between it and the positive x-axis measured in the anticlockwise direction, and assuming the emitter is at the centre of the circle to measure orientation.

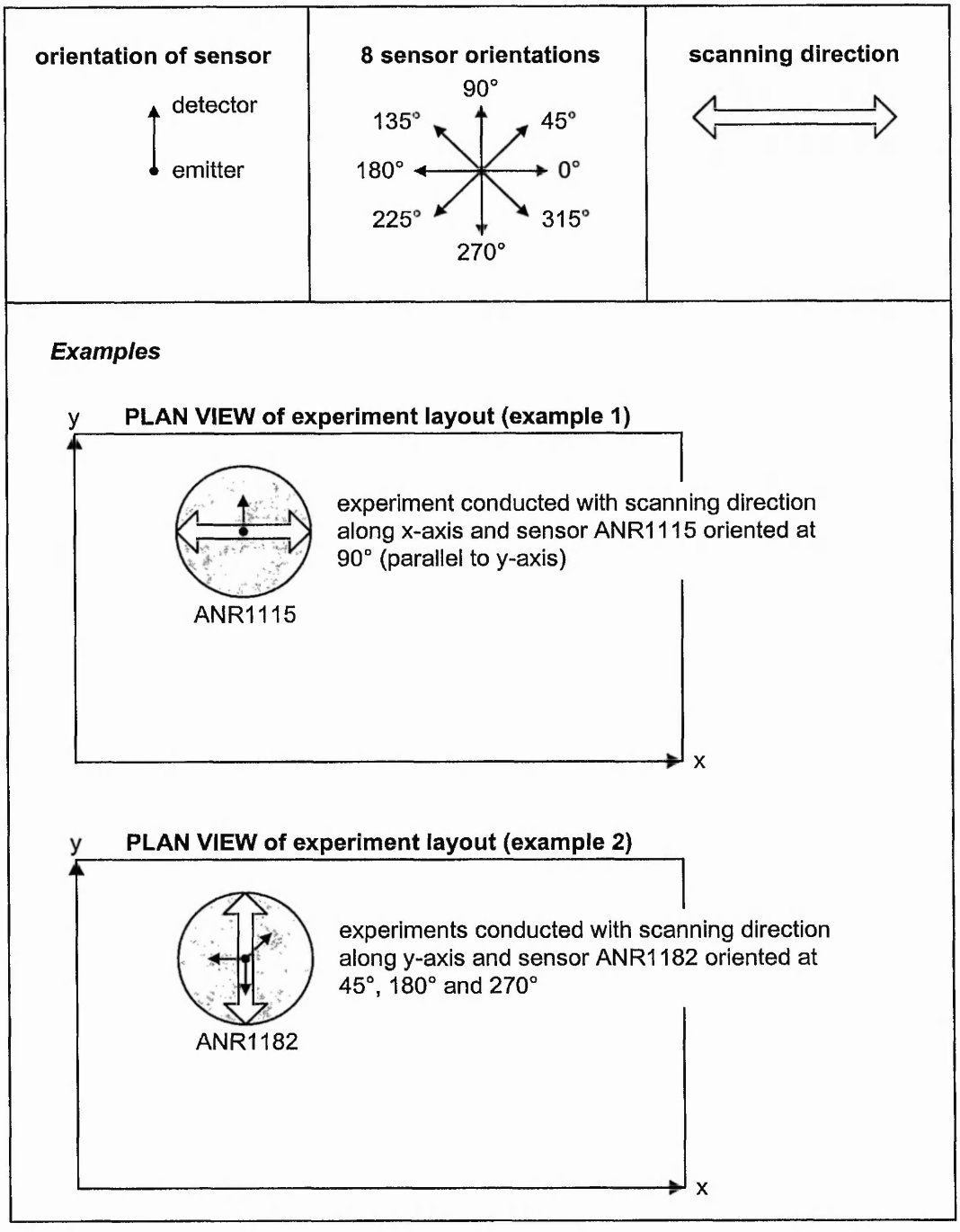

Fig. 3-7: Convention for representing scanning direction and orientation of sensor.

3.3.2 Reflectivity and Noise

As mentioned in Chapter 2, because of the high sensitivity of the PSD, the height detected for the spot image may not be consistent since it can be affected by the diffused reflectivity of the surface of the object. For the analysis of noise, black stripes of varying width were printed on a white piece of A4 paper. The sensor is placed at 90° (parallel to the *y*-axis) while the scanning direction is along the *x*-axis (see Fig. 3-8).

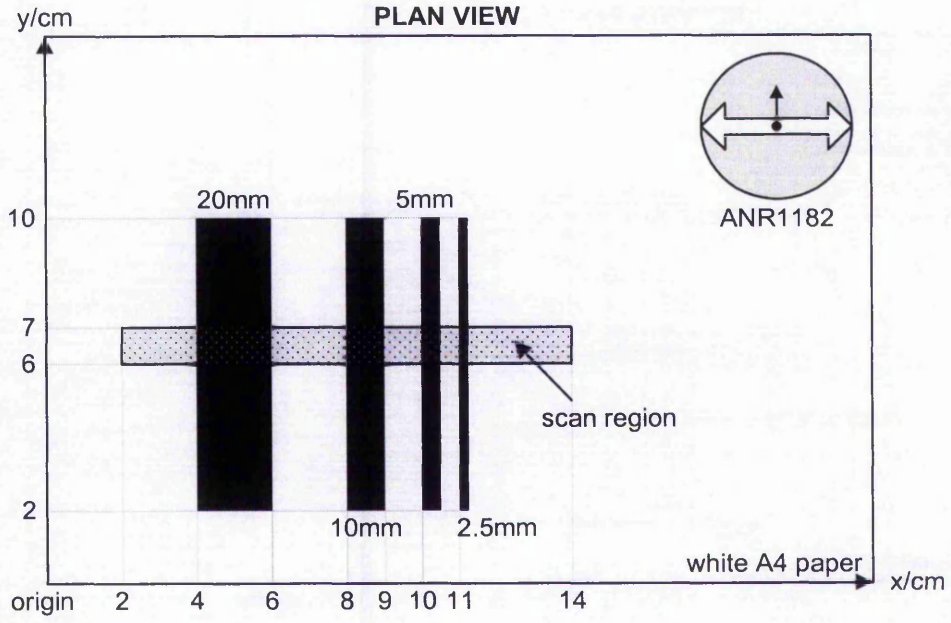

Fig. 3-8: Experiment layout for analysis of reflectivity and noise.

Upon obtaining the range image defined within the scan region, a single scanline was plotted (see Fig. 3-9). It can be seen that the selected scanline has noisier readings when inside the black stripe regions as compared with when on plain white surface. When a spot image traverses from a surface of high reflectivity to a surface of low reflectivity, its intensity changes suddenly, reducing coherence of the spot image. Within the low reflectivity (black) part of the surface, the sensitive PSD produces less consistent readings due to a weaker intensity spot image, resulting in an average height different from the average height for a surface of high reflectivity. Therefore it is suggested that any object that is to be scanned using a triangulated sensor should have a surface of high reflectivity, or it should be treated to be so. This would reduce distortion due to noise.

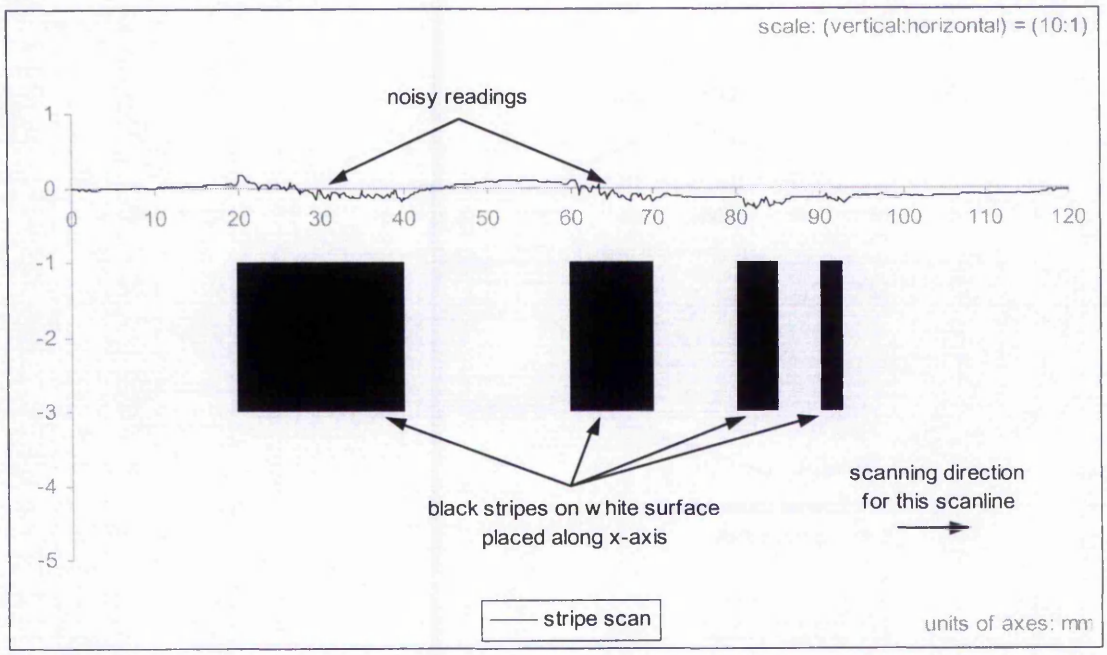

Fig. 3-9: Scanline[3] showing increased noise at region of low reflectivity (scale is increased for greater clarity).

3.3.3 Changes in Surface Reflectivity

With the same experimental layout as in the analysis of noise, another type of distortion was documented when the sensor was oriented at several different angles (see Fig. 3-10). Besides orientation of the sensor at 90°, four more scans were obtained with sensor oriented at 0°, 45°, 135° and 180° – all with respect to *x*-axis. The results of the experiment are shown in Fig. 3-11(a)-(e).

[3] The scanline does not perfectly conform to $z = 0$mm, as the white A4 paper undulated on the surface on which it was placed. Also values on the *x*-axis in Fig. 3-8 were translated towards the origin prior to plotting, giving shifted values as shown in Fig. 3-9. This procedure was performed on most scans to aid the plotting process.

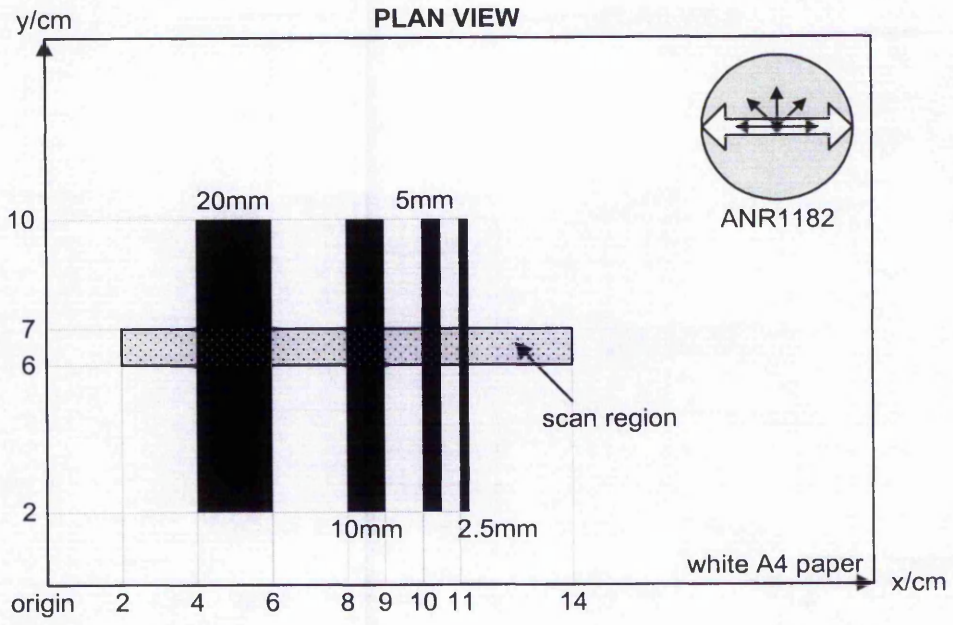

Fig. 3-10: Experiment layout for analysis of changes in surface reflectivity.

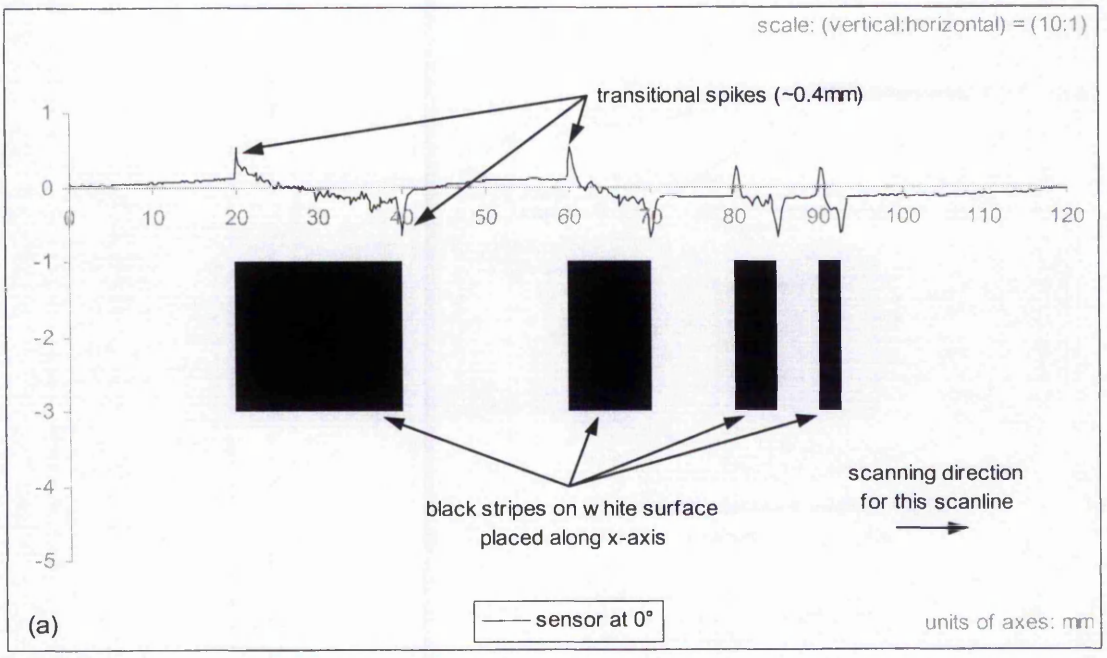

Fig. 3-11: Magnitude and directions of transitional spikes vary with orientation of sensor at (a) 0° ((b)-(e) on following pages – scale is increased for greater clarity).

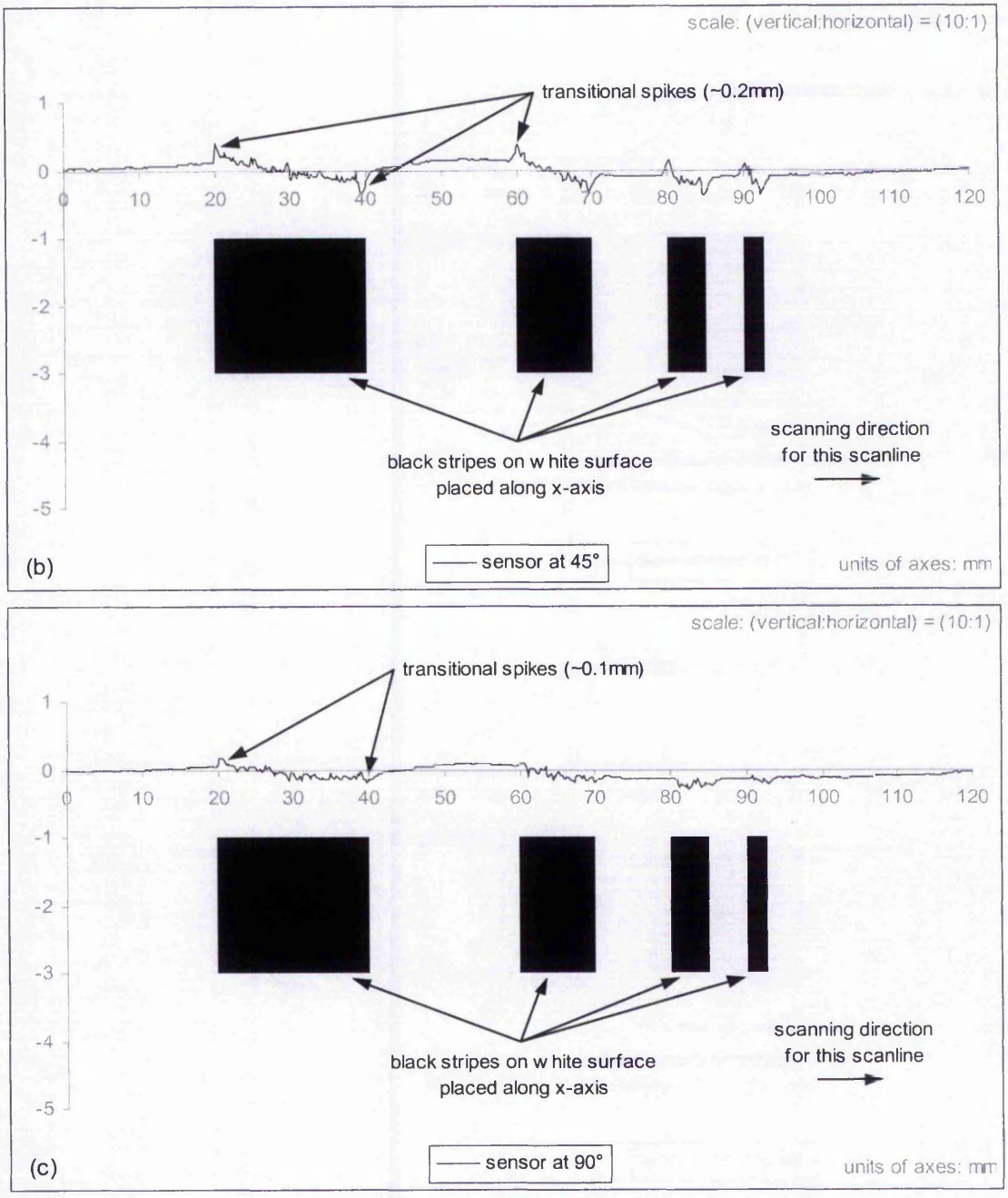

Fig. 3-11: Magnitude and directions of transitional spikes vary with orientations of sensor at (b) 45° and (c) 90° ((d) and (e) on following page – scale is increased for greater clarity).

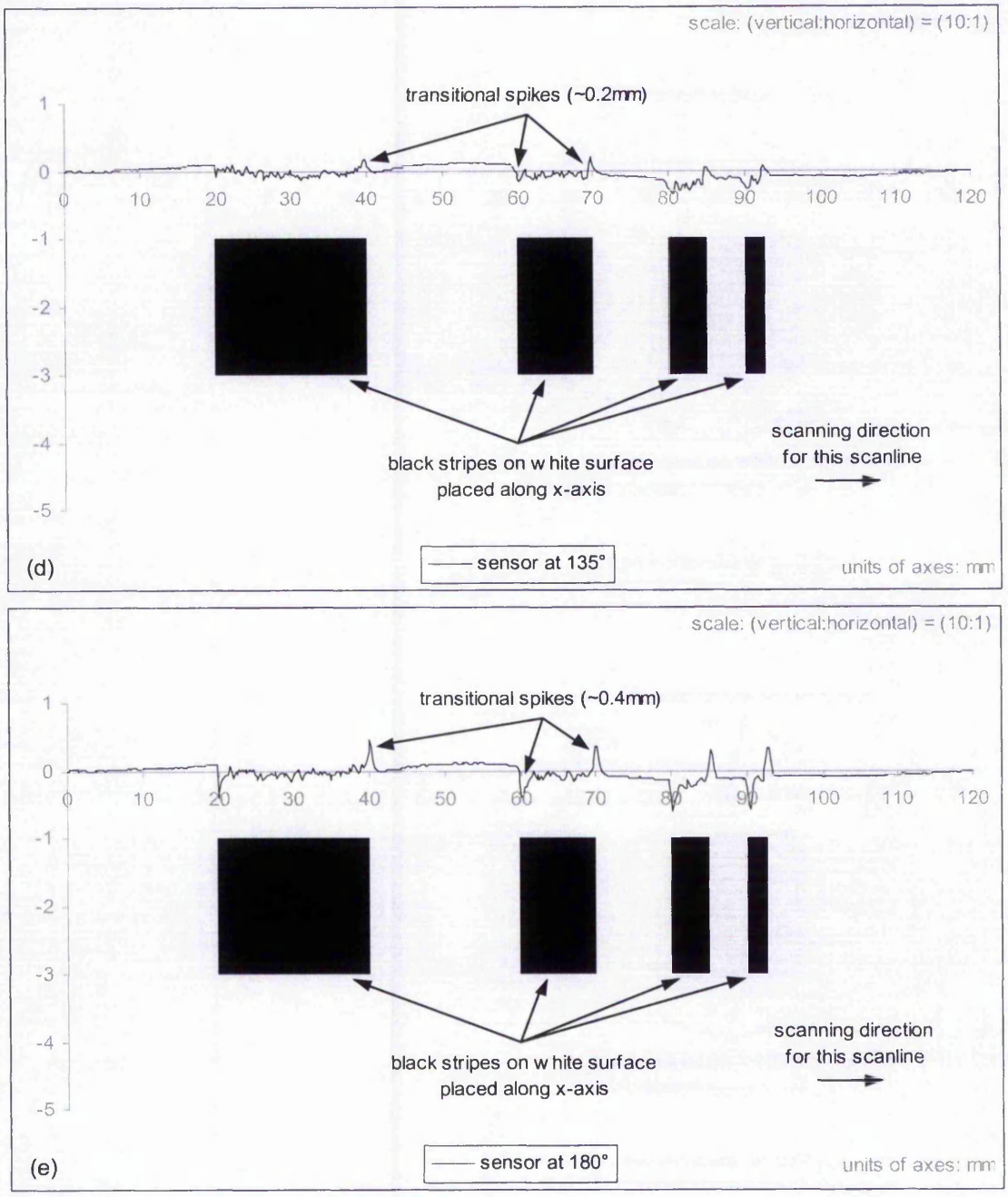

Fig. 3-11: Magnitude and directions of transitional spikes vary with orientations of sensor at (d) 135° and (e) 180° (scale is increased for greater clarity).

When scanlines in Fig. 3-11(a)-(e) are closely scrutinized, small spike distortions are evident at transitions between black stripes and white surface. Compared to the noise within black stripe regions, these distortions have a greater magnitude (except when orientation of sensor is at 90° or parallel to transitions) and are systematic in their behaviour. The directions for these spike distortions were reversed between 0° and 180°

and between 45° and 135°. The reason for this occurrence will be explained below. In this thesis, distortions of this type are termed *transitional spikes*. The sensor's readings stabilized when the spot image was within regions of uniform reflectivity.

To gain an understanding of these spikes, the behaviour of the spot image at the transition between two contrasting regions was analysed. It can be postulated that a single laser beam, emitted from the source of illumination, is made up of multiple paths of light (see Appendix B.2). The sum of these paths forms a spot image when projected on the surface of an object. Based on the fundamentals of the triangulation principle, the normal distance from the surface is determined by the collective average of triangulation angles between each path of light with its detection direction. Suppose that two examples of all these paths reflected into the detector are resolved into two major components, r_1 and r_2 (see Fig. 3-12).

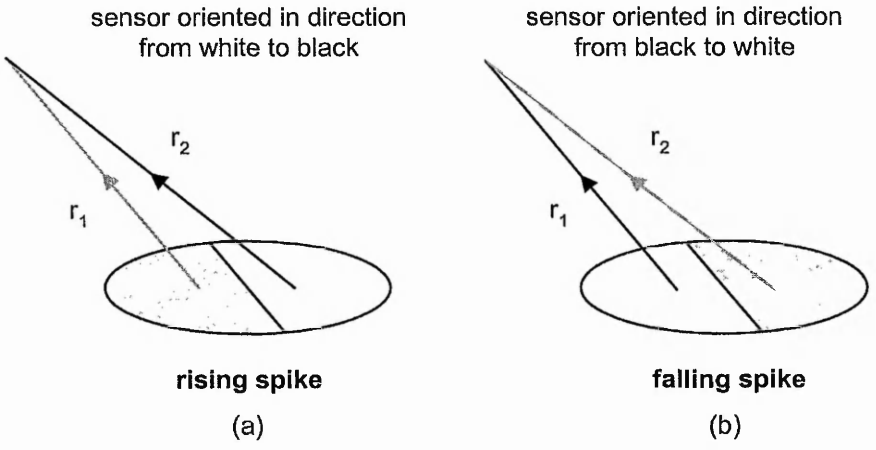

Fig. 3-12: Composition of light reflected at the transition of two contrasting regions when the orientation of the sensor is approximately perpendicular to this transition.

When a laser beam strikes a transition on the surface of an object, as illustrated in Fig. 3-12(a), the contribution of the reflected light path r_1 to the formation of spot image decreases due to its reduced relative intensity. Consequently the weighting of triangulation angle tends toward the reflected r_2 (effectively increasing the triangulation angle), increasing its contribution to the average. The sensor would then perceive this spot image as closer than it actually is, thus explaining incidents of rising spike at the transition of a contrasting surface. Conversely Fig. 3-12(b) shows the reason for a falling

spike when the reflected r_2 is now weaker instead, thereby reducing the overall triangulation angle by tending towards the reflected r_1.

Regardless of scanning direction, the orientation of the sensor, with respect to the transitions, is the determining factor for the directions of these spikes. Therefore Fig. 3-11(a) and Fig. 3-11(b) have transitional spikes of opposing directions compared to Fig. 3-11(e) and Fig. 3-11(d) respectively. The magnitude of these spikes also depends on the orientation of the sensor. When the sensor is oriented approximately perpendicular to a transition, the deviation between triangulation angles of paths of light is most pronounced and the magnitude of the transitional spikes is largest (see Fig. 3-11(a) and Fig. 3-11(e)). However as the orientation of the sensor moves closer to parallel to the transition, the deviation between triangulation angles among the paths of light decreases and thus the magnitude of transitional spikes reduces.

3.3.4 Systematic Distortions depending on Geometry of Object

During empirical study of distortions, it was discovered the types of distortion are dependent on the orientation of the sensor with respect to the geometry of the object (see Fig. 2-15). To illustrate this point, an object of simple geometry, placed on a planar surface, was scanned using a point sensor, mounted on a CNC machine (see Fig. 3-13).

With the sensor oriented in the scanning direction, scanlines profiling the object were obtained. Distortions were then noted near regions of high curvature, namely vertical faces of the object (see Fig. 3-14(a)). Besides noise, there appears to be two different types of distortion: one when sensor is oriented down the edge of a vertical face, known in this thesis as *bow wave* (see Section 3.3.5), and the other when sensor is oriented up the edge of the opposing vertical face, known in this thesis as *occlusion spikes* (see Section 3.3.6). A second set of scanlines was obtained with the same parameters apart from the scanning direction, which was now approximately perpendicular to the orientation of the sensor. In can be seen that the distortions now encountered are of the same type to the first experiment. However, they look different due to the different direction of the scanlines but the types of distortion and their locations remain the same (see Fig. 3-14(b)). Finally a third experiment was conducted, in which the parameters were the same as that of the first experiment but with the sensor rotated by approximately 90°.

This effectively placed the orientation of the sensor approximately perpendicular to the scanning direction. It was found that the types of distortion were the same but their locations had shifted compared to the first and second experiments (see Fig. 3-14(c)). Therefore it can be concluded that the types of distortion depend on orientation of the sensor with respect to the geometry of the object but not on the scanning direction.

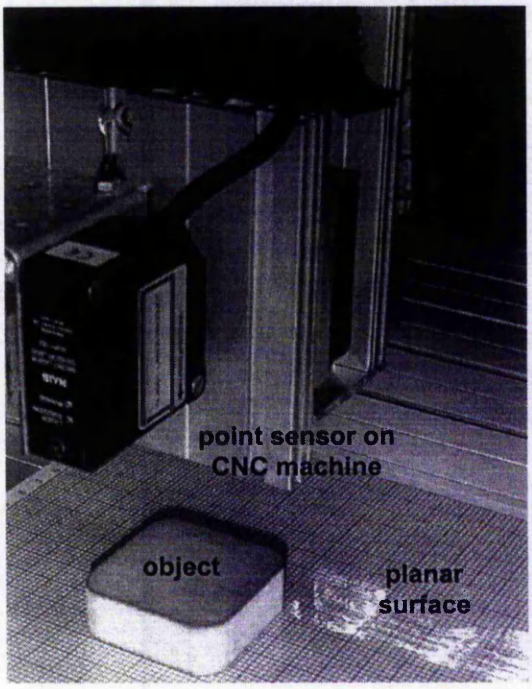

Fig. 3-13: Set up for 3-D scanning of a simple geometry MDF block using a point sensor. The planar surface and the object were then treated with a thin layer of diffusely reflective coating prior to scanning.

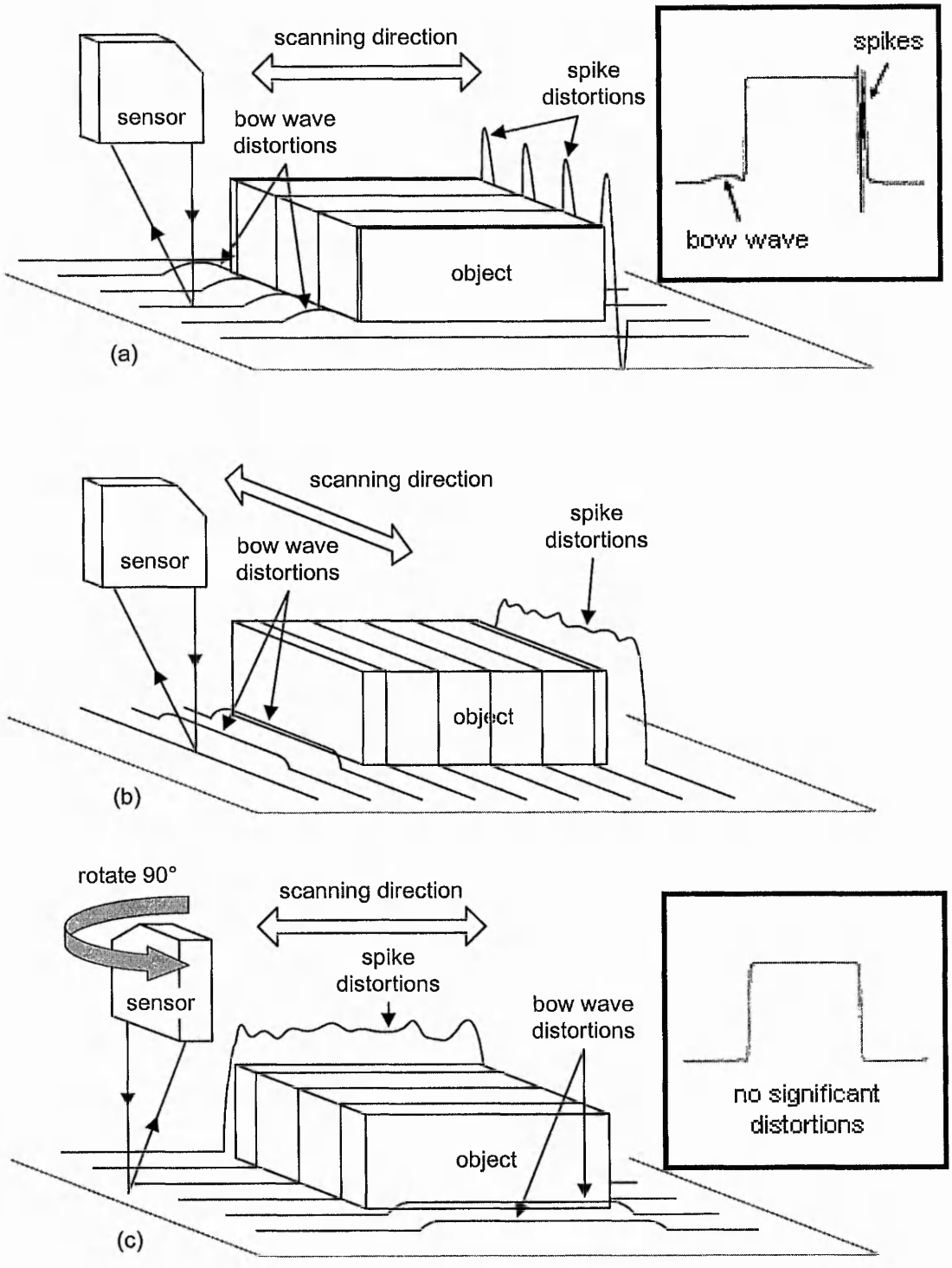

Fig. 3-14: Schematic diagram illustrating how the systematic distortions depend on orientation of the sensor with respect to the geometry of the object and not on the scanning direction. Insets for (a) and (c) from Fig. 2-15 show the scanline extracted from the middle part of the object.

3.3.5 Bow Waves

As described in Section 3.3.4, significant systematic distortions occur near regions of high curvature of the object, especially when the sensor is oriented close to perpendicular to the edge of these regions. These distortions can be divided into two types: one occurs when the sensor is oriented down the edge of regions of high curvature and the other when the sensor is oriented up the edge of these regions. The former type is termed as *bow wave* in this thesis. To analyse the incidence of bow wave, an object of simple geometry[4] has been used because it provides vertical faces. For a clearer profile of these distortions, the scanning direction was set to be parallel to the orientation of the sensor, as only one scanline is required[5]. The effect of surface reflectivity was first analyzed to determine its contribution to the incidence of bow wave. The layout of the experiment is shown in Fig. 3-15.

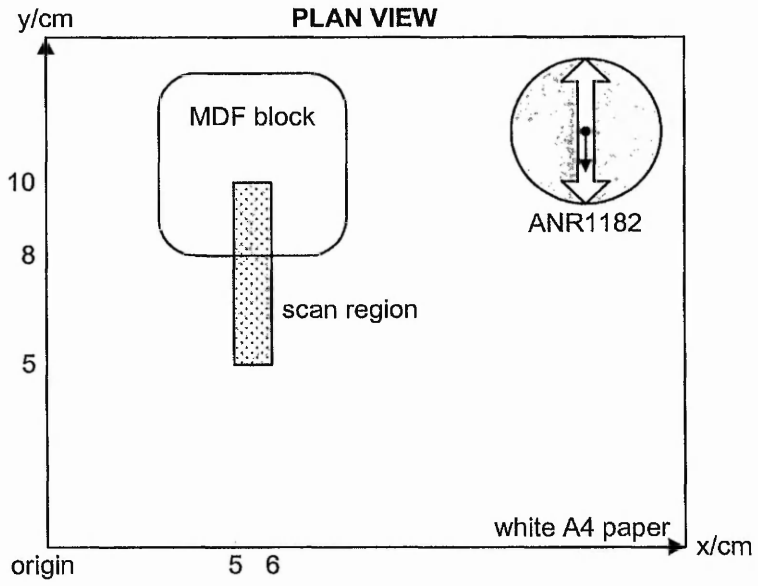

Fig. 3-15: Experiment layout for analysis of bow wave based on surface reflectivity.

[4] MDF block with rounded corners with dimension (50mm × 50mm × 18mm).

[5] Scanning direction need not be parallel to the orientation of the sensor for they could be perpendicular but in order to build a profile of these significant distortions, several perpendicular scanlines would then be required.

Before commencing the scanning process, the planar surface and the object were treated evenly with a thin layer of non-permanent coating[6], ensuring consistent high diffused reflectivity of the spot image. The experimental result (see Fig. 3-16(a)) clearly illustrates the incidence of a bow wave next to a vertical face of the MDF block. Instead of a close fit of the scanline to the planar surface, there appears to be a "bump" in the scanline. Maintaining the same calibration parameter, the next experiment involved treating the planar surface with a dark paint. This was to reduce the surface reflectivity to a much lower value. The scanline shown in Fig. 3-16(b) also exhibits the incidence of a bow wave. However the magnitude of this bow wave is much smaller than the one in Fig. 3-16(a). This shows that the magnitude of a bow wave depends on surface reflectivity. Although making the object have low reflectivity can reduce the size of bow waves, it must be remembered that this will result in greater surface noise.

[6] ROCOL Flawfinder developer spray. Part number RS 693-315.

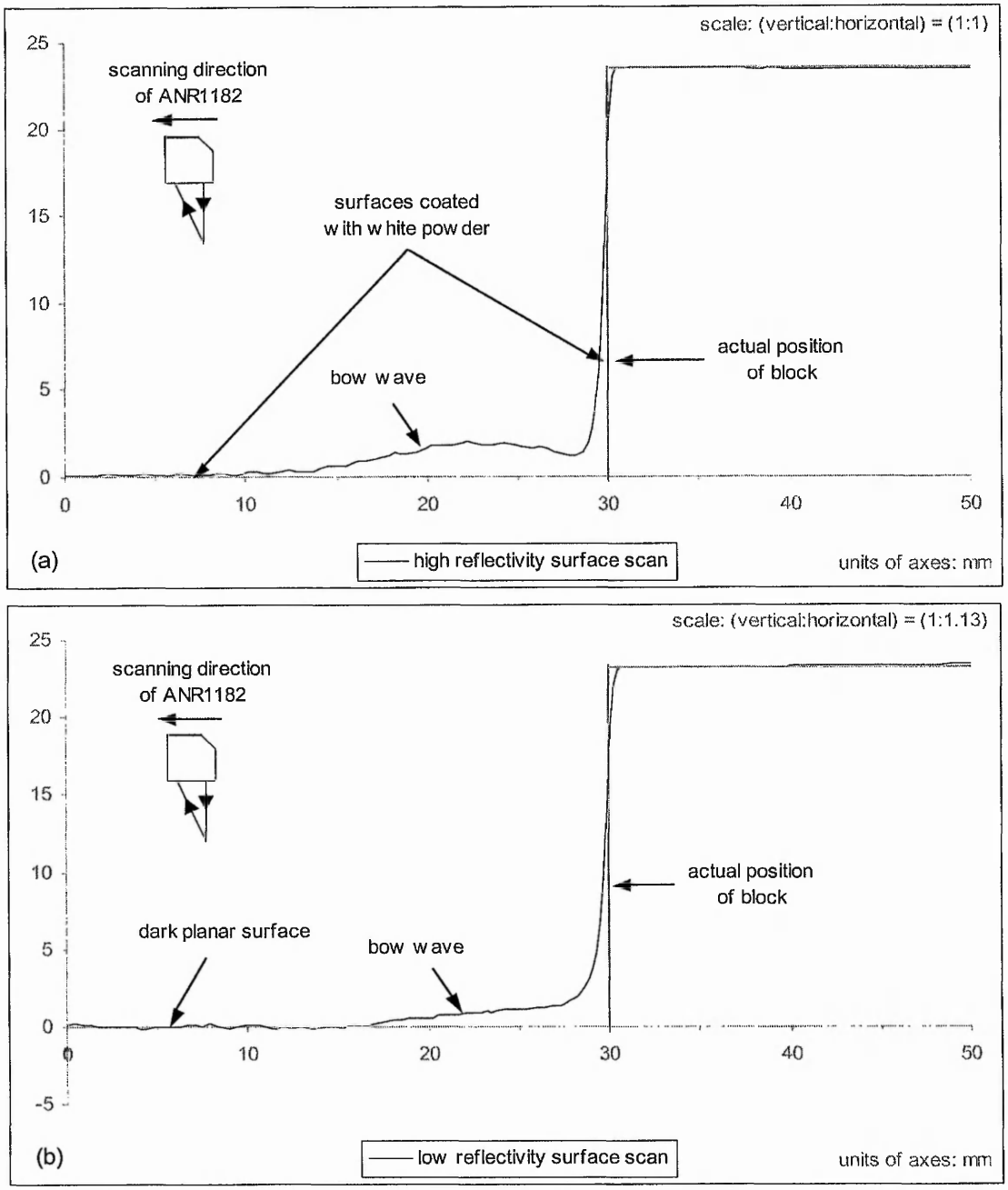

Fig. 3-16: Magnitude of bow waves on surfaces of (a) high reflectivity and (b) low reflectivity (scale is increased for greater clarity).

Further experiments involving bow waves investigated the effect of the orientation of the vertical face relative to the sensor. Four different orientations were chosen: 30°, 45°, 60° and 90°. The layout of the experiment is shown in Fig. 3-17.

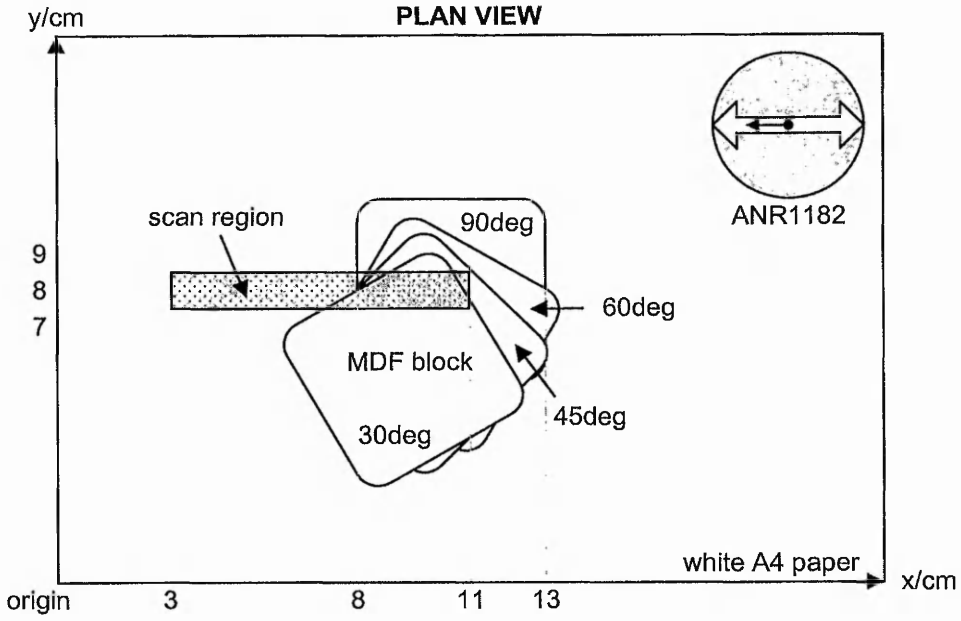

Fig. 3-17: Experiment layout for analysis of bow wave based on orientations of vertical face relative to sensor.

The scanlines in Fig. 3-18 clearly indicate decreasing magnitude of the bow wave as the orientation of the vertical face relative to the sensor changes from approximately perpendicular towards parallel. The magnitude reduces from 1.9mm at 90° in Fig. 3-18(a) to 0.5mm at 30° in Fig. 3-18(d). It can be seen in Fig. 3-19 that the size of the bow wave is roughly proportional to the angle in which the sensor is oriented to the edge of the vertical face.

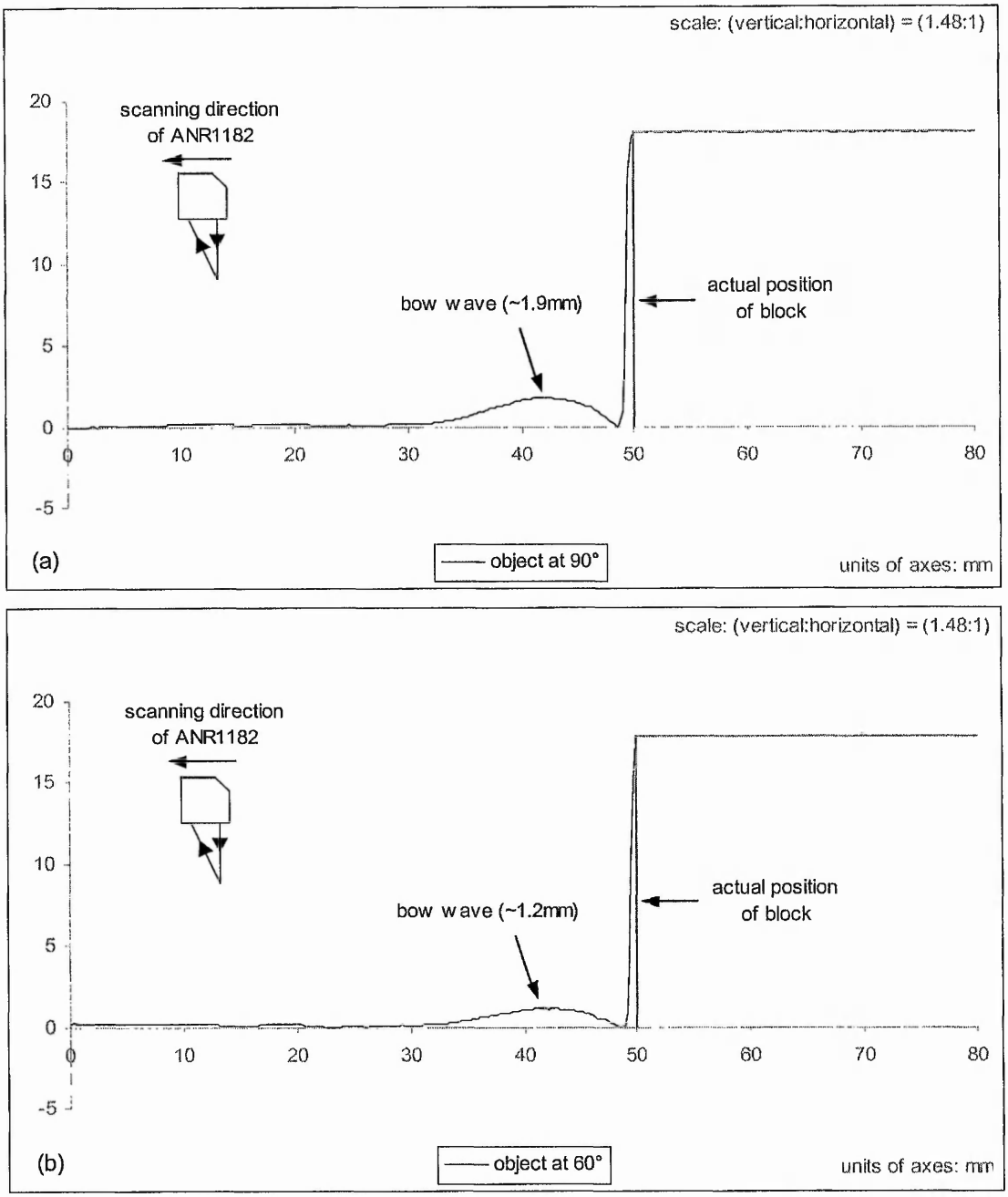

Fig. 3-18: Magnitude of bow wave changes with orientations of vertical face relative to sensor at (a) 90° and (b) 60° ((c) and (d) on following page – scale is increased for greater clarity).

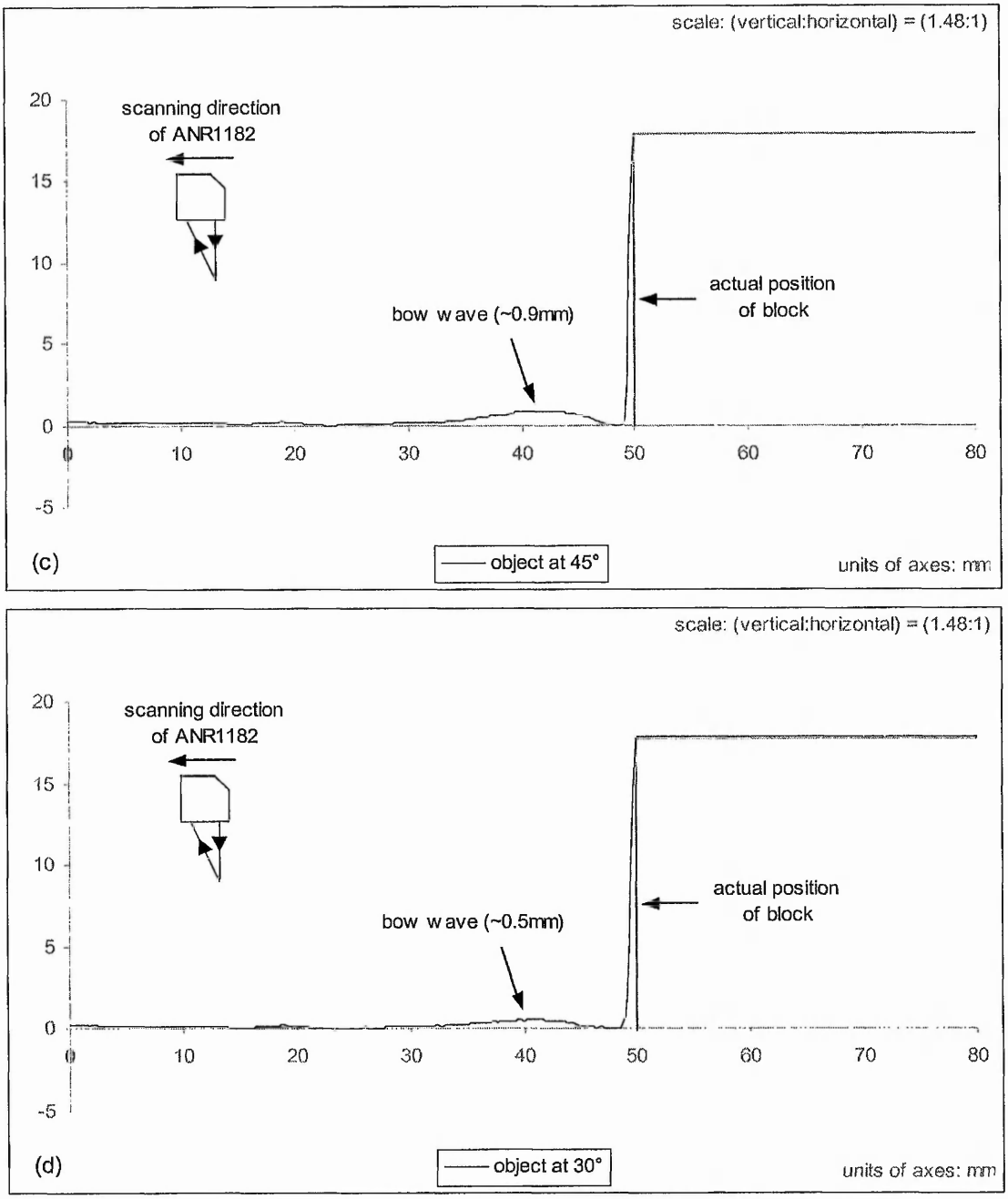

Fig. 3-18: Magnitude of bow wave changes with orientations of vertical face relative to sensor at (c) 45° and (d) 30° (scale is increased for greater clarity).

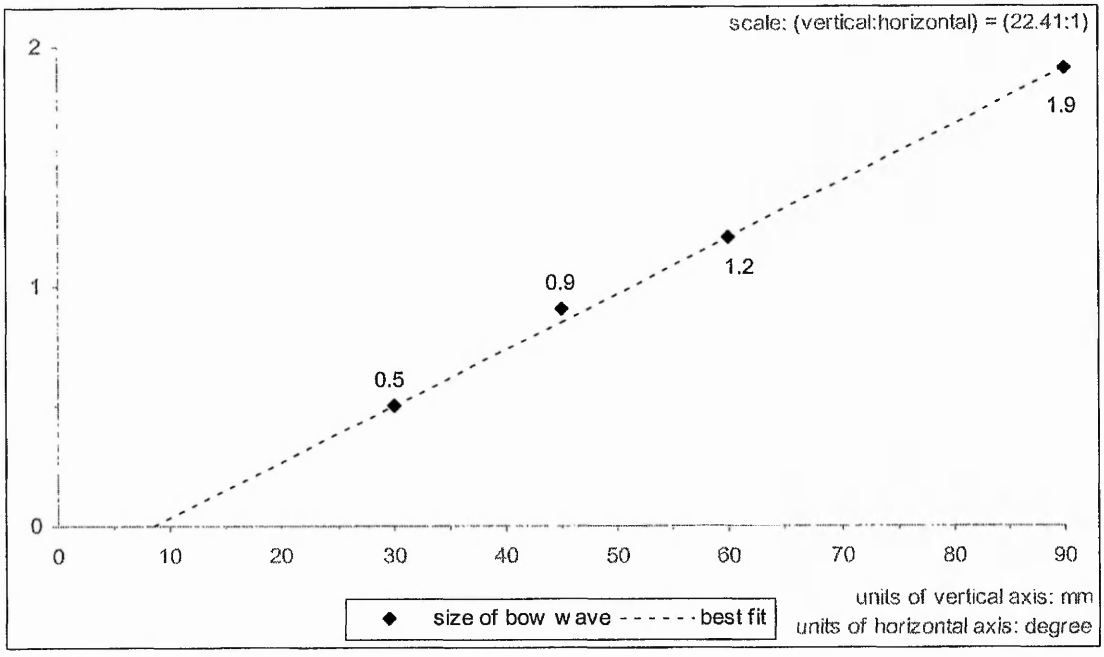

Fig. 3-19: The approximate size of bow wave has been plotted against orientation of the sensor with respect to the vertical face of the object. A least squares fit shows that the effect is proportional to this orientation.

Experiments to establish the behaviour of the bow wave with respect to the gradient of a slope were conducted as well. A second set of experiments was carried out for comparison, where the orientation of the sensor is parallel to the "edge" of the slope. Four different gradients were selected: 30°, 45°, 60° and 90°. Fig. 3-20 shows the layout of these experiments.

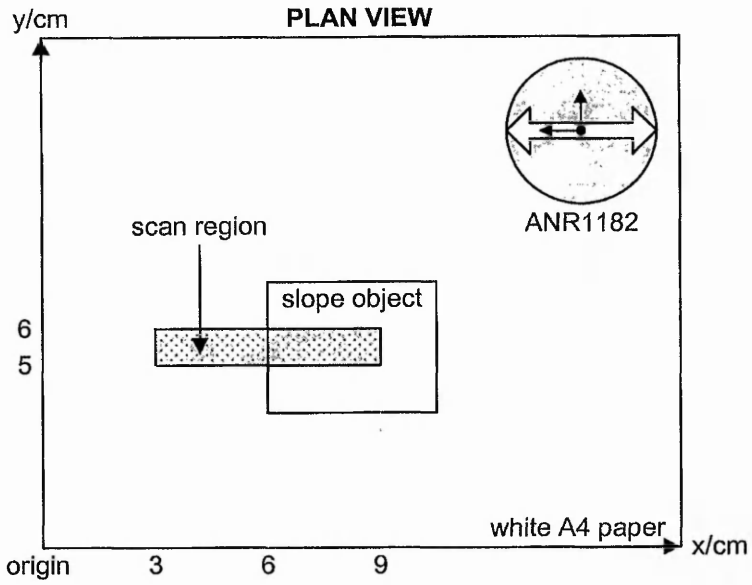

Fig. 3-20: Experiment layout for analysis of bow wave based on gradient of slope.

It can clearly be seen in Fig. 3-21 the magnitude of bow wave increases with increasing gradient. The magnitude increases from approximately 0.5mm at 30° as shown in Fig. 3-21(a) to 1.7mm at 90° (which is when the slope becomes a vertical face) as shown in Fig. 3-21(d). Also note that at 30mm on the horizontal axis, there appears to be a falling spike, which increases with gradient except when the slope becomes a vertical face. The reason for this occurrence will be discussed later in this section. For comparison, when orientation of the sensor is parallel to the edge, Fig. 3-22 shows scanlines closely matching the actual shape of the object.

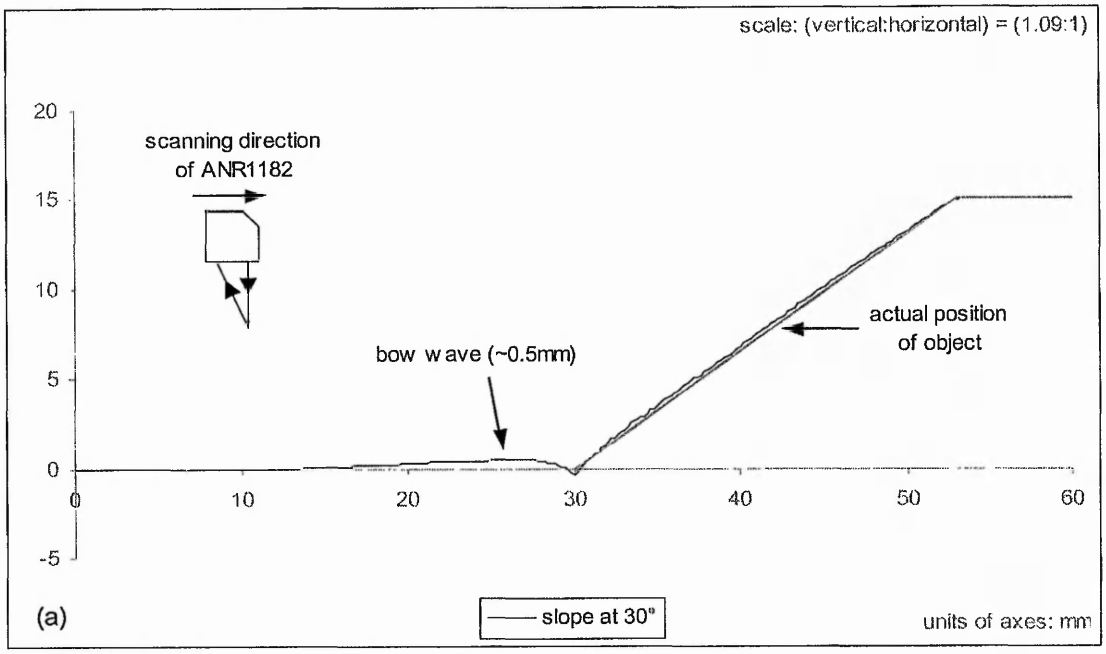

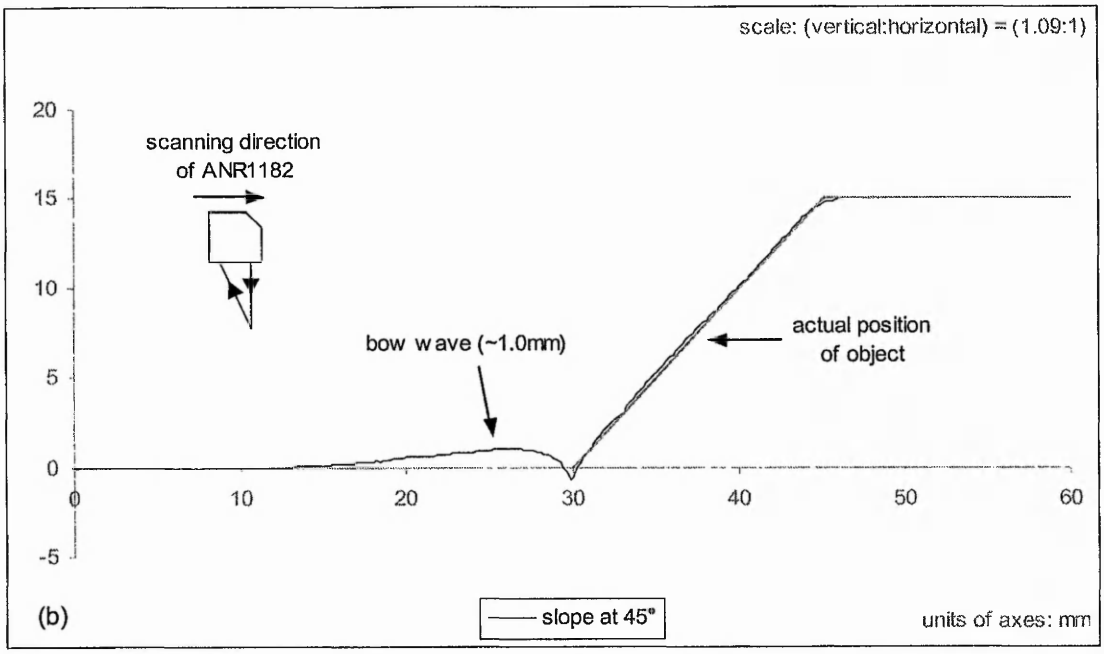

Fig. 3-21: Magnitude of bow wave changes with gradients of slope at (a) 30° and (b) 45° ((c) and (d) on following page – scale is increased for greater clarity).

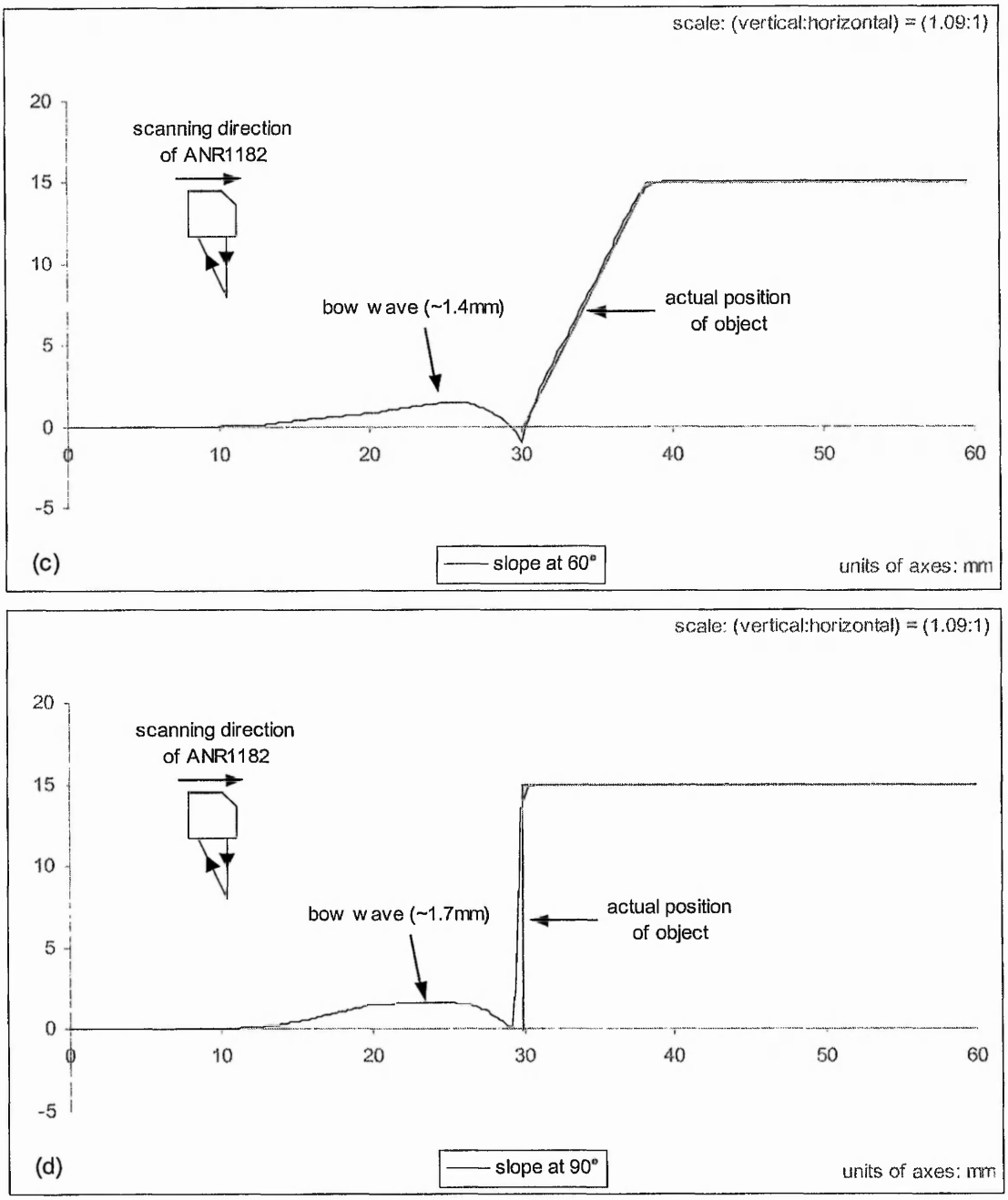

Fig. 3-21: Magnitude of bow wave changes with gradients of slope at (c) 60° and (d) 90° (scale is increased for greater clarity).

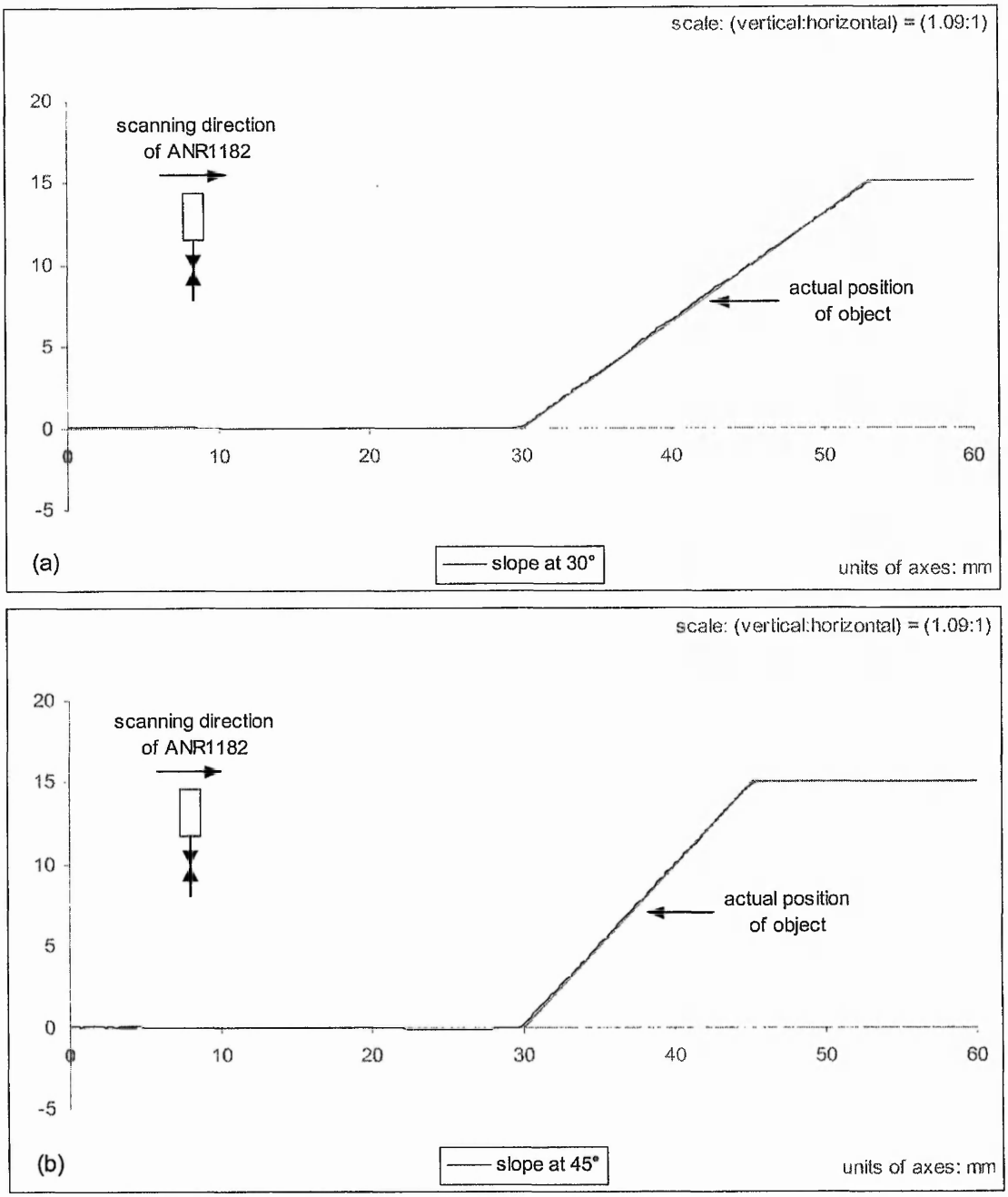

Fig. 3-22: Scanlines closer to slopes with gradients at (a) 30° and (b) 45° when sensor is oriented parallel to "edge" of object ((c) and (d) on following page – scale is increased for greater clarity).

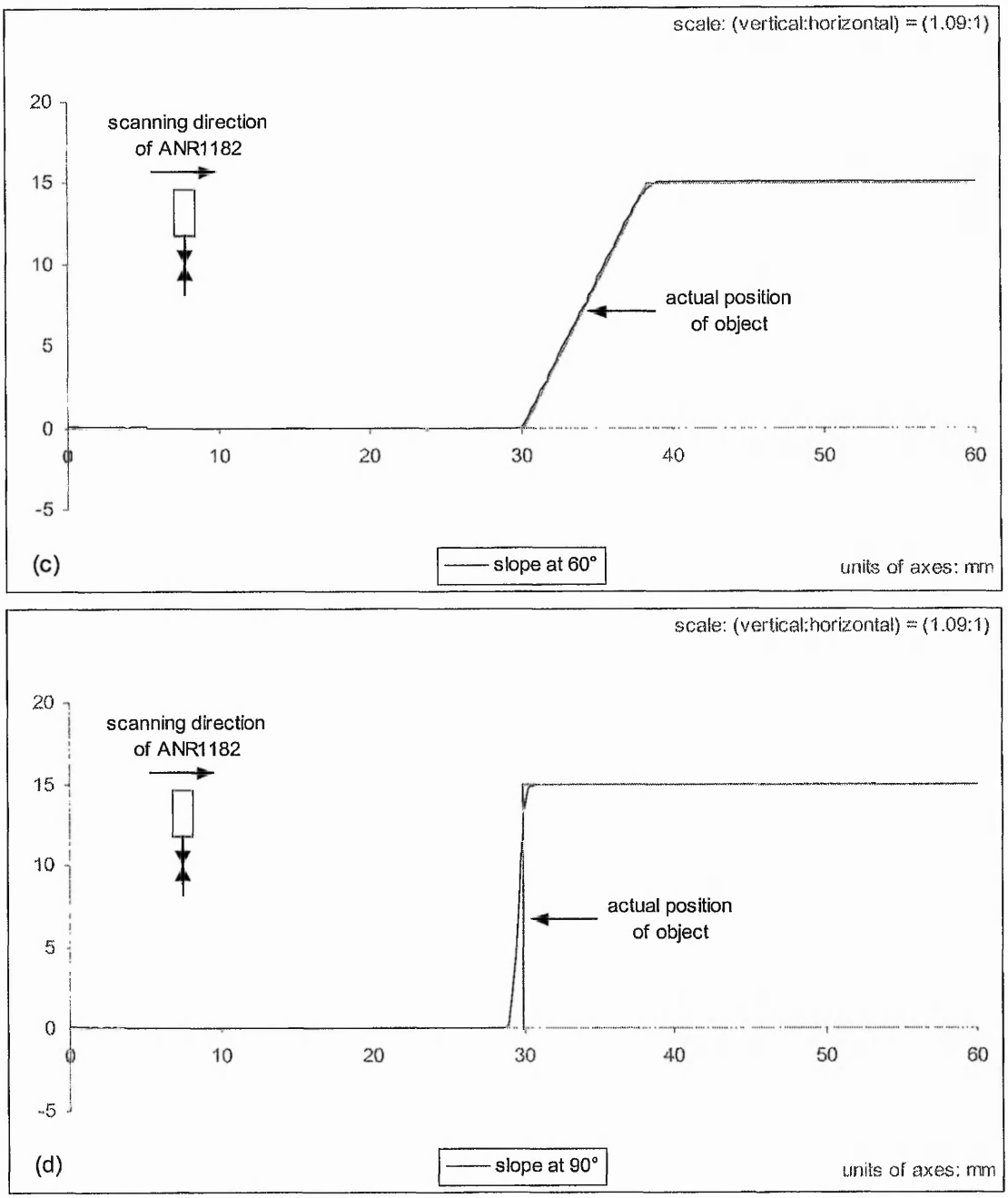

Fig. 3-22: Scanlines closer to slopes with gradients at (c) 60° and (d) 90° when sensor is oriented parallel to "edge" of object (scale is increased for greater clarity).

It is intended that the sensor's detector should detect only the projected spot image on surface of the object to determine the actual distance by the means of triangulation. However instead of a sharply focused spot image on the surface, in practice, it is slightly dispersed around the focal point. The detector, with a fixed field-of-view, will thus perceive a spot image that is dispersed (see Fig. 3-23). The spread of this dispersion

depends on the reflectivity of the surface. Surfaces of high reflectivity will inevitably have higher dispersion as compared to surfaces of low reflectivity, which reflects less light.

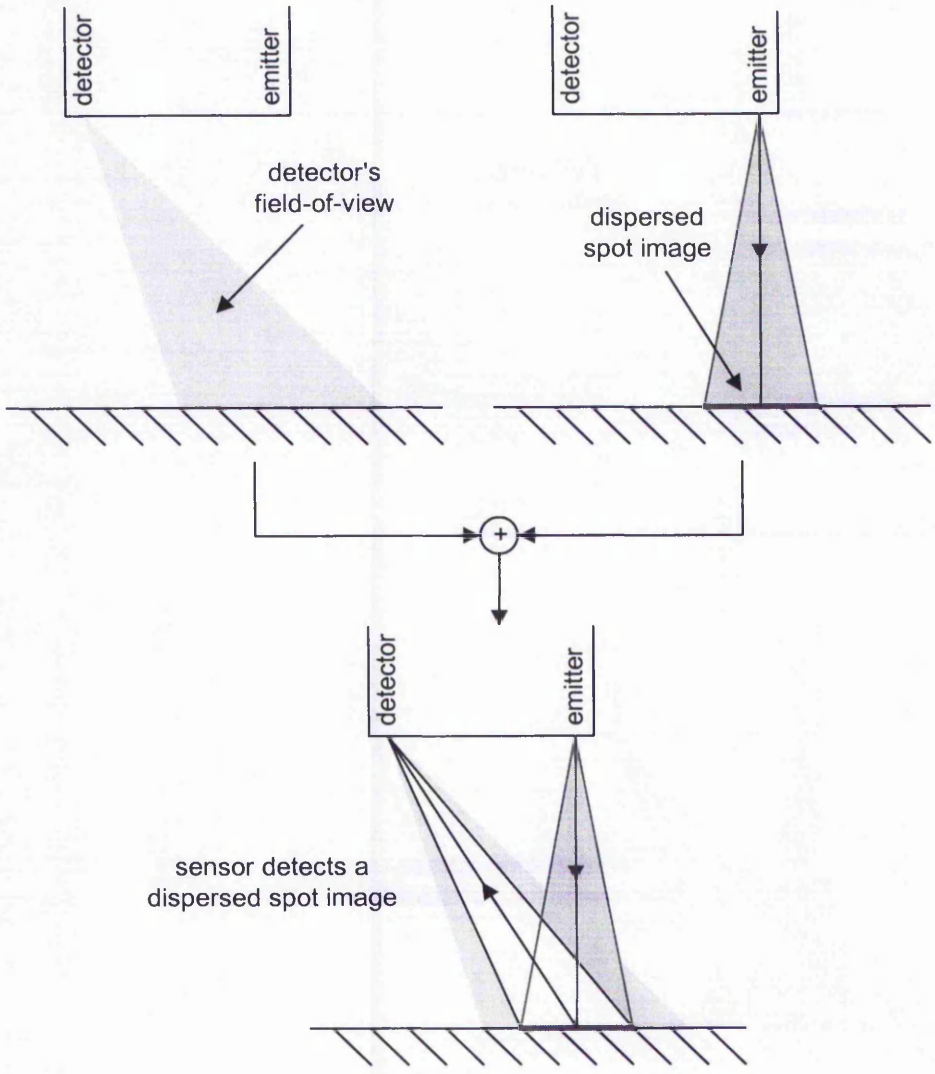

Fig. 3-23: Relationship between detector's field-of-view and a dispersed spot image.

Because of dispersion, when a laser beam is near an object, a secondary spot image is diffusely reflected and dispersed onto the vertical face of the object. Since the detector's field-of-view encompasses a fixed viewing angle, the primary and secondary spot images together with their dispersions are likely to be detected. The inclusion of all these readings would increase the output triangulation angle by shifting the centroid of the reflected spot image on the detector, hence resulting in an incorrect distance measurement by generating a *phantom* spot above the true surface (see Fig. 3-24). As the

laser beam moves away from the object, the magnitude and influence of secondary spot image decreases, thus explaining the tapering bow wave as seen in Fig. 3-16(b). The magnitude of the bow wave is therefore related to the reflectivity of the planar surface and vertical face of the object. Higher reflectivity yields a larger bow wave (see Fig. 3-16(a)). Surfaces with low reflectivity will reflect less of the primary spot image and its dispersion, resulting in faintly reflected secondary spot image off the vertical face. Hence the weightings of triangulation will shift towards the primary spot image, attenuating the size of the bow wave (see Fig. 3-16(b)).

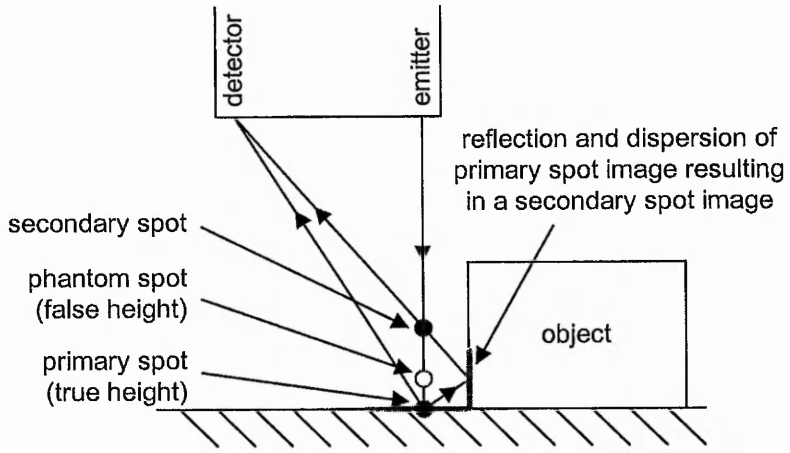

Fig. 3-24: Diagram showing the generation of bow wave distortion. Averaging of the angles from the primary and secondary spots yields a "phantom spot". The phantom spot is closer to the true height because the secondary spot has lower intensity than the primary spot.

As the sensor's detector has a field-of-view lying mainly in a single plane, the magnitude of the bow wave also depends on the orientation of the vertical face relative to the sensor (see Fig. 3-25). The influence of a secondary spot image reduces as the vertical face moves from being perpendicular to being parallel with respect to the orientation of the sensor. This is because the diffusely reflected secondary spot image and its dispersion are not completely in the detector's field-of-view but rather at a certain angle. Hence only part of this secondary reflection and diffusion is detected, resulting in smaller bow waves (see Fig. 3-18). This also explains the reason for scanline closely matching the actual shape of the object when the sensor is oriented parallel to the "edge" of the slope (see Fig. 3-22).

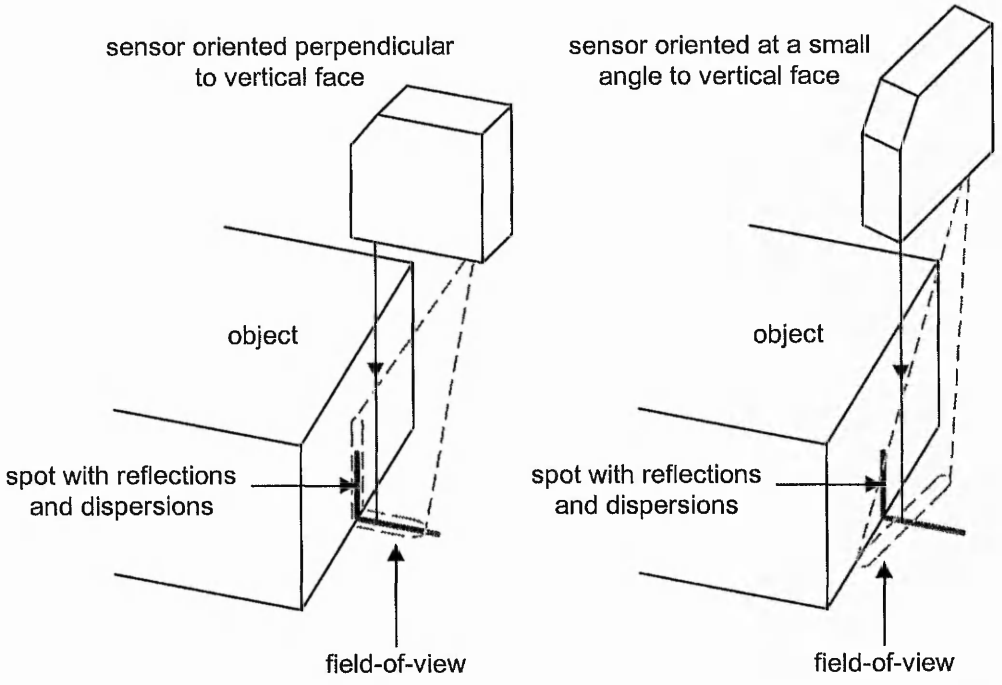

(a) detector's single plane field-of-view detects most of the spot with reflections and dispersions

(b) detector's single plane field-of-view detects only part of the spot with reflections and dispersions

Fig. 3-25: Magnitude of bow wave depends on orientation of vertical face of object relative to sensor. Detector's field-of-view detects (a) more light when oriented perpendicular to vertical face and (b) less light when oriented at an angle to this face.

The amount of light that is detected by the detector depends on the gradient of a slope near a spot image. When this gradient increases, the occurrence of secondary reflection and its dispersion becomes more evident. Therefore more light will be detected from the slope and as such, increases the size of the bow wave (see Fig. 3-21 and Fig. 3-26(a)). However when the spot image is very near the bottom of a slope, there appears to be a falling spike that increases in magnitude with increasing gradient but disappears at 90°. This falling spike is attributed to the detection of secondary reflection and its dispersion on the planar surface by the detector (see Fig. 3-26(b)). The secondary reflection and its dispersion are more prominent when the slope is at higher gradient up until a certain limit. This is when the slope is at 90° where the spot image will no longer be able to position itself on this slope but "drops" straight onto the planar surface.

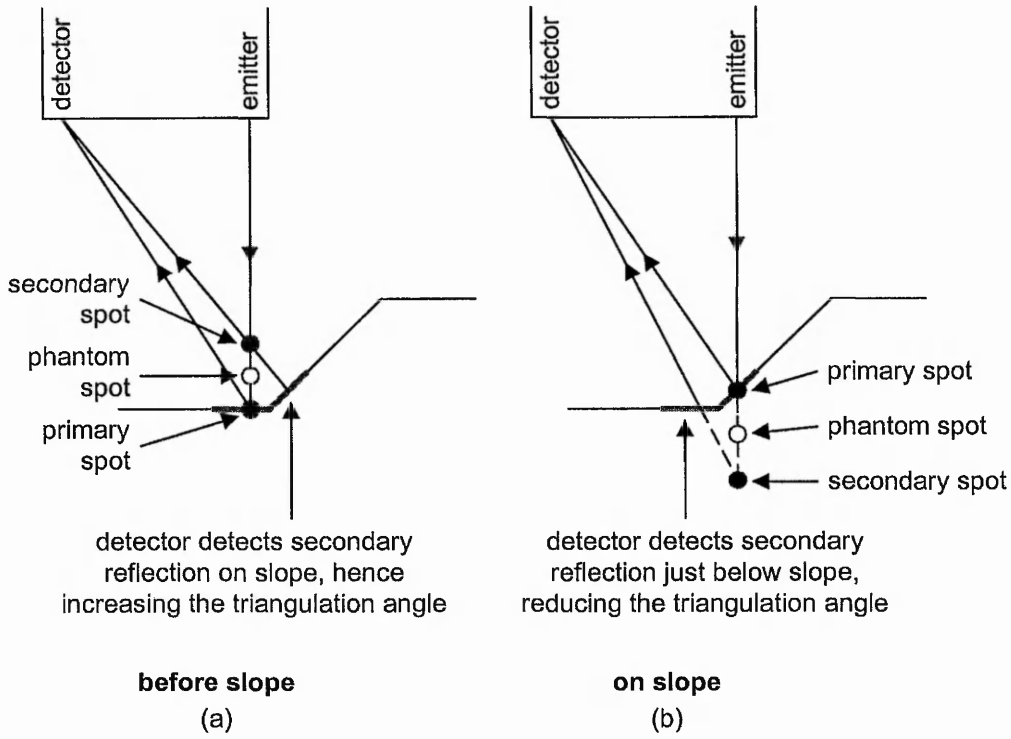

Fig. 3-26: Secondary reflection and dispersion near the bottom of a slope would yield (a) a point on the bow wave and (b) a falling spike.

3.3.6 Occlusion Spikes

Another observable type of significant distortion near the object's regions of high curvature occurs when the sensor is oriented up the edge of these regions. This type of distortion is termed *occlusion spikes* in this thesis. These spikes are due to partial or total occlusion of the spot image from the detector's field-of-view. To investigate the contribution of surface reflectivity to the occurrence of occlusion spikes, the following experiment was conducted, using the same object as in the analysis of bow wave.

As with the analysis of bow wave, the orientation of the sensor with respect to scanning direction is important in simplifying the illustrations (see Section 3.3.5 for details). Therefore they are aligned to be parallel to each other.

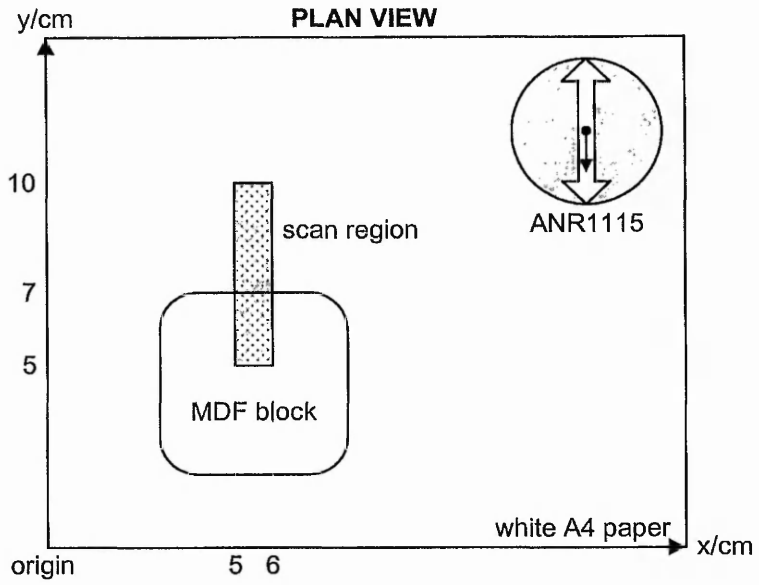

Fig. 3-27: Experiment layout for analysis of occlusion spikes based on surface reflectivity.

The first experimental result represented by a single scanline in Fig. 3-28(a) is obtained from a range image of an MDF block and the planar surface it lies on, both thinly coated with a non-permanent coating, giving a bright, high reflectivity diffused surface. A rising spike appears in close proximity to the object's vertical face and is termed a *crest* in this thesis. By contrast for a surface of low reflectivity – the planar surface has now been painted in black instead – Fig. 3-28(b) shows a falling spike with similar locality as the one shown in Fig. 3-28(a). In this case, the bottom of the falling spike is the depth measurement when there is *no reading* by the sensor, and is thus termed as a *trough* in this thesis. During the scanning process, when there is insufficient light detected by the detector, the sensor outputs a zero value. Upon completion of a scan, the base of the range image, which was initially assigned as the planar surface on which the object lies, is scaled and calibrated to zero. Therefore when readings fall below the base, they become negative values. However there is a valid lowest value on the falling spike as pointed out in Fig. 3-28(b). This isolated reading is the result of a small trace of light being detected by the sensor near the top edge of the object. These experiments show that surface reflectivity plays a role in determining the type of occlusion spikes near regions of vertical faces. This will be discussed in the later part of this section.

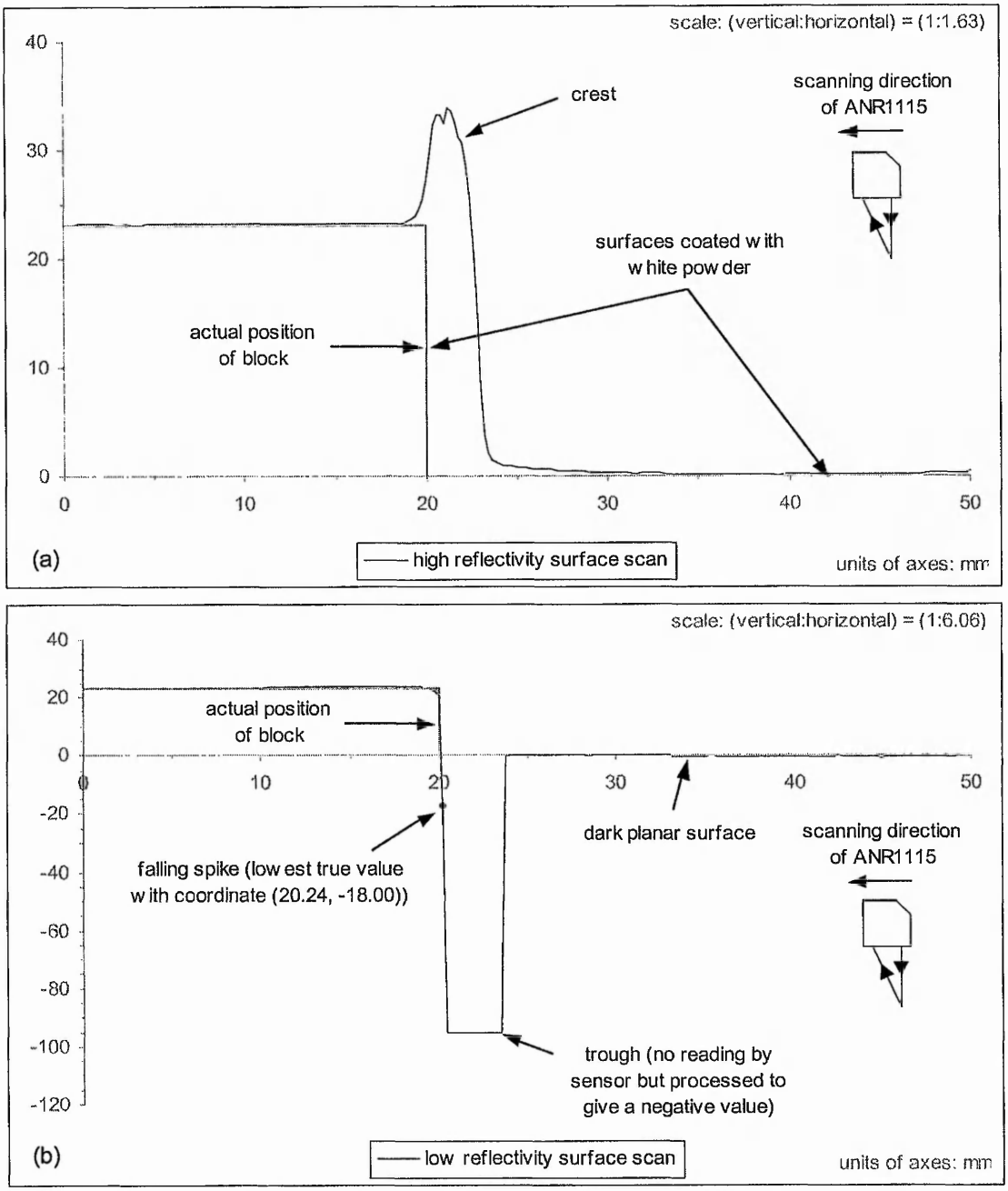

Fig. 3-28: Types of occlusion spikes on surfaces of different reflectivity (scale is increased for greater clarity).

The next experiment involving occlusion spikes is the analysis of the effect of the orientations of the vertical face relative to the sensor. The same four orientations as for bow wave were chosen: 30°, 45°, 60° and 90°. The layout of the experiment is shown in Fig. 3-29.

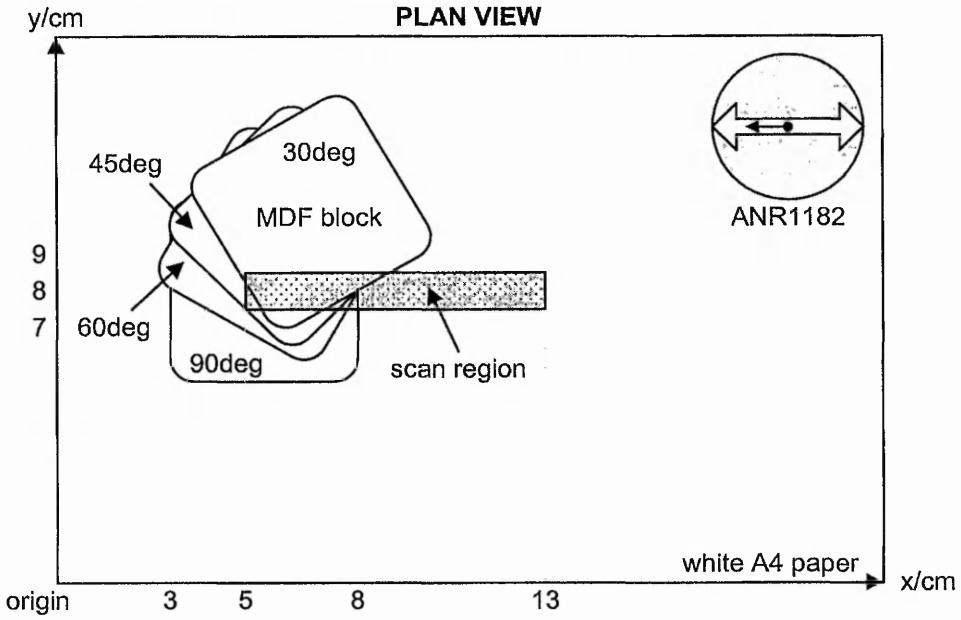

Fig. 3-29: Experiment layout for analysis of occlusion spikes based on orientations of vertical face relative to sensor.

The results for the experiment are as follows:

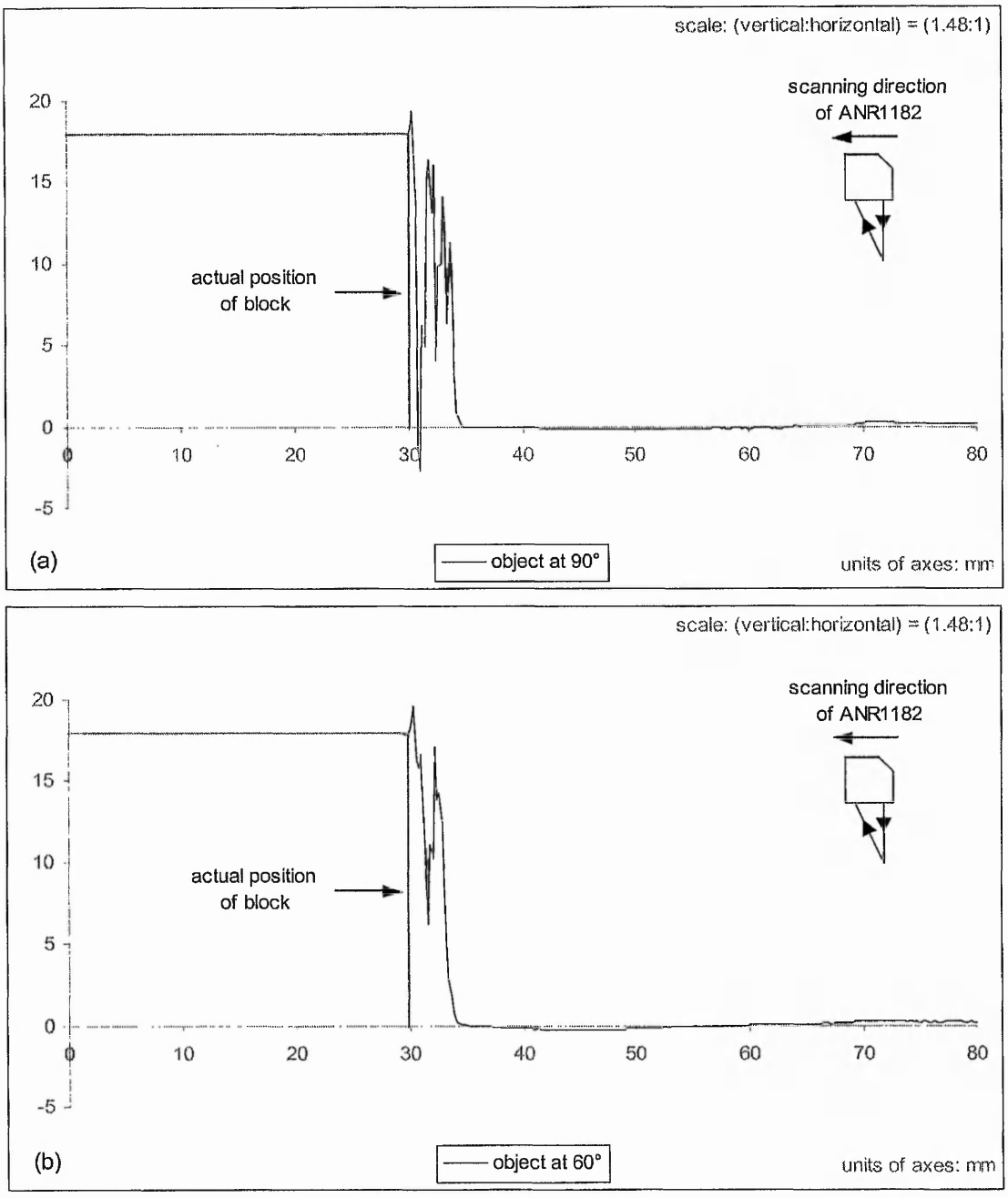

Fig. 3-30: Significance of occlusion spikes changes with orientations of vertical face relative to sensor at (a) 90° and (b) 60° ((c) and (d) on following page – scale is increased for greater clarity).

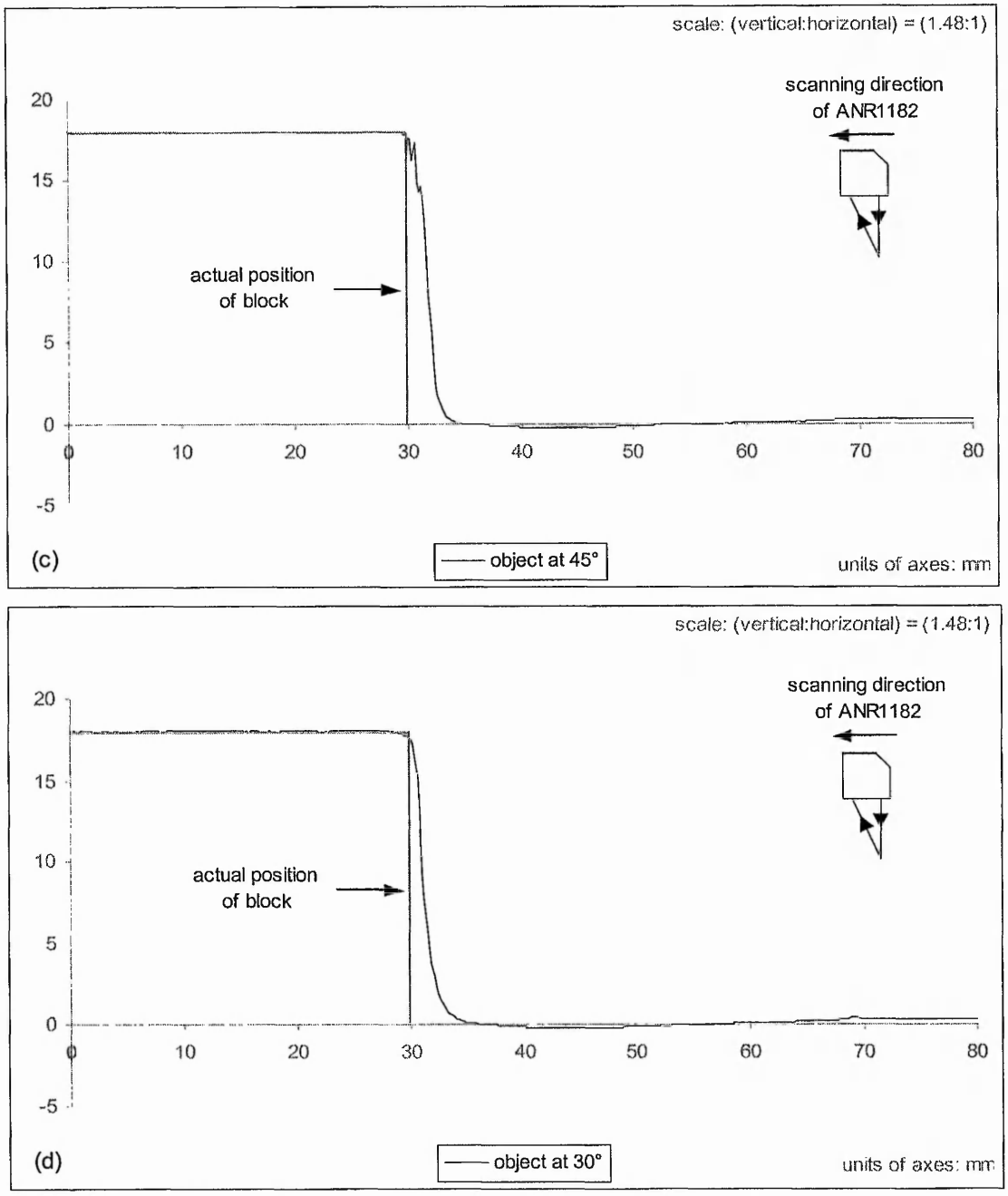

Fig. 3-30: Significance of occlusion spikes changes with orientations of vertical face relative to sensor at (c) 45° and (d) 30° (scale is increased for greater clarity).

When the object's vertical face is at 90° to the orientation of the sensor, there appears to be a significant amount of occlusion spikes. As the object is rotated, these spikes are clearly seen reducing in size until the vertical face is at 30° to sensor's orientation, in which there appears to be no occlusion spikes (see Fig. 3-30). However in Fig. 3-30(d) the gap between the actual scanline and the vertical face is much wider than the one at

30° for bow wave (see Fig. 3-18(d)). Therefore there is still a smaller spike at this orientation.

The effect of the gradient of a slope to the incidence of occlusion spikes was investigated in the following experiments. Four different gradients were chosen: 30°, 45°, 60° and 90°. Fig. 3-31 shows the layout of these experiments.

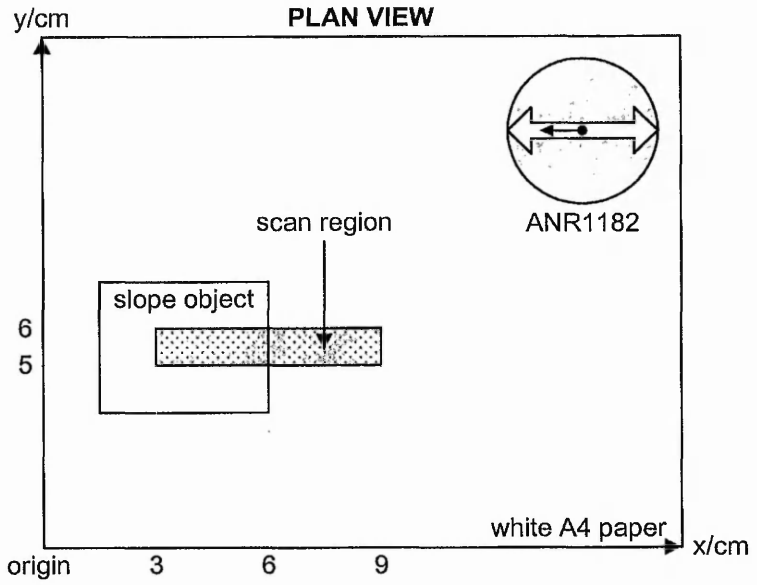

Fig. 3-31: Experiment layout for analysis of occlusion spikes based on gradient of slope.

It can be observed from Fig. 3-32 that as the gradient increases, distortion increases in magnitude (see also Fig. 3-22 for comparison where orientation is parallel to the edge and distortions are very small). On the slope, there appears to be a rising spike, also known as a crest in this thesis, and just before the slope, there appears to be a falling spike, which is not necessarily a trough. Their occurrence can be attributed to the detection of secondary reflection and its dispersion, which will be discussed in greater detail later in this section. In this thesis, these rising and falling spikes are called occlusion spikes even when there is no true occlusion, because they are related to the same orientation of the sensor.

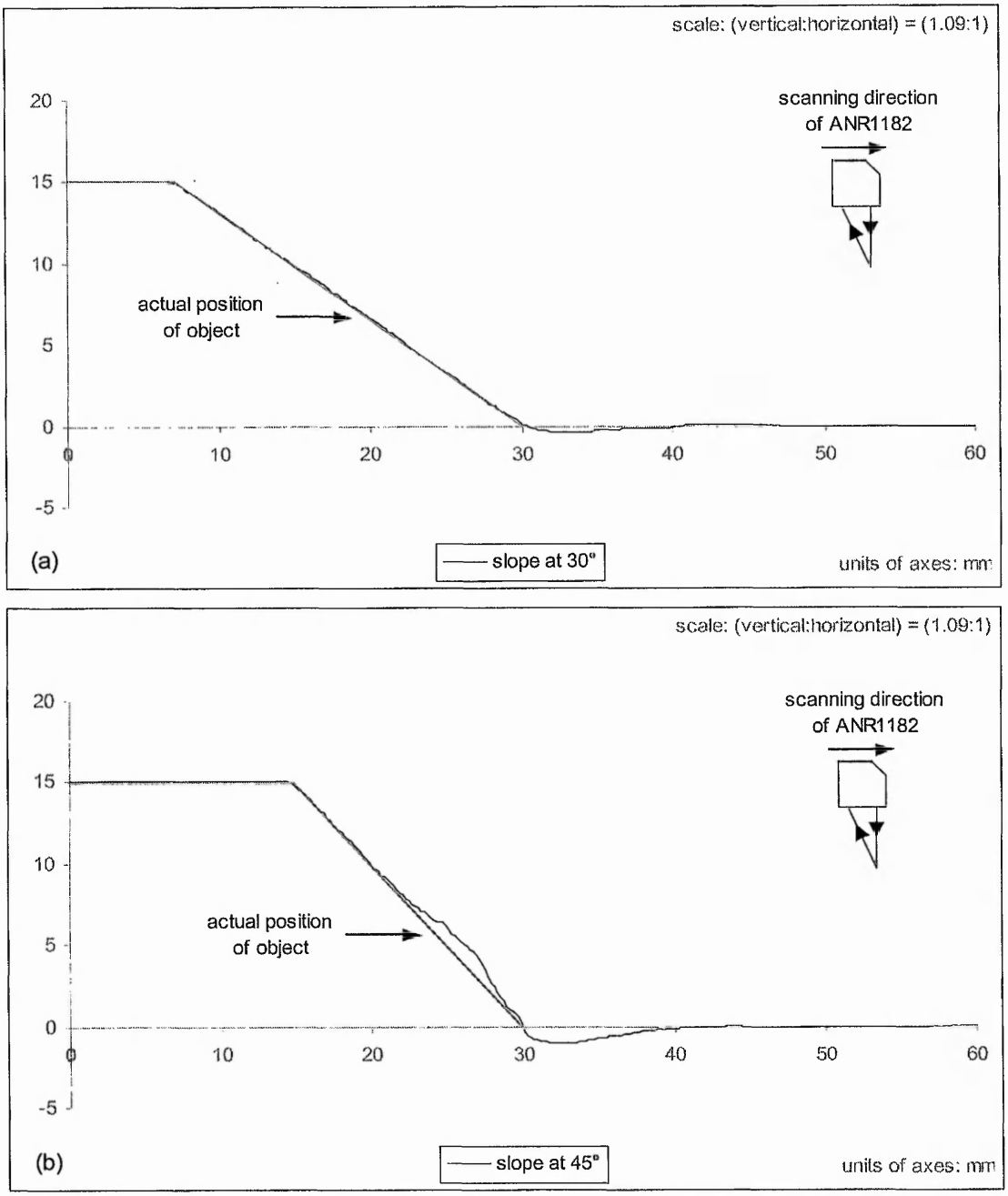

Fig. 3-32: The nature of occlusion spikes changes with gradients of slope at (a) 30° and (b) 45° ((c) and (d) on following page – scale is increased for greater clarity).

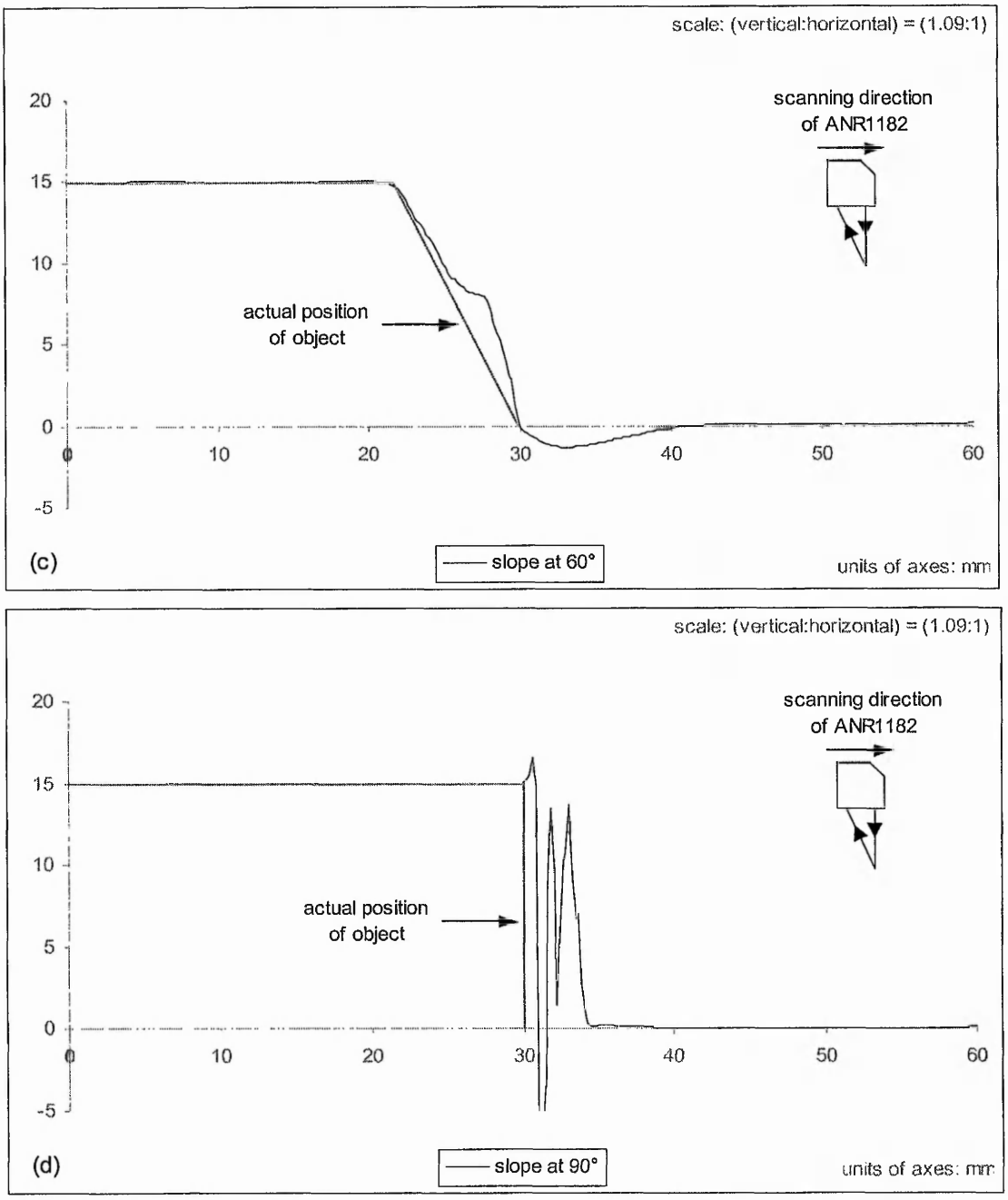

Fig. 3-32: The nature of occlusion spikes changes with gradients of slope at (c) 60° and (d) 90° (scale is increased for greater clarity).

As mentioned earlier, occlusion spikes occur when the spot image is obscured from the detector's field-of-view by the inclined or near-vertical face of an object (see Fig. 3-33). Some authors use the term *shading* in defining the occluding of a spot image. Depending on the sensor's triangulation angle with respect to height and gradient of the inclined face (see Appendix B.1), the size of the region where occlusion occurs varies. The

sensor outputs a zero value when there is insufficient light during scanning. With scaling and calibration of the base to zero upon completion of a scan, this has become negative values, thus producing a *trough* (see Fig. 3-28(b)). But there are valid readings in certain occluded regions because the sensor detects traces of dispersed light or when they are not truly occluded. These readings produce either a rising spike, also known as a *crest* (see Fig. 3-28(a)), or a falling spike with valid readings, depending on the location of the detected traces of light.

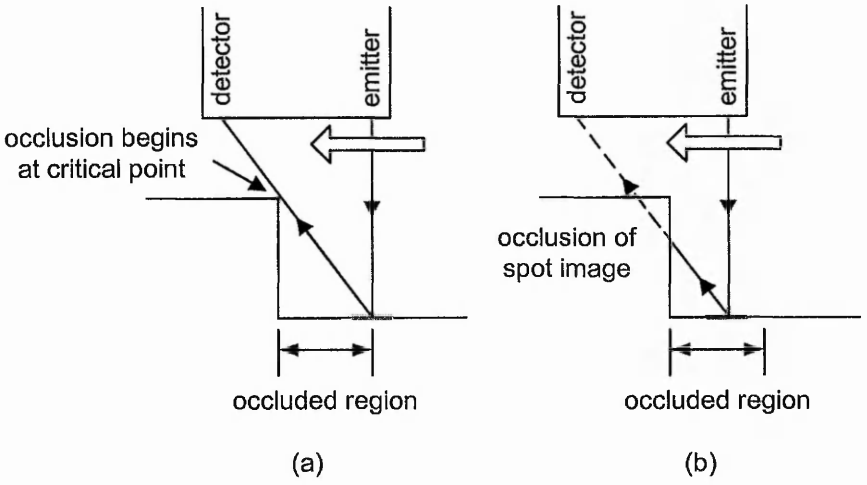

Fig. 3-33: Occluded spot image from sensor's field of view.

In the previous section, it was described how the detector's field-of-view covers a fixed viewing angle. Therefore stray or dispersed light from the projected spot image can be detected as well. The incidence of a rising or falling spike, or some combination of both is determined by the reflectivity of the object's vertical face and the planar surface. Highly reflective surfaces will increase the dispersion of spot image on the planar surface with multiple diffused reflections between it and the vertical face. This dispersion is likely to extend beyond the occluded region and some light may therefore reach the detector. During a scan, the extended trace of light will then be perceived as an elevated point above the true surface because of an increased in triangulation angle (see Fig. 3-28(a) and Fig. 3-34(a)). This perceived new spot, which has false height, is referred to as a *phantom* spot. Surfaces with low reflectivity have lower dispersion of the spot image, which is unlikely to extend beyond the occluded region. Therefore when there is no reading, the sensor will give zero output, which would then be scaled to a negative value, and a trough is thus formed (see Fig. 3-28(b) and Fig. 3-34(b)).

Sometimes for a vertical face, there appears to be a lowest valid reading (see Fig. 3-28(b)). This is because when the centre of the spot image, which has a certain width, is projected very close to the vertical face, part of it is distributed on the top edge of the object (see Fig. 3-35). The sensor would detect this partial spot image and its dispersion, resulting in a phantom point with valid reading below the true surface. In most cases, dispersion of the light varies with small details of the surface, resulting in a combination of rising and falling spikes (see Fig. 3-30). Thus the exact nature of the occlusion spikes obtained depends on the reflectivity of surfaces.

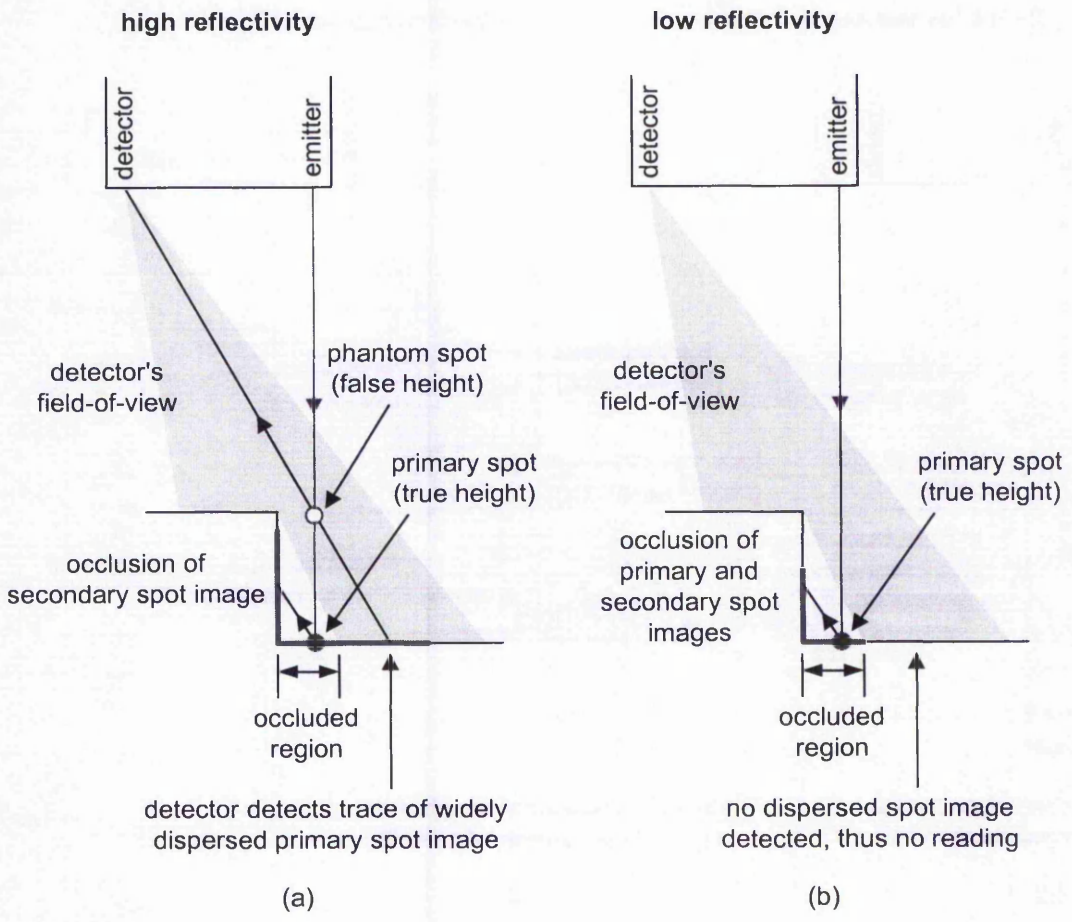

Fig. 3-34: Effects of surface reflectivity in producing a crest and a trough.

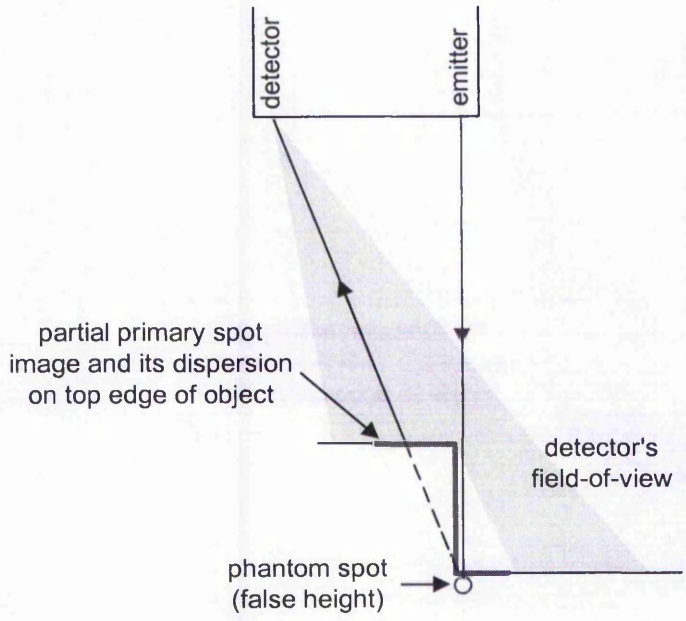

Fig. 3-35: Detecting a partial primary spot image and its dispersion on top edge of object when laser beam is very close to vertical face of object, resulting in a falling spike with valid readings.

As with bow waves, the orientation of the vertical face relative to the sensor also plays a role in determining the magnitude of occlusion spikes. The detector's field-of-view, which lies mainly in a single plane, detects the full effect of the extended trace of reflected and dispersed light when it is at 90° to the vertical face. However the effect of this trace of light reduces as the angle of the vertical face moves towards 30°, in which the detector captures only a small amount of this light, giving a small distortion (see Fig. 3-30).

As mentioned earlier, besides the height and reflectivity of an object, its gradient also plays an important role in determining the incidence of occlusion spikes (see Fig. 3-32). Total occlusion may not happen when the slope of the object is inclined at much less than 90°, which by then would be a vertical face with respect to the detection of the projected spot image. In such circumstances, traces of light from secondary reflection and dispersion will be detected. These traces are more evident with increasing gradient as more light is reflected between the slope and the planar surface. Therefore the magnitude of distortions increases with increasing gradient as well. Falling spike appears

when the primary spot image is positioned just before the slope, in which light is reflected off this incline, resulting in it being picked up by the detector. Consequently the angle of triangulation is reduced and as such, the point registered will be below the true surface (see Fig. 3-36(a)). However when the primary spot image is near the bottom of the slope instead, light is reflected on the planar surface and is thus detected by the detector and as such, increases the overall angle of triangulation. This would then be translated by the sensor's electronics into phantom points, which are above the true surface (see Fig. 3-36(b)).

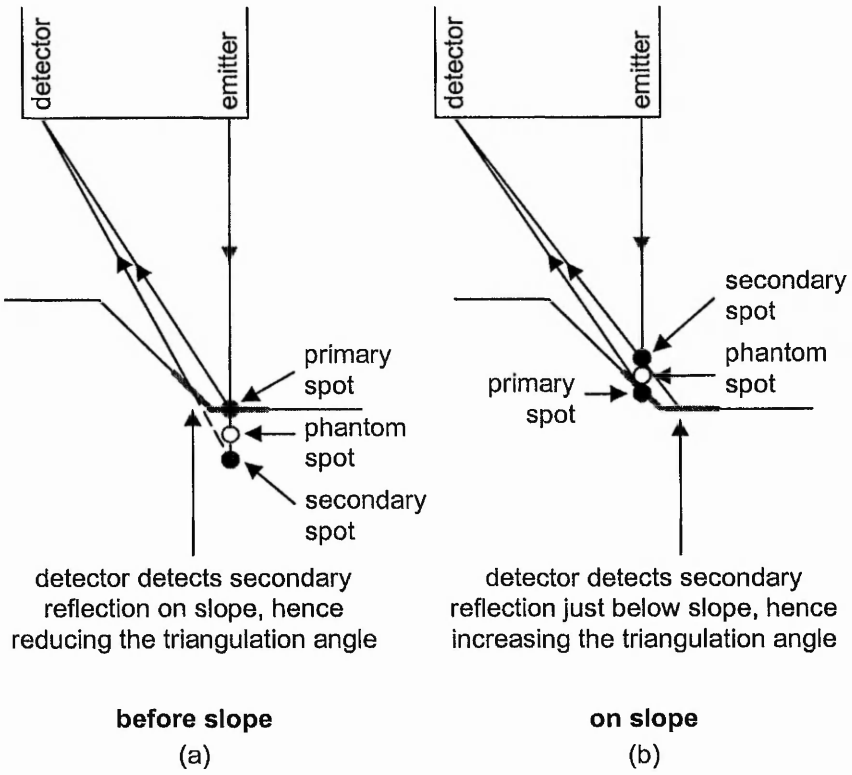

Fig. 3-36: Secondary reflection and dispersion near the bottom of a slope would yield (a) a falling spike (b) a rising spike, or crest.

3.3.7 Variation of Distortions

From the systematic distortions discussed in the previous sections, namely bow waves and occlusion spikes, objects of more varied geometries were scanned and their scanlines evaluated. A combination of these systematic distortions can be observed. They are presented in the following figures.

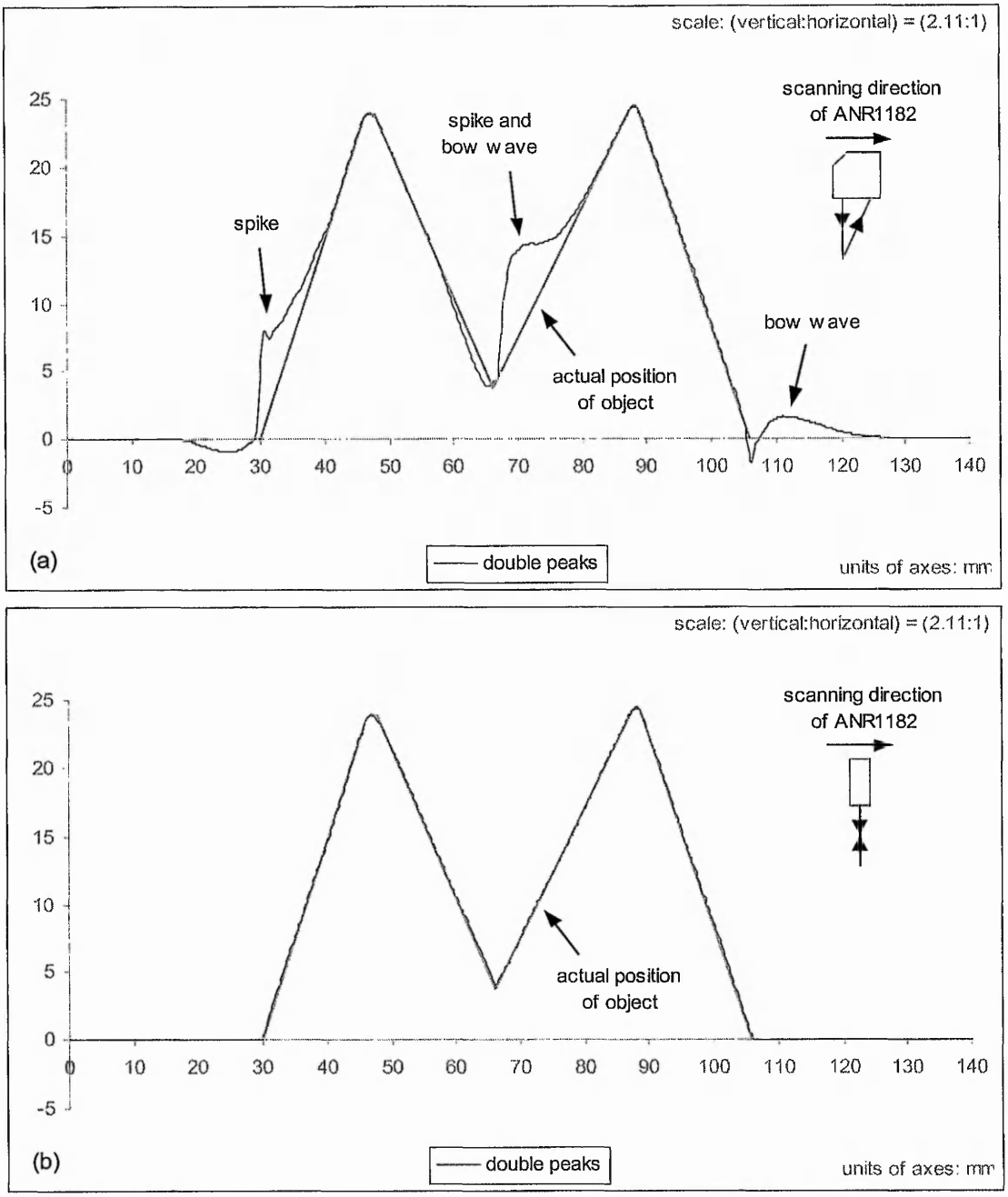

Fig. 3-37: Scanlines for a "double peaks" object (i.e. V-shaped slot) with (a) orientation of sensor perpendicular to "edge" of object, resulting in bow waves and occlusion spikes and (b) orientation of sensor parallel to "edge", leading to closely matched scanline to actual position of object (scale is increased for greater clarity).

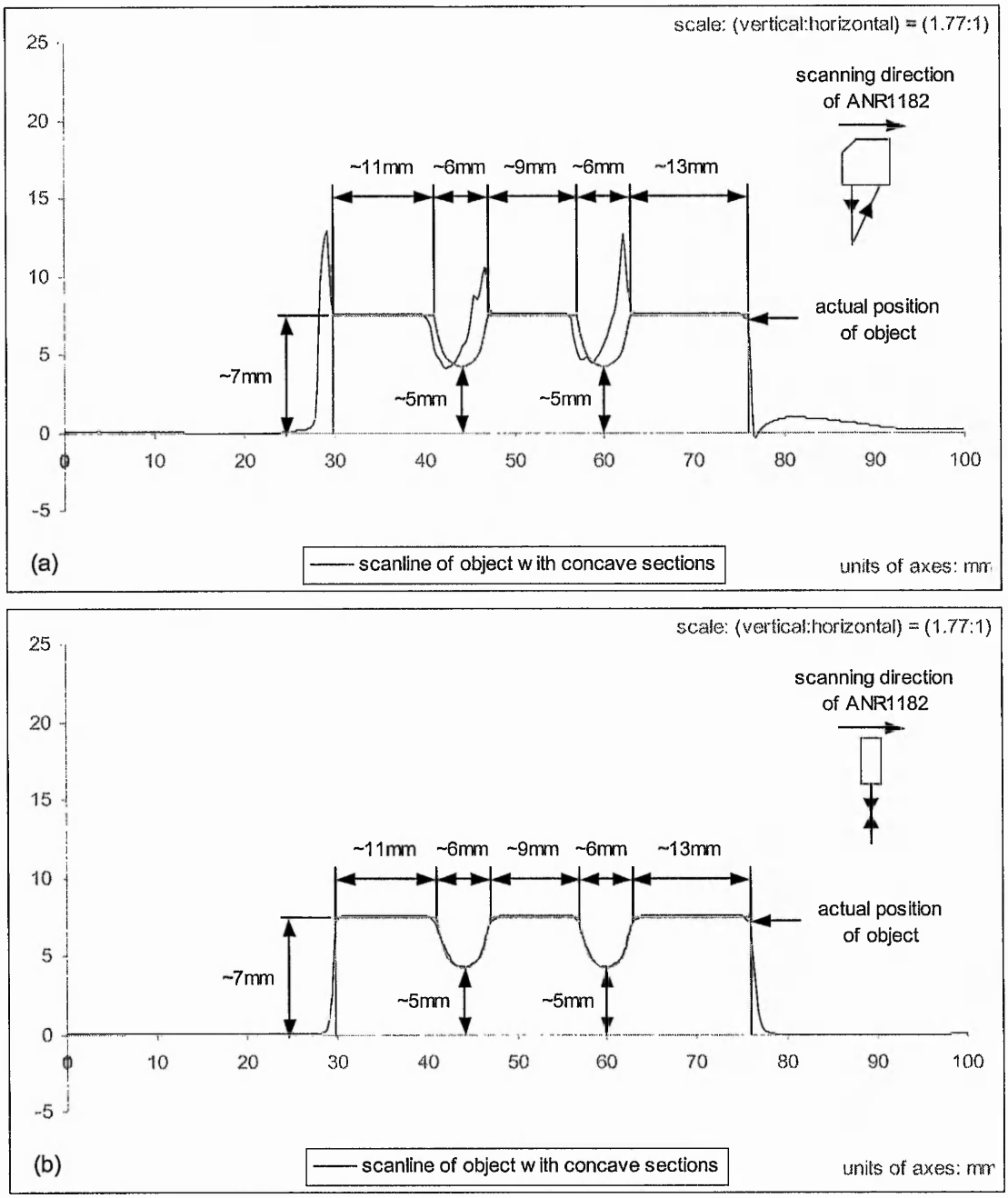

Fig. 3-38: Scanlines for an object with two concave sections on the surface with (a) orientation of sensor perpendicular to the concave sections and (b) orientation of sensor parallel to these sections (scale is increased for greater clarity).

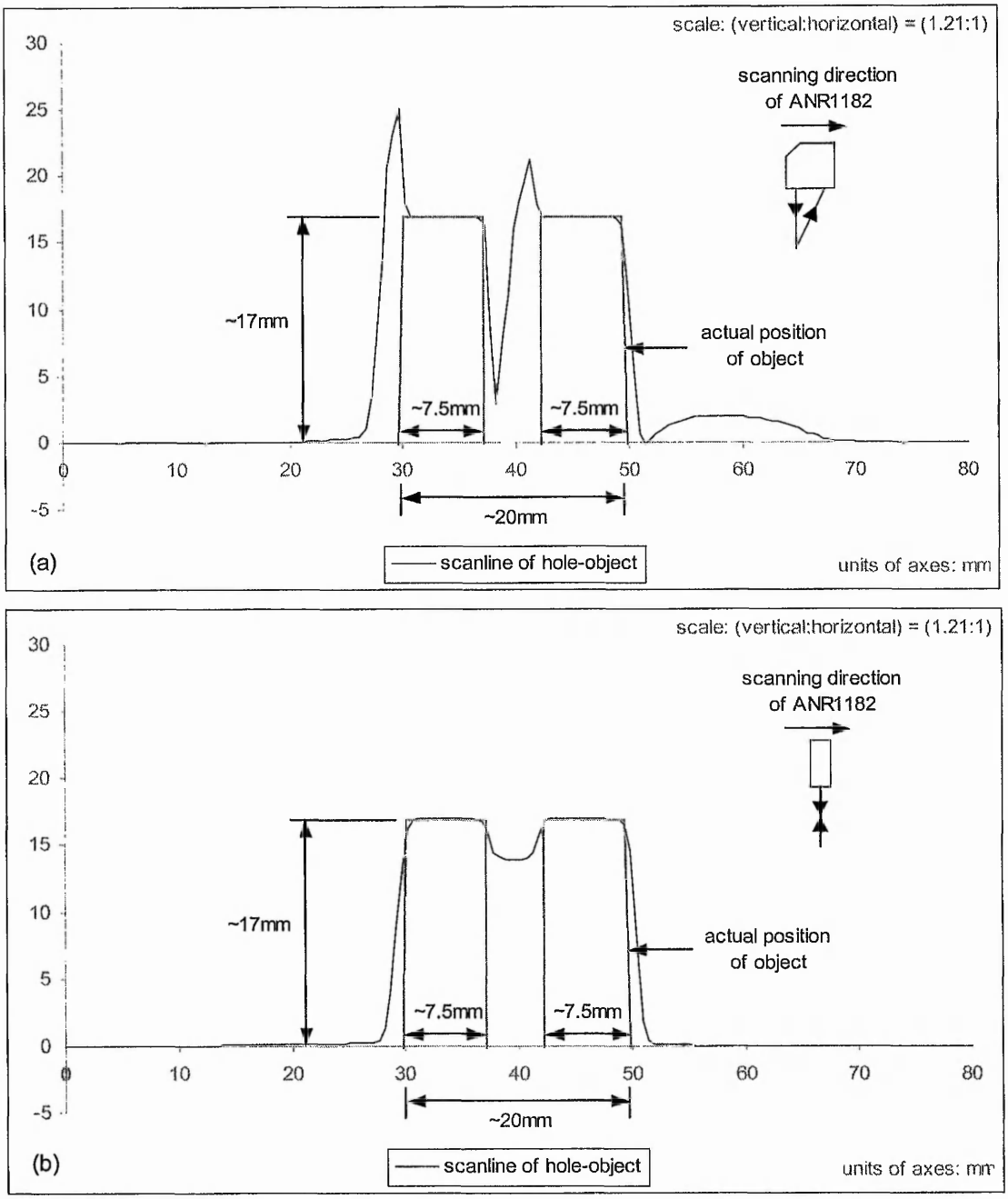

Fig. 3-39: Scanlines for a rectangular block with a 5mm-diameter cylindrical hole with (a) orientation of sensor perpendicular to vertical face of object and (b) orientation of sensor parallel to this face (scale is increased for greater clarity).

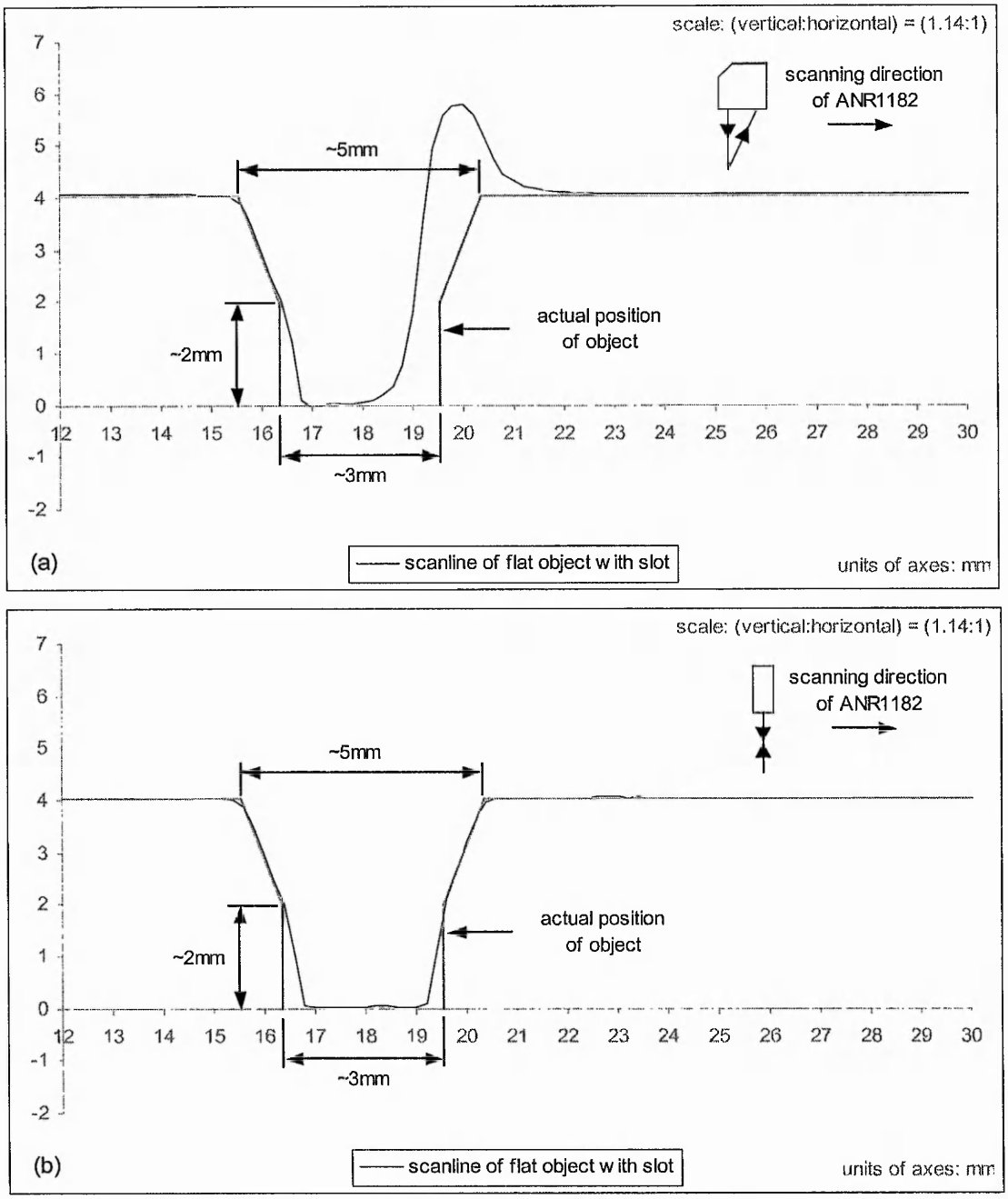

Fig. 3-40: Scanlines for a flat object with a rectangular slot with (a) orientation of sensor perpendicular to "edge" of object and (b) orientation of sensor parallel to this "edge" (scale is increased for greater clarity).

Fig. 3-39(a) shows occlusion spikes and bow waves near the vertical faces of the object. It can also be seen that the scanline does not reach the bottom of the hole because the spot image is occluded from the detector. This occurs even when the sensor is oriented parallel to the vertical faces, as shown in Fig. 3-39(b), because of the other parts of the cylindrical hole which are perpendicular to the orientation of the sensor.

Scanlines for a flat object with a rectangular slot (with a slope at the top half of the slot) are presented in Fig. 3-40. However when the orientation of the sensor is parallel to the "edge" (see Fig. 3-40(b)), the scanline reaches the bottom as compared to Fig. 3-39(b). Although the width of this slot is smaller than the diameter of the hole in Fig. 3-39, it is, however, of much smaller height. Hence the detector is able to detect the spot image at the bottom of this slot. More variation of distortions can be found in Appendix C.1.

3.3.8 Small Systematic Distortions

During the course of this research, another small but noticeable distortion is the occurrence of a "sloping" scanline in place of the vertical face of an object. There is also the effect of "rounding" of sharp corners. Unlike the significant distortions discussed in Section 3.3.5 and Section 3.3.6, these small deviations cannot be attributed to the orientation of the sensor with respect to the geometry of an object because they occur with all orientations of the sensor (see Fig. 3-18 and Fig. 3-39(b)). In Fig. 3-40(b), the "sloping" effect occurs near the bottom of the slot even when orientation of the sensor is parallel to this slot.

One of the reasons they can appear is when the horizontal separation between the scan points is too large. When the points are connected with a line, the result is a small gradient (see Fig. 3-41(a)). Selecting smaller horizontal separation, however, can reduce this effect (see Fig. 3-41(b)).

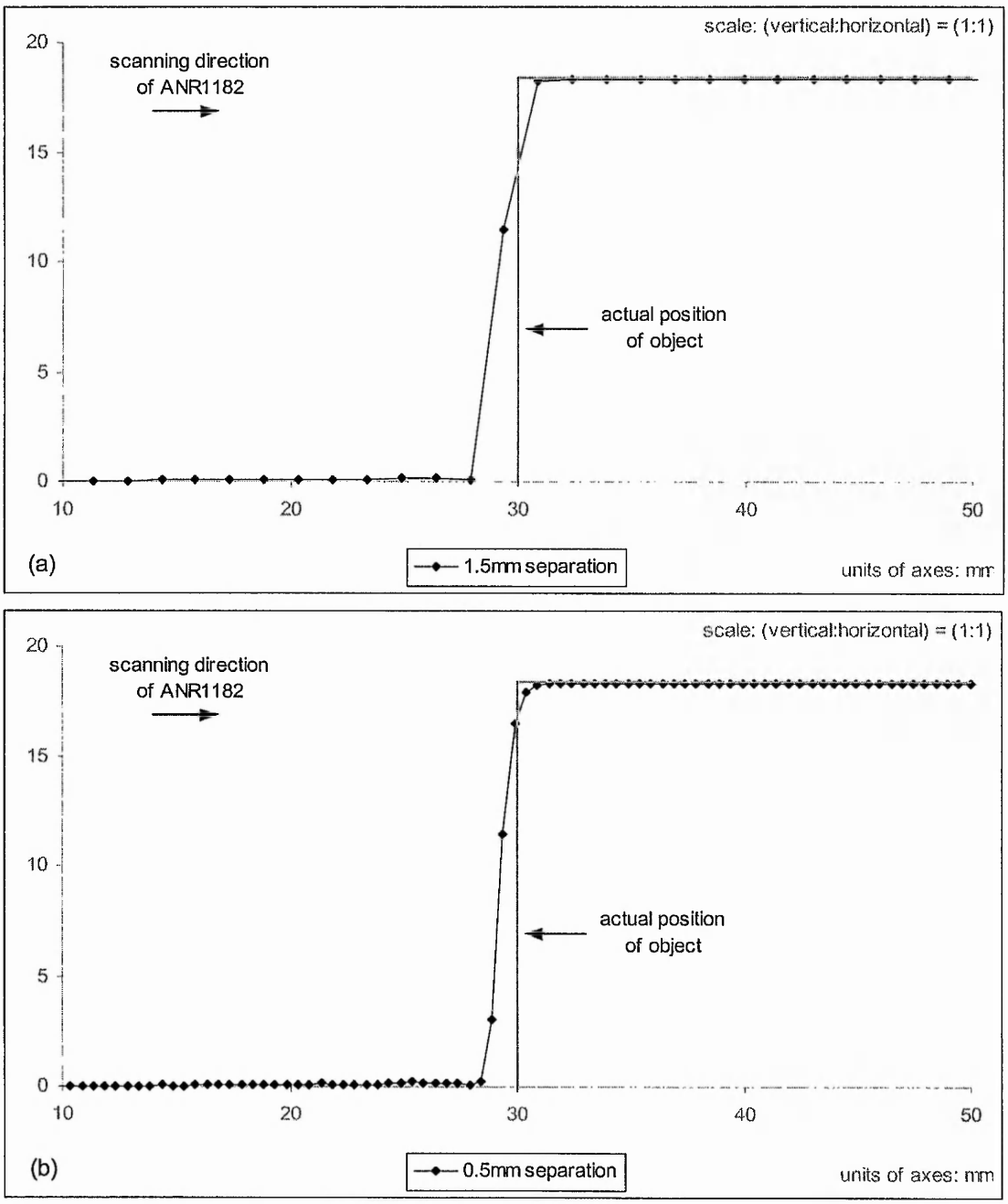

Fig. 3-41: Effect of "sloping" scanline near vertical faces with (a) wider horizontal separation and (b) smaller horizontal separation (width of spot image along horizontal axis is approximately 1.5mm).

Another cause of these effects is the size of the spot image. As the projected spot image has a certain width, a reading is obtained by averaging all the light reflected from the spot (see Fig. 3-41). Hence when the spot image is centred close to the vertical face or the sharp corner of an object, its profile changes considerably. Instead of a single focused spot, the beam may be split between different faces, resulting in readings that are slightly away from the true surface (see Fig. 3-42).

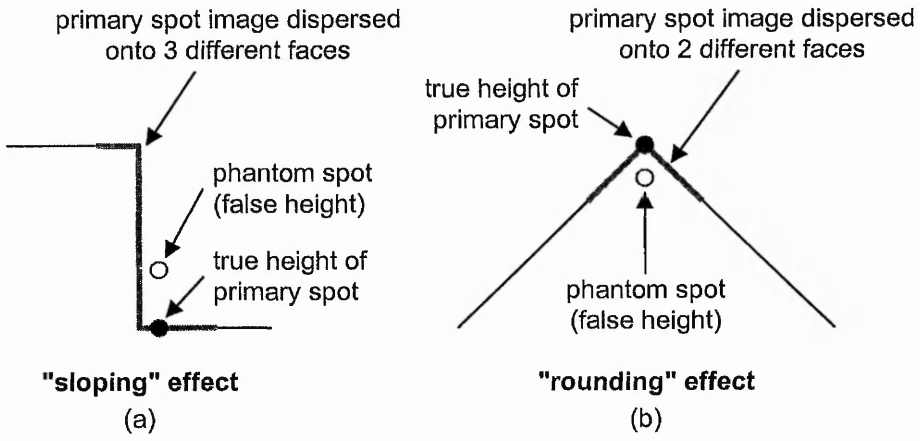

Fig. 3-42: Averaging of primary spot image results in (a) "sloping" of scanlines near vertical face and (b) "rounding" of sharp corners.

3.4 Distortions from Circular-Perspective Point Sensor

The distortions discussed thus far in this chapter have involved a single-perspective point sensor. Analysis of a similar nature was also conducted on a circular-perspective point sensor. Due to radial positioning of multiple PSDs, this type of sensor is much less likely to suffer from total occlusion of the spot image when compared with a single-perspective point sensor (see Section 2.3.3 in Chapter 2). The layout of the experiment is shown in Fig. 3-43.

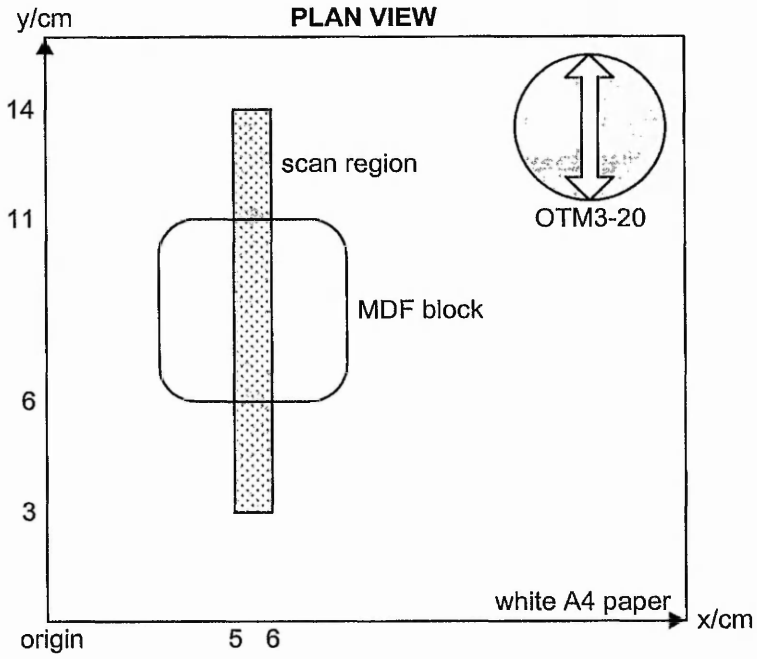

Fig. 3-43: Experiment layout for analysis of distortions of a circular-perspective point sensor.

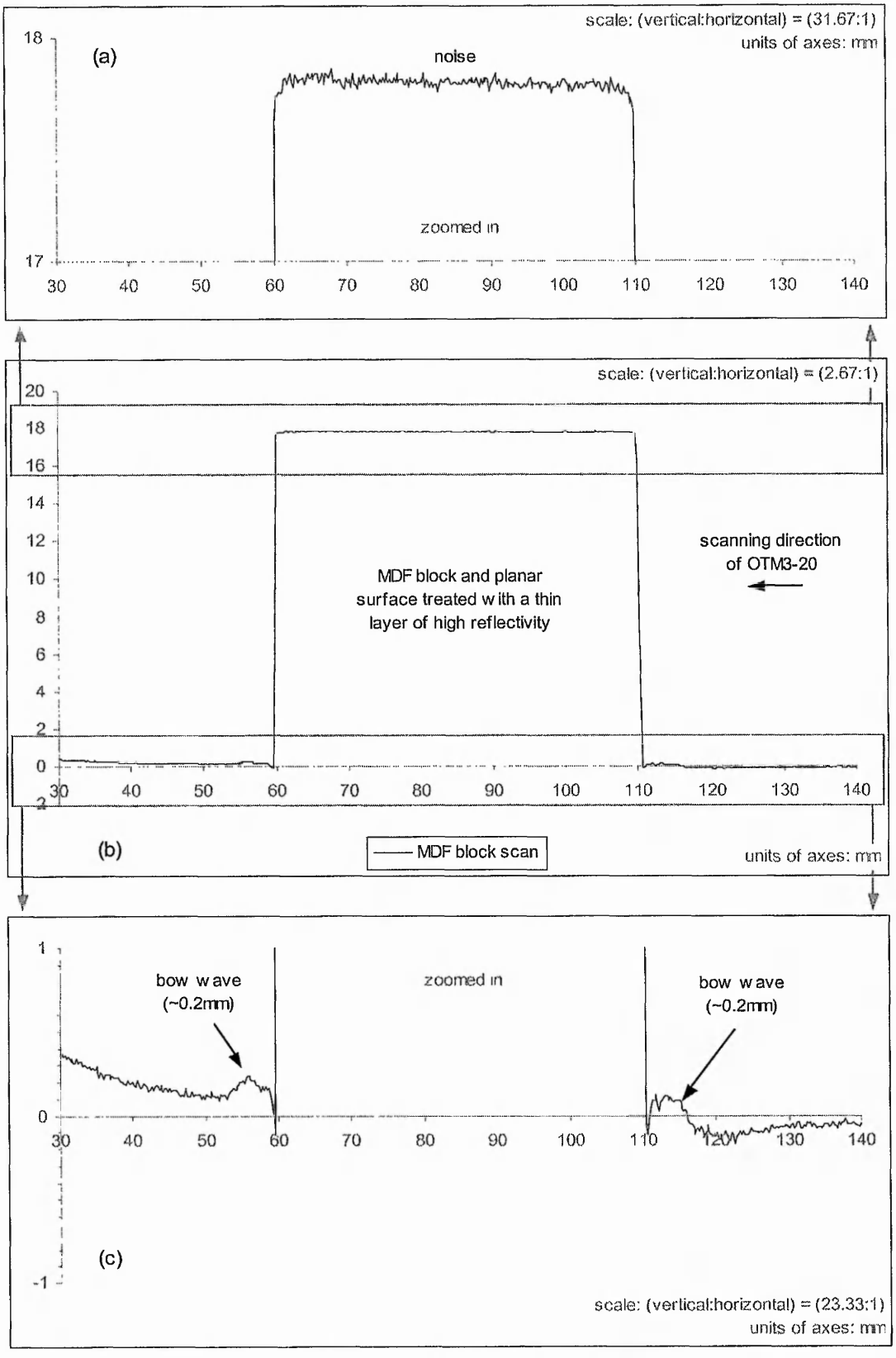

Fig. 3-44: A complete scanline is obtained, (b), and is then zoomed in with greatly increased scale to highlight occurrence of (a) noise and (c) noise and small bow waves.

The experiment was conducted using the same object as the one used in the previous studies. This is to ensure consistency when comparing data sets. In Fig. 3-44(b), the scanline, obtained using a circular-perspective point sensor, appears to show no sign of distortions but upon amplification, it can be seen clearly in Fig. 3-44(a) and Fig. 3-44(c) that it suffers from some noise and that bow waves occur close to both vertical faces of the block. The scanline does not strictly conform to $z = 0$mm, especially visible in the zoomed views, because the planar surface was a piece of paper with small undulations. This, however, is not thought to affect the analysis of the distortions. There does not seem to be any occlusion spike, which is because the spot image is always detectable by some of the detectors, which are placed radially around the emitter, as explained in Section 2.3.3 in Chapter 2. Detectors that are occluded will return no reading and hence, will be excluded from the final output by the sensor's processing electronics. The outputs from the remaining detectors will then be combined and their readings averaged. Therefore the sensor is still able to measure the distance from this partial detection without the occlusion effects. However the effect of secondary diffusely reflected spot image and its dispersions still appears to contribute to the generation of bow waves in close proximity to the vertical faces. The size of these bow waves is considerably smaller, in both height and width, than those of the single perspective sensor. This is because of the implicit averaging of affected and unaffected detectors. The effect of sloping scanline and rounding of corners can also be seen in Fig. 3-44(b), thus affecting the circular-perspective point sensor as well.

Fig. 3-45 shows the effect of a surface with different reflectivity on the scanline. Changes in reflectivity between black and white stripes also affect the circular-perspective sensor, resulting in a small difference in average height. Also incorporated in the scanline is the occurrence of a small bow wave near the vertical face of the block.

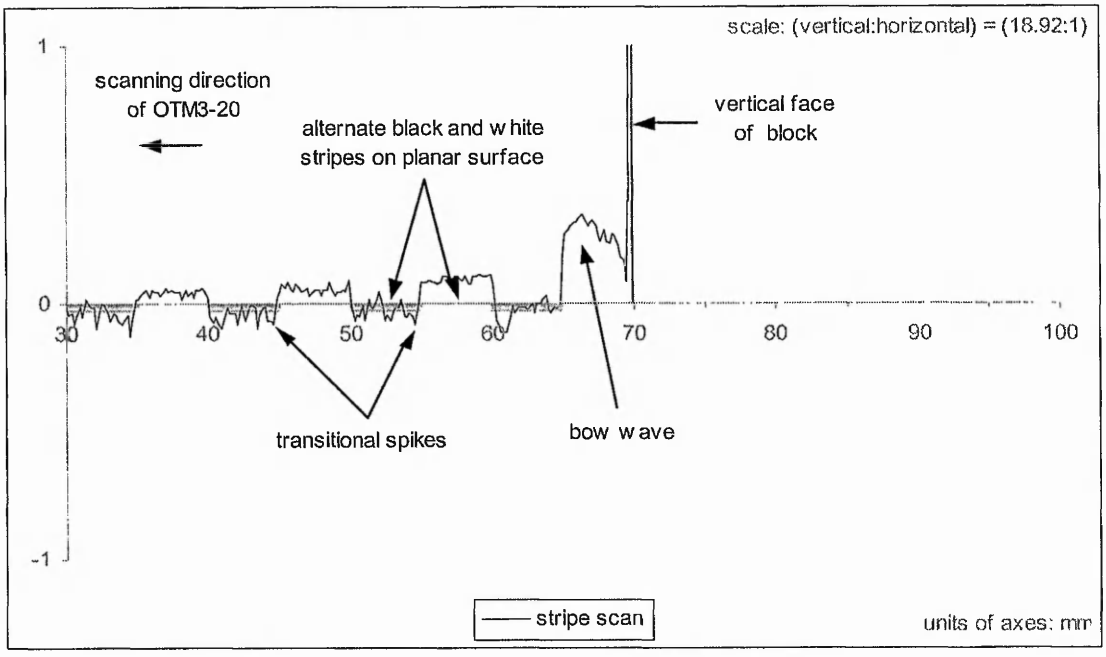

Fig. 3-45: Occurrence of transitional spikes on top of a bow wave in the scanline when using circular-perspective point sensor (scale is increased for greater clarity).

3.5 Summary

By conducting various empirical studies, a good understanding of distortions in point sensors have been established, especially the single-perspective variety. Single-perspective point sensors undoubtedly yield much more significant distortions than circular-perspective point sensors because of detection using only a single detector. Distortions that have been investigated include:

1. Noise – increases with lower surface reflectivity;
2. Transitional spikes – magnitude and direction depend on the orientation of the sensor with respect to the direction of transition between regions of different reflectivity;
3. Bow waves – depending on the orientation of the sensor, the detected spot image can be shifted due to multiple diffused reflections and dispersions off inclined faces;
4. Occlusion spikes – depending on the orientation of the sensor, the spot image can be obscured from sensor's detector by inclined faces, producing unreliable readings or no reading;
5. Small systematic distortions.

From the many experiments that have been carried out, it has been observed that in cases 2, 3 and 4, the orientation of the sensor, but not the scanning direction, plays a pivotal role in determining the nature of distortion that will be encountered. This is a very important point to be taken into account when trying to formulate compensation strategies to combat distortions. Although both bow wave and spike distortions can be reduced by lowering reflectivity, they are still present and noise will be increased. Transitional spikes (case 2) can be avoided by ensuring a homogenous diffusely reflective scan surface.

Circular-perspective point sensor produces better results but it is a much more expensive solution in 3-D scanning. An important consideration in engineering is the cost-effectiveness of the system. Therefore the aim is to develop algorithms to compensate for the distortions obtained, so that the quality of 3-D scanning using single-perspective point sensors can be improved. Another focus is that the circular-perspective point sensor uses implicit averaging in determining the final output, which may also be distorted to some extent. By using a single-perspective point sensor, there can be multiple solutions and strategies to compensating for distortions instead of just averaging.

In Chapter 4, after simple smoothing algorithms to deal with noise, the main focus of the work is on compensation for distortions by combining multiple range images, collected with different orientations of the sensor. This approach can deal with bow waves and occlusion spikes (cases 3 and 4). However the small systematic distortions (case 5), which do not change with orientation of the sensor, will not be affected.

Chapter 4

Compensation for Distortions from Single-Perspective Point Sensor

4 Compensation for Distortions from Single-Perspective Point Sensor

With the understanding of distortions derived from the empirical studies conducted in Chapter 3, the next step is to develop algorithms to compensate for these distortions. One of the fundamentals of improving the quality of 3-D range images is to reduce or to filter noise from the acquired data. A simple smoothing algorithm has been developed to compensate for noise. The method proposed to reduce noise can be employed after removal of the significant distortions, as described in Section 4.2. This algorithm is appropriate for range images where the scanlines contain points which are approximately evenly spaced.

4.1 Compensation for Noise in Range Images

An important part of compensation for distortions is to reduce noise from scanned freeform objects. Otherwise such noise can cause problems during the physical implementation stage, i.e. CNC machining. Experiments conducted by the Author using a single-perspective point sensor have found noise in range images of selected scanned objects. For example, Fig. 4-1(a) shows the scanlines from scanning a smooth planar surface. Unfortunately the acquired range image contains some noise. Therefore compensation for noise is performed via a smoothing operation, resulting in a range image with less noise (see Fig. 4-1(b)).

The noise in range images may be due to several causes, such as spot image variation, low reflectivity of the surface, mechanical vibration of the scanning machine, etc. Besides noise, the collated scan points were irregularly spaced along the scanning direction. It is often useful to organize these points into a fixed sampling lattice. Not only does it improve the image aesthetically but it also facilitates subsequent processing, which includes optimisation and vectorisation of the range image, and for smoother physical implementation.

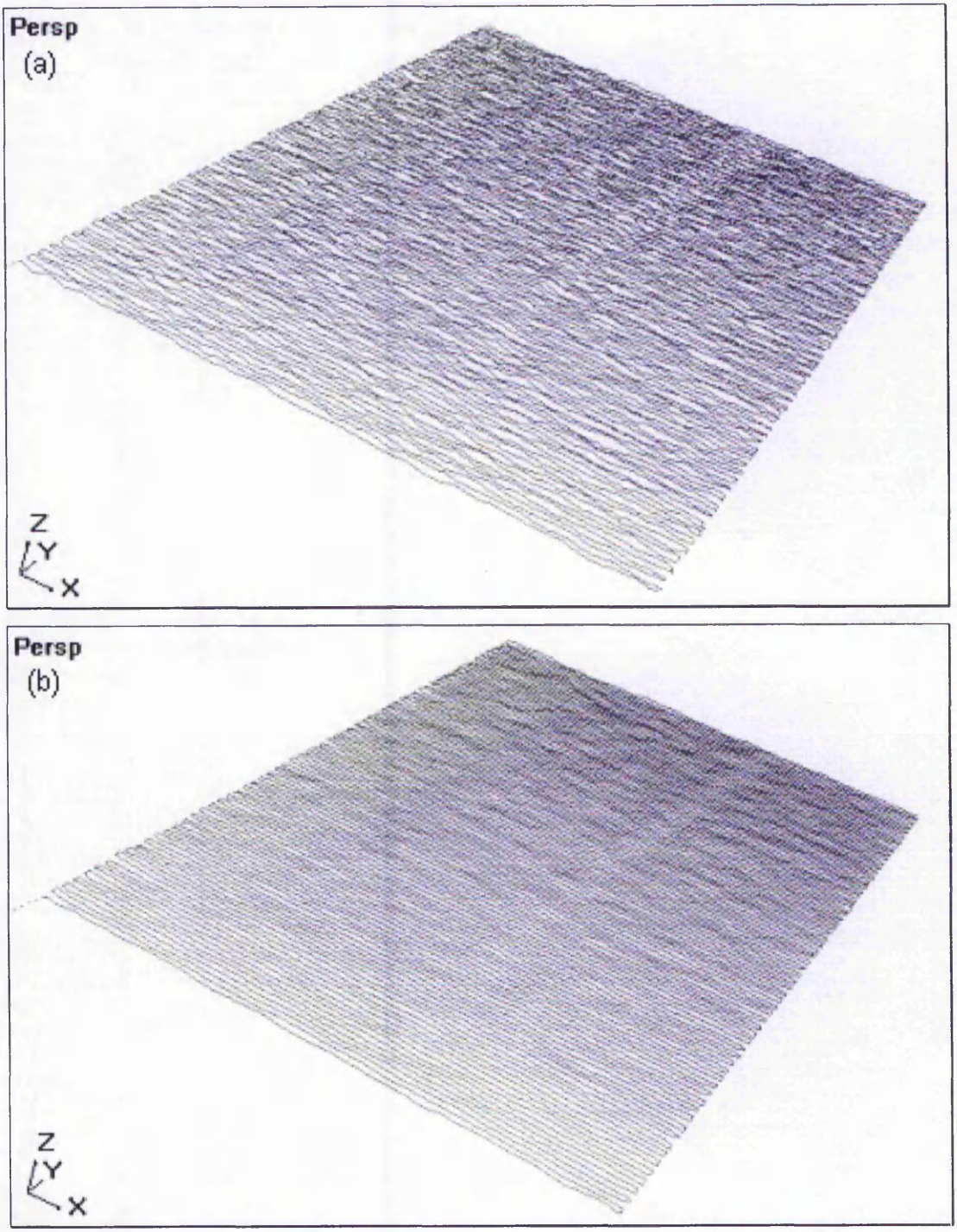

Fig. 4-1: Scanlines for a planar surface[7] (a) before compensation for noise (approximately 0.05mm variation) and (b) after compensation for noise (approximately 0.02mm variation).

[7] The scanned surface has dimension (17mm × 25mm), and distance between 3-D points along x-axis and y-axis are approximately 50μm and 200μm respectively.

Some simple algorithms have been developed to deal with noise, especially for regions of low curvature in an object, and the process consists of three phases. The first phase involves smoothing along the scanning direction by employing a simple averaging technique based on the estimated noise level. The second phase is concerned with organizing and possibly merging the irregularly spaced points into a fixed-width configuration. The final phase performs a second smoothing operation using a square grid.

4.1.1 First Phase: Smoothing of Scanlines

Several different averaging methods can be used for this phase. Initially a weighted averaging method based on the distance of nearby scan points to the point that will be smoothed (see Equation 4-1) was implemented [87]. In this thesis, the point that will be smoothed is known as the *focus point* (FP) (see Fig. 4-2). Using the weighted averaging method, as the distance of the nearby point increases, its effect on the FP decreases. It works better than simple averaging, especially for regions of an object with high curvature, for it does not quickly iron out details so much in the range image (see Fig. 4-3).

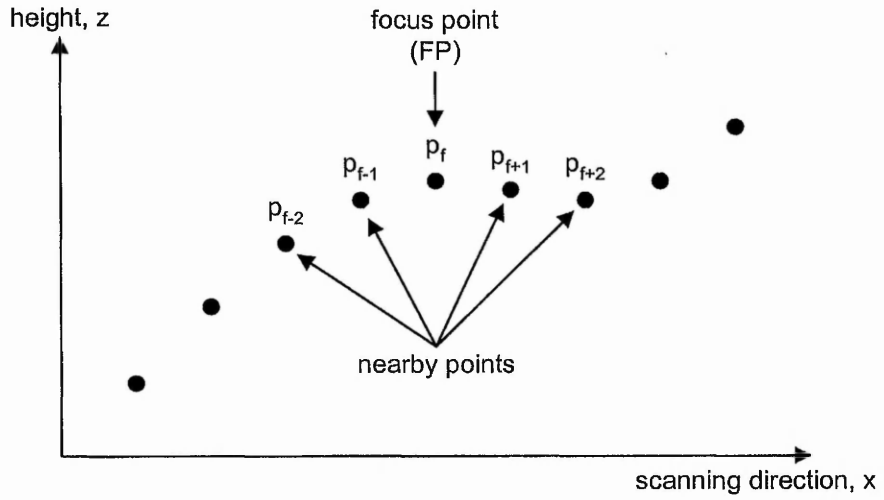

Fig. 4-2: Illustration of the focus point and points nearby from a small section of a scanline.

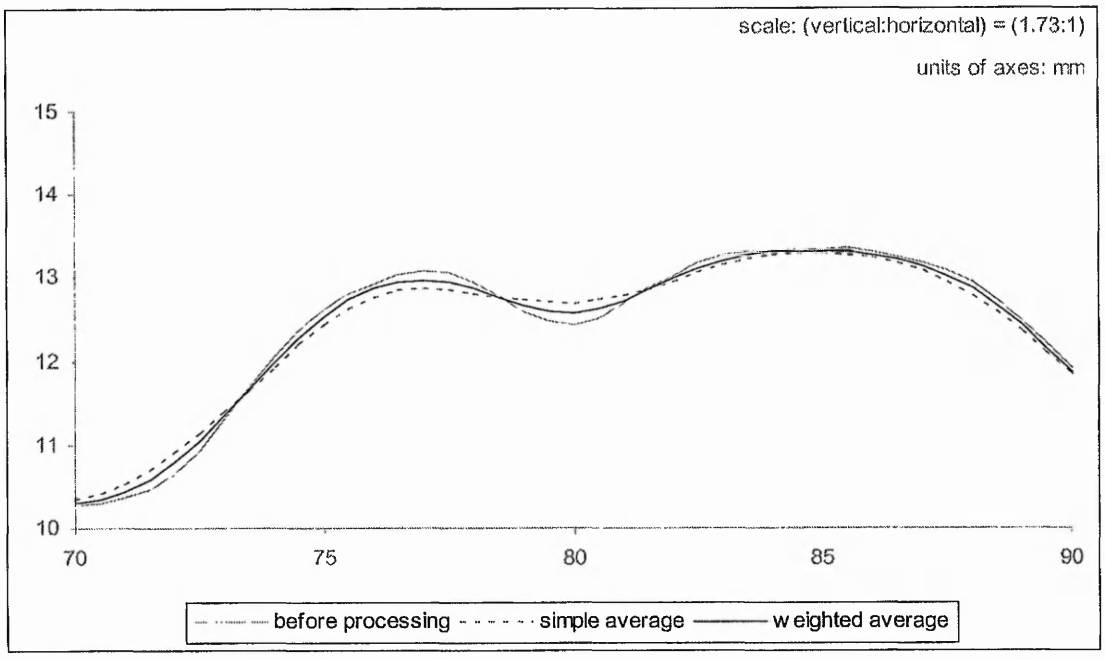

Fig. 4-3: Simple averaging and weighted averaging on a high curvature surface. Both averaging methods employed 4 points on each side of the FP and $k = 1$ for weighted averaging (scale is increased for greater clarity).

The new height is calculated as the weighted average, z_f', using the formula,

$$z_f' = \frac{\sum_{i=-n}^{n} \frac{z_{f+i}}{k + \|\vec{p}_f - \vec{p}_{f+i}\|}}{\sum_{i=-n}^{n} \frac{1}{k + \|\vec{p}_f - \vec{p}_{f+i}\|}} \tag{4-1}$$

where n is the number of points on each side of the FP and k must be non-zero and positive (see Fig. 4-2). Note that when $k \to \infty$, the weights of all points tend closer to the same value. Hence the formula will tend towards Equation (4-2).

Simple averaging formula,

$$z_f' = \frac{1}{2n+1} \sum_{i=-n}^{n} z_{f+i} \tag{4-2}$$

Regions of an object with lower curvature, however, require more iterations of the averaging process to reduce the noise when compared to regions of the object with higher curvature. Research has been conducted to segment an object into regions based

on curvature [88, 89]. Different averaging techniques and their number of iterations can then be employed for each of these regions based on the curvature. A simple averaging technique of a number of nearby points with no weightings was used for surfaces with low curvature. It was observed that the range images for objects of low curvature, such as planar surfaces improved significantly (see Fig. 4-4).

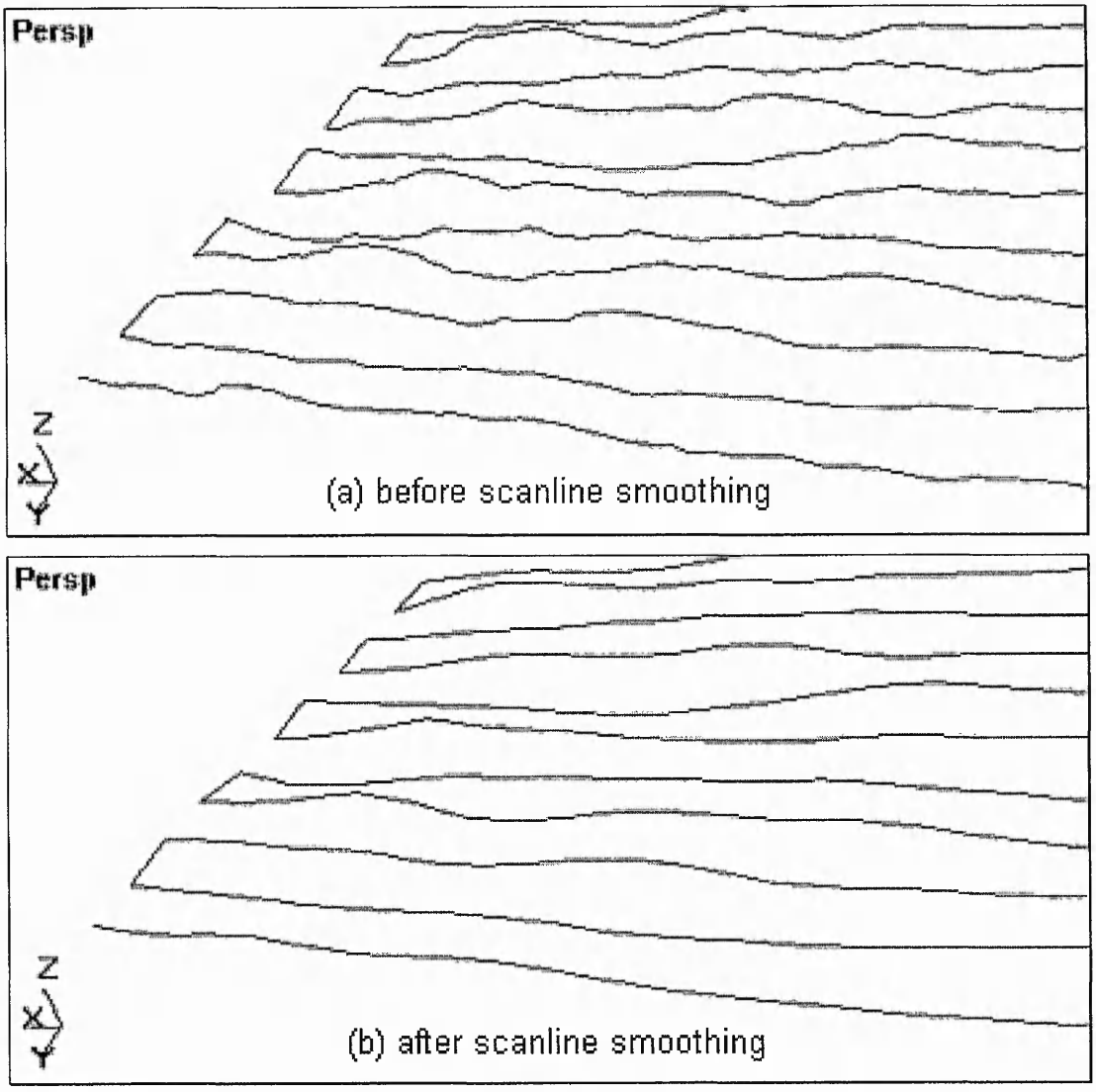

Fig. 4-4: First phase: zoomed views of range image (a) before smoothing and (b) after smoothing with a single pass of the simple averaging formula.

With Equation (4-2), using too many nearby points will result in excessive smoothing, which may remove some of the surface details. Insufficient nearby points, however, may not produce the required smoothing. Therefore the appropriate number of nearby points is determined by *noise level* in a range image. The noise level is calculated based on

the standard deviation of the acquired z-coordinates from true surface – whereby a planar section of the scan is selected to compute this noise level (see Section 4.3.2 for more details). The number of nearby points on each side of FP is a ratio of twice the noise level and selected horizontal separation, which is the distance between two points either along x- or y-axis (see Equation (4-3)). The value of twice the noise level is selected to cover sufficient points on both side of FP for processing without excessive averaging.

The number of points on each side of the FP used for averaging is determined using the formula,

$$n = \frac{2\sigma}{\lambda} \tag{4-3}$$

where σ is noise level and λ is the selected horizontal separation.

For example, if the noise level is 0.4mm and the separation is 0.2mm, the number of points on each side of FP is thus $(2 \times 0.4) / 0.2 = 4$. It can be seen that the bigger the separation, the smaller the number of points that will be available for averaging.

Scan points near the range image's boundaries have to be treated as a special case because there may not be enough nearby points on a particular side of the FP, depending on its position in the range image. Hence in such circumstances when the actual number of nearby points is less than the required number computed using Equation (4-3), averaging is performed with what is available on each side of the FP.

4.1.2 Second Phase: Organization of Smoothed Points

After smoothing every scanline of a range image, the next phase involves aligning the points into a regular sampling lattice. Before a scanning process commences, separation along the x and y axes must be defined. It is preferable for both axes to have similar separations, thus providing symmetry to a range image. It will greatly aid post-processing and enhance visualisation. However points are often collected with smaller spacing along the scanline and are not evenly distributed, whereas the distance between scanlines is larger and evenly spaced, conforming to the defined separation. Therefore the main objective of this phase is to prepare the range image for the final phase of grid

smoothing. Replication of the physical object from these symmetrical scan points may also ensure a better finish.

New points in the *xy* plane are chosen which have the horizontal separation of points along the scanline equal to the separation between scanlines. Hence when there is more than a single point within a defined region along a scanline, they are averaged to form a new point (see Fig. 4-5). The defined region is set equivalent to the separation between scanlines. The generation of new points on the *xy* plane using Equation (4-4) has a smoothing effect as several points are averaged to form a new one.

The height of the new point is determined by using the following formula,

$$z_{new} = \frac{1}{n}\sum_{i=1}^{n} z_i \tag{4-4}$$

where n is number of original scan points within a defined region and z_i is height of existing points within the same region.

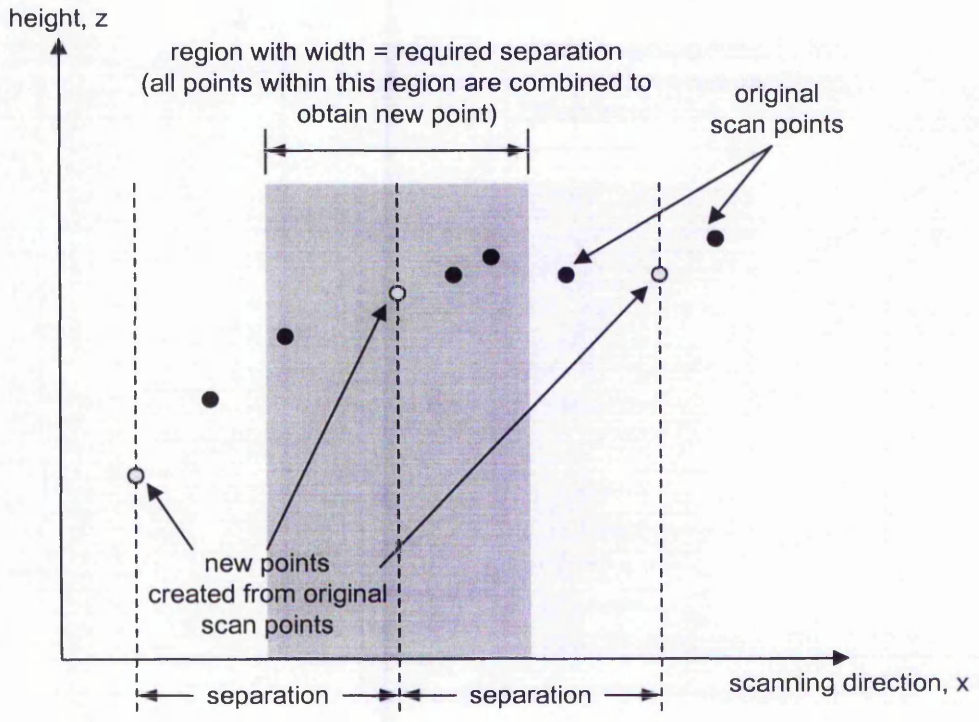

Fig. 4-5: Equal distribution of new points on a scanline, conforming to required separation.

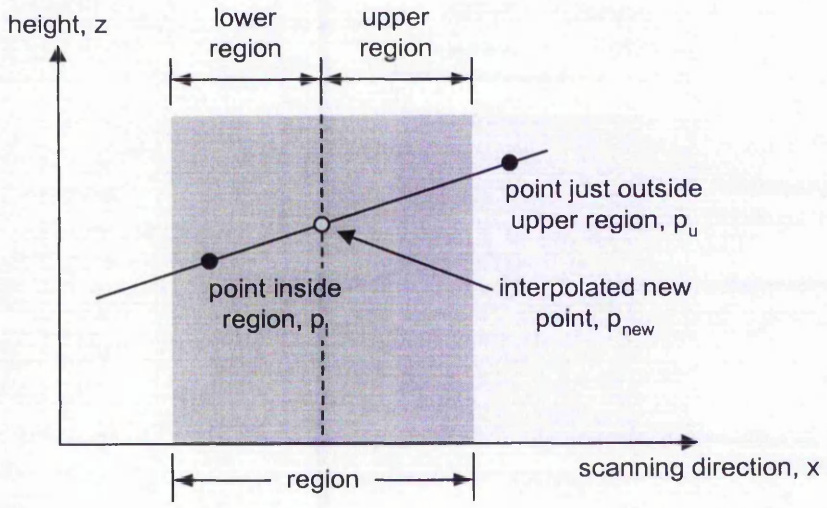

Fig. 4-6: Example of interpolated new point when only one point inside region.

However, when the closest point on one (or both) side of the location of the new point is outside the region, interpolation of the two closest points is employed to identify this new point (see Fig. 4-6 and Fig. 4-7).

If the scanning direction is along *x*-axis (see Fig. 4-6), then the formula for interpolation is,

$$z_{new} = z_l + \frac{z_u - z_l}{x_u - x_l}(x_{new} - x_l) \tag{4-5}$$

where z_{new} and x_{new} are the coordinates of new point, p_{new} while z_l and x_l correspond to the point, p_l, the point closest below, and z_u and x_u are the coordinates of scan point, p_u, the point closest above.

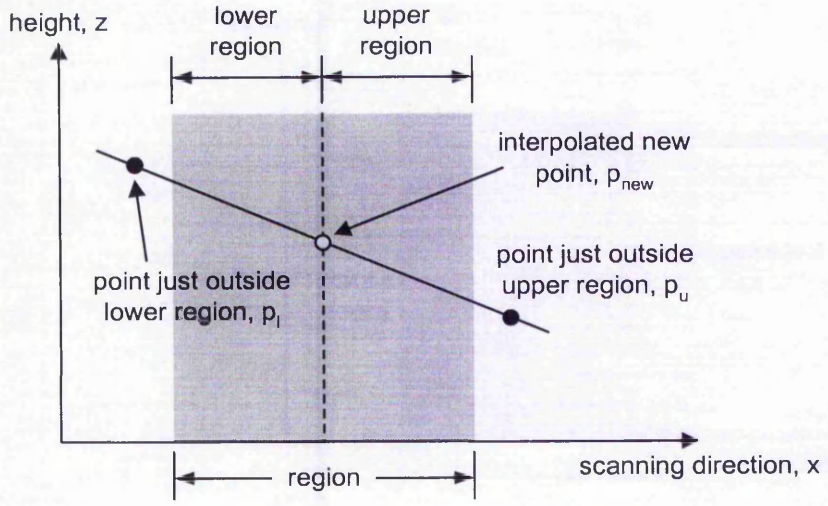

Fig. 4-7: Example of interpolated new point when no point inside the defined region.

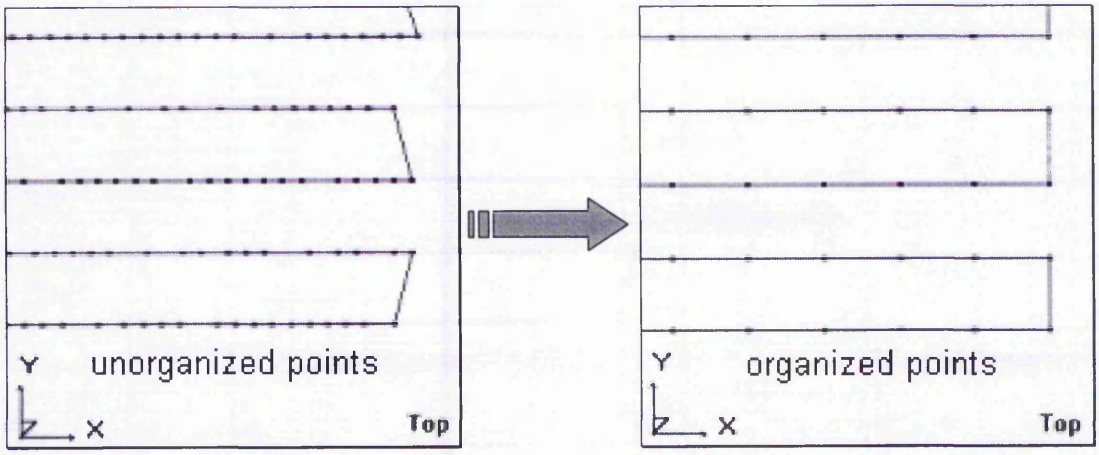

Fig. 4-8: Plan view of scanlines after second phase of compensation for noise with points organized into equal separation (or spacing) in both *x* and *y* axes.

Upon execution of this phase, a whole new set of computed points is obtained with an organized framework while still resembling the original profile of the range image (see Fig. 4-8).

4.1.3 Third Phase: Grid Smoothing

The final phase introduces smoothing using a *square grid*. This phase is easier to implement with the organization of point cloud into a regular sampling lattice, as it

encompasses points not only along the scanning direction but also along the axis perpendicular to this direction.

In the following example a 3×3 grid is used surrounding the FP, in which smoothing can be 5-point or 9-point. The 5-point smoothing involves two adjacent points that lie on each side of FP on a particular scanline, two more adjacent points along the axis perpendicular to the scanning direction on adjacent scanlines, and FP itself (see Fig. 4-9). The 9-point smoothing employs the same points as 5-point smoothing except it includes four extra points from the corners of the grid. These four points would lie on the two adjacent scanlines (see Fig. 4-10).

The formula[8] for 5-point smoothing is given below,

$$z_{i,j}' = \frac{1}{8}\left(z_{i-1,j} + z_{i+1,j} + z_{i,j-1} + z_{i,j+1}\right) + \frac{1}{2}z_{i,j} \tag{4-6}$$

and for 9-point smoothing,

$$\begin{aligned} z_{i,j}' = {} & \frac{1}{16}\left(z_{i-1,j-1} + z_{i+1,j-1} + z_{i-1,j+1} + z_{i+1,j+1}\right) \\ & + \frac{1}{8}\left(z_{i-1,j} + z_{i+1,j} + z_{i,j-1} + z_{i,j+1}\right) + \frac{1}{4}z_{i,j} \end{aligned} \tag{4-7}$$

where i is the location of a point in the scanline, j is the scanline number and $z_{i,j}$ is height of point $p_{i,j}$, and $z_{i,j}'$ is new height for FP.

This stage is vital in reducing irregularities on points along the axis perpendicular to scanning direction. The implementation of the first and second phases may affect the continuity of points between one scanline and the next. Therefore the 3×3 grid method can smooth a range image using some or all of the points adjacent to the FP.

---

[8] The weights for Equation (4-6) and Equation (4-7) were set at these values but different weights could also be used.

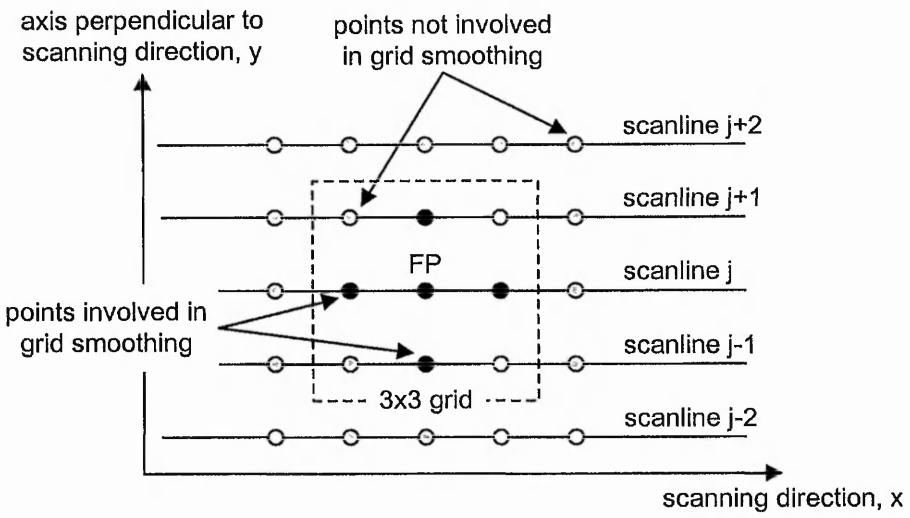

Fig. 4-9: 3×3 grid smoothing with 5 points (plan view).

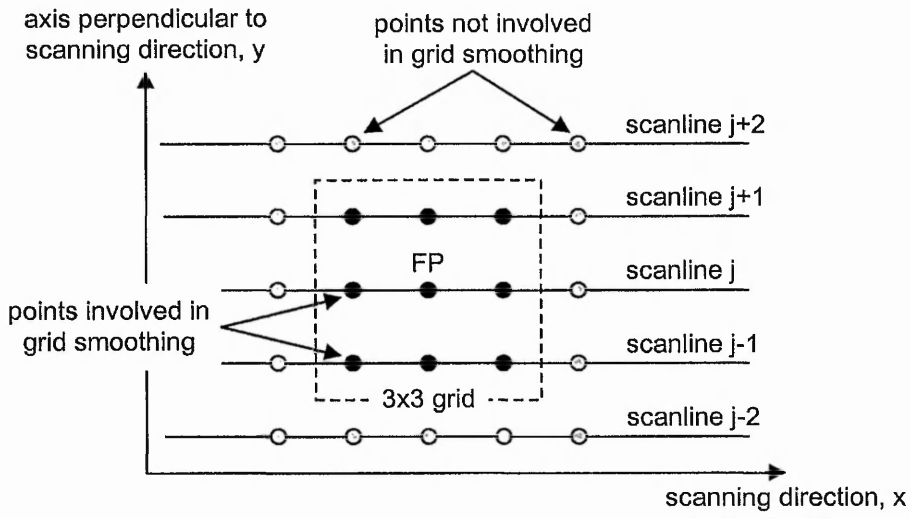

Fig. 4-10: 3×3 grid smoothing with 9 points (plan view).

Since grid smoothing requires adjacent points, it could not be performed on points at the edges of a range image, e.g. those on the first and last scanlines. The 3×3 grid would have insufficient points for computation in those regions. Therefore it is necessary (and good practice) to define a scan region that is slightly larger than that covered by the object of interest. The output of the organized range image after the process of grid smoothing is illustrated in Fig. 4-11.

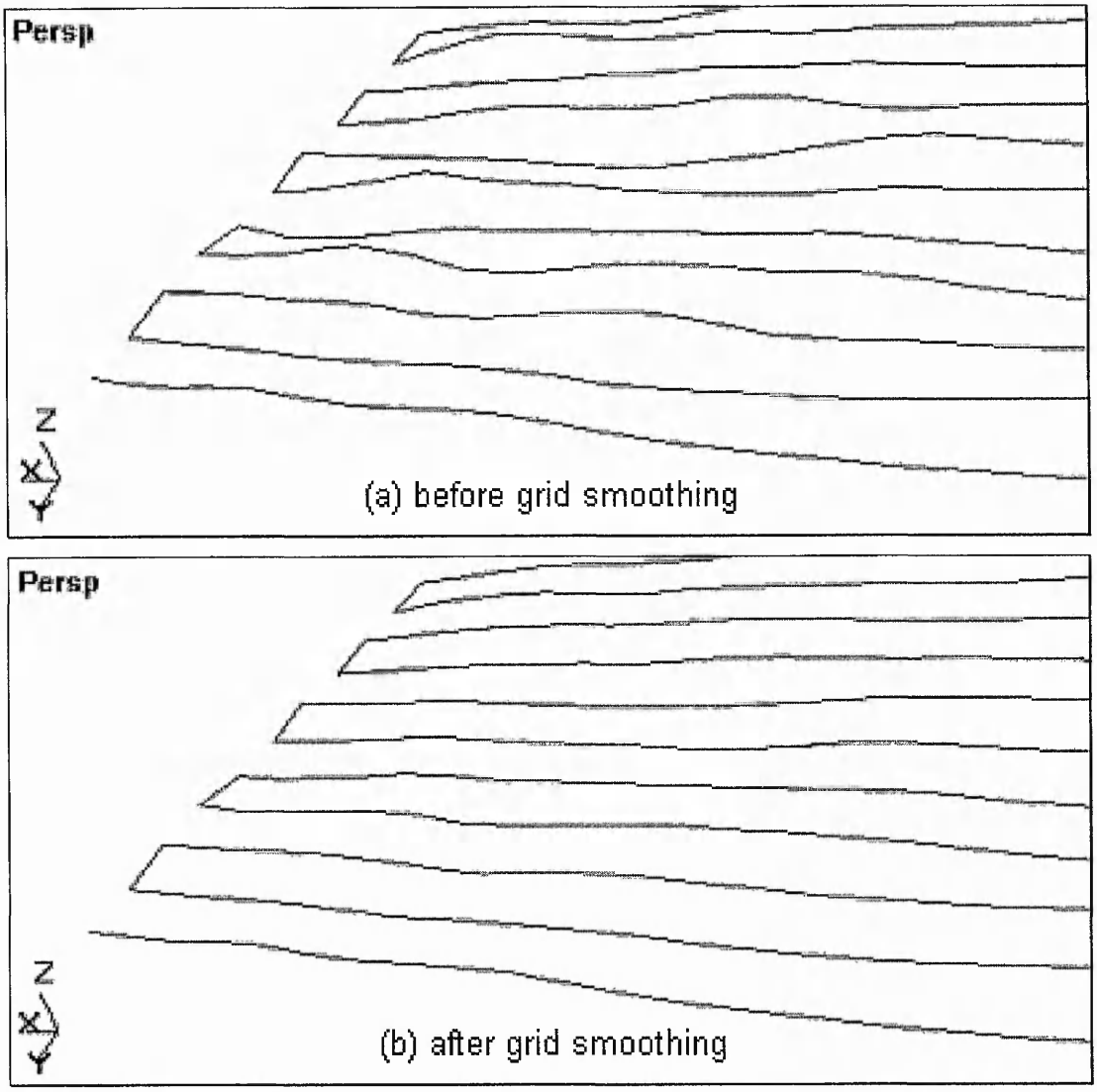

Fig. 4-11: Third phase: zoomed views of range image (a) before grid smoothing and (b) after 9-point 3×3 grid smoothing.

4.1.4 Evaluation and Conclusions

The simple smoothing algorithms described have been implemented and tested on real objects with more complicated geometry (see Appendix C.3). Further research is needed into the averaging and interpolation methods to yield better results. Another approach is to classify an object into different regions based on the curvature of the surface, and then those with high curvature may be treated using a different smoothing, such as the proposed weighted averaging, in the first phase instead of straightforward averaging to prevent excessive smoothing, which may result in unwanted removal of small, intricate details. Organization of points and grid smoothing will further smooth these regions but

they need not be employed if the output of the first phase is found to be satisfactory. However when using weighted averaging for regions with low curvature, numerous iterations will be needed to achieve the desired results, leading to longer processing time.

When there are insufficient scan points to build an organized new point, as discussed in phase two, multiple interpolations with points on adjacent scanlines may produce more accurate results. Also instead of a 3×3 grid, a grid of another size, such as 5×5 or 9×9 could be employed. Although larger-sized grids may result in better smoothing, the power of computation required will increase exponentially. Also it could result in over-smoothing. Hence it is important to consider this trade-off during implementation. Some type of grid smoothing is essential to ensure continuity across the entire surface and not just along the scanlines of a range image. Reducing noise by means of smoothing is most appropriate towards the end of the compensation process after dealing with significant distortions. This is discussed in the next section.

4.2 Compensation for Geometry-based Distortions

The compensation method discussed in Section 4.1 will not remove nor sufficiently reduce significant distortions, such as bow waves and spikes from range images. For such distortions, other methods need to be explored. However, to compensate or rebuild regions where these significant distortions occur, more information is needed. Therefore a new approach, proposed by the Author, involves combining information from multiple range images, each acquired with different orientations of the sensor. The extensive empirical studies described in Chapter 3 showed that the occurrence of significant distortions depends on the orientation of the sensor with respect to the geometry of an object. Hence the functionality of the compensation algorithms developed is based on this knowledge.

4.2.1 Other Approaches to Compensation

Most of the solutions for eliminating or reducing distortions available today involve some form of interactive manipulation of the acquired range image. One of the simplest forms of compensation involves automatic identification and trimming of occlusion spikes that fall or rise beyond the predetermined range of measurement from a single

range image. The missing points are then rebuilt by means of averaging or interpolation with nearby points. This is likely to lead to loss of information in those trimmed regions. Also some less severe distortions may not be detected.

In many situations, a single range image is inadequate to build a complete description of an object. This is due to the orientation of the sensor with respect to the geometry of the object, which may cause some parts of the object to be occluded from the sensor's field-of-view. Therefore multiple range images, taken with different orientations of the sensor, are often required to cover the object in its entirety. Next, truncation of these range images can be performed by the user, whereby distortions are either interactively or intuitively identified and trimmed. The different range images are then registered under a common coordinate system to form a complete digital representation of the object. Such a system relies on the expertise of the user to retain only the "good" portions of the various range images, for which prior knowledge of the object's geometry is essential.

Another method to reduce distortions involves a process whereby, prior to scanning, the optimum scanning direction and orientation of the sensor are either manually or automatically planned for different regions of the object. Such a method would require prior knowledge of the geometry of the object and a good understanding of the genesis of distortions. For example, for a circular object, it is recognised that distortions will be expected around the periphery of the object's inclined or near-vertical face. A radially diverging scanning direction, with sensor oriented parallel to this direction, originating from the centre of the circular object can be employed (see Fig. 4-12(a)), hence preventing occlusion of the spot image. However bow waves can be anticipated near the object's periphery, which is due to the inclusion of diffuse reflection and dispersion of the spot image from the object's inclined face in computing the readings (see Section 3.3.5 in Chapter 3). Therefore a better solution would be to orientate the sensor perpendicular to the scanning direction, making it always oriented at a tangent to the circle (see Fig. 4-12(b)).

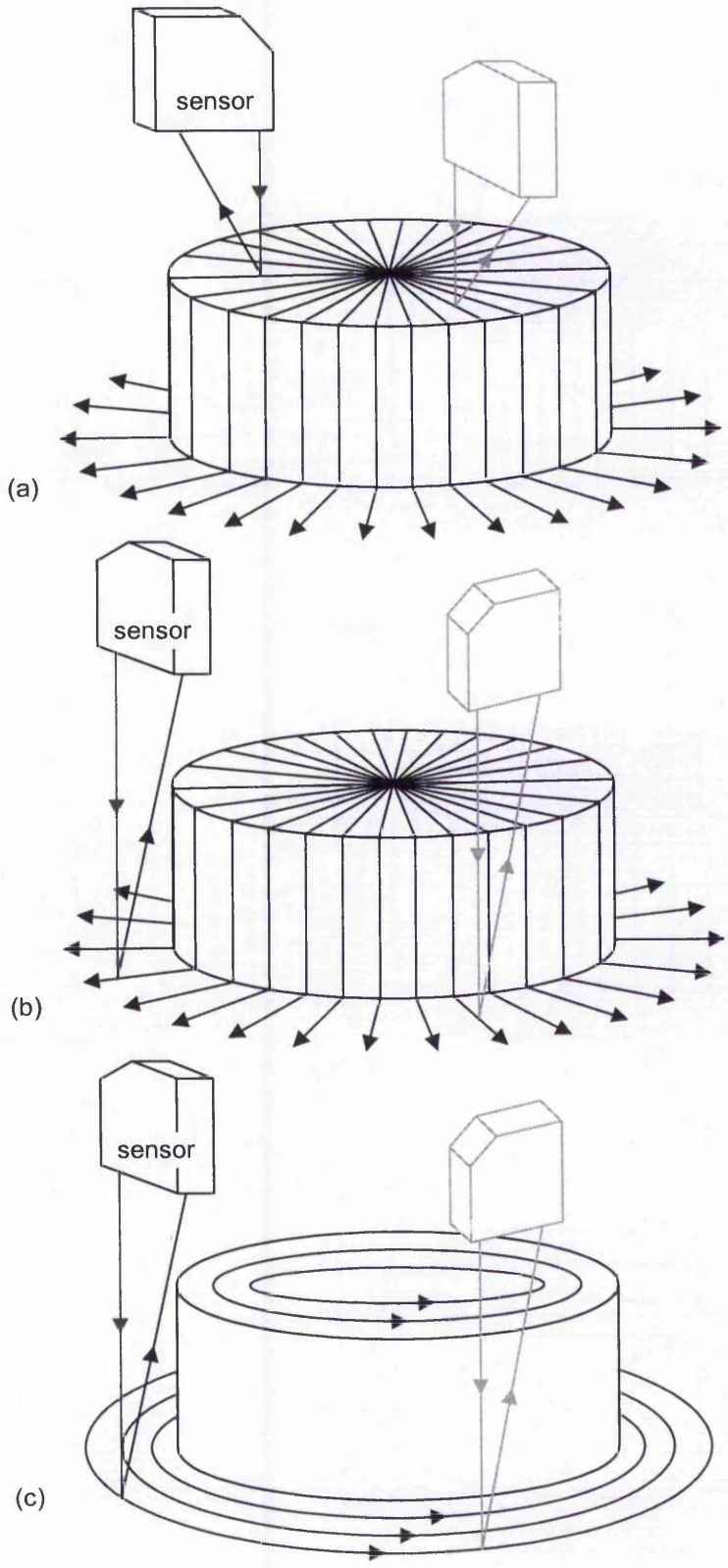

Fig. 4-12: Possible plans of scanning direction and orientation of sensor to achieve minimal distortions.

Alternatively a circular scanning direction, with the sensor oriented parallel to this direction, could be set (see Fig. 4-12(c)). This can be achieved either by translating the sensor circularly around the object or by rotating the object itself. Unlike the two previously suggested scans, the acquired scanlines should resemble concentric circular rings growing outwards from the centre of the object with the sensor, once again, always oriented at a tangent to the circle. Around the object's periphery, there would be little or no significant distortions, as the orientation of the sensor, which is parallel to the scanning direction, is at a tangent to the object's inclined face. Consequently secondary reflections or occlusion of the spot image would not be able to afflict the integrity of the scanning process, thus providing a better quality range image than that of the radially diverging scan.

Automated algorithms for definition of scanning direction and orientation of the sensor prior to scanning would need to be very complex, since most objects are not so simple in geometry. Every curve of these objects would have to be identified for their possible contributions to distortions. Therefore numerous interactions may be needed from the user and as such, it could be quite time consuming to map out the optimal scanning direction and orientation of the sensor. Another requirement for such a method to work efficiently is to have a flexible mounting for the sensor or for the platform on which the object is placed. High degrees of freedom, such as translation and rotation along the three axes, are needed to cover all possible permutations of scanning direction and orientation of the sensor. Also, if points are collected while the sensor is moving at a constant speed, finely tuned mechanical joints are important in ensuring a smooth transition between scanning direction and orientation of the sensor, thus reducing occurrences of noise. Such a mechanical stage is expensive and is therefore prohibitive for a cost-effective solution to 3-D imaging. Another approach is to capture and combine multiple range images as described in the next two sections.

4.2.2 Simple Algorithms for Multiple Range Images

For a cost-effective 3-D scanning system, the CNC machine that is being used for this research has three degrees of freedom: translations along the *xyz* axes. Initially two simple compensation algorithms were developed to combine multiple range images for comparison with the new geometry-based algorithms. As mentioned earlier, multiple range images were captured to avoid missing any details in distorted regions when using

a single-perspective point sensor. These images – eight of them, all captured using laser sensor model ANR1182 – were acquired by positioning the sensor at eight different orientations, each at an angle of 45° from the next, while maintaining the same scanning direction. Two objects were selected to illustrate the simple compensation algorithms: the MDF block and a technical object of more complex geometry, shown in Fig. 4-13, where one out of the eight range images is shown for each object. The complete set of range images – scanned with 0.5mm horizontal separation along x and y directions – is shown in Appendix C.3 for each object.

After acquisition of eight range images of an object, they were restructured and interactively registered (described in greater detail in Section 4.3.1) so that they were correctly aligned. Then the results could be investigated for the two simple algorithms described below: averaging of z-values and selection of lowest z-values.

The first algorithm tested was a simple combination of all the images by means of averaging. At each point in the xy plane, all eight z-values corresponding to the eight range images were averaged to form a new point. As can be seen in Fig. 4-14, regions with small or no distortions produced reasonably good outputs. However regions with significant distortions yield new points that are also distorted (see Section 4.3.2 for more details). In Fig. 4-14(a) there are distortions around the base of the block. For the technical object, in Fig. 4-14(b) it can be seen that distortions occur near its higher tiers of inclined faces. The periphery of the object's base does not have any large distortions in spite of the inclined face. Compared to the other elevated inclined faces on the object, the inclined face close to the base is not so high, hence the projected spot image was not totally occluded from the sensor's field-of-view. Small bow waves, however, were still present but their magnitudes were reduced when all eight images were averaged. From the acquired multiple range images, the ones afflicted by distortions at a particular region depends on the orientation of the sensor for that image with respect to positioning of the inclined face (see Fig. 4-13). Therefore in those regions, averaging will still leave some distortions.

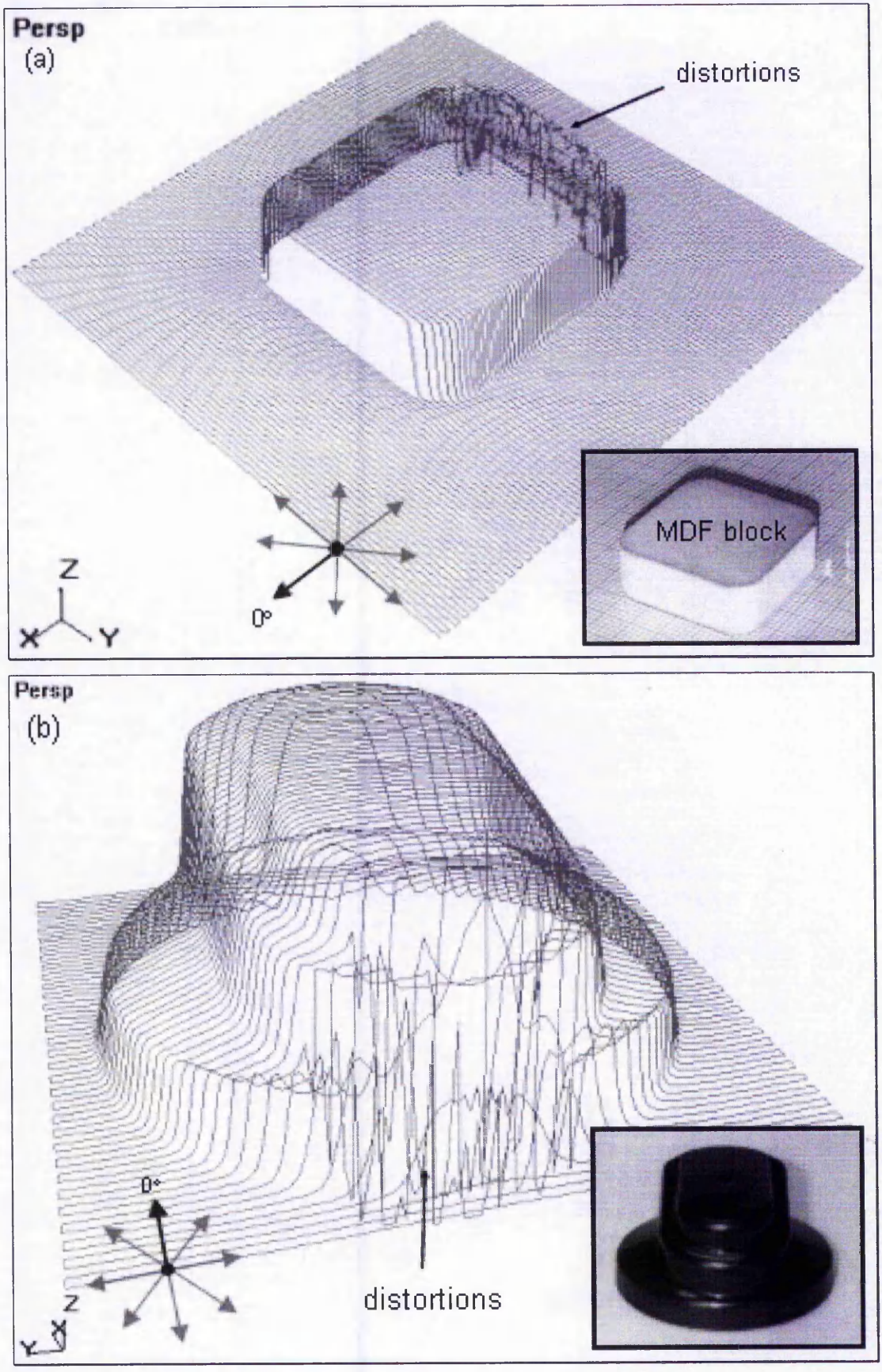

Fig. 4-13: The range image with sensor oriented at 0° (x and y separation 0.5mm).

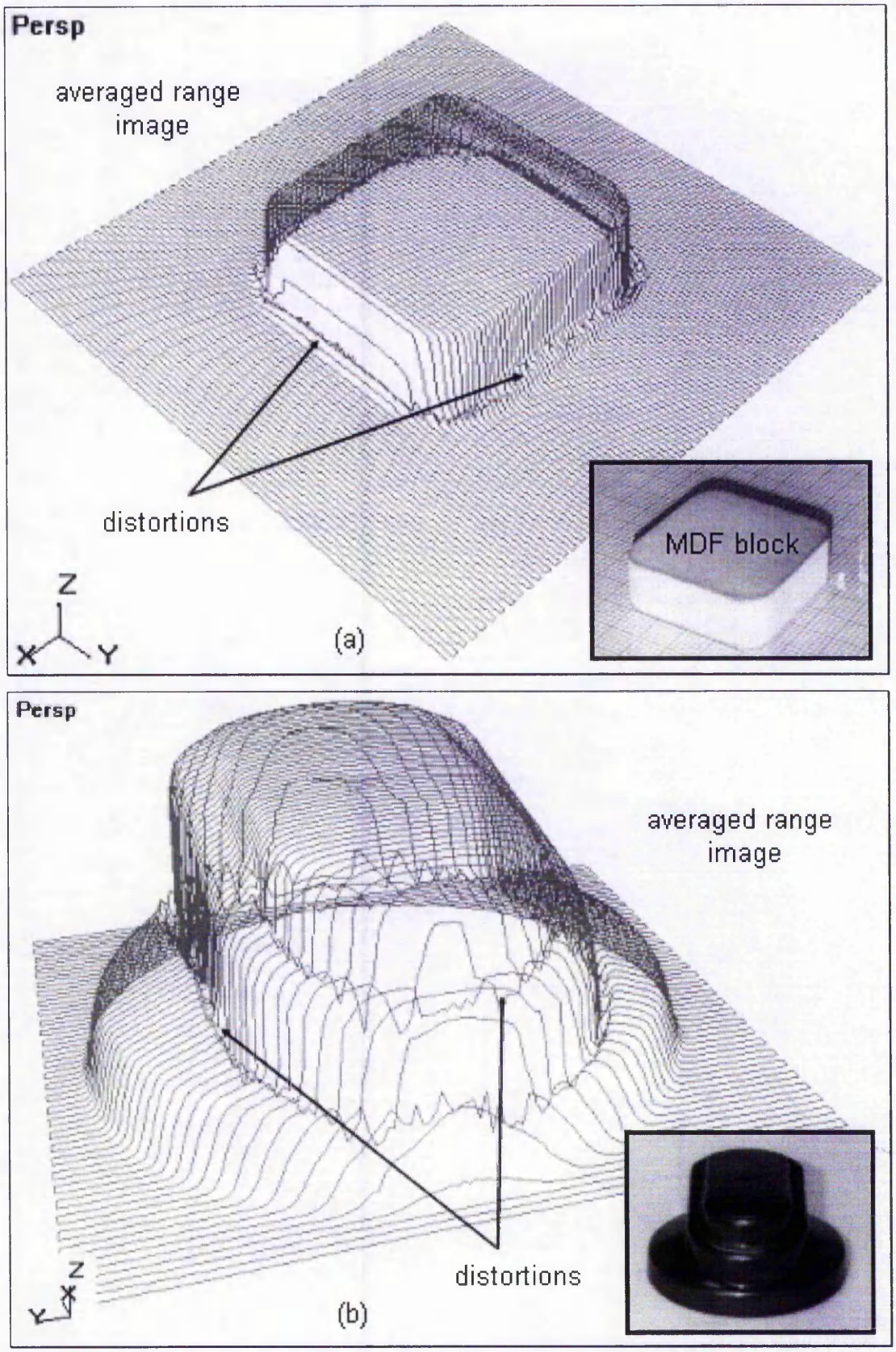

Fig. 4-14: Averaging of multiple range images of objects (inset) produces distortions in new range images.

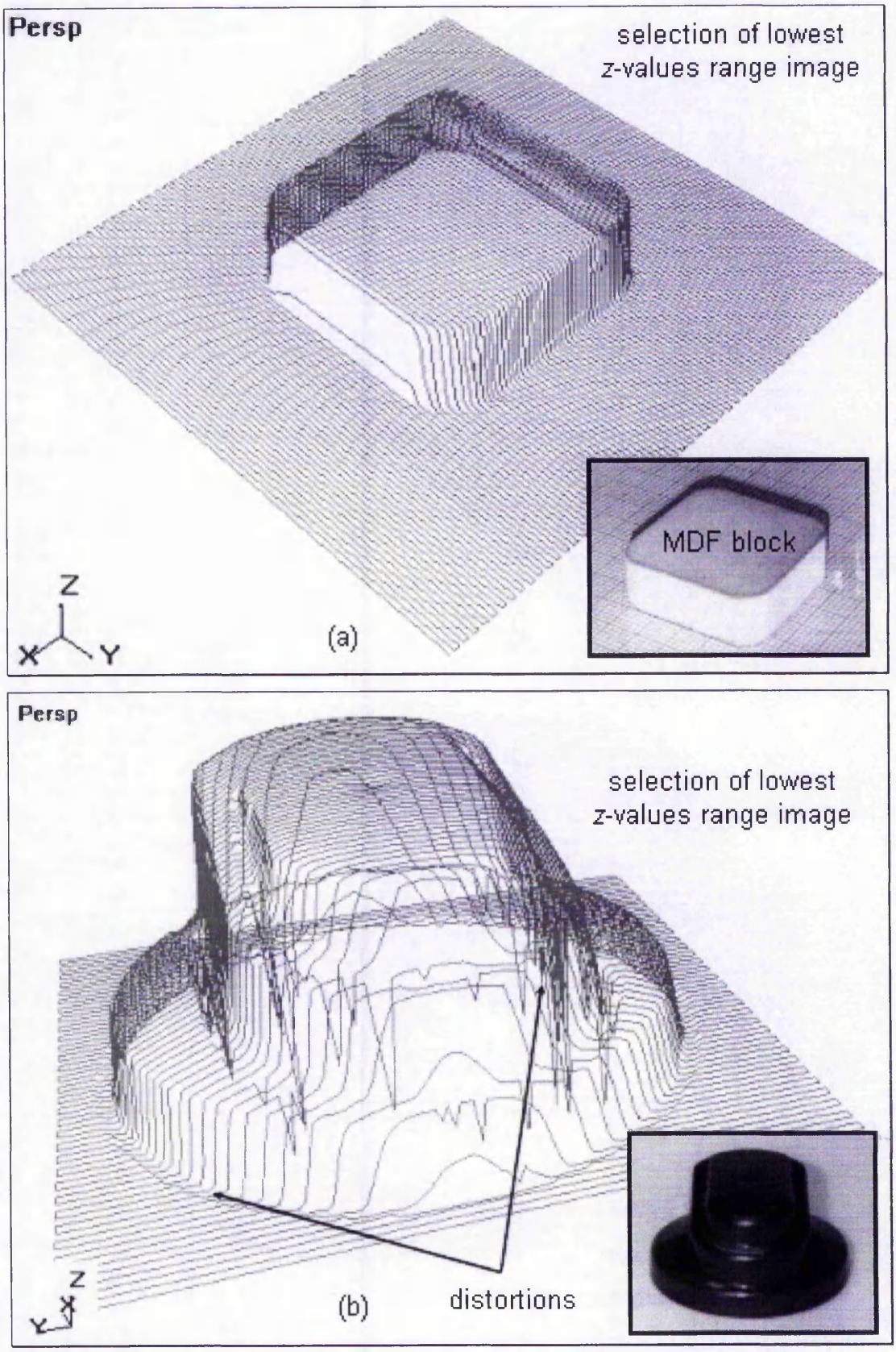

Fig. 4-15: Selection of lowest *z*-values from multiple range images of objects (inset) produces distortions in new range images.

The second algorithm tested selects the lowest *z*-values from the multiple range images in the distorted regions. However any points below the planar surface on which the object rested were disregarded. In regions with no significant distortion, the corresponding points were averaged to produce a new point. But in regions with significant distortions, points from other range images at the same location were then compared and the point with lowest *z*-value was elected the new point. The example of its implementation on an object of simple geometry can be seen in Fig. 4-15(a). For an MDF block of only a single tier or height, selection of lowest *z*-values works well and significant distortions, i.e. bow waves and occlusion spikes, were removed, giving a new range image that conforms to the original object. However such an approach to compensation is flawed due to the fact that occlusion spikes, specifically falling spikes, do not always fall below the planar surface, especially for multi-tiered objects. These occlusion spikes are therefore included in the selection of lowest *z*-values, hence giving incorrect new points that are below their true positions (see Fig. 4-15(b)). Hence the selection of lowest *z*-values is effective when only bow waves (and no occlusion spikes) are present in the range images. Also when only one point – the one with the lowest *z*-values – from multiple range images is selected for every *xy* coordinate in the regions of significant distortions, it will be slightly lower than the one processed by simple averaging. Therefore where a region with significant distortions meets a region with no significant distortion, there may be a noticeable change in height, resulting in a small step appearance. This, however, may be rectified with blending but further research is needed.

4.2.3 Edge Detection with Multiple Range Images

From the results for the two algorithms described in the previous section, it can be seen that better compensation algorithms need to be developed. The realisation that distortions depend not on scanning direction but rather on orientation of the sensor with respect to the positioning of inclined faces led to the development of compensation algorithms based on the geometrical structure of objects. It is understood that distortions are likely to be smallest when the sensor is oriented parallel to the direction of an inclined face in the horizontal plane and largest when the sensor is perpendicular to the direction of this face in the same plane (see Chapter 3). If multiple range images are collected, then it is possible to construct a new improved range image

whereas one range image is insufficient due to the limited field-of-view of the sensor's detector.

The idea of the method is as follows:

1. Identify regions with significant distortions by comparing the multiple range images, thus generating what is known as an *error map* in this thesis.
2. Look for inclined faces, henceforth known as *edges* in this thesis, adjacent to the regions of distortion.
3. Select best range image for points in regions of distortion.

This approach to compensation produces much better results, be it for visualisations or reproduction, than simple averaging or the selection of lowest z-values methods. A more detailed explanation of the algorithms is presented in the next section.

4.3 Compensation based on Edge Detection

In Chapter 3, several types of distortion have been identified, namely noise, transitional spikes, bow waves and occlusion spikes as well as small systematic distortions. All of these are caused by interactions between the sensor and the geometry of the object and are not due to calibration errors of the scanning machine. Apart from noise and transitional spikes, the magnitudes and nature of the distortions depend on the orientation of the sensor with respect to the object's edges. For example, when scanning an MDF block with orientation of the sensor parallel to the scanning direction, bow waves and spikes occur at different edges from when the scanning direction is unchanged but the orientation of the sensor is perpendicular. Therefore compensation algorithms have been developed based on this knowledge.

Section 4.3.1 gives details of the first phase of the developed edge detection algorithms, which is the capture and registration of multiple range images into a common coordinate system. Then Section 4.3.2 describes the determination of the threshold value for isolating distortions into different categories, thus generating a map of regions of distortion. Finally Section 4.3.3 highlights how the algorithms employ the knowledge of these error regions together with the defined edges for each point in those regions to compensate for distortions, resulting in new improved range images.

4.3.1 Capture and Registration of Multiple Range Images

The first phase was to obtain several range images of an object with the same scan region but with different orientations of the sensor, in which the projected beam was always normal to the planar surface on which the object rested. Using the convention defined in Chapter 3 for orientation of the sensor and scanning direction, eight range images were collected for each object. Before beginning with the first scan with sensor oriented at 0° (perpendicular to scanning direction), the spot image was moved towards the origin and its position recorded by the software running the CNC machine (see Fig. 4-16) where *xy* coordinates were set at (0, 0). This procedure was then repeated for the remaining scans with different orientations of the sensor before commencing the scanning process. This is important because the origin is the common point used to align and register the eight range images before processing.

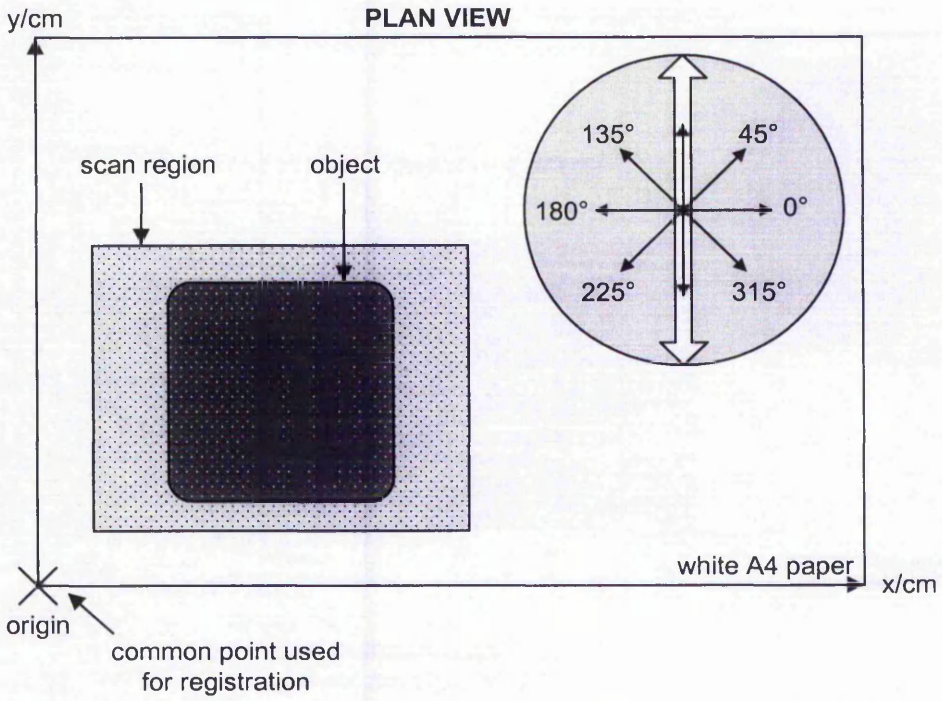

Fig. 4-16: Capturing eight range images of object with orientations of the sensor spaced at 45° from each other but scanning direction remains the same for all scans along *y*-axis.

Once the origin of the sensor was set, an object was placed on a planar surface, on top of a piece of white A4 paper. Thereafter the object and the surface were sprayed with a non-permanent coating to create a homogenous diffusely reflective scan surface. A scan

region encompassing the whole object was then defined. Also, the separations of points along x- and y-axis were defined. The dimensions of the scan region, together with other parameters such as horizontal separations along x and y axes, and scan speed, were noted and fixed for all subsequent scans of the same object. This was to ensure consistent conditions for all scans, so that all the range images will scan the same lines in the xy plane. After the required CNC machine and laser calibrations, the scanning commenced. Upon completion of a scan, the range image was saved. Thereafter the sensor was moved to the origin before being rotated by 45°. Its spot image was then realigned at the origin. With the same calibration parameters as the first scan, including scan region and separations, another range image was collected. The process was repeated for six more scans at 90°, 135°, 180°, 225°, 270° and 315°.

When all the range images had been collected, the first stage of the process consisted of restructuring the scanlines so that all range images have the same separation between scan points. This was to facilitate comparison of points between images during different stages of the compensation algorithms. Instead of simple averaging, as applied in phase two of compensation for noise (described in Section 4.1.2), weighted averaging of points on the scanline within a defined region was used. The weights were based on the distance of the points from the new point. The region was equal to the horizontal separation of points along the scanline (see Fig. 4-5). This provided a better estimation of z-values for the new points without excessive smoothing when compared to simple averaging. (Interpolation could be employed instead but further research is needed to determine if it provides better results.) When there is already a point at the required position, then it is employed. Otherwise a new point is computed using Equation (4-1) with $k = 0$.

When restructuring was completed for all range images, scan points for each of these images would project onto the same points in the xy plane after registration and be equally spaced in the x and y directions.

4.3.2 Determination of Threshold and Error Map Generation

The next stage of the process is to determine regions in the xy plane where significant distortions, such as bow waves and occlusion spikes, occur. These distortions are

classified into medium and large errors by comparing the different range images. The difference in *z*-values between the eight range images at a particular *xy* coordinate is calculated. When the difference between highest and lowest points from the eight images is below a certain threshold, the distortion at the *xy* coordinate is designated as being in a small error region. When it exceeds the threshold, it is designated in the medium error region. However, when the difference exceeds a higher threshold, the distortion is designated as being in a large error region. To determine these thresholds, the extent of noise in the eight range images is established. The idea is to isolate noise from the other more significant distortions. Therefore a selected portion of scan region of the planar surface, far from where significant distortions would most likely occur, is used. The noise deviation – which is the standard deviation of *z*-values – in this region is recorded for each range image (see Fig. 4-17) before being combined to obtain the averaged noise deviation, σ.

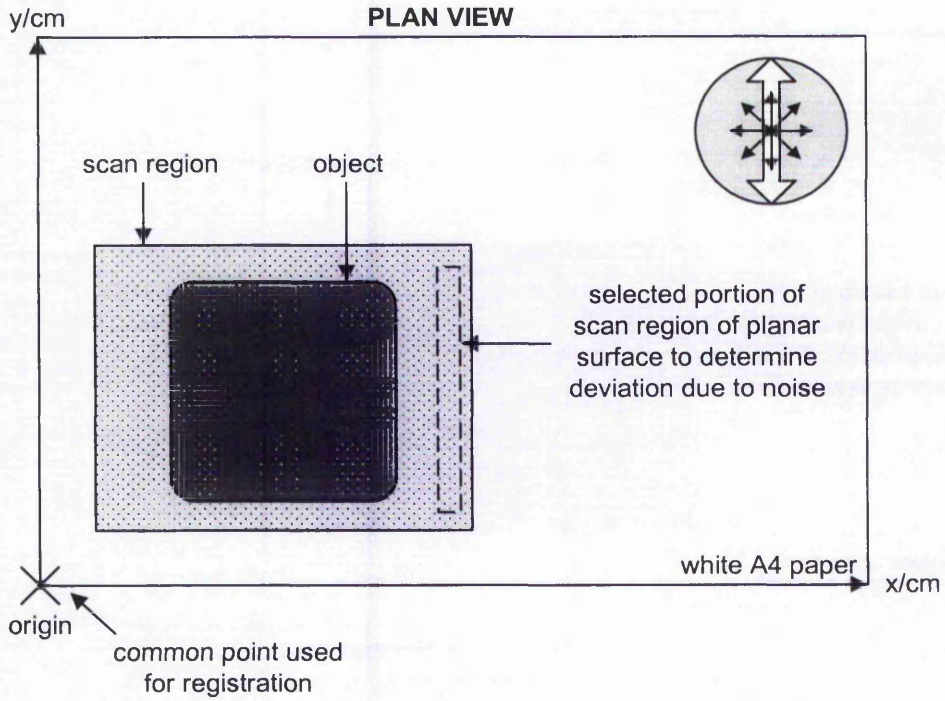

Fig. 4-17: Selected portion of scan region of planar surface for all eight range images used in determining deviation, σ, due to noise.

Based on the study of the effect of the orientation of an edge in the *xy* plane relative to the sensor in the generation of bow waves (see Chapter 3), the magnitude of this distortion was most significant when the sensor is oriented perpendicular to the edge.

The size of bow waves decreased as the direction of the edge approached to being parallel to the orientation of the sensor. It was found that the magnitude of bow waves ranged from 3σ to 12σ, whereas spikes often had magnitude over 12σ. Therefore these thresholds have been used to separate the points in the *xy* plane into three types of small, medium and large errors. For each point in the *xy* plane, the eight range measurements at that point from the eight orientations of the sensor are taken and their maximum and minimum *z*-values found. A value, $|\Delta z_{map}|$, for that point is then assigned as the absolute difference between these extremes. If $|\Delta z_{map}|$ falls below the threshold 3σ, the distortion at this position is classified as being in the small error region (i.e. no significant distortion). If it is between 3σ and 12σ, it is classified as being in the medium error region, which is expected to correspond to bow waves. Finally when $|\Delta z_{map}|$ exceeds 12σ, then the point in the *xy* plane is classified as being in the large error region, which is expected to correspond to bow waves and occlusion spikes.

Threshold	Regions
$\|\Delta z_{map}\| < 3\sigma$	small error
$3\sigma \leq \|\Delta z_{map}\| < 12\sigma$	medium error
$\|\Delta z_{map}\| \geq 12\sigma$	large error

Table 4-1: Classification of distortions based on thresholds in generation of error map.

The complete classification of points into different regions in the *xy* plane constitutes what is known in this thesis as an *error map*. The error map is important for determining the type of compensation to be employed on points in the range images. It also aids in identifying edges of an object, a process known as *edge detection*.

The two illustrations in Fig. 4-18 exemplify the creation of error maps for the two selected objects. For the MDF block, the medium error region is more expansive compared to the large error region close to the edges of the object, as would be expected. For the technical object, however, the medium error region still exists but is much narrower because the height of its edge at the base of the object was lower. This is because there is a shorter face here for secondary diffuse reflection and dispersion of the spot image.

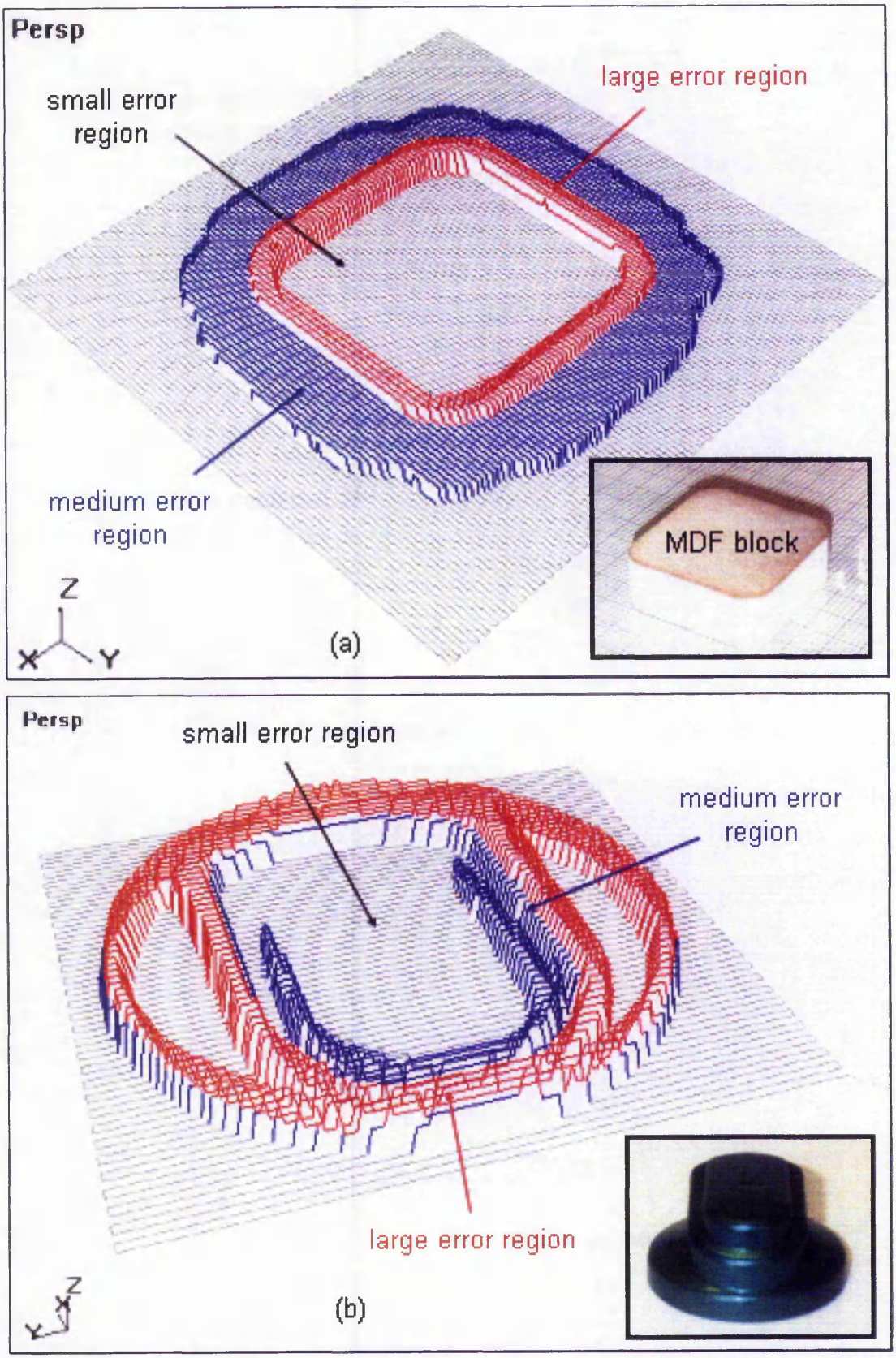

Fig. 4-18: Error maps highlighting small, medium and large error regions, each of which was set to a different height for clarity.

4.3.3 Edge Detection

After generation of the error map, the next phase is to detect edges of an object. With the aid of a new range image, created from simple averaging of eight range images (see Section 4.2.2), an approximation of the object's geometry was obtained. Using this averaged range image, every point in the *xy* plane within the regions of medium or large distortion, as defined by the error map, was subjected to searching the *z*-values corresponding to points in its vicinity in order to detect edges. The search was conducted for eight directions, matching the eight orientations of the sensor. A limit must be set on how many nearby points from the point in the *xy* plane need to be searched before they become irrelevant in edge detection. This limit was based on the maximum width of the occluded region cast by the highest point of the object (see Fig. 4-19).

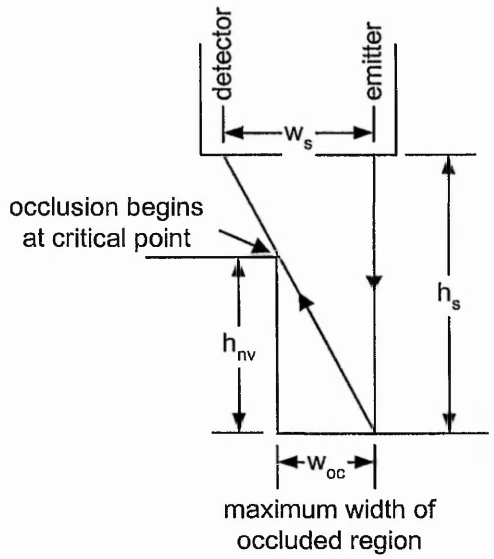

Fig. 4-19: Maximum width of occluded region cast by highest point of the object.

Maximum width of occluded region,

$$w_{oc} = h_{nv} \times \frac{w_s}{h_s} \tag{4-8}$$

where h_{nv} is maximum height of the object, h_s is distance of the sensor from the surface on which the object is placed, and w_s is the width between detector and emitter.

This computed maximum width should therefore correspond to the greatest width of the large error region, where spike distortions are expected to occur.

Using the calculated width from Equation (4-8) and the information of horizontal separation, s_{xy}, along x and y axes, the number of points inside this occluded region is,

$$n_{oc} = \frac{w_{oc}}{s_{xy}} \tag{4-9}$$

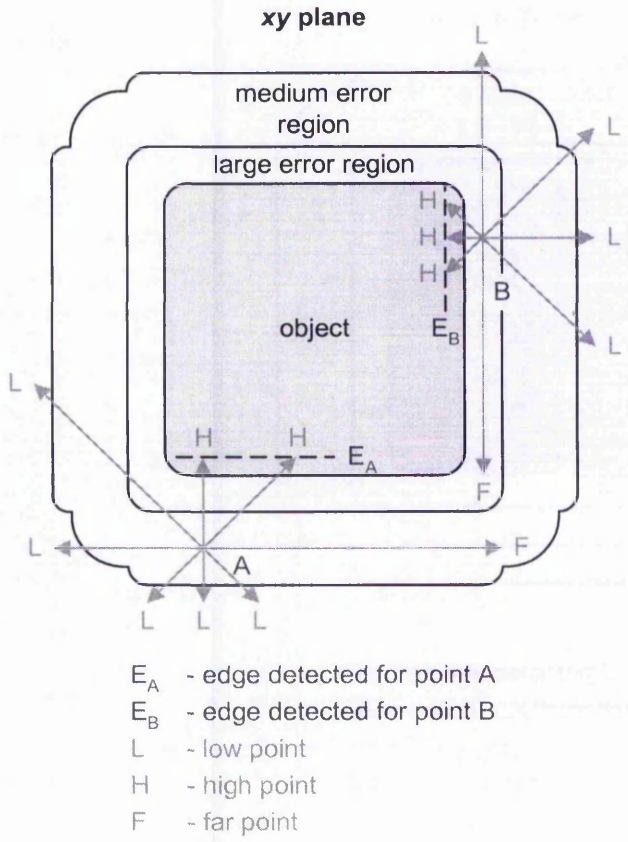

Fig. 4-20: Detecting edges for points within regions defined by the error map. Point A is in medium error region and point B is in large error region.

It was discovered, in most circumstances, medium error regions, which encapsulate only bow wave distortions, are much wider than the large error regions, which correspond to occluded regions. In order not to neglect the medium error regions, the maximum number of nearby points to search from a point in the *xy* plane was set to be four times n_{oc}. This formula was used for the experiments conducted in this research but could be altered for different objects by computing the ratio of the widths of medium and large

error regions locally. This may reduce processing time if fewer points are searched. (During development of the algorithms, a distinction was made between medium and large distortions. In the end, the algorithms, as developed, do not distinguish between them.)

For a point in the *xy* plane within a region of medium or large distortion, a search begins by looking at its nearby points along a particular direction. For example, along 0°, the first nearby point in the *x* direction from the point in the *xy* plane is examined (see Fig. 4-20 and Fig. 4-21). If this point is also in the region of significant distortion, then the search moves on to the second point (see Fig. 4-22). If a point in the small error region is found, its coordinates are stored in the buffer. However if the maximum number of points to search – which was set at $4n_{oc}$ – is reached, then the search along this direction terminates with designating that last point with marker F (meaning "far" and therefore irrelevant). The whole process is repeated for the other seven directions. The eight range measurements for all of the points identified by the neighbourhood search are taken and the maximum and minimum *z*-values found. A value, $|\Delta z_{adj}|$, for the point in the *xy* plane, which is at the centre of the search, is then assigned as the absolute difference between these extremes.

If $|\Delta z_{adj}|$ exceeds noise deviation, σ, the average of all *z*-values of these points is computed and used to determine their designation as follows. If the *z*-value of a point is lower than the average, then it is marked L (meaning "low"), otherwise it is marked H (meaning "high").

If, however, $|\Delta z_{adj}|$ is less than σ, then all the nearby points, except those marked F, are assumed to be on a plane of low or no incline, hence they are all given an L mark[9]. All points in the *xy* plane within medium or large error regions go through the same process, each producing sets of eight nearby points in the form of F, L or H markers.

[9] The marking of all nearby points with L is of no significance, for they could all be marked with H or F. It is just to facilitate processing later on during the compensation stage (see Section 4.3.4).

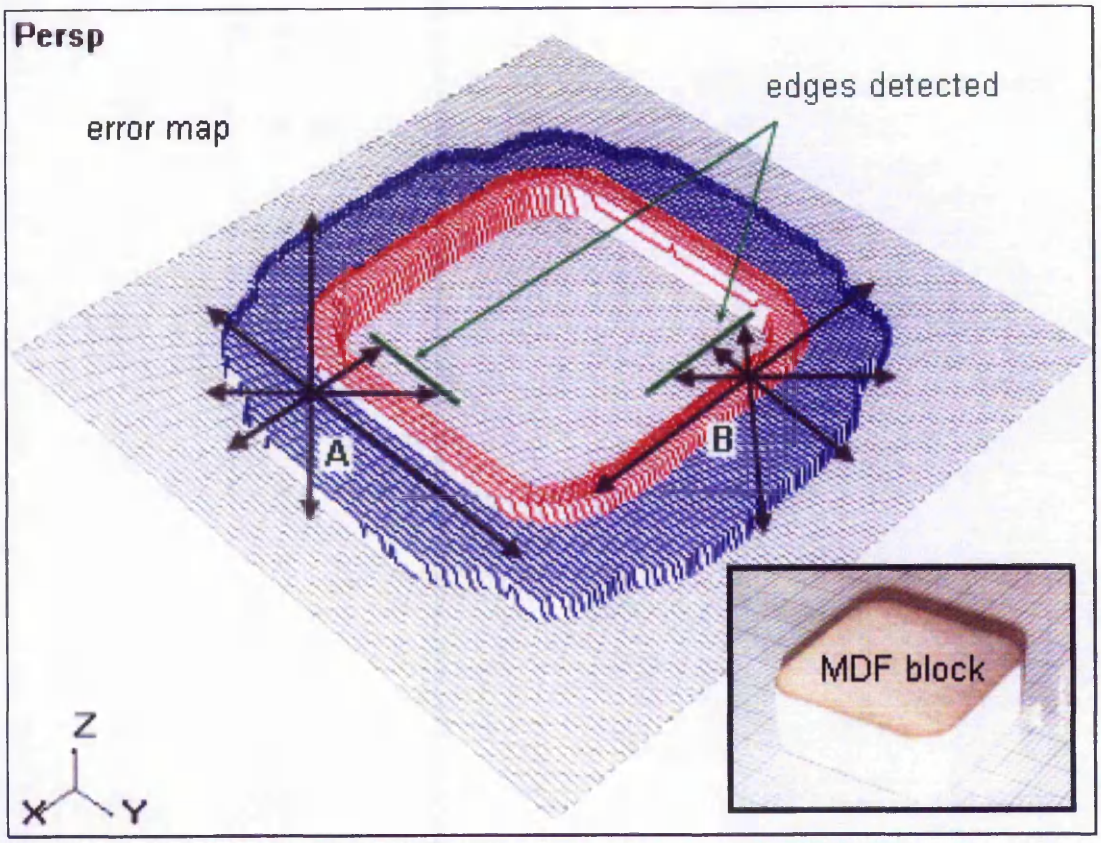

Fig. 4-21: Example from a real range image illustrating edge detection for points within regions defined by error map (as shown in Fig. 4-20).

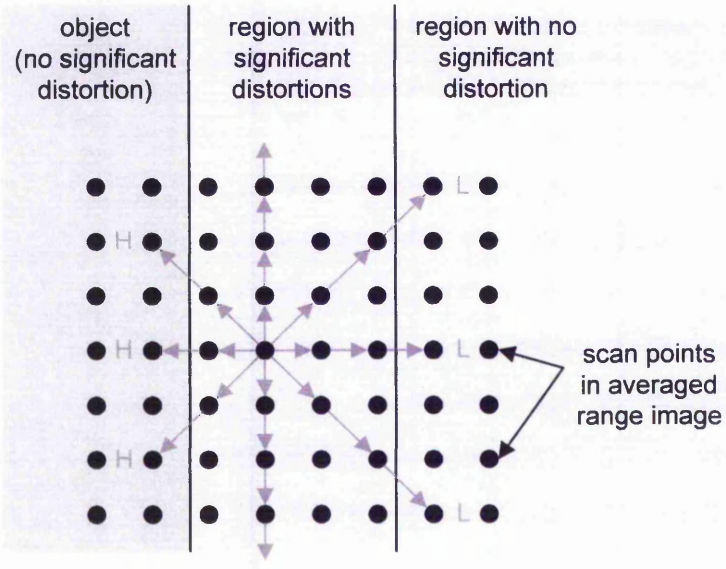

Fig. 4-22: Example of point-by-point search in eight directions for points in vicinity with no significant distortion.

The algorithm for detecting edges is as follows:

For each point in the *xy* plane in regions of significant distortion;

For each of the eight directions (corresponding to orientations of the sensor);

Search all points in selected direction up to maximum of $4n_{oc}$;

If a point found in region with low distortion;

Store in buffer;

Else;

Mark last searched point with F;

Compute $|\Delta z_{adj}|$ for all stored unmarked points;

If $|\Delta z_{adj}| < \sigma$ (noise deviation);

Mark all these stored unmarked points with L;

Else;

Compute average *z*-values of all stored unmarked points;

For all stored unmarked points;

If *z*-value is below the average;

Mark with L;

Else;

Mark with H.

4.3.4 Compensation using Edges

The final phase in compensation is to use the sets of nearby points associated with points in the *xy* plane to create a new range image from the original eight range images, which has no significant distortions. For each point in the *xy* plane within regions of significant distortion, a decision must be made on which of the eight *z*-values from the eight range images to accept. The algorithms are based on the understanding of distortions in Chapter 3, whereby a scan with orientation of the sensor parallel to an inclined face, or edge, has least distortions. Therefore, given a particular point in the *xy* plane within the region of significant distortion, the idea is to plot a least squares line through *xy* positions of the marked points, representing the tangent to an edge closest to that point, as in case 1(i) below. The *z*-values at an *xy* position from range images with orientations of the sensor close to parallel to this tangent are then selected and averaged to create a new *z*-value to replace the *z*-value at that particular point.

This phase is done in a number of different ways, depending on the number and types of markers for the given point in the *xy* plane:

1. Mixed L and H markers;

   Depending on the position of markers, the compensation is done in three different ways:

   i. When the number of H-marked nearby points for the *xy* coordinate is two or three and they are arranged in adjacent positions around the eight orientations of the sensor, a least squares line is fitted to the projections of these H-marked points onto the *xy* plane. Subsequently *z*-values from the eight range images with orientations of the sensor closest to parallel to this least squares line are selected and averaged to produce a new *z*-value (see Fig. 4-24(a)). The selection of *z*-values from the eight range images depends on the angle, $\angle\varphi$, in the *xy* plane of the least squares line with respect to orientation of the sensor. When $\angle\varphi$ is within 10° of a particular orientation of the sensor, then *z*-values with that and the opposite orientation are averaged to form a new *z*-value. For example, if it is near 45°, then the two directions of 45° and 225° are chosen. However when $\angle\varphi$ is not within 10° of any orientation of the sensor but between two of them, the *z*-values with both these two and their two opposite orientations are averaged to form a new *z*-value (see Fig. 4-23). For example, if it is between 45° and 90°, then the four directions of 45°, 90°, 225° and 270° are chosen. The pairing of *z*-values with orientations of the sensor closest to parallel to the direction of the least squares line is illustrated in Fig. 4-25;

   ii. When it is not the case covered in (i) and there remains at least one pair of L-marked points with opposite orientations, then the *z*-values with orientation in the directions of those L-marked points are averaged to produce a new *z*-value (see Fig. 4-24(b));

   iii. When it is not the case covered in (i) or (ii), then the *z*-values with orientation in the directions of all L-marked points are averaged to produce a new *z*-value (see Fig. 4-24(c)).

2. All markers are L;

   Each z-value at an *xy* position is compared with the others and the one with the most other z-values clustered within a distance of 3σ is chosen. That chosen z-value is then averaged with all the other z-values within the distance 3σ to produce a new z-value.

3. No markers.

   In this situation, the point in the *xy* plane is located in region with no significant distortion. Hence all the corresponding z-values from the eight range images are averaged to create a new z-value.

The employment of the above method of compensation based on edge detection is thus expected to result in selecting and averaging z-values with the least distortions from the eight range images, producing a new z-value corresponding to each point in the *xy* plane in a region of significant distortion – as defined in the error map.

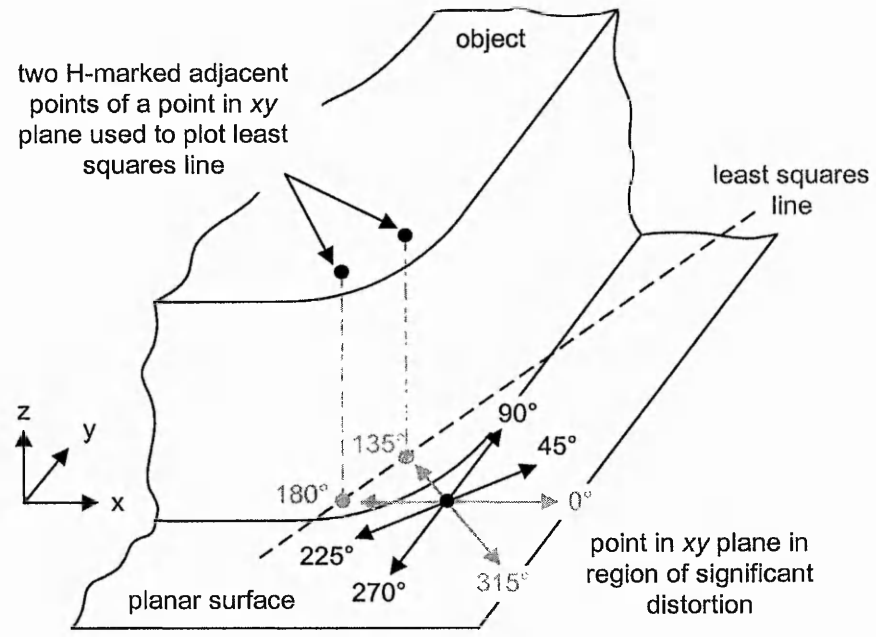

Fig. 4-23: Plotting least squares line using H-marked nearby points for a point in the *xy* plane and selecting four *z*-values from the four range images with orientations of the sensor closest to parallel to the least squares line.

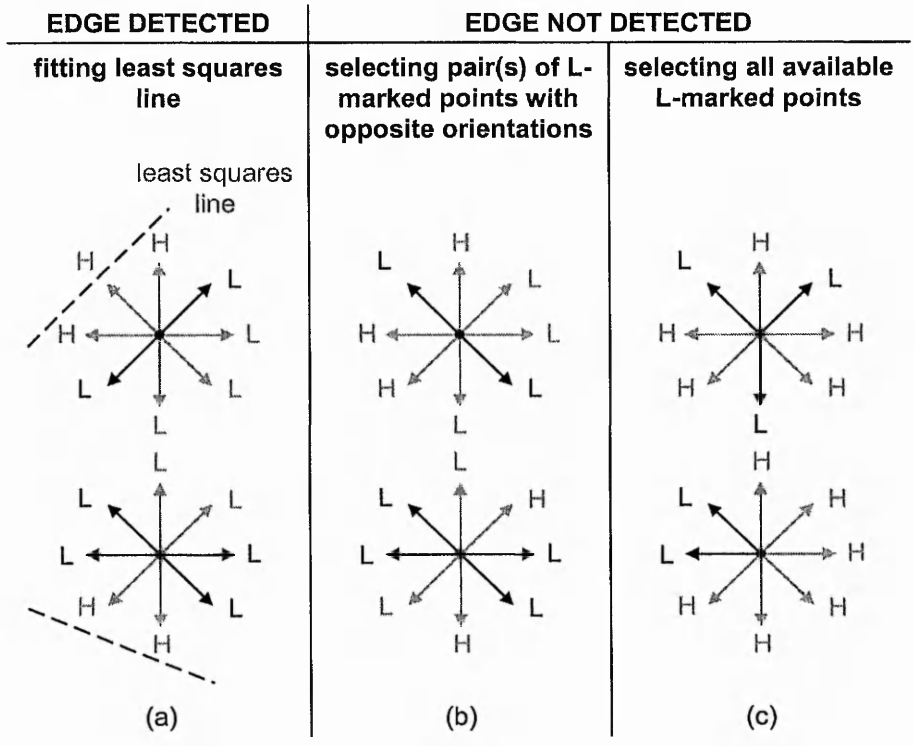

Fig. 4-24: Method of compensation for case 1 with mixed L and H markers.

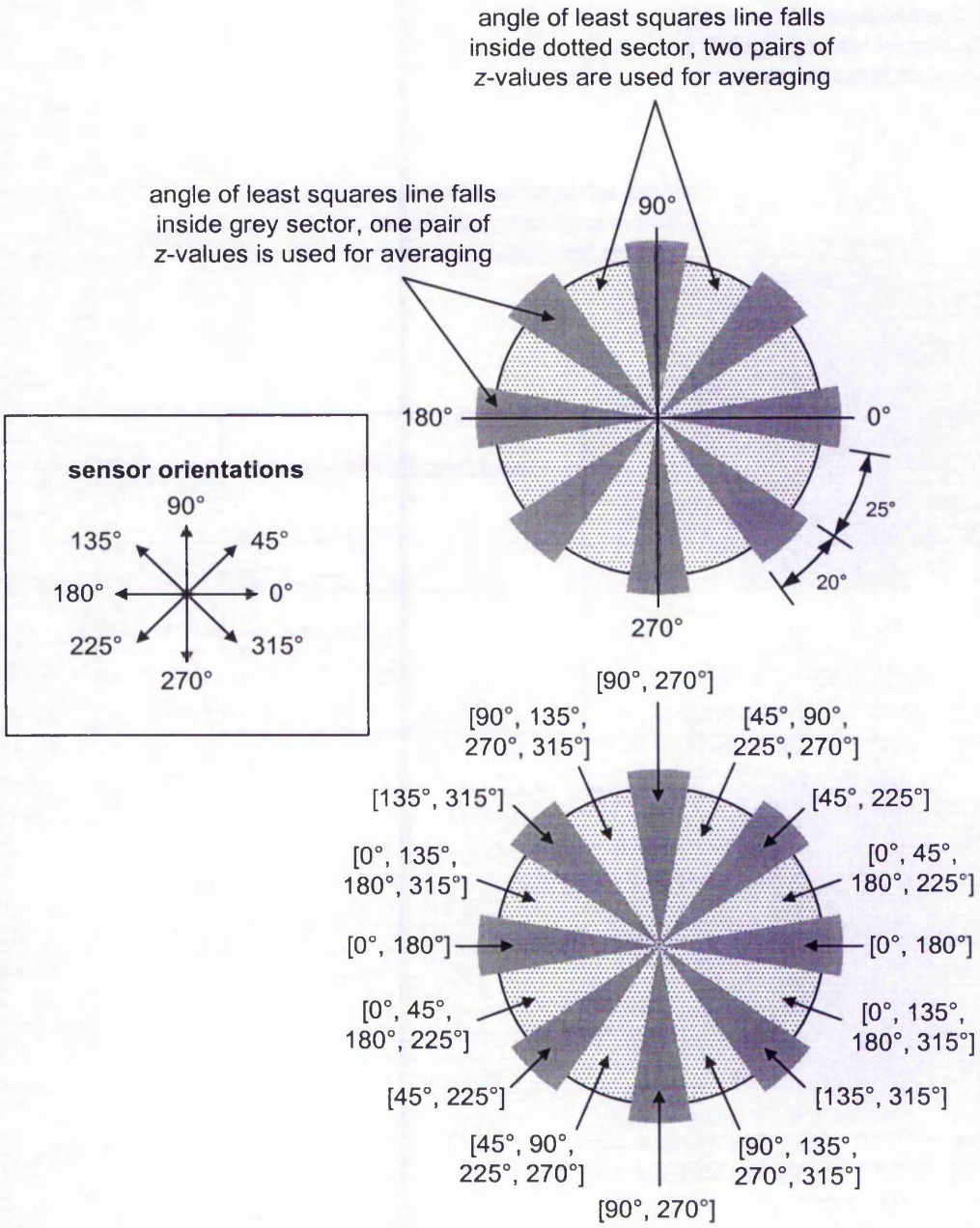

Fig. 4-25: Selection for averaging one or two pairs of *z*-values with opposite orientations when the angle of the least squares line falls inside grey or dotted sectors.

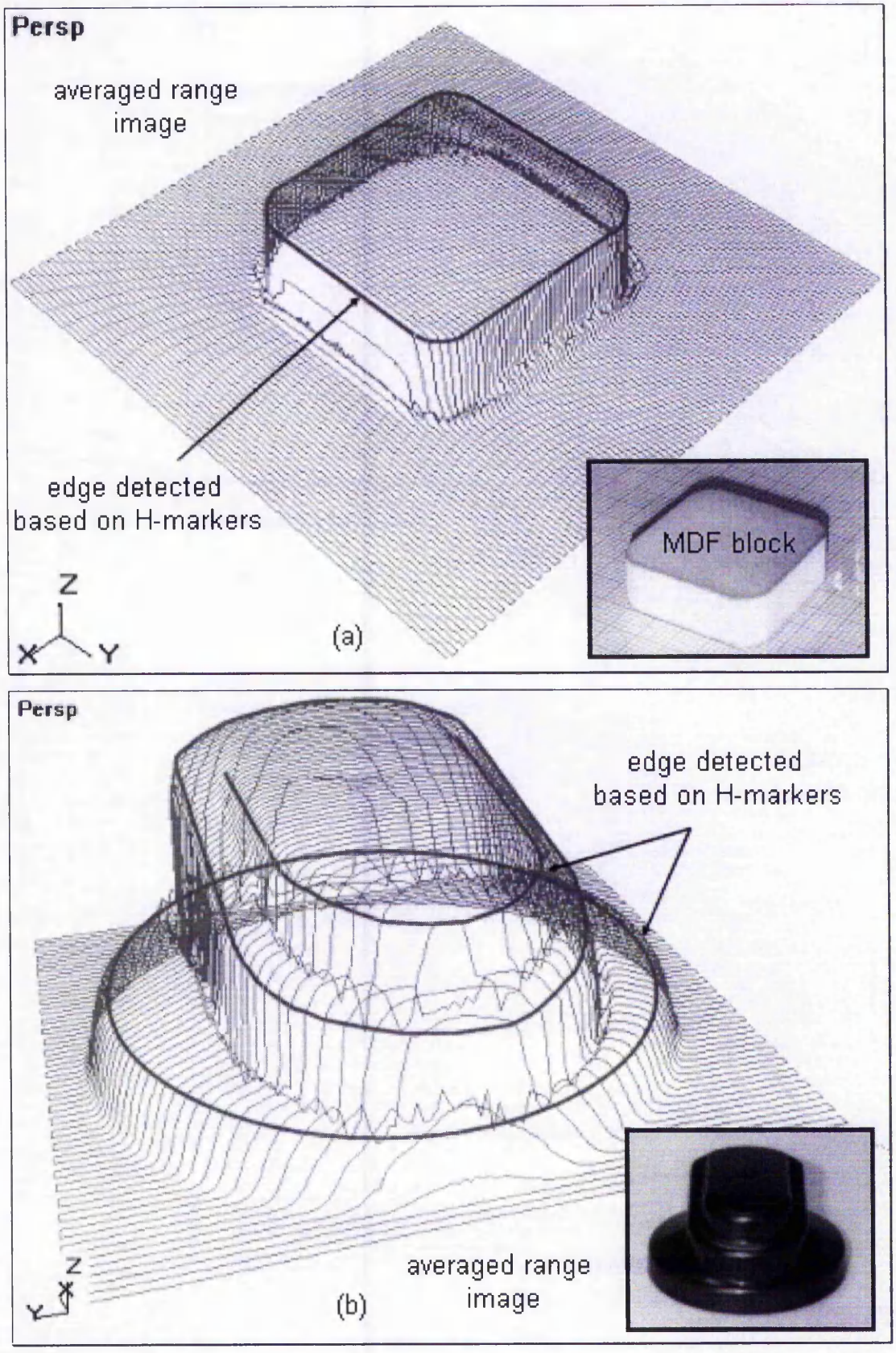

Fig. 4-26: Edges detected based on H-markers for points in regions of distortion (using small sections from individual edge tangents).

4.3.5 Results of Application of Compensation Algorithms

After every point in the *xy* plane in regions of significant distortion has been compensated using the new algorithms, a new range image is produced. For the examples tested, this new range image has been found to be free from significant distortions, i.e. bow waves and occlusion spikes, which afflict regions close to the edges. The final results after applying compensation based on edge detection are shown in Fig. 4-27 for the two examples used throughout this chapter. The classification of scan points by type of processing used is shown in Table 4-2. A marked improvement is observed when using compensation based on edge detection in comparison with simple averaging or selection of lowest *z*-values from multiple range images. An evaluation of this improvement will be discussed in Chapter 5. The removal of bow waves and occlusion spikes from the simple MDF block and multi-tiered technical object can clearly be seen in Fig. 4-27 when compared with the eight original range images (see Appendix C.3).

In Fig. 4-27(b), there appears to be small distortions on the inclined face close to the base of the technical object. This is thought to be due to the pairing of opposite oriented points at this face changes abruptly from point to point with changing tangent of the edge, resulting in uneven transition. Therefore in such a situation, a blend between transitions of paired *z*-values could be used but further research needs to be conducted. Once the significant distortions have been removed, subsequent processing, such as compensation for noise (see Section 4.1), can be applied to reduce surface noise.

Process of Compensation based on Edge Detection	Number of Scan Points	
	MDF Block	Technical Object
1. mixed L and H markers		
i. fitting least squares line	15935	10711
ii. selecting pair(s) of L-marked points	7	21
iii. selecting all available L-marked points	2	3
2. all markers L	1	13
3. no markers (because points in low error region)	32896	68213
Total	48841	78961

Table 4-2: Classification of scan points after applying compensation based on edge detection algorithms.

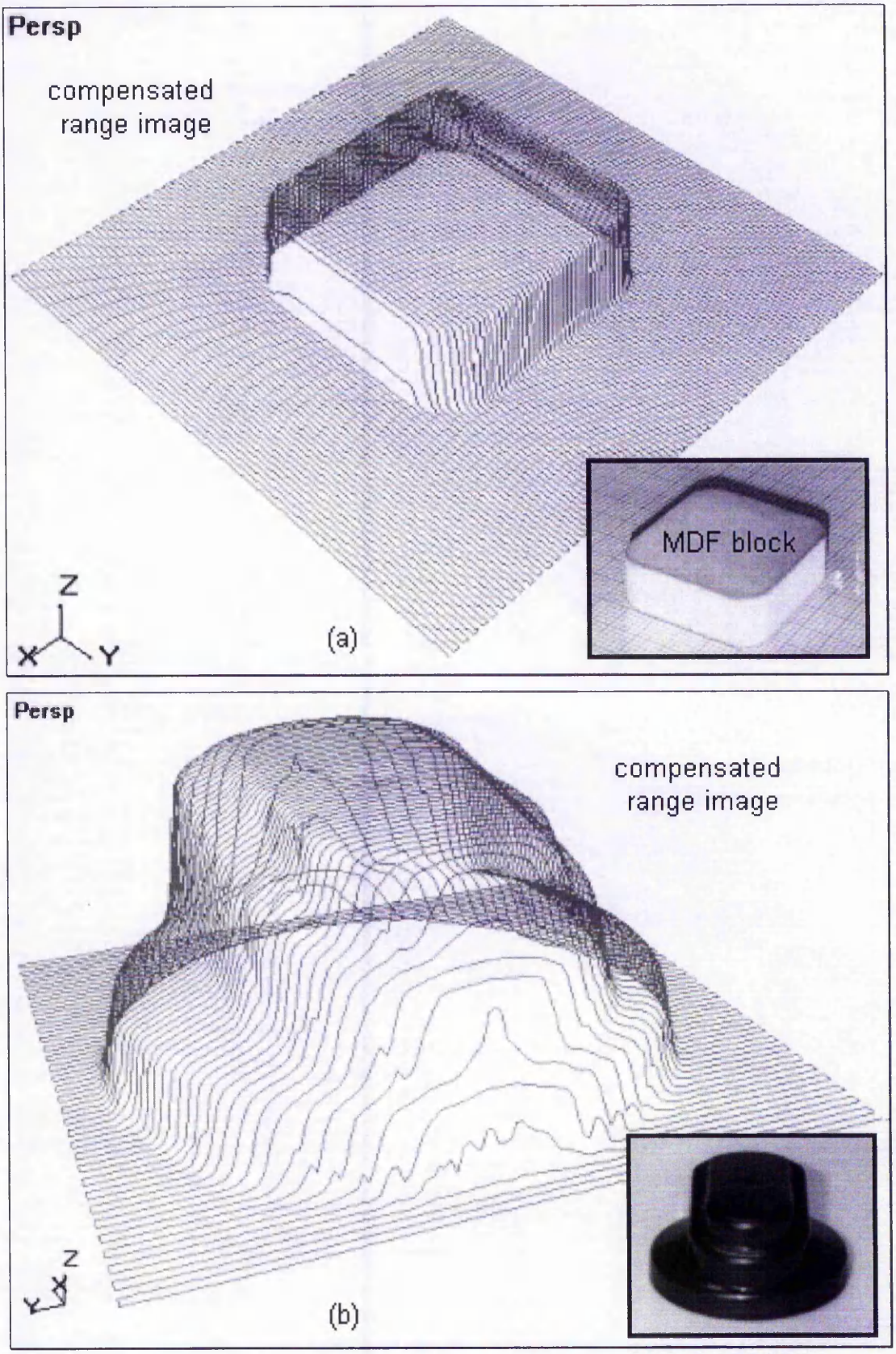

Fig. 4-27: Range images obtained after applying compensation algorithms based on edge detection.

4.4 Summary

The limitations of using a single-perspective active triangulation point sensor in 3-D imaging have led to development of a more cost-effective method to reduce distortions to an acceptable level for visualization or physical reproduction. Several algorithms have been developed and applied to range images containing regions with significant distortions. Before applying any compensation algorithms, it is necessary that the point cloud of a range image be equally spaced in the x and y directions to aid processing. Weighted averaging is thus used to restructure the point cloud. With range images regularly spaced in the x and y directions but heavily distorted in the z direction, compensation algorithms can thus be applied. Multiple range images, each with different orientations of the sensor, were needed to capture all the details of an object. Eight different orientations of the sensor have been used in this research, resulting in eight range images of an object. The number of orientations required depends on the geometry of an object. However it is expected that eight will cover sufficiently the geometries of most objects without being too time-consuming in completing the cycle of scanning and processing of range images of an object.

One of the first methods of compensation was to simply take the average of all corresponding points of the multiple range images. For regions with noise alone, simple averaging yields points that are close to the true surface. However for regions with significant distortions, simple averaging cannot remove these distortions. The magnitude of these distortions may reduce but the points are still away from their true positions. Simple averaging, however, is useful because it presents a rough representation of the object albeit with distortions, which can then be used for part of the algorithms for compensation using edge detection.

Another simple algorithm is to select the lowest z-values of points from multiple range images in regions of distortion. The computation of regions of distortion is based on the differences in z-values between corresponding points from the multiple range images, and is known as an error map in this thesis. Bow wave distortions are often successfully removed by the selection of lowest z-values method. However selection of lowest z-values is not reliable in removing occlusion spikes, especially for multi-tiered objects where these spikes for an inclined face may dip below the lower tier. By

employing this method of compensation, such occlusion spikes would be included in the resulting range image.

With the understanding that incidence of distortions depend not on scanning direction but rather on orientation of the sensor and the geometry of an object, the Author has developed more effective algorithms for compensation based on this idea. By employing an error map to identify points in the *xy* plane in regions of significant distortion together with the simple averaged range image, the edges of an object can be detected by searching nearby points. After detecting the object's edges, a process of selecting the points expected to be least distorted from among eight range images begins. Points expected to have least distortions are those with orientations of the sensor close to parallel to the detected edge. Compared to the previous two methods of compensation, edge detection offers a more intelligent method of removing significant distortions, resulting in range images with much smaller distortions.

Chapter 5

Evaluation of New Algorithms

5 Evaluation of New Algorithms

5.1 Visual Assessment of Scanlines and Original Shapes of Selected Objects

The improvements afforded by the compensation algorithms based on edge detection were evaluated in more detail against the original eight range images as well as the averaged range image and the lowest *z*-values range image. The two objects used for this detailed evaluation were from the examples in Chapter 4 (see MDF block in Fig. 5-1(a) and technical object in Fig. 5-1(b)). For each object, one scanline position was chosen and the corresponding lines were taken from all the eight range images for comparison.

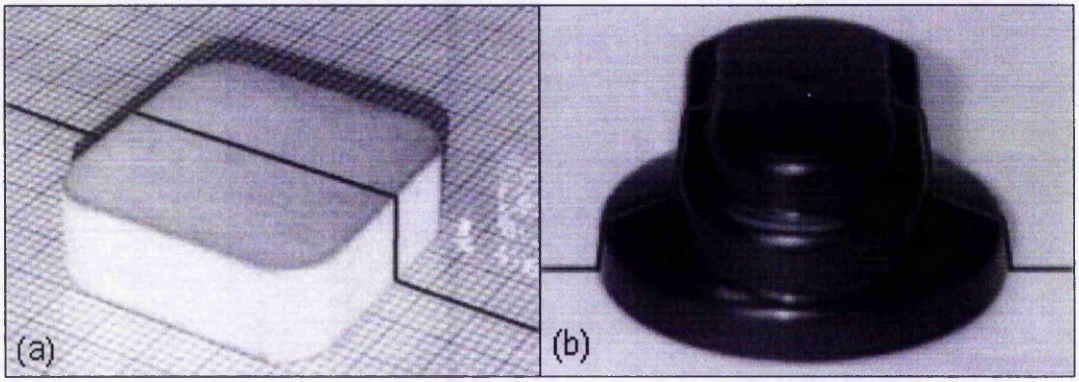

Fig. 5-1: Scanlines extracted from (a) an MDF block and (b) a technical object for evaluation.

Then the corresponding lines were again taken from range images after processing in the three different ways: by simple averaging, by selection of lowest *z*-values and by compensation based on edge detection. They were plotted and compared with the original shape of the objects, which were measured using a Vernier caliper. Their maximum and average deviations from the original shapes were also computed for comparison with those from the original eight range images. These eight original and their compensated range images are shown in Appendix C.3.

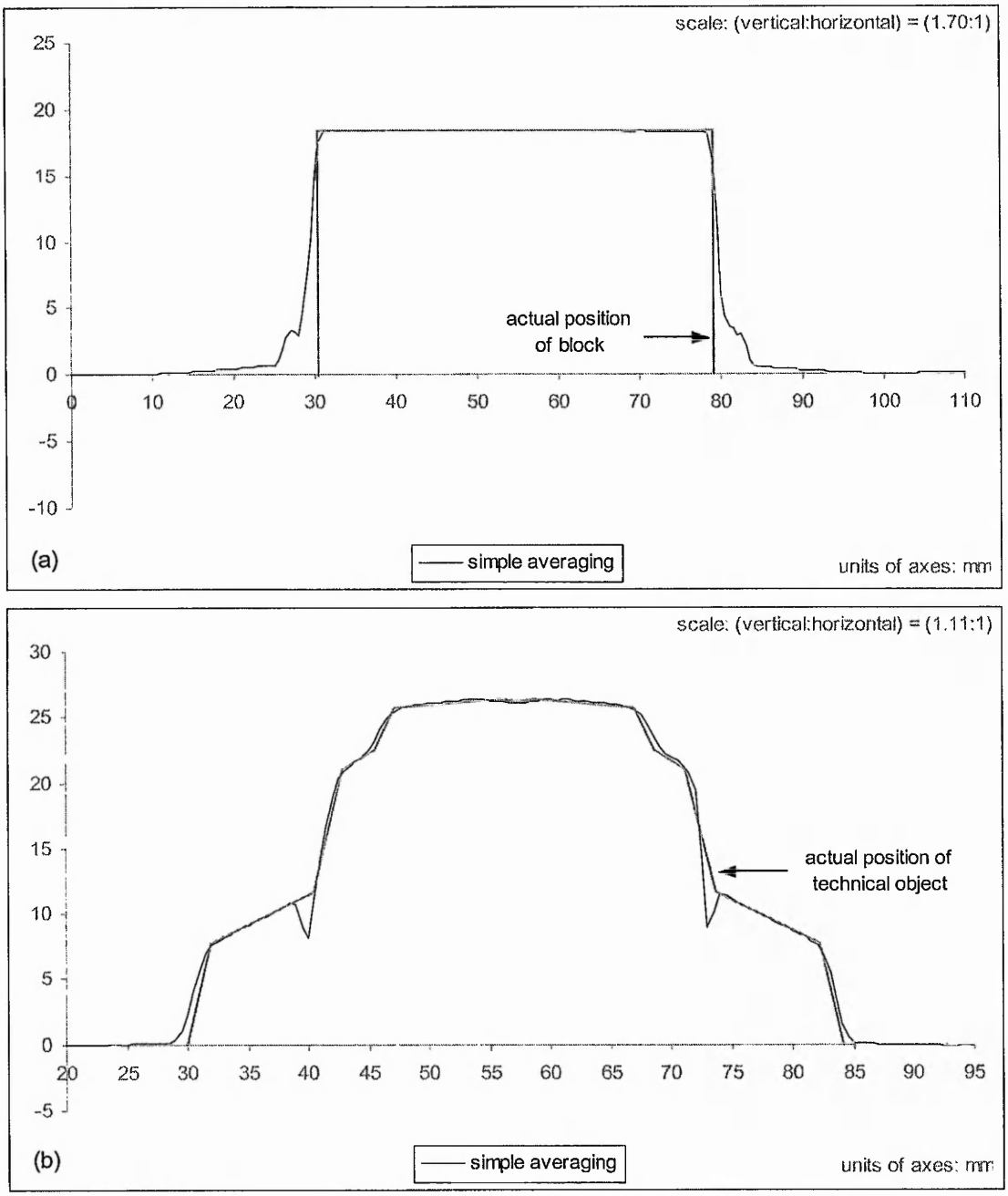

Fig. 5-2: One scanline from each simple averaged range image of (a) an MDF block from Fig. 5-1(a) and (b) a technical object from Fig. 5-1(b).

After averaging, points in regions with significant distortions in one or more of the original images still have distortions, although their magnitudes have decreased.

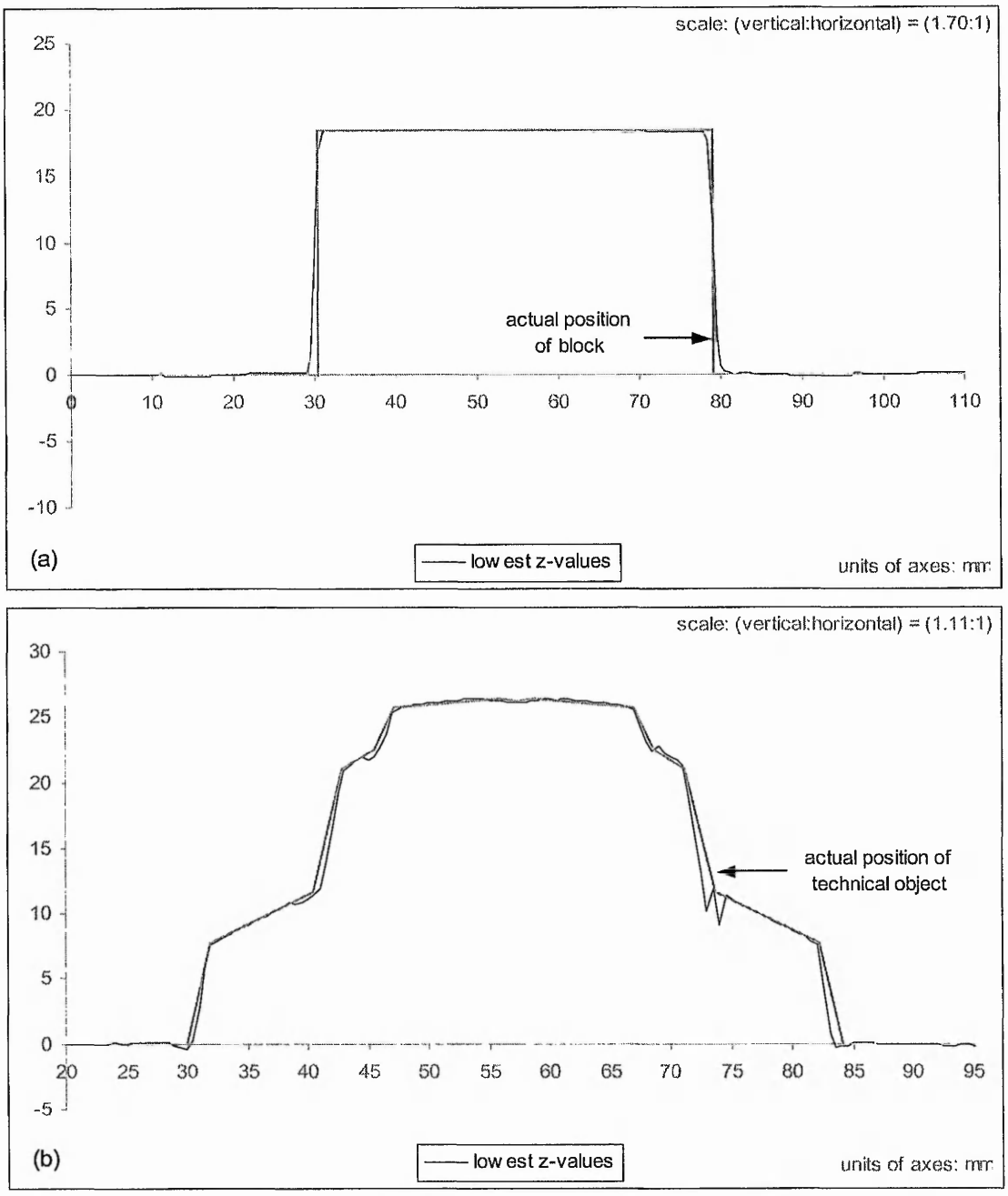

Fig. 5-3: Corresponding scanlines to those in Fig. 5-2 after selection of lowest *z*-values range images of (a) an MDF block and (b) a technical object.

As can be seen in Fig. 5-3(a), the scanline conforms more closely to the original shape of the block. However the algorithms are less effective for the multi-tiered technical object (see Fig. 5-3(b)). Therefore it is not reliable because the result is sometimes good, as in the case of the MDF block, but other times bad, as in the case of the technical object.

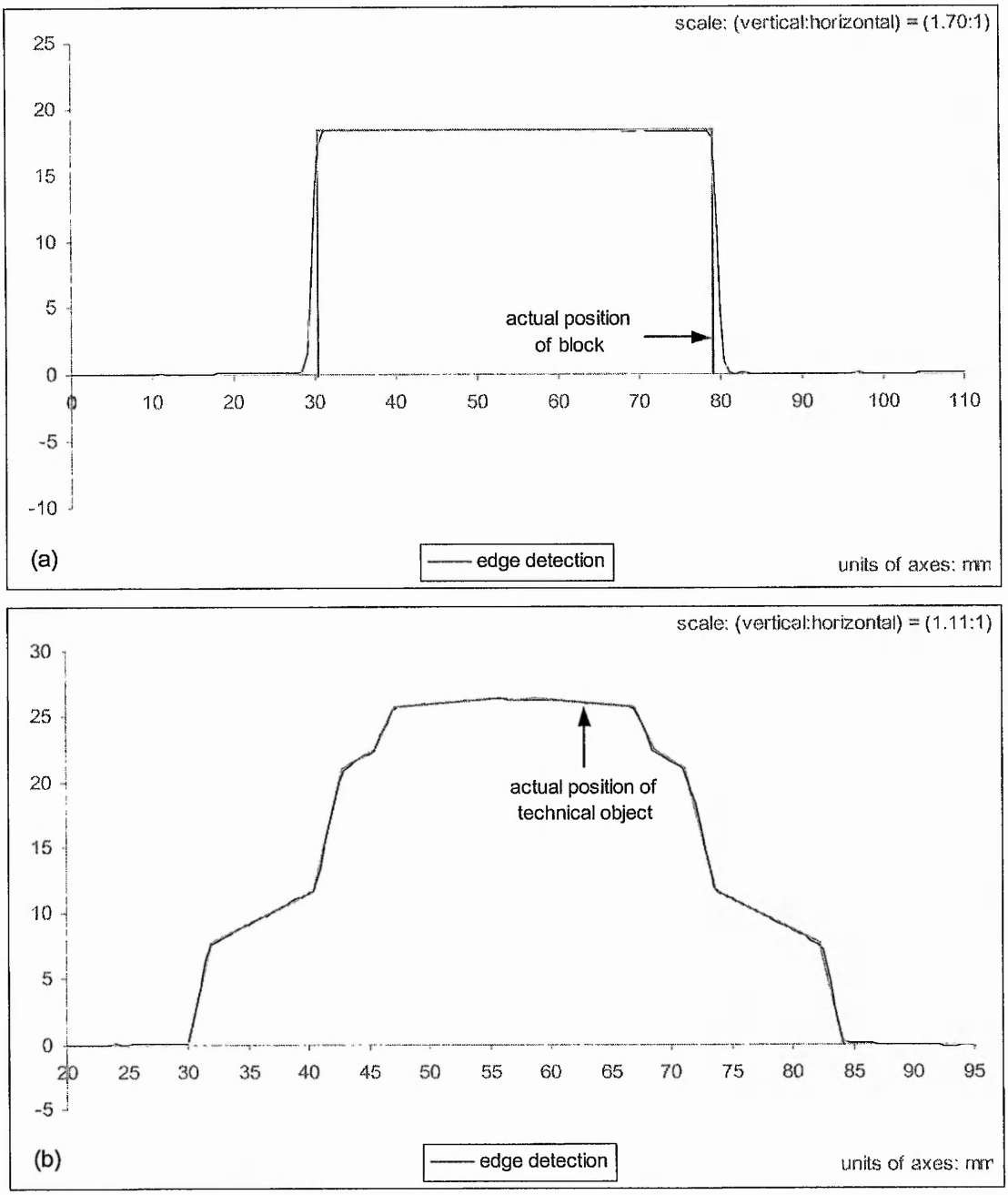

Fig. 5-4: Corresponding scanlines of those in Fig. 5-2 from range images after compensation based on edge detection for (a) an MDF block and (b) a technical object.

As shown in Fig. 5-4, after processing the range images with edge detection algorithms, scanlines appear to be free from significant distortions, such as bow waves and occlusion spikes, and they conform closely to the original shapes of the objects. However for vertical faces (see Fig. 5-4(a)), there still exist small spaces between the original shape and the scanline. Some of this is because of the horizontal separation

between points. When the points in regions with vertical faces are connected with a line, this line will always have a small gradient. This is also the cause for rounding of sharp corners and vertices of an object. Another contributory factor to these effects is due to averaging of the spot size (see Section 3.3.8 in Chapter 3).

5.2 Maximum and Average Deviations of Scanlines from Original Shapes of Selected Objects

For each point on a scanline, its deviation, $|\delta|$, from the original shape of the object was computed and then averaged to obtain the scanline's average deviation, ε (see Table 5-1 and Table 5-2).

Average deviation,

$$\varepsilon = \frac{\sum_{i=1}^{n} |\delta_i|}{n} \qquad (5\text{-}1)$$

where n is number of points on a scanline.

Scanlines of MDF Block	$\lvert\delta_{max}\rvert$	$\Sigma\lvert\delta\rvert$	ε
with orientation of the sensor at 0°	13.04	54.94	0.25
with orientation of the sensor at 45°	18.97	134.99	0.61
with orientation of the sensor at 90°	20.24	184.99	0.84
with orientation of the sensor at 135°	18.94	159.12	0.72
with orientation of the sensor at 180°	14.23	57.72	0.26
with orientation of the sensor at 225°	19.52	140.09	0.63
with orientation of the sensor at 270°	18.75	160.77	0.73
with orientation of the sensor at 315°	18.97	148.27	0.67
after simple averaging	14.65	124.46	0.56
after selection of lowest z-values	9.47	40.72	0.18
after compensation based on edge detection	9.52	45.86	0.21

Table 5-1: Maximum and average deviations of corresponding scanlines from original shape of the MDF block (units in mm).

From Table 5-1, it can be seen that among the original eight range images with different orientations of the sensor, the distortions are smallest when sensor is oriented close to parallel, [0°, 180°] to the edges of MDF block, as expected. As orientation of the sensor changes to being perpendicular, [90°, 270°] to these edges, the magnitudes of distortions increased. Simple averaging has reduced the distortions but ε is larger than the smallest value. By applying compensation based on either selection of lowest *z*-values or edge detection, ε is reduced considerably further. In this case the lowest *z*-values appears to be slightly better.

Scanlines of Technical Object	$\lvert\delta_{max}\rvert$	$\Sigma\lvert\delta\rvert$	ε
with orientation of the sensor at 0°	3.93	57.45	0.38
with orientation of the sensor at 45°	6.06	68.39	0.45
with orientation of the sensor at 90°	16.02	141.77	0.94
with orientation of the sensor at 135°	12.03	113.65	0.75
with orientation of the sensor at 180°	2.37	53.18	0.35
with orientation of the sensor at 225°	5.90	84.90	0.56
with orientation of the sensor at 270°	19.50	145.48	0.96
with orientation of the sensor at 315°	16.28	72.48	0.48
after simple averaging	4.49	66.93	0.44
after selection of lowest *z*-values	3.21	48.56	0.32
after compensation based on edge detection	1.52	36.57	0.24

Table 5-2: Maximum and average deviations of corresponding scanlines from original shape of the technical object (units in mm).

For the technical object, the maximum and average deviations are shown in Table 5-2. Again ε is smallest when the sensor is oriented parallel, [0°, 180°], and largest when the sensor is oriented perpendicular, [90°, 270°] to the edges of the technical object, as expected. Simple averaging makes ε larger than the smallest value and it still has unsightly distortions. Selection of lowest *z*-values has reduced the value of ε but the new compensation based on edge detection yields the best result with smallest ε.

Although compensation based on selection of lowest z-values provides good fit in the case of the MDF block, this method is less effective for a multi-tiered object, such as the technical object. Therefore it is not reliable for objects of more varied geometries.

5.3 Further Examples of Compensation

The results for further objects were evaluated upon application of the three different algorithms. These are shown in the following diagrams (Fig. 5-5 and Fig. 5-7 show one of eight range images but their complete set can be found in Appendix C.3). Averaged range images (see Fig. 5-6(a) and Fig. 5-8(a)) and range images after selection of lowest z-values (see Fig. 5-6(b) and Fig. 5-8(b)) still show significant distortions. Improvements are obvious in range images that were compensated using the edge detection algorithms (see Fig. 5-6(c) and Fig. 5-8(c)).

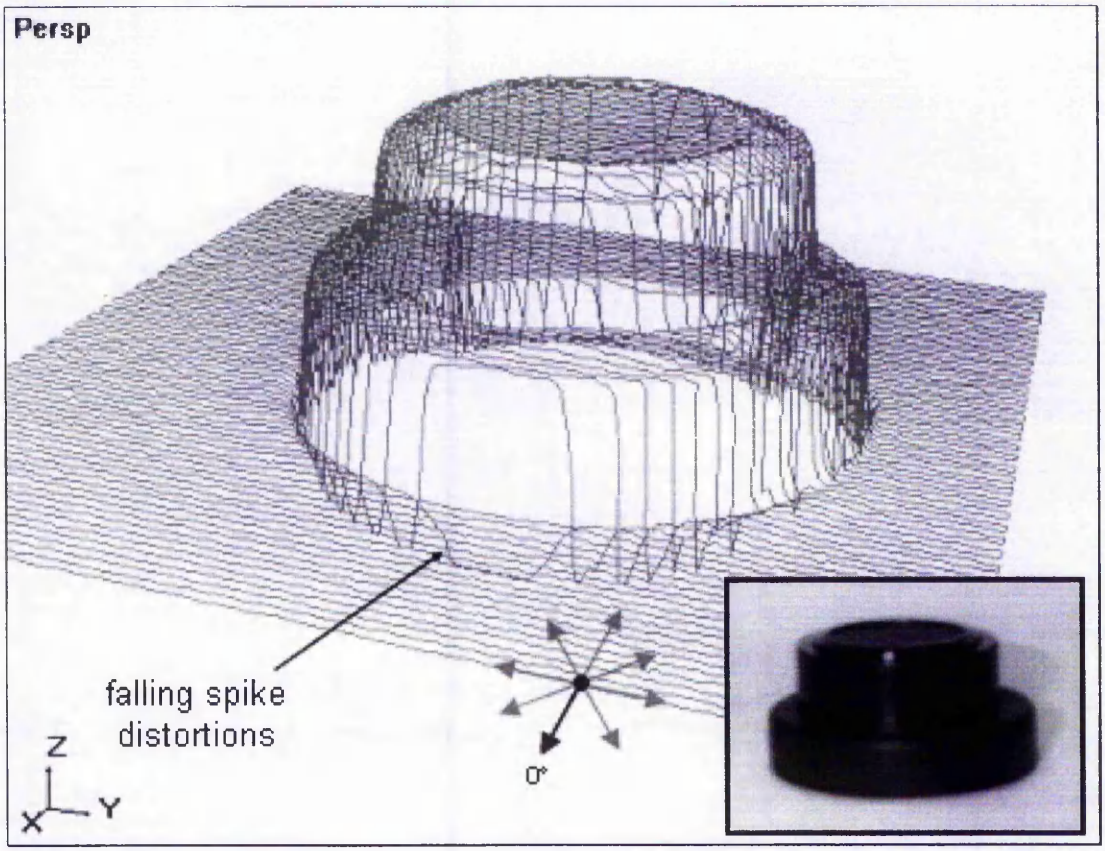

Fig. 5-5: One of eight range images of stacked camera caps with sensor oriented at 0° (x and y separation 0.5mm).

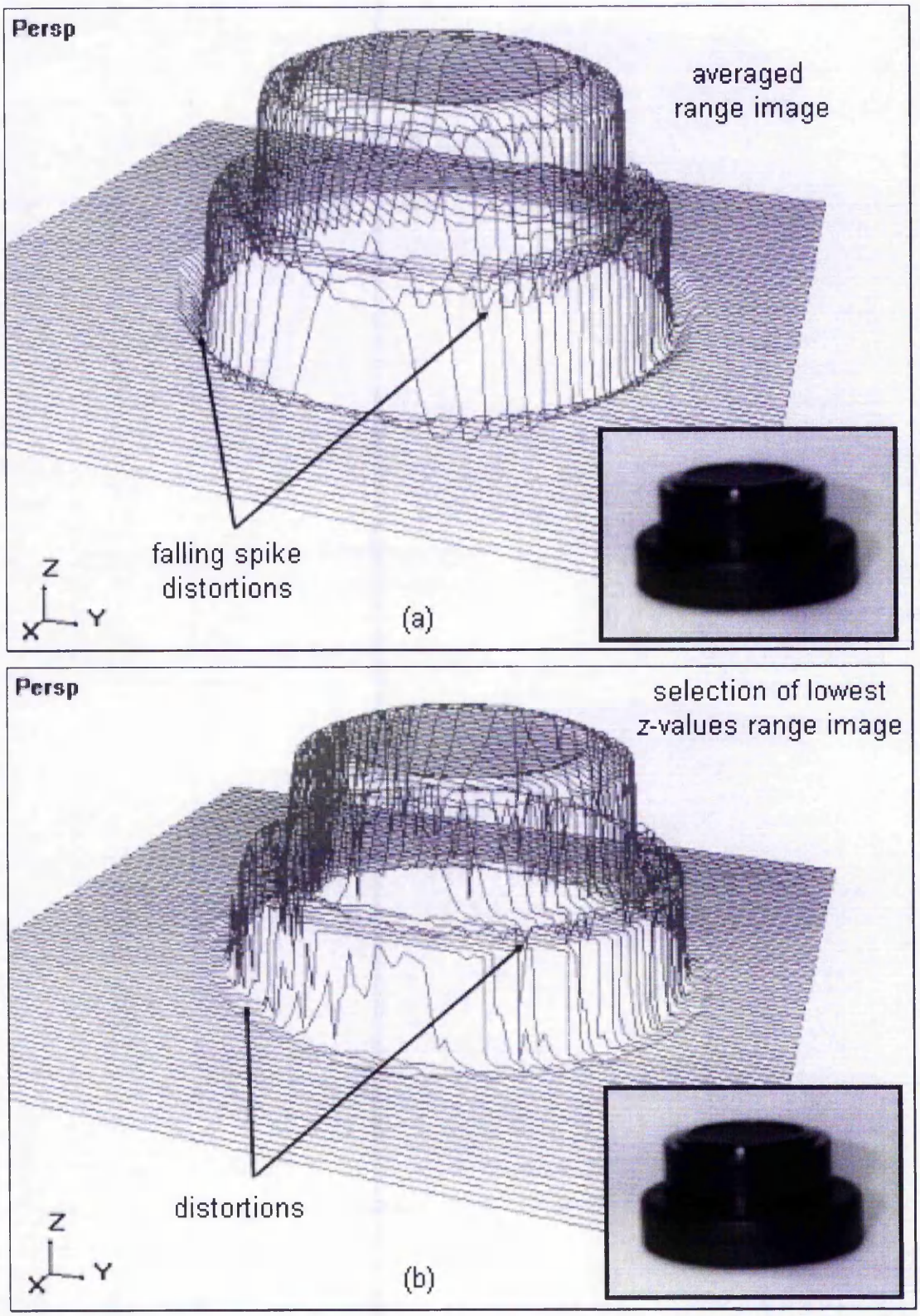

Fig. 5-6: Range images of stacked camera caps after (a) simple averaging and (b) selection of lowest *z*-values ((c) on following page).

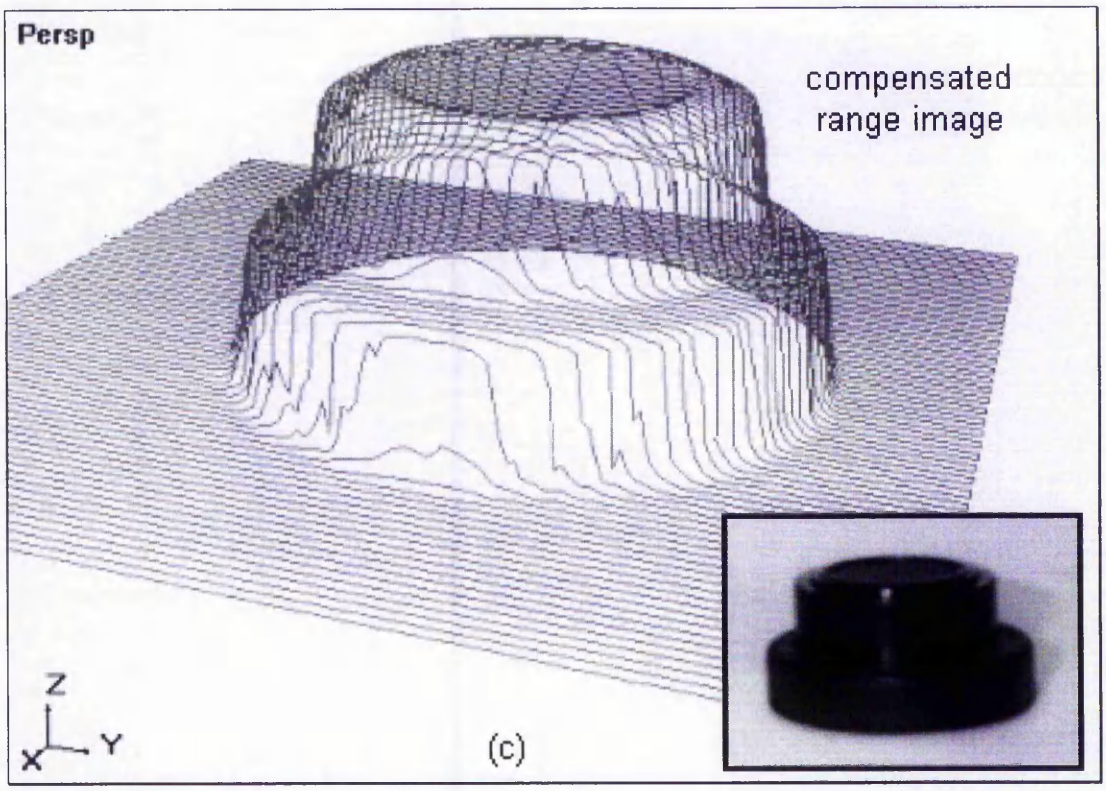

Fig. 5-6: Range image of stacked camera caps after (c) compensation based on edge detection.

Range images of the stacked camera caps that were processed with the three different ways are shown in Fig. 5-6. Distortions, albeit reduced in magnitudes, still exist in range images that were compensated by simple averaging and selection of lowest *z*-values. Compensation based on edge detection managed to successfully remove these distortions. However on the vertical face of the lower camera cap close to the base, there appears to be small distortions where the scanline direction suddenly changes twice in succession. It is thought that this is because of an abrupt change in the pairing of opposite oriented *z*-values during compensation and it may be possible to rectify it by modifying the algorithms to use a blend between the paired *z*-values (see Section 4.3.5 in Chapter 4).

For the tile object in Fig. 5-8, when observed carefully, it can be seen that there are distortions along the raised curves in both the averaged range image and the range image after selection of lowest *z*-values. The scan points at these locations dipped slightly below the true surface. These are no longer present after compensation based on edge detection.

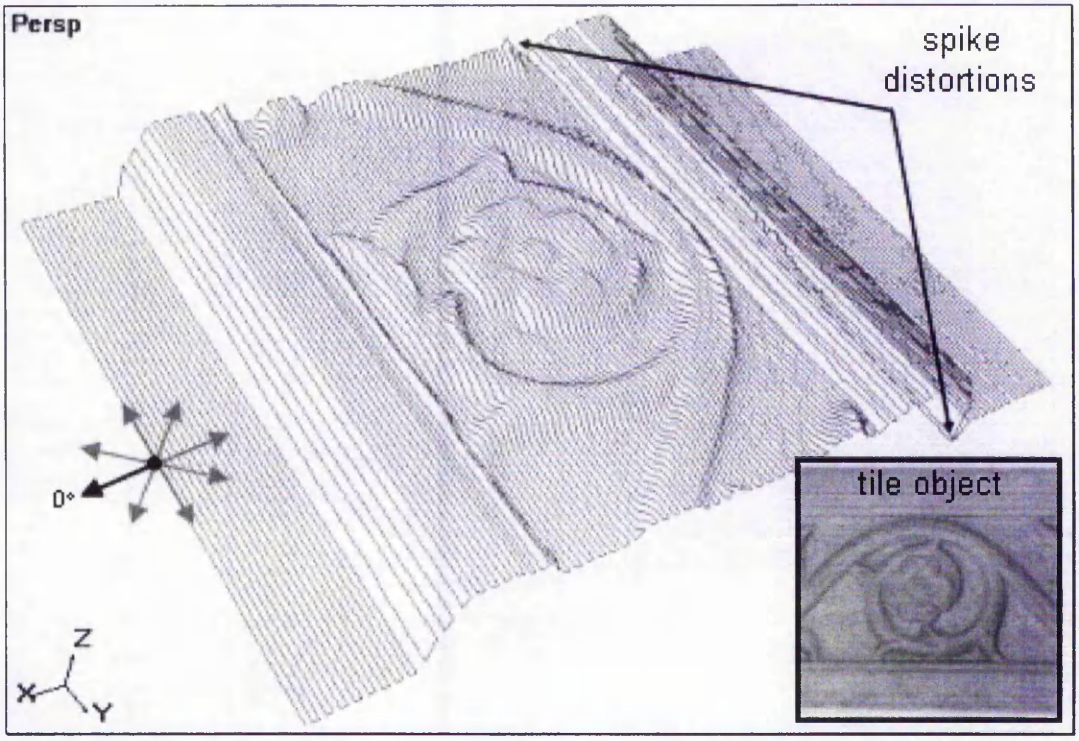

Fig. 5-7: One of eight range images of the tile object from Fig. 1-5 with sensor oriented at 0° (x and y separation 0.5mm).

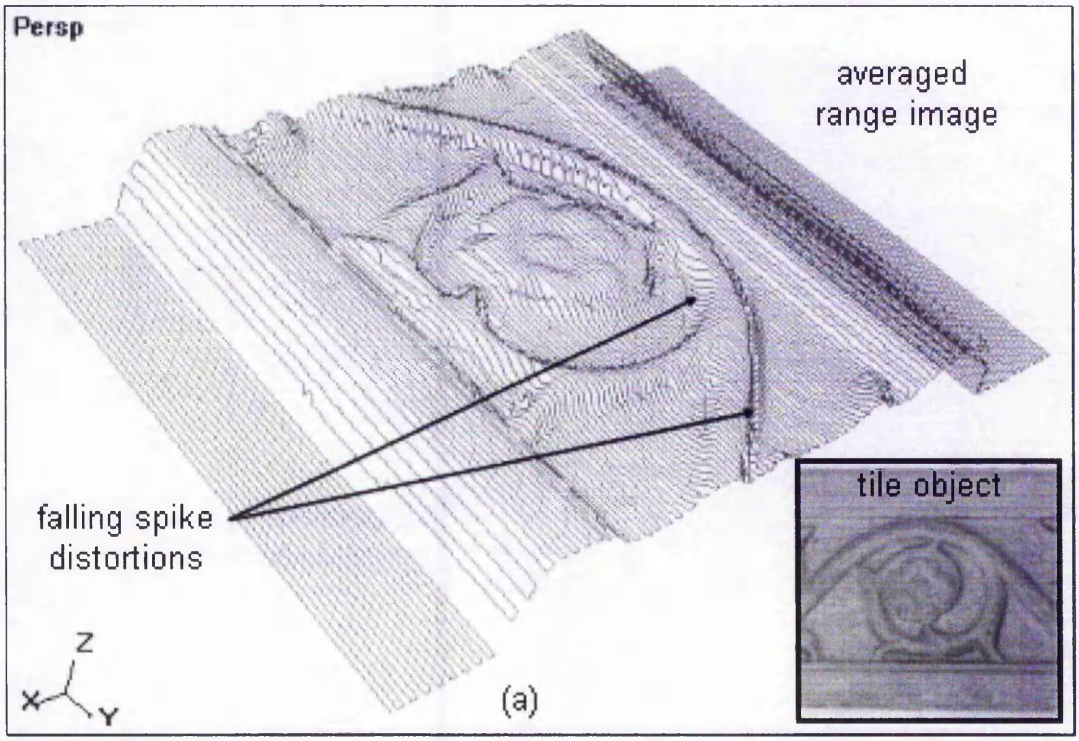

Fig. 5-8: Range image of tile object after (a) simple averaging ((b) and (c) on following page).

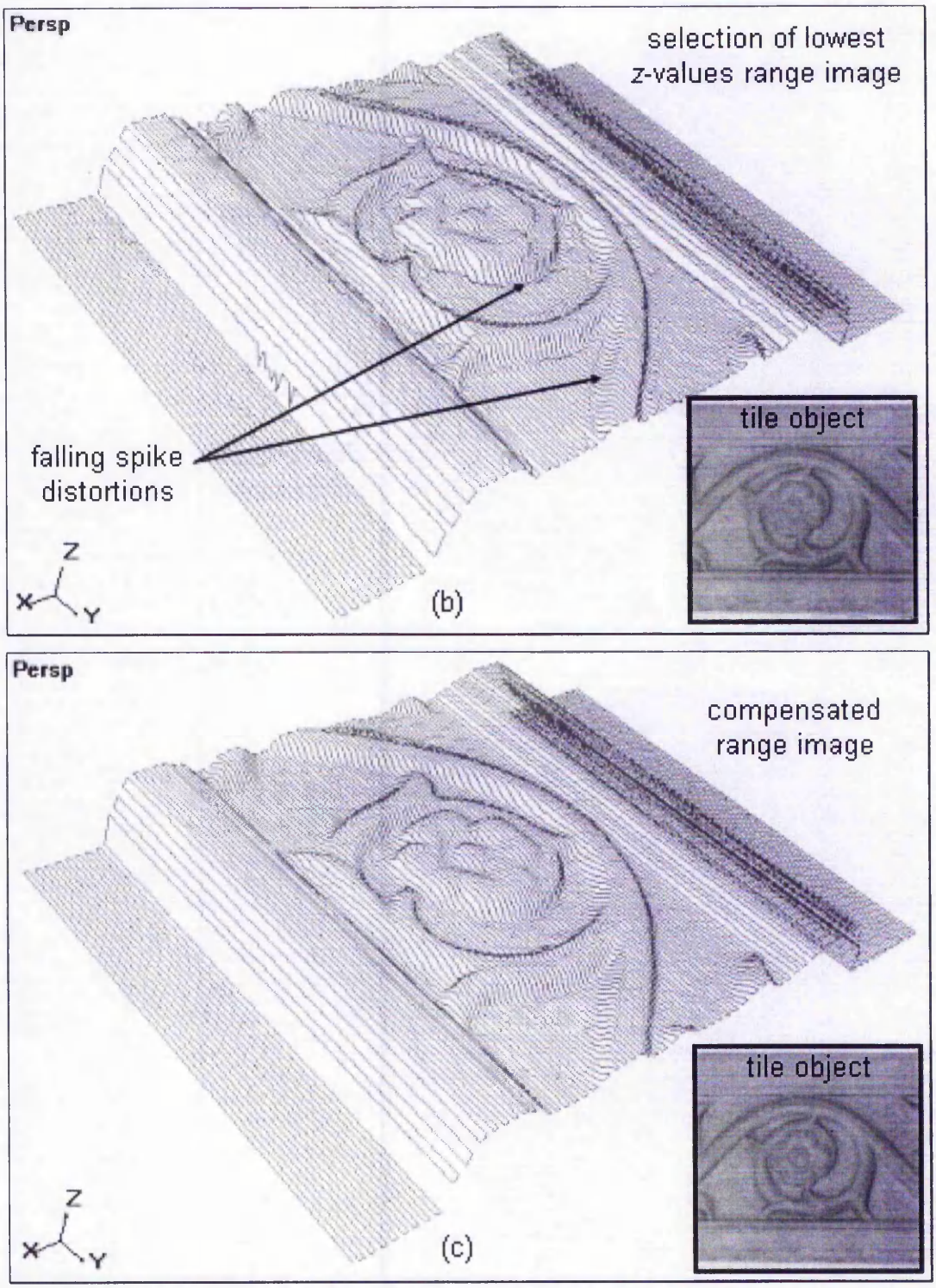

Fig. 5-8: Range images of tile object after (b) selection of lowest z-values and (c) compensation based on edge detection.

5.4 Summary

For the test objects discussed in this chapter, each of the original eight range images has significant distortions of its own. It can be seen from the evaluation that when they are combined by means of simple averaging, the magnitudes of these distortions are reduced significantly compared to the original range images. However regions of distortions occur in more places than in any one of the original eight. In some cases the distortions are reduced even further with compensation based on selection of lowest *z*-values but in other cases the results are worse. Compensation based on edge detection gave good results in all the examples. In the particular case of the MDF block, selection of lowest *z*-values is slightly better but it is much less effective when applied to objects of more varied geometries, such as the technical object. Therefore selection of lowest *z*-values is not a reliable method for removing significant distortions whereas compensation based on edge detection has been found to be more reliable for all the test objects.

The edge detection algorithms have managed to improve significantly the quality of a range image. However there are still some small distortions that are difficult to remove. One of them is the appearance of small distortions in scanlines on inclined faces of an object, which is thought to be a side-effect of the algorithms and it may thus be possible to reduce it by using blending in the algorithms (see Section 4.3.5 in Chapter 4 and Section 5.3). Further investigation needs to be conducted for suitable blending methods. Other types of distortions are sloping scanlines and rounded corners (see Section 3.3.8 in Chapter 3). These distortions are difficult to resolve without prior knowledge that the face of the object is truly vertical or that the corners of the object are actually sharp and not already rounded. Further research is required to study and thus to formulate compensation methods for these distortions.

Chapter 6

Discussion and Future Work

6 Discussion and Future Work

6.1 Discussion

This research has thus far dealt with problems, specifically distortions, in range images, which occur when using a single-perspective active triangulation point sensor. This sensor has only one detector adjacent to the emitter, so distortions due to occlusion of the primary spot image are likely to occur in some scans of objects with inclined and near-vertical faces. When the primary spot is occluded from the detector's field-of-view and no other light is detected, no reading can be computed, and a zero value is produced by the sensor, which then causes a negative value when processed by the CAM software (see Section 3.3.6 in Chapter 3). Even when there is no occlusion, distortions can occur due to the detection of stray reflections, in which the centroid of the detected spot image is not that of the primary spot, causing false depth measurement. The precise nature of the distortions thus depends to a large extent on the detailed local geometry of the object, which affects not only the profile of the spot image but also reflections and dispersions near it. The colour or reflectivity of a surface is also an influencing factor in the genesis of distortions. Surfaces of low reflectivity yield more noise than those of higher reflectivity. The magnitude of significant distortions, such as bow waves and spikes, is also determined by surface reflectivity. All the above problems are inherent to an imaging system that employs triangulation as its principle in depth measurement. However, distortions are less obvious in range images captured using a circular-perspective point sensor, because several detectors, positioned radially around the emitter, are used to collect and implicitly average the detected spot image. This type of sensor is much more expensive than the single-perspective point sensor.

For the experiments, the single-perspective point sensor was mounted on a 3-axis CNC machine. For a detailed investigation of distortions, several carefully selected objects were used, especially to highlight occurrences of distortions in regions adjacent to inclined faces. Before performing any scanning process, it is crucial to calibrate the test rig properly to prevent calibration errors from exacerbating distortions, as exhibited by the problem with scan height calibration. It is also paramount that objects to be scanned

reflect light diffusely, with homogenous high surface reflectivity. When acquiring multiple range images, registration is performed via a common point, the origin, where the spot image from the sensor is calibrated for each scan. Four distinct types of distortion have been identified: noise, transitional spikes, bow waves and occlusion spikes as well as some small systematic distortions. It was discovered during the course of the empirical study that the incidence of the more significant distortions depends on the orientation of the sensor and not on the direction of scanning. This is an extremely important point in the development of compensation algorithms. Noise is more evident on surfaces of low reflectivity than those of high reflectivity. Transitional spikes can be located at the transitions of two regions of highly different reflectivity, where they have larger magnitudes than noise. They are systematic and also depend on the orientation of the sensor. At these transitions, part of the spot image has lower intensity, thus slightly increasing or decreasing the angle of triangulation. This produces inaccurate readings, which appears to rise above or fall below the true surface by a small distance, depending on the orientation of the sensor with respect to these transitions.

When the sensor is oriented down the edge of an inclined face, the spot image is diffusely reflected and dispersed off this face. The detector detects this secondary reflection, together with the primary reflection of the spot image, producing a depth measurement that is above the true surface. A bow wave is thus a combination of several of these errorneous measurements along a scanline. The magnitude of the bow wave depends on the orientation of the sensor relative to an inclined face as well as surface reflectivity and gradient of this face. Surfaces of high reflectivity yield higher bow waves than surfaces of low reflectivity, as more stray light is detected. When orientation of the sensor is perpendicular to the edge of the object, the magnitude of the bow wave is at its largest. This decreases as the orientation of the sensor moves closer to parallel to the direction of the edge. Also as the gradient of the inclined face decreases, the size of bow waves is reduced, because a smaller area of this face is available for secondary reflection and dispersion.

Occlusion spikes occur when the spot image is likely to be occluded, as its name implies, from the sensor's field-of-view. This happens when the sensor is oriented up the edge of an inclined face of an object. The size of the occluded region depends on the height of the inclined face, the distance between sensor's emitter and detector, and the height

of sensor above the spot image. It also depends on the gradient of the inclined face. If the face is inclined to the vertical at an angle smaller than the angle of triangulation, the projected spot image will be occluded. Readings within these occluded regions are dependent on the reflectivity of the inclined face and the surface below it. When these are of low reflectivity, the spot image inside an occluded region has smaller dispersion and reflection. Therefore there may be no extended trace of light to be detected, resulting in no reading, which is represented by a zero value from the sensor but is then calibrated and scaled to a negative *z*-value by the CAM software. This negative *z*-value when plotted gives an impression of a falling spike, known as a trough, but this can then be detected and excluded from further processing. However when these surfaces are of high reflectivity the secondary reflections and dispersion of the spot image is likely to extend beyond the occluded region. The detector picks up this weak trace of light, producing a phantom point, which is a point of false height above the surface. One or more of these phantom points results in a rising spike, known as a crest, and together with troughs, they constitute occlusion spikes. (It is important to note that a falling spike in an occluded region may not necessarily be a trough with no reading. When stray light is detected, it may contribute to a falling spike with valid albeit incorrect reading.) In most cases of scanning, a combination of rising and falling spikes ensues because of varying dispersions and reflections. The incidence of occlusion spikes reduces as the orientation of the sensor moves away from perpendicular to the edge of the inclined face and is closer to being parallel to the direction of the edge.

An evaluation of distortions when using a circular-perspective point sensor was conducted. Although no occlusion spikes were found, bow waves, transitional spikes and noise are still evident although smaller in magnitudes. Circular-perspective point sensors do provide better results but some distortions can occur. Compared to single-perspective point sensors, circular-perspective point sensors are much more expensive.

Once an understanding of distortions had been established, the next phase in this research was to develop compensating algorithms to reduce these distortions. It has been understood that when using a single-perspective point sensor, some regions of an object may be obscured from the detector's field-of-view, and any details in those regions will then be lost if only a single range image with a single orientation is obtained. Therefore to fully represent an entire object, it is necessary to perform more than a

single scan with one orientation of the single-perspective point sensor. Multiple range images were therefore obtained with different orientations of the sensor. Most methods currently available for reducing distortions involve highly interactive manipulation of these multiple range images by a user, who has knowledge of the object's geometry. Portions of range images with distortions are trimmed off and the remainders are assembled, rather like a jigsaw puzzle, to form a complete digital representation of the object. This process is extremely time-consuming. Another, more automated, approach to reducing distortions is to determine for different parts of the object the optimum scanning direction and orientation of the sensor with respect to the geometry of that part prior to any scanning. A rough scan is therefore first used to segment the object into different regions according to its geometry. Thereafter different orientations of the sensor are automatically assigned to these segmented regions. Some sort of edge detection could prove useful in the assignment process. This procedure is complicated, especially for objects with complex geometry. The test rig that is required to successfully implement this approach would need to have many degrees of freedom to rotate the sensor to many possible angles.

Algorithms have been developed that automate compensation for distortions by collecting and combining multiple range images. The focus is on the significant distortions, which occur in regions adjacent to inclined faces of the object. The algorithms require multiple range images of the object, each with different orientations of the sensor on the scan region. One way of combining these multiple range images is by taking the average of the corresponding points on the *xy* plane. The averaged range image still has distortions, albeit reduced in size but it, nevertheless, provides a rough idea of the shape of the object (see Fig. 4-14). Using multiple range images, an error map can be calculated by detecting regions where the deviation between *z*-values is much greater than the noise. Another approach to reducing distortions is to select the lowest *z*-values for points in regions of distortion (identified by the error map). Before this selection process, any points that are below the planar surface are disregarded. This idea was conceived because significant distortions like bow waves and crests rise above the true surface of an object whereas troughs dip below the planar surface, or so it was initially assumed. Therefore the algorithms work quite well for single-tiered objects but become ineffective for multi-tiered objects. It was found that falling spikes at higher tiers do not necessarily fall below the planar surface, and as such, these spikes will be

selected since they are the lowest z-values at those points. Therefore in many cases selection of lowest z-values is not effective in reducing significant distortions (see Fig. 4-15).

The next approach involves identifying inclined faces, or edges, of an object. With the knowledge that orientation of the sensor and not scanning direction determines incidence of distortions, the identified edges are thus used for points in regions of distortion (from the error map) to select points from range images with orientations of the sensor least likely to have distortions. Eight range images were obtained for each object for the results presented here in this research. More range images could be used, in which the selection of points can be more focused, depending on the direction of the detected edge. This, however, would inevitably lead to longer acquisition time and may not make much improvement. The error maps, which demarcate regions of significant distortions (i.e. much greater discrepancies than with just noise), are produced using selected thresholds. The results here used thresholds which are multiples of noise deviation, calculated from planar regions of the eight range images. With an error map and the averaged range image of an object, edges can be detected and then used to select and combine points from range images with orientations of the sensor least likely to have distortions (i.e. with orientations close to parallel to the direction of these edges). Regions with small errors (noise) are processed by simple averaging. The new algorithms have been evaluated on several objects, producing range images that conform closely to the original shape of the objects. Operating the algorithms on multi-tiered objects as well as objects with slopes, sharp or rounded vertices yield vastly improved range images, whereby significant distortions are removed and replaced with the appropriate details (see Fig. 4-27). This compensation method based on edge detection could also be used with a circular-perspective point sensor if separate outputs from the multiple detectors could be obtained.

The fundamental idea behind these compensation algorithms based on edge detection is the selection and merging of points with smallest distortions, and these points are obtained when the sensor is oriented close to parallel to the edges. The algorithms rely on there being at least one point with low distortion from eight range images. Therefore if all the range images at an xy coordinate are distorted, the resulting new point will be distorted as well. Such a situation would occur when scanning a small but deep crevice

or cavity, whereby the projected spot image inside this crevice or cavity will be occluded from the detector's field-of-view at all the orientations of the sensor (see Fig. 6-1). As this is an inherent problem with triangulation, in which emitter and detector are not coaxial, user intervention is thus needed to manually fill in the correct *z*-values. Even if they are coaxial, distortions may still occur in the event of scanning extremely narrow and deep holes. (Also in the highly improbable event that all these distorted range images an at *xy* plane are at the same level, it will thus be incorrectly assigned to the small error region in the error map. Then, since simple averaging is employed for such regions, the new point will inevitably be distorted.)

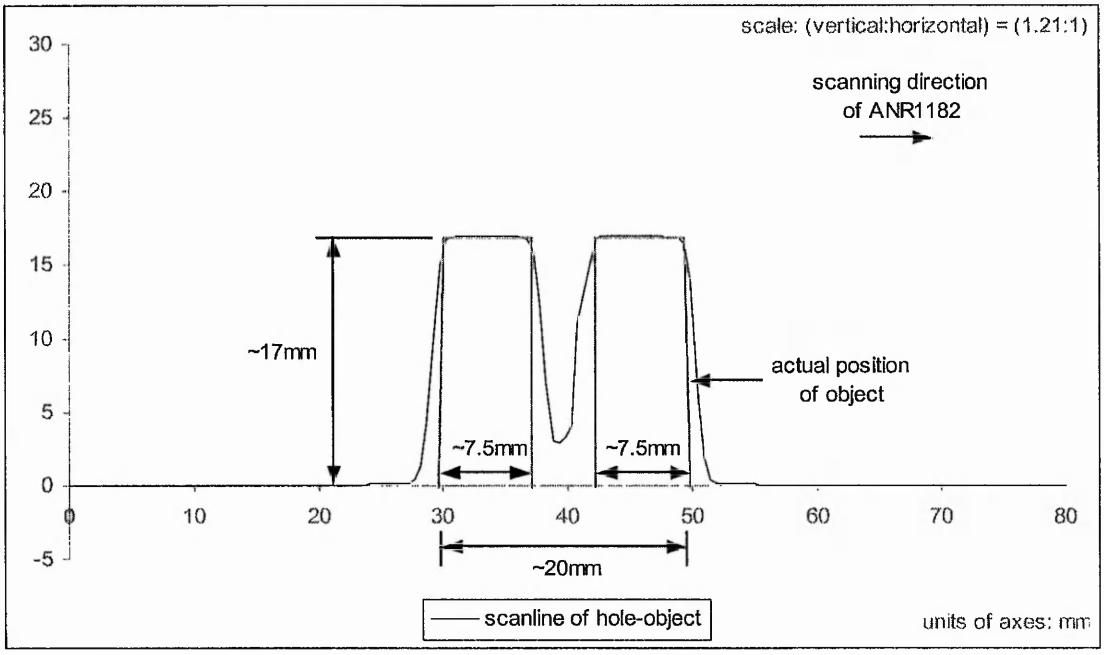

Fig. 6-1: Corresponding scanline of those in Fig. 3-39 of a rectangular block with cylindrical hole after compensation based on edge detection (scale is increased for greater clarity).

With significant distortions removed, reduction of noise through smoothing can further refine the range image. Grid smoothing with weighted averaging, as described in Section 4.1.3 in Chapter 4, can be performed, yielding range images with less undulation. Excessive smoothing, however, will remove some small details on the surface of the object, especially on regions with high curvature. Therefore user intervention may be needed to decide the number of iterations of smoothing to achieve the desired results. This process could be automated by segmenting a surface into regions of different

curvatures. More iterations of smoothing can be employed to treat regions with low curvature while those of higher curvature may require fewer or no smoothing or they may employ curvature-based smoothing. Also the detected edges can be used to decide which points to smooth in the grid. For example, when smoothing a point next to an edge, neighbouring points that are at a different height (i.e. those that are way above or below the point), are ignored – without this any rounding of edges will be made worse.

The newly improved range image can thus be used for visualization or be fed into a CAD system for further optimisation, such as mesh generation or surface rendering. It can also be vectorised by a CAM system for CNC machining or stereolithography to produce a replica of the original object.

6.2 Future Work

This thesis has presented an investigation into distortions generated when using a single-perspective point sensor. The focus was on regions of high curvature, whereby distortions were systematic, depending on the orientation of the sensor relative to the geometry of the object. It is understood that distortions are likely to be at their maximum when an inclined or near-vertical face is perpendicular to the orientation of the sensor. The size of these distortions reduces as the orientation of the sensor rotates to parallel to the edge of the inclined face. More work could be carried out in the investigation of distortions by extensively mapping the relationship between types of distortion and objects of more varied geometry. It was noted that surfaces of high reflectivity yield less noise than those of low reflectivity. Therefore the incidence of noise in relation to different surface reflectivity or varying colours can be investigated in greater detail. Also the effect of the size of a spot image in contributing to "sloping" scanlines and "rounding" of sharp corners could be further investigated (see Section 3.3.8 in Chapter 3).

The developed compensation algorithms based on edge detection can be extended by refining the selection of scan points with orientations of the sensor close to parallel to the computed least squares line, which defined the edge relating to the point in the *xy* plane. Currently this selection is based solely on the angle in the horizontal plane of the edge with respect to different orientations of the sensor. However computation of the

normal distance of the *xy* coordinate from the edge could be incorporated. When the *xy* coordinate is far away from the edge, some improvements may be possible by combining more points, including those with sensor oriented up the edge – beyond the spikes. On the other hand, when *xy* coordinate is closer to the edge, the selection of points may need to become stricter. Further investigation is needed.

In situations where there is no pair of points with opposite orientations, all L-marked points are combined. This may produce a small distortion in the new scan point. Instead for such situations, a further search of neighbouring *xy* coordinates to determine the edges they have detected in relation to its position will aid in the decision of which points, from which range images, are to be accepted. For example, edges relating to neighbouring points can be interpolated to produce a more definite edge for a particular *xy* coordinate.

Instead of smoothing every scan point in a range image, selective smoothing can be implemented. For example, after compensation based on edge detection, newly generated scan points at the periphery of regions of significant distortions may not have smooth continuity to nearby points outside these regions. This is because for regions of significant distortions, only a few selected points from the eight range images were averaged compared to the averaging of all eight points in regions with low distortion. A blend can thus be applied, resulting in smoother transitions between these regions. Modification of the algorithms using blending methods could also be investigated to prevent the sudden fluctuations in the scanline on inclined faces of objects (see Section 4.3.5 in Chapter 4).

Another idea for smoothing is that instead of using a fix-sized grid, a grid of varying size can be implemented based on geometry of the object. For example, regions of higher curvature may employ a smaller grid while those of lower curvature or near planar may use a much bigger grid. The method of smoothing, such as weighted or simple averaging, can also be determined by taking into account the curvature of the object (i.e. fitting least squares curve or surfaces to points rather than straight lines or planes). More extensive investigation is thus required. More complex smoothing could be developed, which takes into account the curvature of the object.

Chapter 7

Conclusions

7 Conclusions

The aim of this research was to investigate distortions which occur when using an optical triangulation sensor, specifically a single-perspective point sensor, and then to establish the relationship between these distortions and their possible sources, followed by the development of algorithms to compensate for the distortions, thus improving range image quality for CNC machining. The work described in this thesis represents a significant advance towards the aims of the research and all the stated objectives have been achieved. Several types of distortion have been investigated and their source identified. Promising results of the compensation algorithms based on edge detection have been achieved.

A single-perspective point sensor is a cost-effective solution in the acquisition of 3-D range images when compared with circular perspective point sensors or tactile sensors. Range images produced when using a single-perspective point sensor that employs the triangulation principles have high resolution because of its high spatial accuracy. However they are not without their shortcomings. Besides noise, significant distortions are generated due to the limitation of the detector's field-of-view with respect to the position of the projected spot image on the surface of an object. A circular-perspective point sensor suffers less significant distortions, since it is effectively similar to using several single-perspective point sensors with detectors oriented around a single projected spot image. The final range image that is produced when using a circular-perspective point sensor is the result of implicit averaging. Although total occlusion may not occur, the range image still suffers from small bow waves as a result of multiple reflections and dispersions but they are reduced by the sensor's implicit averaging. Not only is it a cheaper alternative but a single-perspective point sensor can also be used to capture several range images at different orientations of the sensor, offering flexibility in processing the images.

Noise is inherent in any 3-D range images and its basis depends on the types of sensor used. In triangulation, its occurrence in a range image can be attributed to different surface reflectivity, with high surface reflectivity yielding less noise than surfaces of low reflectivity. Simple smoothing algorithms have been developed and are effective for objects of low curvature.

Another type of distortion investigated is transitional spikes. When scanning using the triangulation principles, surfaces with contrasting regions yield rising or falling distortions at the borders of these regions. This is due to a sudden change of the amount of light reflected from the spot image. Such distortions can be avoided by ensuring the surface that is to be scanned is homogenously reflective with no distinct contrast.

More significant distortions were the main subject of investigation. They are systematic and it was found that their incidence depends on the orientation of the sensor with respect to an inclined or near-vertical face rather than on the direction of scanning. One of them is named bow wave for its appearance in a range image resembles a wave in regions adjacent an inclined face. On the other hand occlusion spikes occur when the spot image is hidden from detector's field-of-view by an inclined face. The two types of occlusion spikes, i.e. rising spike and falling spike, depend on the details and surface reflectivity of the inclined face and regions near it. Rising spike, or crest, occurs when traces of the spot image extend beyond the occluded region and are picked up by the detector. When the detector can detect no trace of light, the sensor produces no reading, resulting in a trough, which is a type of falling spike. However for cases of a slope, reflection and dispersion near the base of this slope would result in a falling spike, which has a valid reading, albeit inaccurate.

After detailed investigation of the bow wave and spike distortions, compensation algorithms have been developed using the knowledge that significant distortions depend on orientation of the sensor and not on scanning direction. The compensation algorithms are based on error mapping and edge detection, using multiple range images of objects. Regions with significant distortions are detected, based on comparing these multiple range images. Then edge detection allows points expected to have least distortions to be selected and combined to form a new improved range image. The outcomes of the algorithms were evaluated for objects with simple geometry and others of more complex geometry. The improvements in the range images were considerable, compared to the original multiple range images and to those that were compensated using simple averaging or selection of lowest z-values.

The research conducted so far contributes significant progress towards the goal of automatic identification and compensation for distortions generated when using an optical triangulation point sensor. However further investigation should explore in particular the area of compensation for surfaces with more varied curvatures such as those with small crevices and cavity.

References

[1] Ingle K. A., *Reverse Engineering*, McGraw-Hill Professional Publishing, 1994.

[2] Brown A. J., *Specifications and Reverse Engineering*, Journal of Software Maintenance: Research and Practice, vol. 5, pp. 147-153, 1993.

[3] Pressman R. S., *Software Engineering – A Practitioner's Approach*, McGraw-Hill Publisher, 5th Edition, pp. 843-867, 2000.

[4] Lehman B. A., *Intellectual Property and the National Information Infrastructure*, The Report of the Working Group on Intellectual Property Rights, Washington, USA, September 1995.

[5] Vàrady T., Martin R. R. and Cox J., *Reverse Engineering of Geometric Models – An Introduction*, Journal of Computer-Aided Design, vol. 29, no. 4, pp. 255-268, 1997.

[6] Karbacher S., Häusler G. and Schönfeld H., *Reverse Engineering using Optical Range Sensors*, Handbook of Computer Vision and Applications, Academic Press, vol. 3, pp. 359-380, 1999.

[7] Hoschek J. and Lasser D., *Fundamentals of Computer Aided Geometric Design*, AK Peters, Wellesley, Massachusetts, 1993.

[8] Karbacher S., Babst J., and Häusler G., *Visualization and Detection of Small Defects on Car-Bodies*, Vision, Modeling and Visualization '99, pp. 1-8, Sankt Augustin, Germany, 1999.

[9] Byrne G., Dornfeld D., Inasaki I., Ketteler G., Konig W. and Teti R., *Tool Condition Monitoring (TCM) – The Status of Research and Industrial Application*, Annals of the CIRP, vol. 44, no. 2, pp. 541-562, 1995.

[10] Heinz I., Mettenleiter M., et al., *3-D Lidar for Inspection of Real World Environments*, Proceedings of 5th Conference on Optical 3-D Measurement Techniques, Vienna, Austria, October 2001.

[11] Levoy M., *The Digital Michelangelo Project*, Proceedings of Second International Conference on 3-D Digital Imaging and Modeling (3DIM '99), pp. 2-11, Ottawa, Canada, October 1999.

[12] Lassiter J., ***Principles of Traditional Animation Applied to 3-D Computer Animation***, Proceedings of SIGGRAPH '87, pp. 35-44, July 1987.

[13] Lynch M., ***Computer Numerical Controls for Machining***, McGraw-Hill Professional Publishing, 1992.

[14] Allen P. K. and Michelman P., ***Acquisition and Interpretation of 3-D Sensor Data from Touch***, IEEE Transactions on Robotics and Automation, vol. 6, no. 4, pp. 397-404, August 1990.

[15] Leick A., ***GPS Satellite Surveying***, John Wiley and Sons Publications, New York, 1995.

[16] Rohling R. N., ***3-D Freehand Ultrasound: Reconstruction and Spatial Compounding***, Ph.D. Thesis, University of Cambridge, September 1998.

[17] Chen F., Brown G. M. and Song M., ***Overview of 3-D Shape Measurement using Optical Methods***, Proceedings of SPIE, Optical Engineering, vol. 39, pp. 10-22, January 2000.

[18] Schwarte R., Heinol H., et al., ***Principles of Three-Dimensional Imaging Techniques***, Handbook of Computer Vision and Applications, Academic Press, vol. 1, no. 18, pp. 463-484, 1999.

[19] Ross B., ***A Practical Stereo Vision System***, Proceedings of IEEE International Conference on Computer Vision and Pattern Recognition, pp. 148-153, 1993.

[20] Kang S. B., Webb J. A., Zitnick C. L. and Kanade T., ***An Active Multibaseline Stereo System with Real-Time Acquisition***, Proceedings of Image Understanding Workshop, pp. 1325-1334, Monterey, CA, November 1994.

[21] Lu C., ***A Modulation Projection Method for 3-D Shape Measurement***, Proceedings of 5th Conference on Optical 3-D Measurement Techniques, Vienna, Austria, October 2001.

[22] Dey T., Bajaj C. and Sugihara K., ***On Good Triangulations in Three Dimensions***, International Journal of Computer Geometry and Applications, vol. 2, pp. 75-95, 1992.

[23] Journet B. and Poujouly S., ***High-Resolution Laser Rangefinder based on a Phase-Shift Measurement Method***, Proceedings of SPIE, Three-Dimensional Imaging, Optical Metrology, and Inspection IV, vol. 3520, pp. 123-132, December 1998.

[24] Delaye V. and Labeye P., ***High-Resolution Eye-Safe Time-of-Flight Laser Rangefinding***, Proceedings of SPIE, Laser Radar Technology and Applications V, vol. 4035, pp. 216-225, September 2000.

[25] Besl P. J. and McKay D. N., ***A Method for Registration of 3-D Shapes***, IEEE Transactions on Pattern Analysis and Machine Intelligence, vol. 14, no. 2, pp. 239-256, 1992.

[26] Pulli K., ***Multiview Registration for Large Data Sets***, Proceedings of Second International Conference on 3-D Digital Imaging and Modeling (3DIM '99), pp. 160-168, Ottawa, Canada, October 1999.

[27] Nguyen V. D., Nzomigni V. and Stewart C. V., ***Fast and Robust Segmentation of 3-D Surfaces using Low Curvature Patches***, Proceedings of Second International Conference on 3-D Digital Imaging and Modeling (3DIM'99), pp. 201-208, October, 1999.

[28] Dietz U., ***Fair Surface Reconstruction from Point Clouds***, Proceedings of International Conference on Mathematical Methods for Curves and Surfaces, pp. 79-86, Lillehammer, Norway, July 1997.

[29] Bajaj C. L., Bernardini F. and Xu G., ***Reconstruction Surfaces and Functions on Surfaces from Unorganised Three-Dimensional Data***, Algorithmica, vol. 19, pp. 243-261, 1997.

[30] Hoschek J., Dietz U. and Wilke W., ***A Geometric Concept of Reverse Engineering of Shape: Approximation and Feature Lines***, Proceedings of International Conference on Mathematical Methods for Curves and Surfaces, pp. 253-262, Lillehammer, Norway, July 1997.

[31] Encarnacao J. L., Linder R. and Schlechtendahl E. G., ***Computer Aided Design: Fundamentals and System Architectures***, Springer-Verlag, 1990.

[32] Turk G. and Levoy M., ***Zippered Polygon Meshes from Range Images***, Proceedings of SIGGRAPH '94, ACM Press, pp. 311-318, Orlando, Florida, July 1994.

[33] Hoppe H., ***Surface Reconstruction from Unorganised Points***, Ph.D. thesis, University of Washington, 1994.

[34] Hoppe H., DeRose T., Duchamp T., et al., ***Piecewise Smooth Surface Reconstruction***, Proceedings of SIGGRAPH '94, ACM Press, pp. 295-302, Orlando, Florida, July 1994.

[35] Holder M. and Richardson J., ***Genetic Algorithms, another Tool for Quad Mesh Optimisation?***, Proceedings of 7 International Meshing Roundtable, pp. 497-504, Michigan, USA, October 1998.

[36] Diaz-Morcillo A., Bernal-Ros A. and Nuno L., ***Mesh Generation Methods over Plane and Curved Surfaces***, Proceedings of 7 International Meshing Roundtable, pp. 397-407, Michigan, USA, October 1998.

[37] Hoppe H., DeRose T., Duchamp T., et al., ***Mesh Optimisation***, Proceedings of SIGGRAPH '93, ACM Press, pp. 19-26, New York, USA, August 1993.

[38] Edelsbrunner H. and Mücke E. P., ***Three-Dimensional Alpha Shapes***, ACM Transactions on Graphics, vol. 13, pp. 43-72, January 1994.

[39] Manohar S., ***Advances in Volume Graphics***, Computer & Graphics, pp. 73-84, 1999.

[40] Curless B. and Levoy M., ***A Volumetric Method for Building Complex Models from Range Images***, Proceedings of SIGGRAPH '96, ACM Press, pp. 303-312, New Orleans, LA, August 1996.

[41] Lorensen W. E. and Cline H. E., ***Marching Cubes: A High Resolution 3-D Surface Construction Algorithm***, Proceedings of SIGGRAPH '87, vol. 21, pp. 163-169, July 1987.

[42] Leong K. F., ***Rapid Prototyping & Manufacturing: Fundamentals of Stereolithography***, McGraw-Hill Professional Publishing, 1993.

[43] Carocci M., Lazzari S., Rodella R. and Sansoni G., ***3-D Range Optical Sensor: Analysis of the Measurement Errors and Development of Procedures for their Compensation***, Proceedings of SPIE, Three-Dimensional Image Capture and Applications, vol. 3313, pp. 178-188, March 1998.

[44] Wong K. H, Poliakoff J. F. and Thomas P. D., ***Automated Compensation for Distortion from a Single-Perspective Optical Triangulation Scanner***, Proceedings of 3rd Conference on Postgraduate Research in Electronics, Photonics, Communications and Software, Keele, UK, April 2001.

[45] Wong K. H., Poliakoff J. F. and Thomas P. D., *Compensation Techniques For Distortions From A Single-Perspective Optical Triangulation Sensor*, Proceedings of 5th Conference on Optical 3-D Measurement Techniques, Vienna, Austria, October 2001.

[46] El-Hakim S. F., Beraldin J. A. and Blais F., *A Comparative Evaluation of the Performance of Passive and Active 3- D Vision Systems*, Proceedings of SPIE, Conference on Digital Photogrammetry, vol. 2646, pp. 14-25, St. Petersburg, Russia, June 1995.

[47] Buelthoff H. H., *Shape from X: Psychophysics and Computation*, Computational Models of Visual Processing, Cambridge, MA: MIT Press, pp. 305-330, 1991.

[48] Mu Z. and Plemmons R. J., *Regularization Methods for Image Restoration based on Autocorrelation Functions*, Proceedings of SPIE, Advanced Signal Processing Algorithms, Architectures and Implementations X, vol. 4116, pp. 375-384, November 2000.

[49] Schneider C. T., *3-D Measurement by Digital Photogrammetry*, Proceedings of SPIE, Computer Vision for Industry, vol. 1989, pp. 370-374, December 1993.

[50] Besl P. J., *Active, Optical Range Imaging Sensors*, Machine Vision and Applications, vol. 1, pp. 127-152, 1998.

[51] Beraldin J. A., El-Hakim S. F. and Blais F., *Performance Evaluation of Three Active Vision Systems built at the National Research Council of Canada*, Proceedings of the Conference on Optical 3-D Measurement Techniques, pp. 352-361, Vienna, Austria, October 1995.

[52] Michelson A. A., *On the Application of Interference Methods to Astronomical Measurements*, Philosophical Magazine and Journal of Science, vol. 30, pp. 1-20, July 1890.

[53] Lihachev D. I., *Prospects of Laser Interferometers*, Proceedings of SPIE, International Conference on Lasers for Measurements and Information Transfer, vol. 4316, pp. 43-45, November 2000.

[54] Xue M., Xiangli B. and An B., *Optical Systems of Imaging Interferometers*, Proceedings of SPIE, International Optical Design Conference, vol. 3482, pp. 474-483, September 1998.

[55] Laskin R. A., *Technology for Space Optical and Infrared Interferometry*, Proceedings of SPIE, Astronomical Interferometry, vol. 3350, pp. 654-664, July 1998.

[56] Koskinen M., Kostamovaara J. T. and Myllyla R. A., *Comparison of Continuous-Wave and Pulsed Time-of-Flight Laser Range-Finding Techniques*, Proceedings of SPIE, Optics, Illumination and Image Sensing for Machine Vision VI, vol. 1614, pp. 296-305, March 1992.

[57] Moody S. E., *Commercial Applications of Lidar: Review and Outlook*, Proceedings of SPIE, Optical Remote Sensing for Industry and Environmental Monitoring, vol. 3504, pp. 41-44, August 1998.

[58] Marszalec J. A. and Myllyla R. A., *Shape Measurements using Time-of-Flight-based Imaging Lidar*, Proceedings of SPIE, Three-Dimensional Imaging and Laser-based Systems for Metrology and Inspection III, vol. 3204, pp. 48-54, December 1997.

[59] Fisher P. F. and Lindenberg R. E., *Distinctions among Cartography, Remote Sensing and Geographic Information Systems*, Photogrammetric Engineering and Remote Sensing, vol. 55, no. 10, pp. 1431-1434, 1989.

[60] Jansa J., Huang Y. R. and Trinder J. C., *Problems of Precise Target Location and Camera Orientation in Digital Close-Range Photogrammetry*, Proceedings of SPIE, Videometrics II, vol. 2067, pp. 151-161, October 1993.

[61] Silva Sthel M. and Moreira de Castro R., *Simple Method of Theodolite Alignment using Laser*, Proceedings of SPIE, Second Iberoamerican Meeting on Optics, vol. 2730, pp. 569-571, February 1996.

[62] Engelhardt K. and Häusler G., *Acquisition of 3-D Data by Focus Sensing*, Applied Optics, vol. 27, no. 22, pp. 4684, 1988.

[63] Engelhardt K., *Acquisition of 3-D Data by Focus Sensing utilizing the Moiré Effect of CCD Cameras*, Applied Optics, vol. 30, no. 11, pp. 1401, 1991.

[64] Kozera R., *A Note on Existence and Uniqueness in Shape-from-Shading*, Proceedings of 4th International Conference on Computer Vision, pp. 507-511, Berlin, Germany, 1993.

[65] Kozera R., *Shape-from-Shading from Photometric Stereo*, Proceedings of Asian Conference on Computer Vision, pp. 802-805, Osaka, Japan, 1993.

[66] Rioux M., *Laser Range Finder based on Synchronised Scanners*, Applied Optics, vol. 23, no. 21, pp. 3837-3843, 1984.

[67] de Bakker M., Verbeek P. W. and Steenvoorden G. K., *Smart PSD Array for Sheet-of-Light Range Imaging*, Proceedings of SPIE, vol. 3965, pp. 21-32, May 2000.

[68] Gaertner H., Lehle P., Tiziani H. J. and Voland C., *Structured Light Measurement by Double Scan Technique*, Proceedings of SPIE, Vision Systems: Sensors, Sensor Systems and Components, vol. 2784, pp. 21-30, August 1996.

[69] Harthong J., Becker A., *Inverse Moiré*, Proceedings of SPIE, Optical Inspection and Micromeasurements II, vol. 3098, pp. 2-9, September 1997.

[70] Altschuler M. D., Altschuler B. R. and Taboda J., *Laser Electro-Optic System for Rapid 3-D Topographic Mapping of Surfaces*, Optical Engineering, vol. 20, no. 6, pp. 953-961, December 1981.

[71] Sato K. and Inokuchi S., *Three-Dimensional Surface Measurement by Space Encoding Range Imaging*, Journal of Robotic Systems, vol. 2, no. 1, pp. 27-39, 1985.

[72] Reichmann W., *Fast Object Recording by means of Structured Light and Photogrammetric Techniques*, Proceedings of IAPRS, vol. 30, pp. 195-200, 1995.

[73] Srinivasan V., Liu H. C. and Halioua M., *Automated Phase-Measuring Profilometry: A Phase Mapping Approach*, Applied Optics, vol. 24, no. 2, pp. 185-188, 1985.

[74] Fang Q. and Zheng S., *Linearly Coded Profilometry*, Applied Optics, vol. 36, no. 11, pp. 2401-2407, 1997.

[75] Wolff L. B., *Relative Brightness of Specular and Diffuse Reflection*, Optical Engineering, vol. 33, no. 1, pp. 285-293, January 1994.

[76] Maekynen A. J., Rahkonen T. E. and Kostamovaara J. T., *CMOS Binary Position-Sensitive Photodetector (PSD) Array*, Proceedings of SPIE, Sensors, Sensor Systems and Sensor Data Processing, vol. 3100, pp. 101-109, September 1997.

[77] Xu Y., Tang J. and Zhong W., *New Method of Processing the Signals of a Position-Sensitive Detector*, Proceedings of SPIE, Advanced Photonic Sensors: Technology and Applications, vol. 4220, pp. 260-263, October 2000.

[78] Harrison L. J., Reaves D. C., Vu P. and Suni P. P., *Performance of 1024-element High-Dynamic-Range CCD Detector Array*, Proceedings of SPIE, Advances in Optical Information Processing IV, vol. 1296, pp. 296-303, September 1990.

[79] Costa M. F., *Use of CCD Arrays versus PSD Detectors in an Optical Triangulation-based Microtopographer*, Proceedings of SPIE, Optical Inspection and Micromeasurements, vol. 2782, pp. 79-86, September 1996.

[80] Häusler G. and Herrmann J., *Physical Limits of 3-D Sensing*, Proceedings of SPIE, Optics, Illumination and Image Sensing for Machine Vision VII, vol. 1822, pp. 150-158, March 1993.

[81] Häusler G., *Three-Dimensional Sensors – Potentials and Limitations*, Handbook of Computer Vision and Applications, Academic Press, vol. 1, no. 19, pp. 485-506, 1999.

[82] Dorsch R., Herrmann J. and Häusler G., *Laser Triangulation: Fundamental Uncertainty of Distance Measurement*, Applied Optics, vol. 33, no. 7, pp. 1306-1314, 1994.

[83] Amann M. C., Bosch T. M., et al., *Laser Ranging: A Critical Review of Unusual Techniques for Distance Measurement*, Optical Engineering, vol. 40, no. 1, January 2001.

[84] Toubin M., Laligant O., et al., *Multiscale Analysis for the Characterization of 3-D Objects*, Proceedings of SPIE, Intelligent Robots and Computer Vision XVII: Algorithms, Techniques and Active Vision, vol. 3522, pp. 414-423, October 1998.

[85] Karbacher S. and Haeusler G., *New Approach for the Modeling and Smoothing of Scattered 3-D Data*, Proceedings of SPIE, Three-Dimensional Image Capture and Applications, vol. 3313, pp. 168-177, March 1998.

[86] Shu C. and Xi F., *Model-based Scanning Path Generation for Inspection*, Proceedings of Second International Conference on 3-D Digital Imaging and Modeling (3DIM '99), pp. 118-124, Ottawa, Canada, October 1999.

[87] Derived from verbal discussion with Dr. Rainer Sacchi, 2000.

[88] Sacchi R., Poliakoff J. F. and Thomas P. D., *Curvature Estimation for Segmentation of Triangulated Surfaces*, Proceedings of Second International Conference on 3-D Digital Imaging and Modeling (3DIM '99), pp. 536-543, Ottawa, Canada, October 1999.

[89] Sacchi R., Poliakoff J. F., Thomas P. D. and Häfele K. H., *Improved Extraction of Planar Segments for Scanned Surfaces*, Proceedings of IEEE International Conference on Information Visualization, pp. 325-330, London, UK, July 2000.

Appendices

Appendix A – Specification of Sensors

Listed in the table below is the specification for single-perspective point sensors (model ANR1115 and ANR1182) and circular-perspective point sensor (model OTM3-20), which were employed in this research. Most of the examples of range images collected were from model ANR1182.

model	ANR1115	ANR1182	OTM3-20
laser class	1		2
measurable range	130 ± 50mm	80 ± 20mm	60 ± 10mm
scanning range	100mm	40mm	20mm
beam dimension	0.7 x 1.4mm	0.7 x 1.2mm	0.15 - 0.2mm
response frequency	10/100/1000Hz		1000Hz
resolution	100/330/1000μm	20/65/200μm	10μm
laser wavelength	685nm		680nm
protective construction	IP67		IP40
pulse duration	15μs		5μs
maximum laser output	0.4mW		< 4mW
size	60 x 60 x 20mm		160 x 52 x 52mm
weight	300g		350g

Table A-1: Specification for optical triangulation point sensor.

Appendix B – Mathematical Formula

Listed in this appendix are mathematical equations relating to data distortions in 3-D imaging.

B.1 Extent of Occluded Region

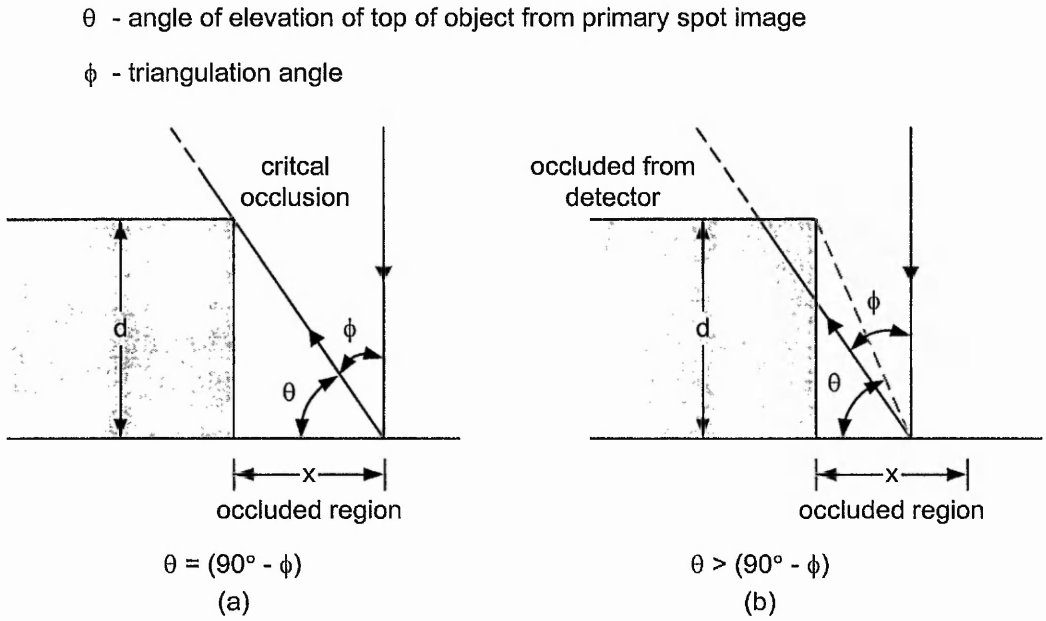

Fig. B-1: Occlusion occurs when (a) primary spot image begins to move into occluded region and when (b) inside this region.

Total occlusion of primary spot image only when $\theta > (90° - \phi)$. If the scanning is from right to left, the occluded region spans from the critical moment when occlusion occurs till the return of line-of-sight of spot image, which is at the top edge of the object and is given by $d = h \tan \phi$, where h is the vertical height of the sensor to the projected spot image on the surface. However in most circumstances, when the spot image is inside the occluded region, the detector may still be able to detect a faint trace of light reflected and dispersed near this spot image.

B.2 Primitive Formula for Triangulation Angle

It is postulated that a single laser beam contains of many paths of light. Therefore the normal distance from sensor to surface is given by $h = \frac{w}{\tan\phi_{ave}}$ where w is the width between emitter and detector of the sensor and $\phi_{ave} = \frac{\sum_{i=1}^{n}\phi_i}{n}$ is the averaged triangulation angles, ϕ_i from n paths of light.

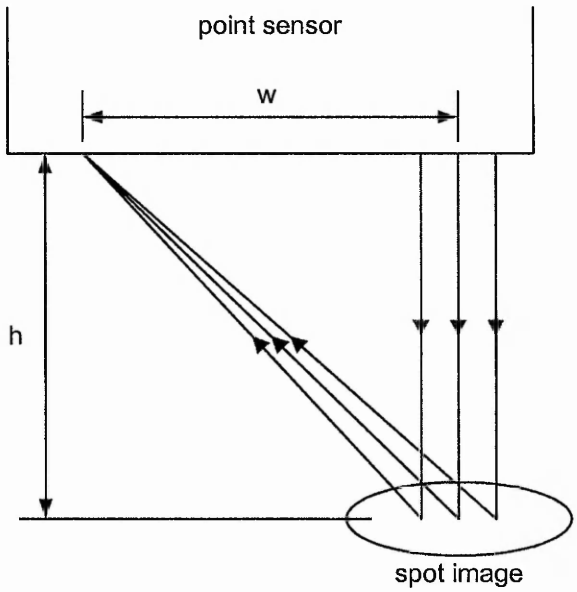

Fig. B-2: Paths of light establishing a spot image.

Appendix C – Range Images

This section is divided into three parts, all of which deal with range images. For clarity, the orientation of the sensor for each range image is indicated by a symbol, lying on the *xy* plane (see Fig. C-1).

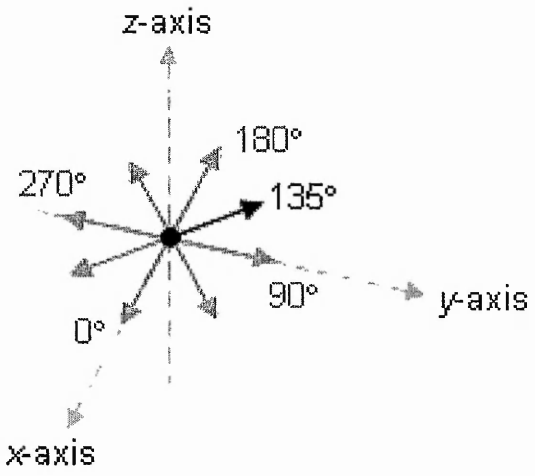

Fig. C-1: The symbol above indicates that the orientation of the sensor is 135° where the emitter is aligned on the *z*-axis. Orientations of 0° and 180° would therefore lie along the *x*-axis while that of 90° and 270° would lie along the *y*-axis.

C.1 Variation of Distortions with Different Orientations of Sensor

To establish the incidence of significant distortions for different orientations of a sensor relative to a vertical face, several range images were captured using a square block with sharp corners (see Fig. C-14). The object and the surface on which it lies were treated with a non-permanent coating, providing a homogenous high diffusely reflective surface for scanning. Three different orientations of the block relative to the *x*-axis were chosen: 10°, 22.5° and 30°. With the vertical face of the block at each of these angles, it was scanned using two different orientations of the sensor, 0° and 180°. Horizontal separations along *x* and *y* axes are 0.2mm and 0.5mm respectively. The layout of the experiment is shown in Fig. C-2.

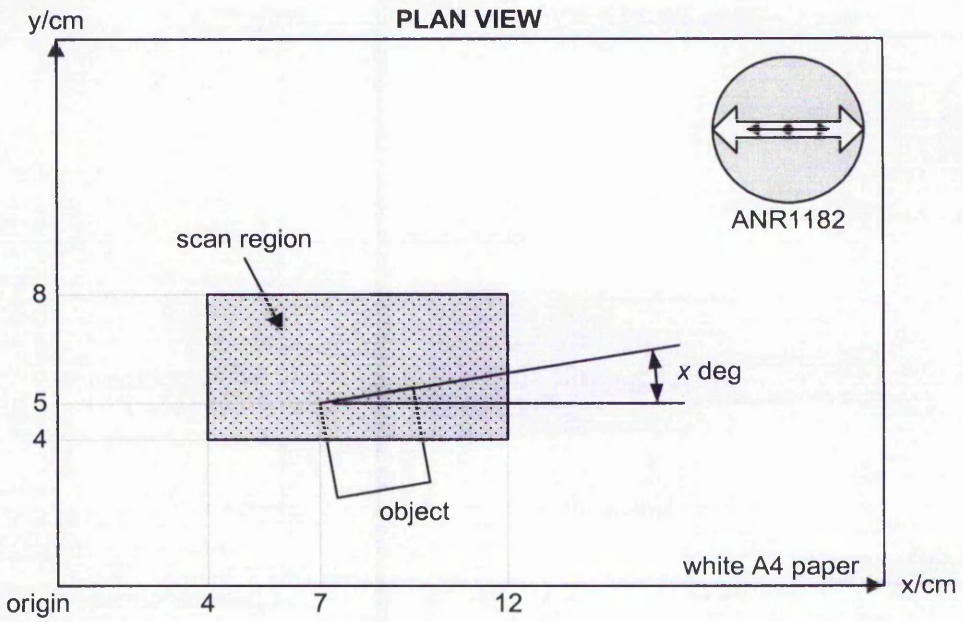

Fig. C-2: Experiment layout for analysis of significant distortions based on different orientations of vertical face relative to sensor.

The scanning results are presented in the following diagrams.

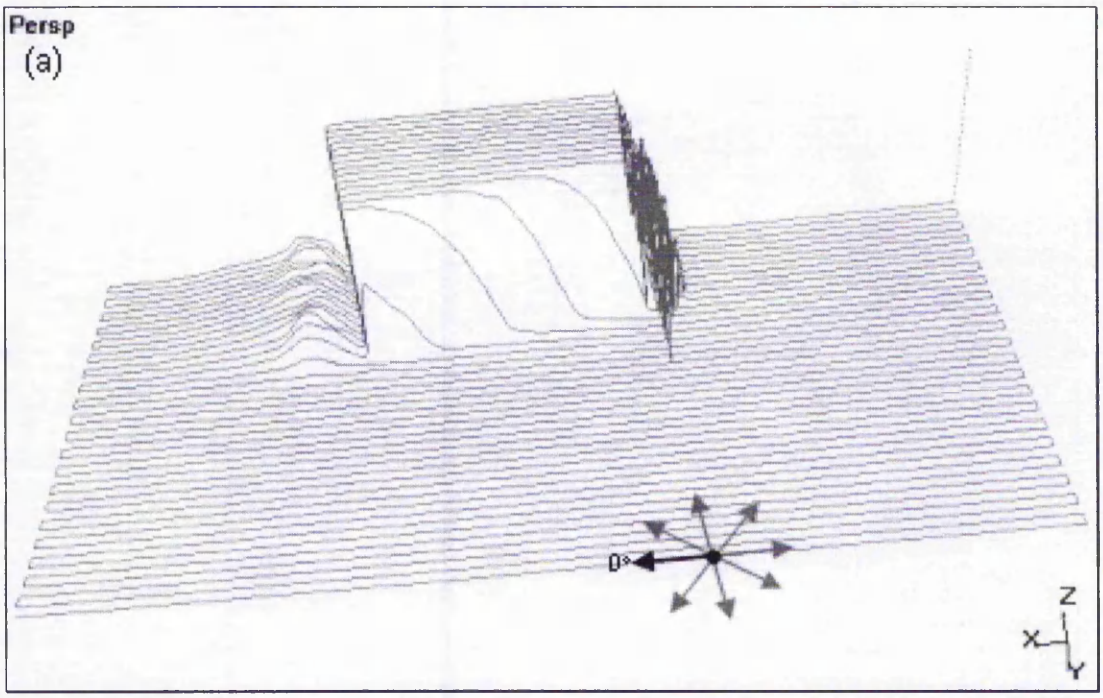

Fig. C-3: Incidence of bow waves and occlusion spikes near vertical faces when sensor is oriented at 0° while block is angled at (a) 10° ((b) and (c) on following page).

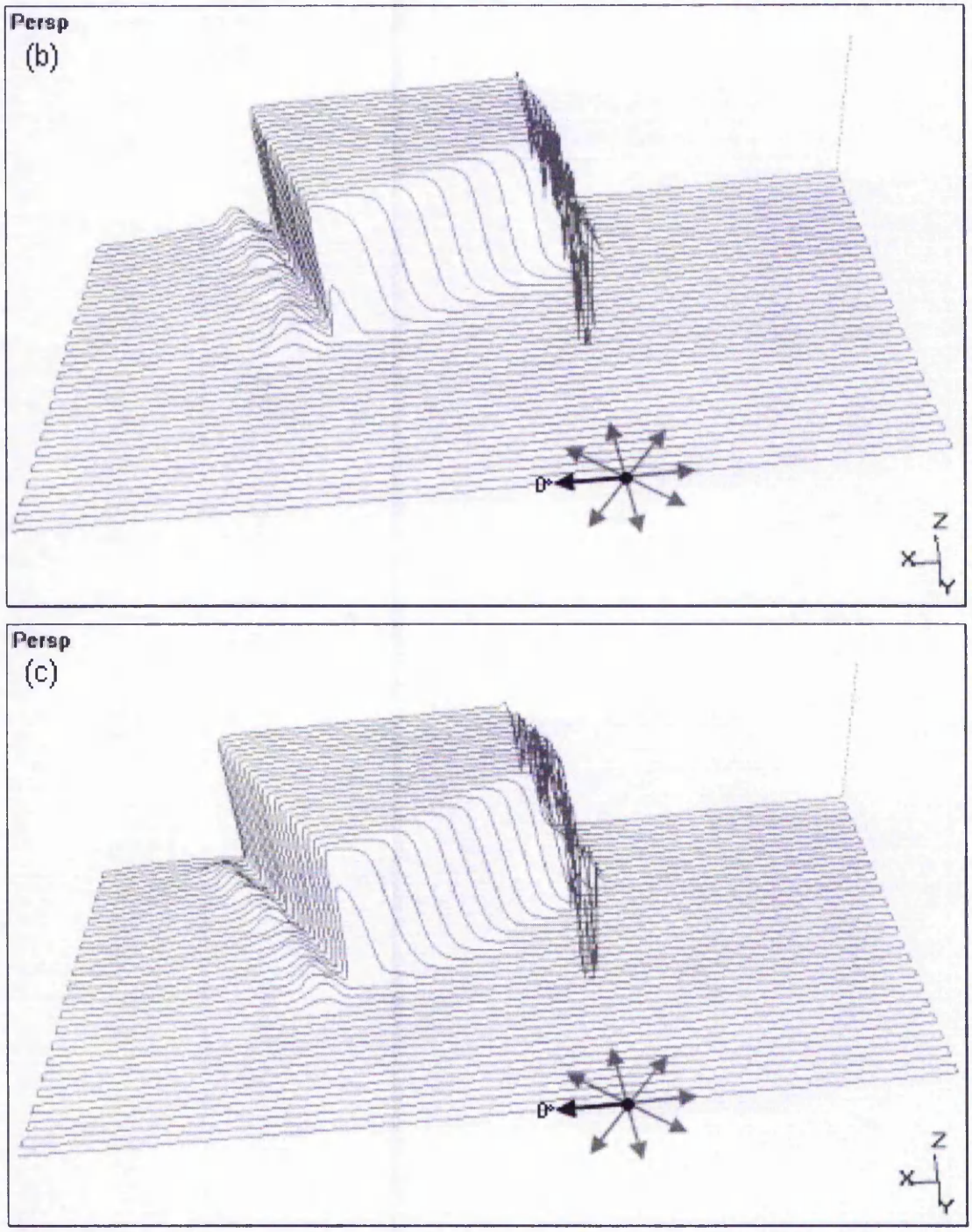

Fig. C-3: Incidence of bow waves and occlusion spikes near vertical faces when sensor is oriented at 0° while block is angled at (b) 22.5° and (c) 30°.

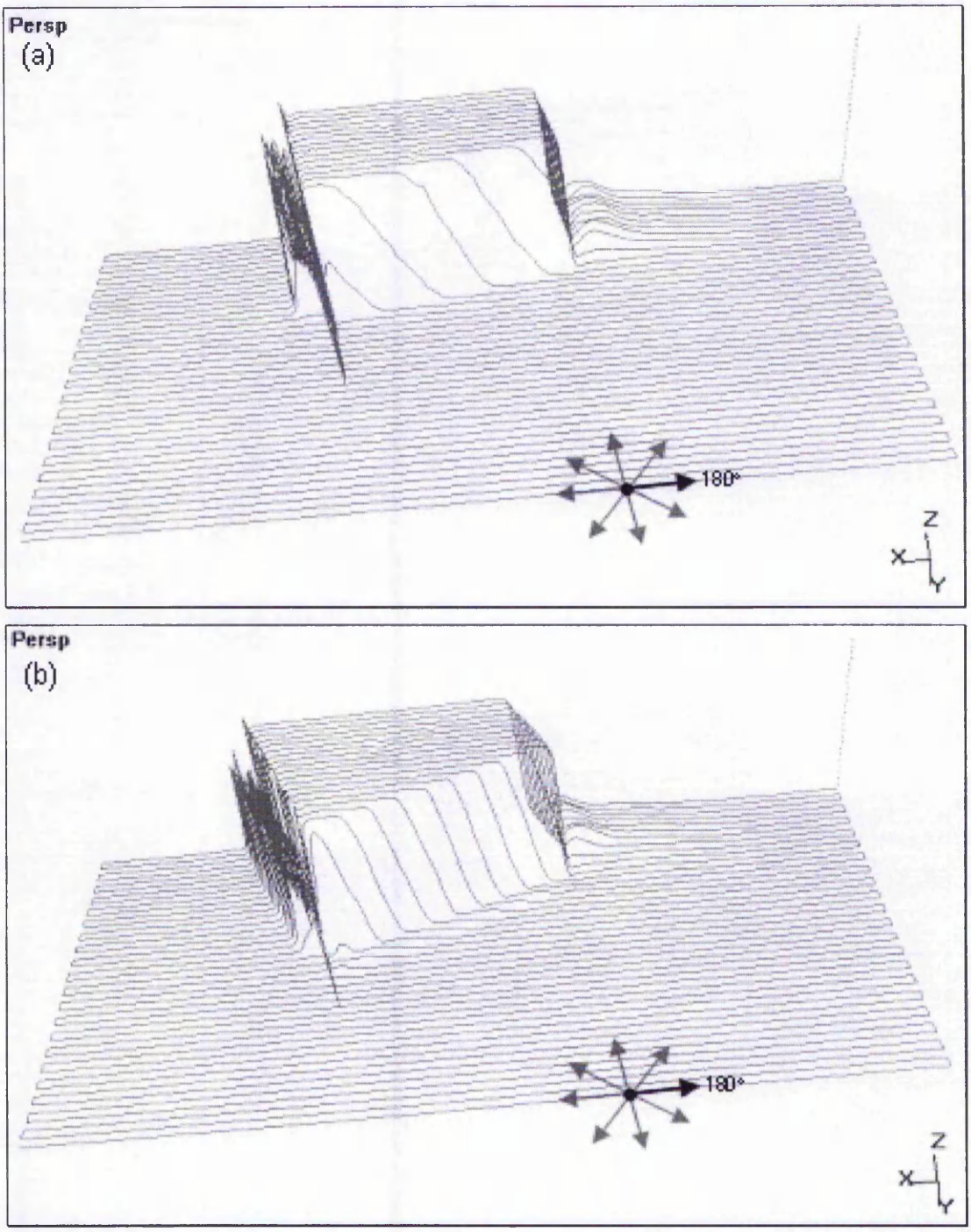

Fig. C-4: Incidence of bow waves and occlusion spikes near vertical faces when sensor is oriented at 180° while block is angled at (a) 10°, (b) 22.5° ((c) on following page).

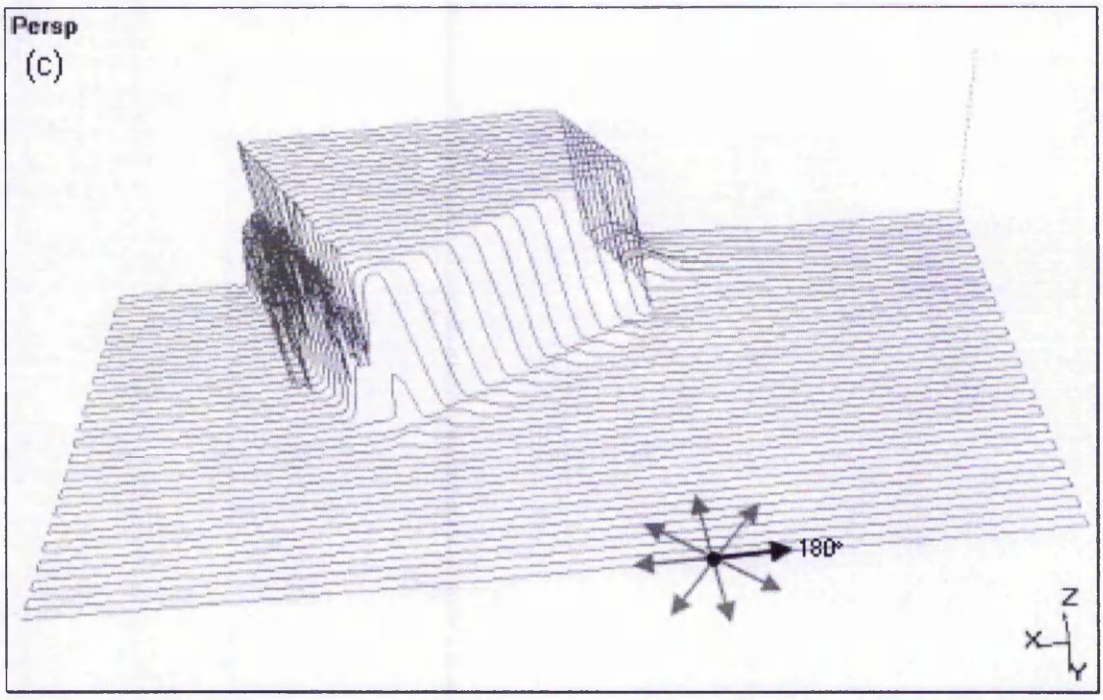

Fig. C-4: Incidence of bow waves and occlusion spikes near vertical faces when sensor is oriented at 180° while block is angled at (c) 30°.

C.2 Compensation for Noise in Range Images

To illustrate the results of compensation for noise (see Section 4.1 of Chapter 4), the range image of a slightly tilted inverted saucer was used. The diameter of the saucer is 153mm and height is 28mm. Horizontal separations of points along x and y axes are 3.0mm and 0.6mm respectively.

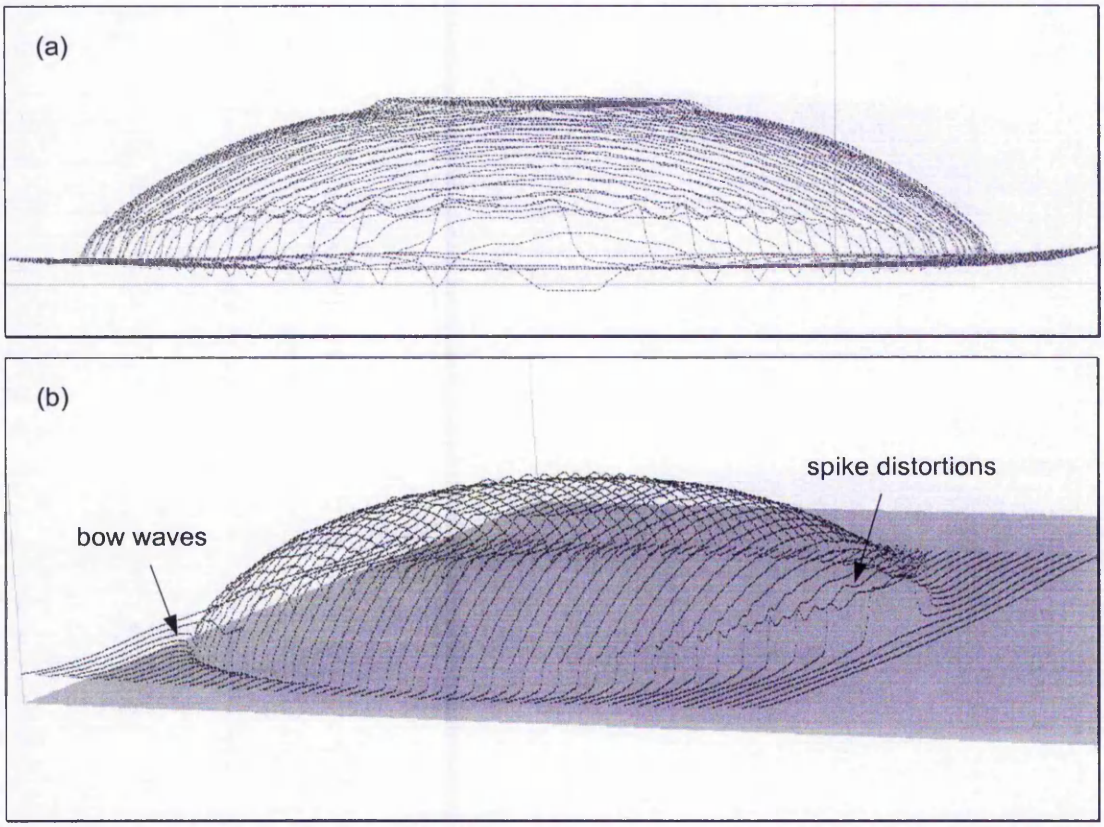

Fig. C-5: Original range image of a saucer with (a) view from front and (b) perspective view from left side before compensation with noise calculated at approximately 0.41mm variation. Note the existence of bow waves and spike distortions.

Both bow waves and spike distortions are present here. It is expected that in normal circumstances, these will be compensated before compensation for noise is performed.

Execution of first phase (smoothing of scanlines) employed simple averaging with one point on each side of the FP. Thereafter the points were reorganized, producing an equally spaced range image.

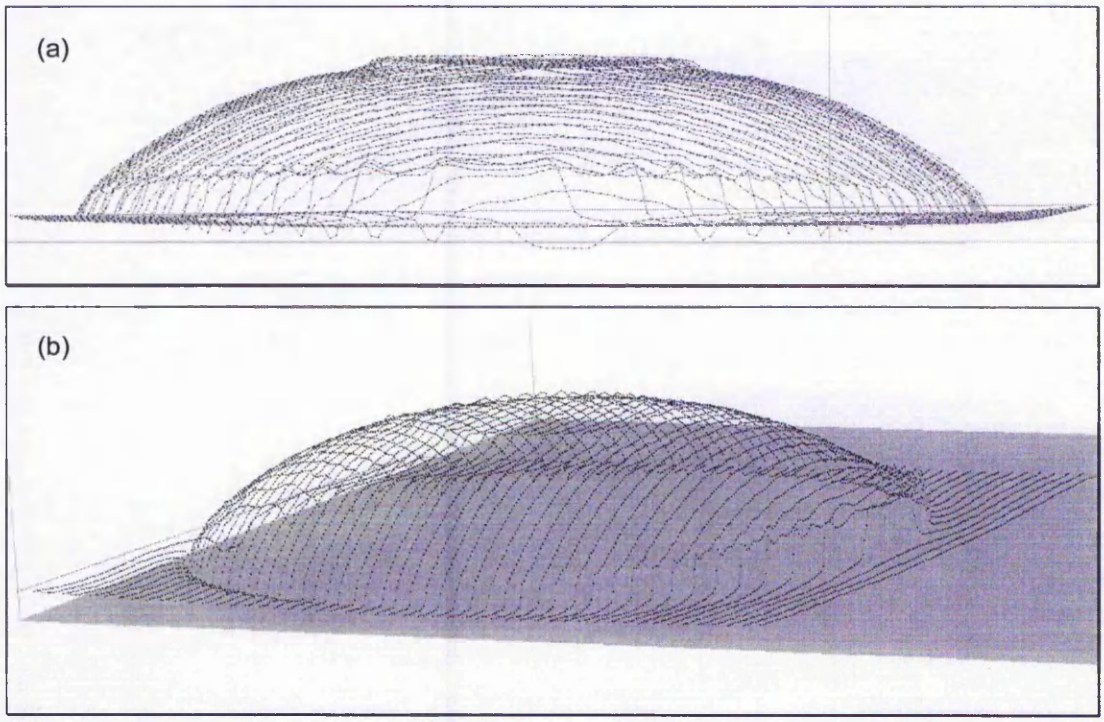

Fig. C-6: Processed range image of saucer from Fig. C-5 after smoothing of scanlines using simple averaging (first phase) and reorganization of points (second phase) with (a) view from front and (b) perspective view from left side.

Fig. C-7 and Fig. C-8 show outputs for 5-point and 9-point grid smoothing. Notice, especially when comparing Fig. C-7(a) and Fig. C-8(a) near the top-right side of the saucer, the latter produces a smoother output. When employing the compensation for noise algorithms, the base of the saucer (now at the top of the range images) has not been flattened out. This is imperative in ensuring small details are retained. Also significant distortions such as bow waves and spikes have been somewhat smoothed but they still exist in the compensated range images. By reducing their magnitudes during smoothing, they will be more difficult to identify when employing compensation based on edge detection. Therefore it is always recommended that significant distortions be removed prior to any smoothing.

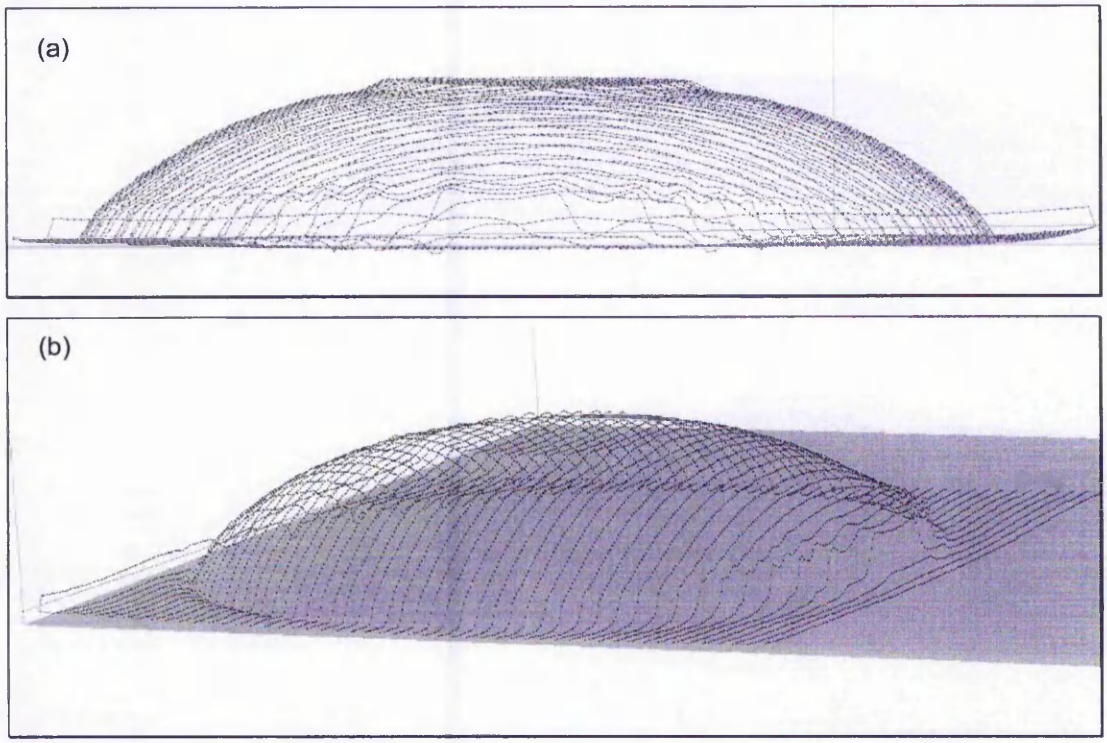

Fig. C-7: Processed range image of saucer from Fig. C-5 with 5-point 3×3 grid smoothing.

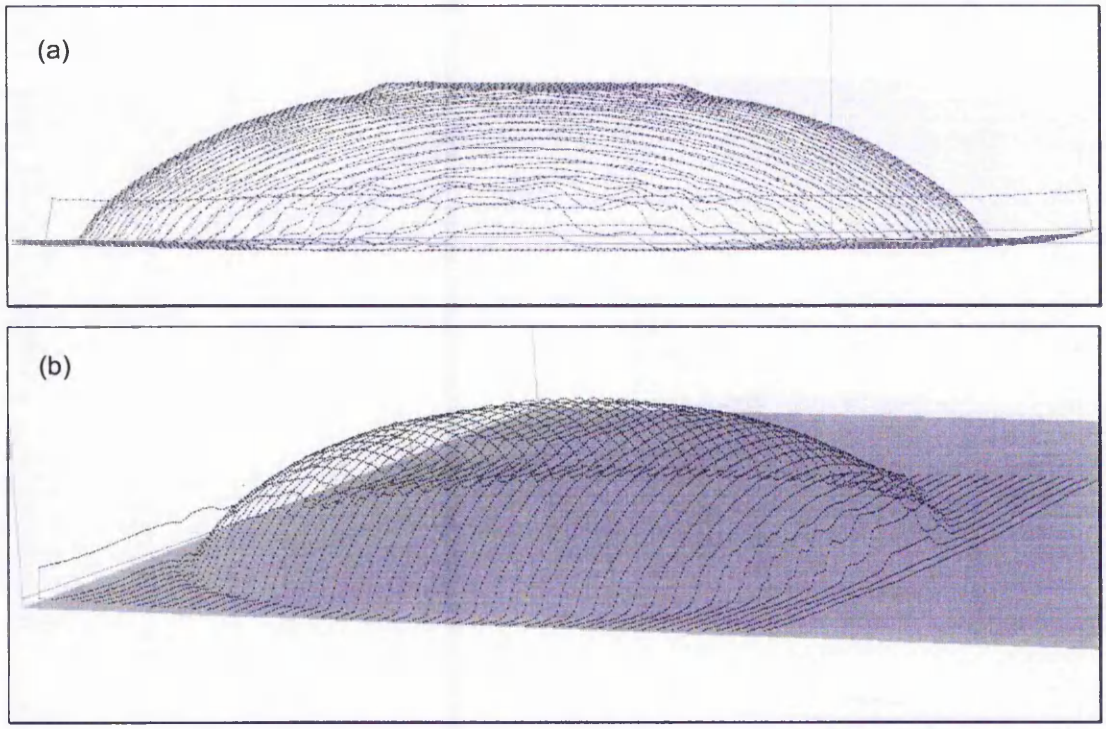

Fig. C-8: Processed range image of saucer from Fig. C-5 with 9-point 3×3 grid smoothing.

C.3 Multiple Range Images and their Compensations

Several selected objects were scanned with different orientations of the sensor (model ANR1182) and their multiple range images were used in the compensation process. Each object and the surface on which it lies were treated with a non-permanent coating to provide a homogenous high diffusely reflective surface for scanning. This section illustrates all these objects and their range images. The dimensions of each object are provided and prefixes are employed to denote the object's height (H), width (W), length (L) and diameter (D).

The list of objects is as follows:

1. Fig. C-9: MDF block with horizontal cross-section a square with rounded corners (height at 18mm, length at 50mm and width at 50mm).
2. Fig. C-14: Rectangular block with sharper corners.
3. Fig. C-19: Block with square horizontal cross-section and 5mm-diameter cylindrical hole in the centre (sides not quite vertical).
4. Fig. C-24: Stacked cylindrical camera caps.
5. Fig. C-29: Technical object (height at 27mm and diameter of base at 54mm).
6. Fig. C-34: Double peaks and square object.
7. Fig. C-39: Tile object (height at 16mm).

Prior to any scanning, the horizontal separations for all of the above objects were set to 0.5mm in both x and y directions. The restructuring process for the range images adhered to this separation as well.

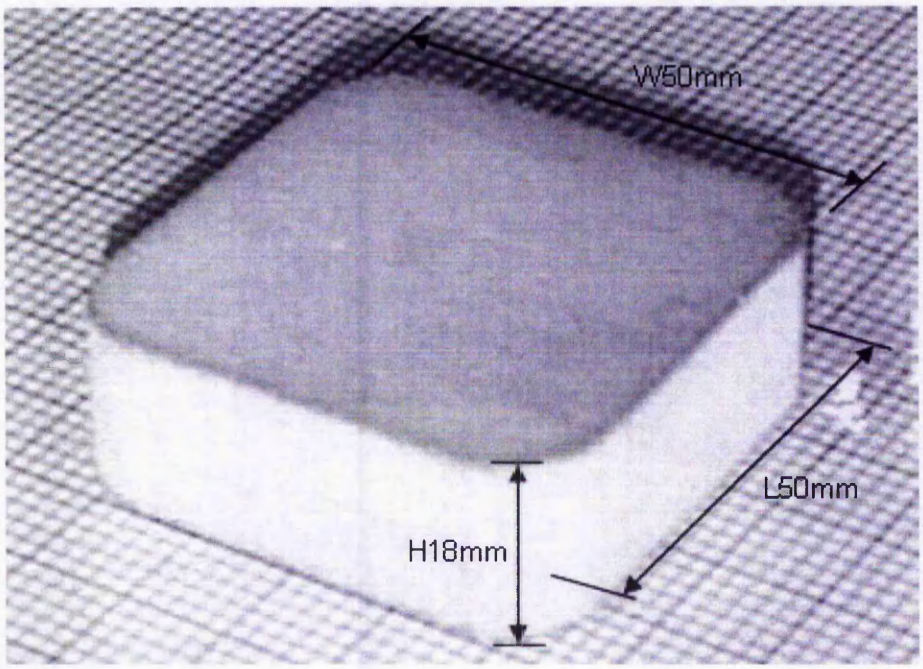

Fig. C-9: MDF block with horizontal cross-section a square with rounded corners (height at 18mm, length at 50mm and width at 50mm).

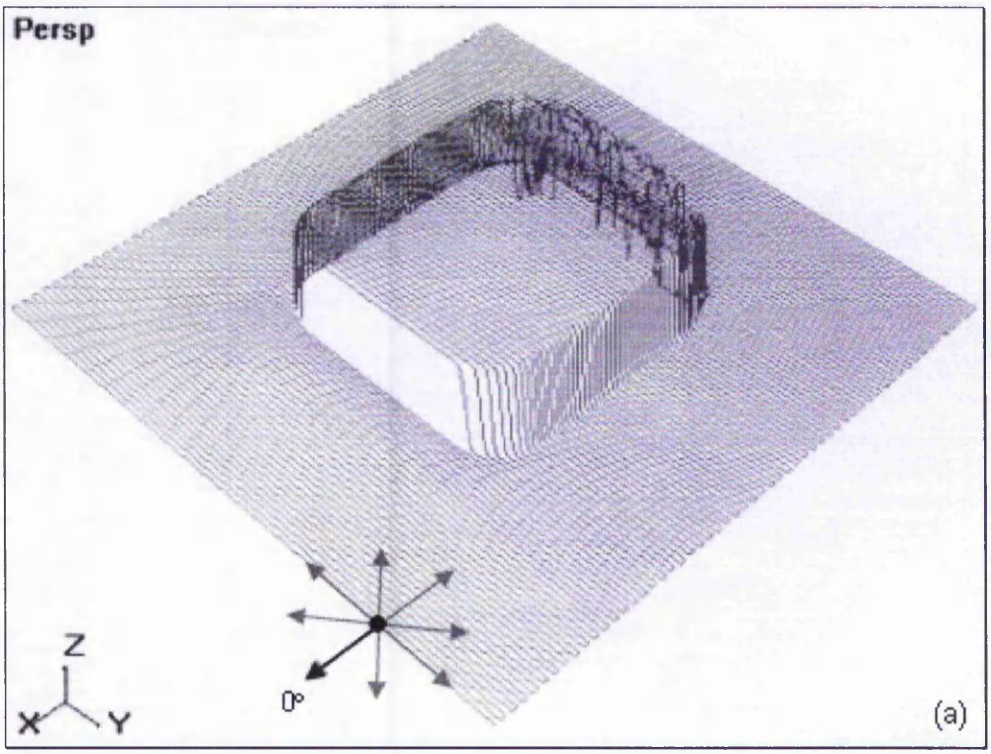

Fig. C-10: Range image of Fig. C-9 with orientation of sensor at (a) 0° ((b)-(h) on following pages).

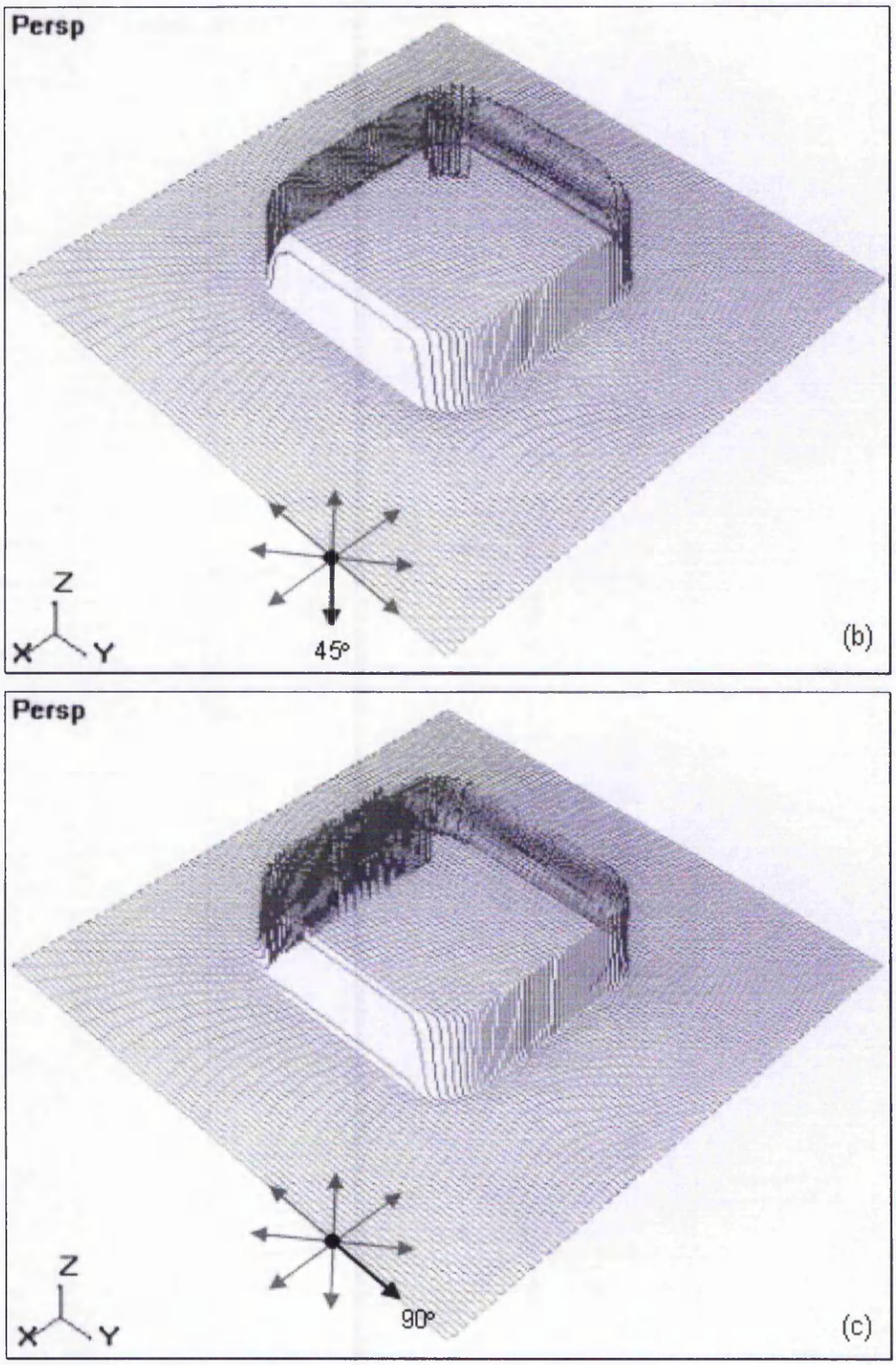

Fig. C-10: Range images of Fig. C-9 with orientations of sensor at (b) 45° and (c) 90° ((d)-(h) on following pages).

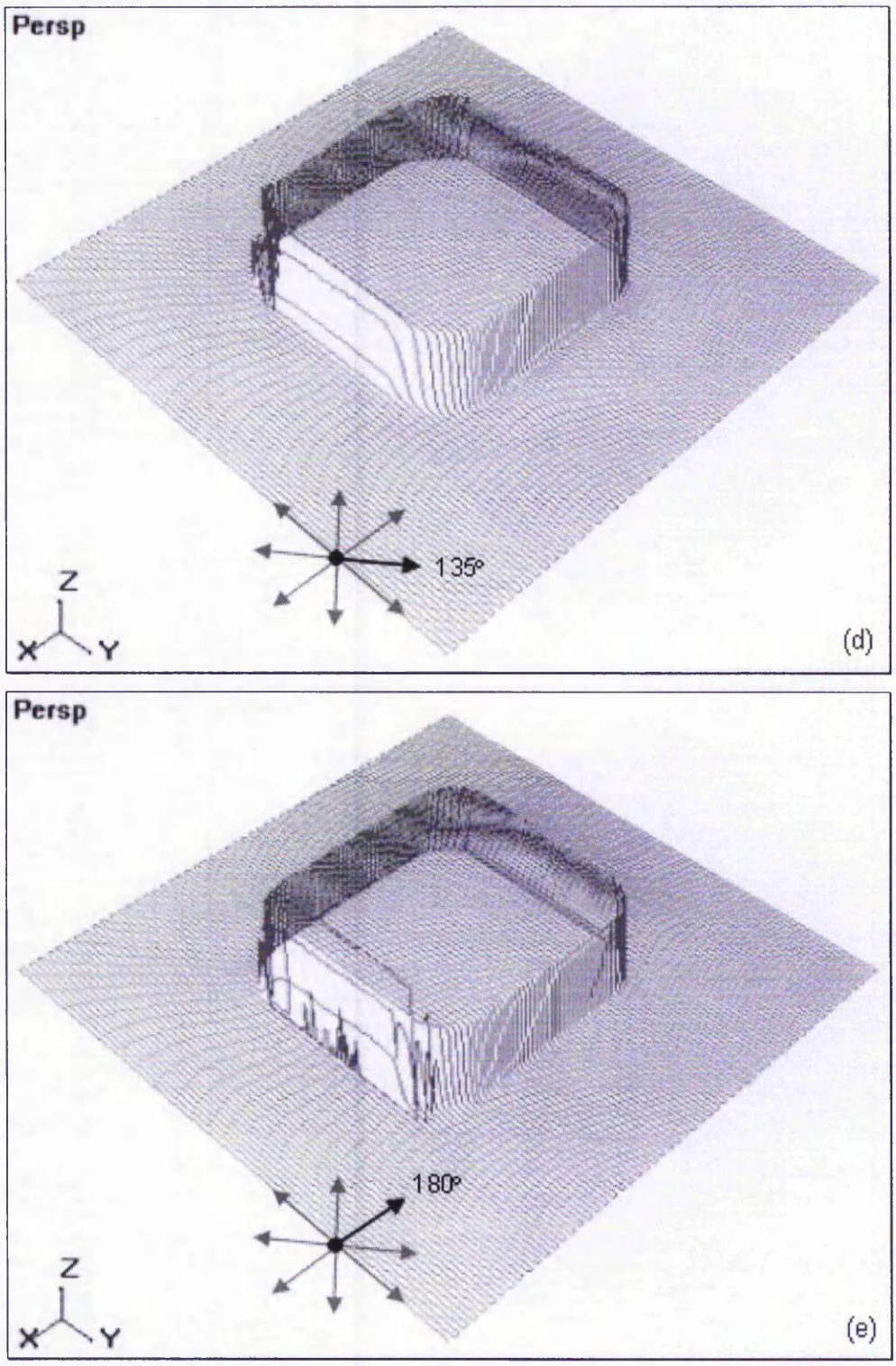

Fig. C-10: Range images of Fig. C-9 with orientations of sensor at (d) 135° and (e) 180° ((f)-(h) on following pages).

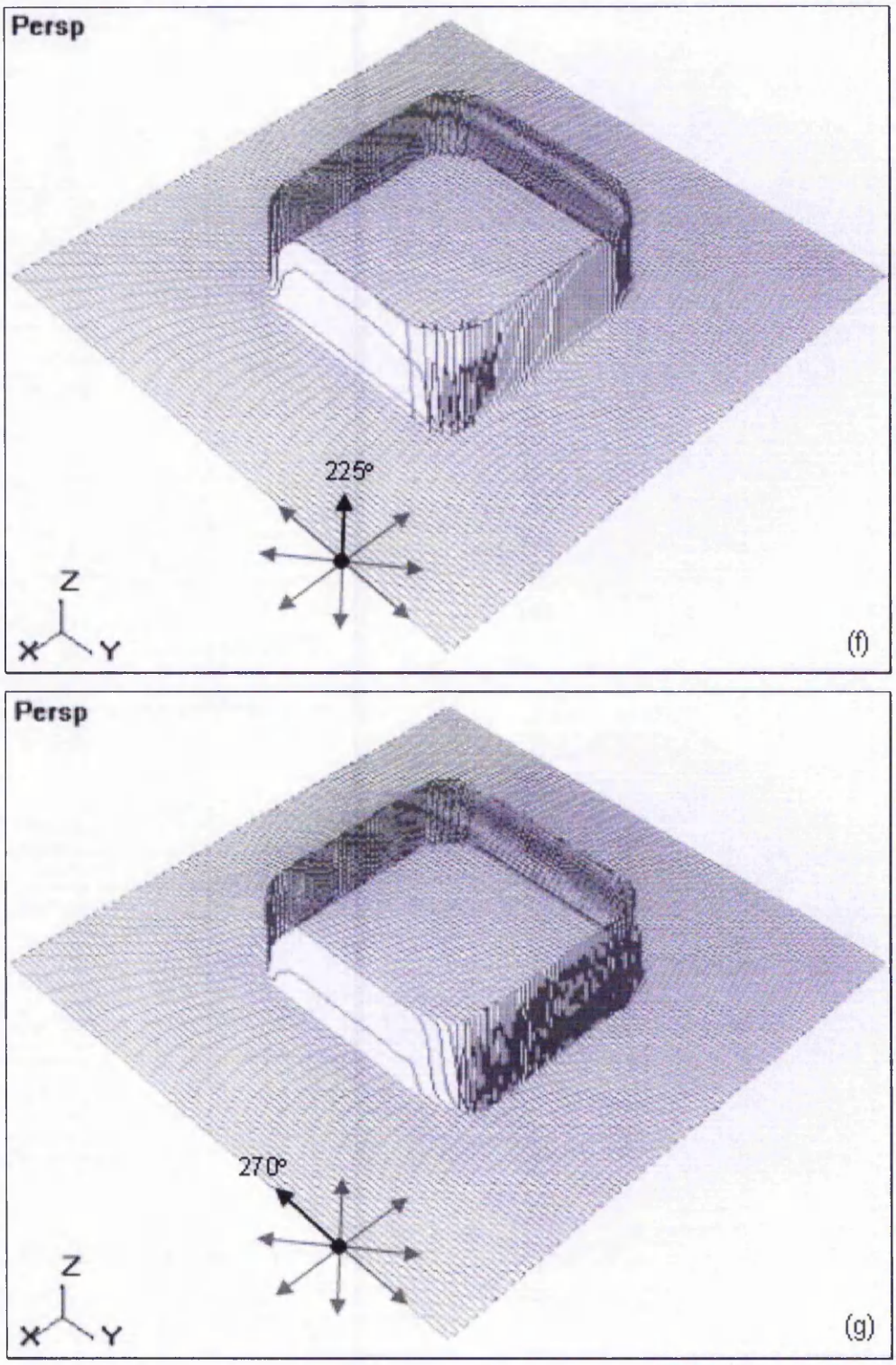

Fig. C-10: Range images of Fig. C-9 with orientations of sensor at (f) 225° and (g) 270° ((h) on following page).

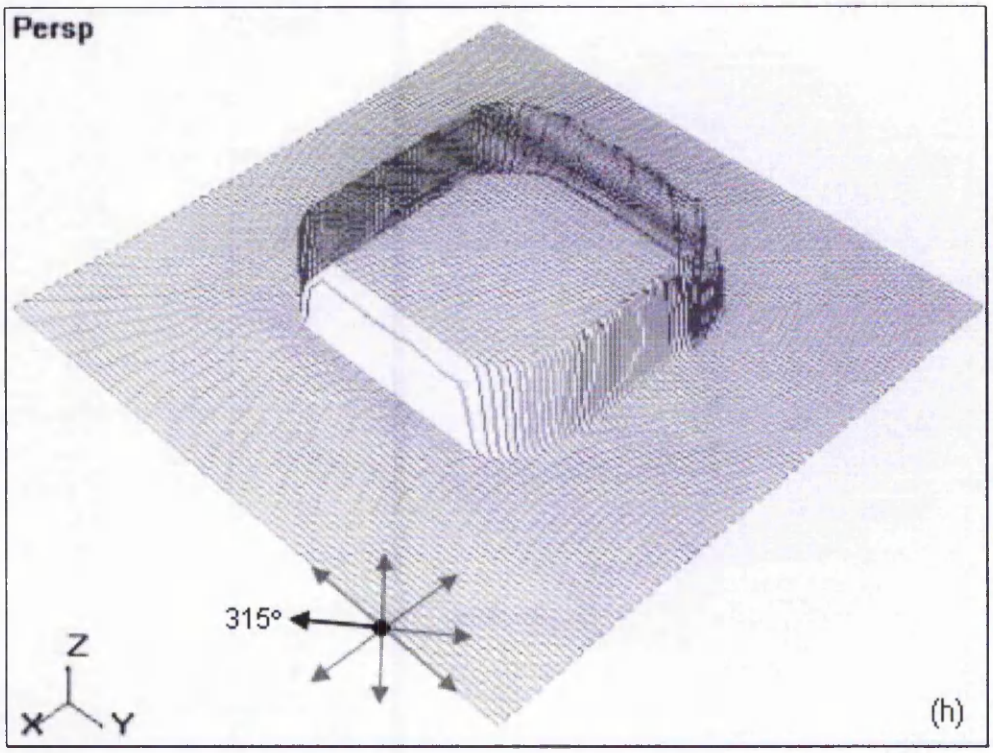

Fig. C-10: Range image of Fig. C-9 with orientation of sensor at (h) 315°.

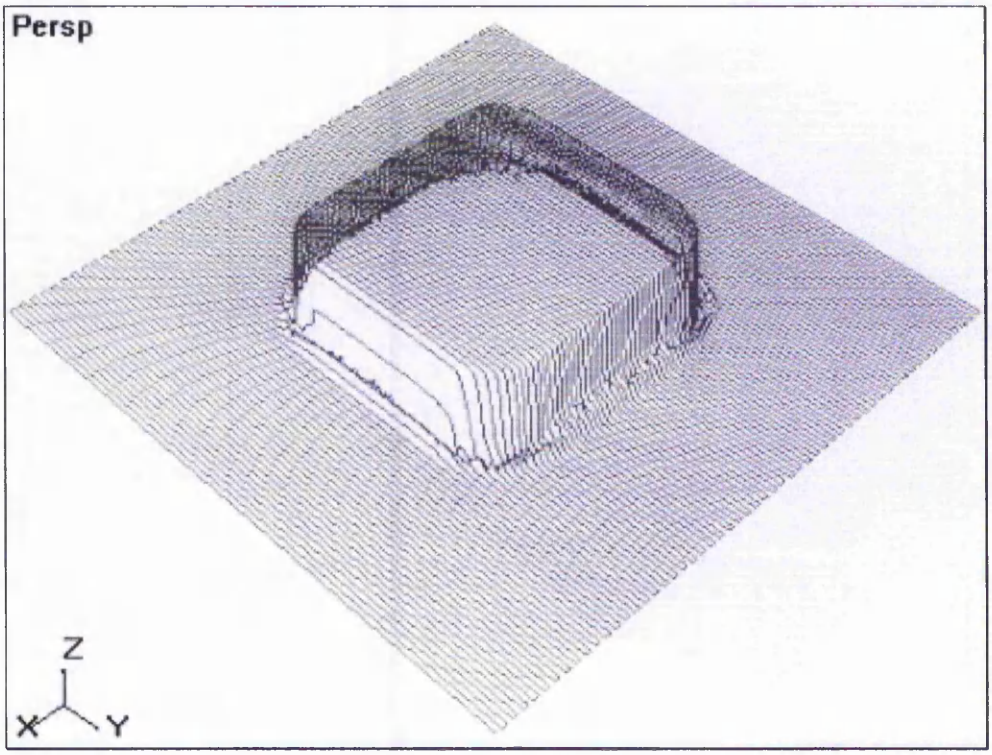

Fig. C-11: Averaging of eight range images of Fig. C-9.

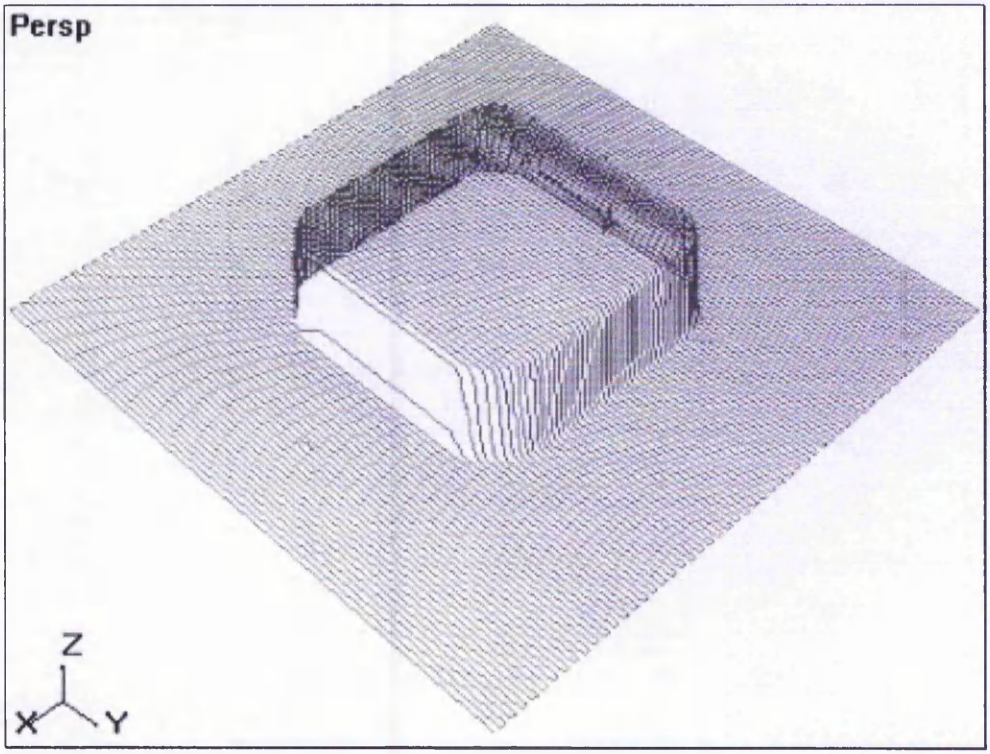

Fig. C-12: Selection of lowest *z*-values from multiple range images of Fig. C-9.

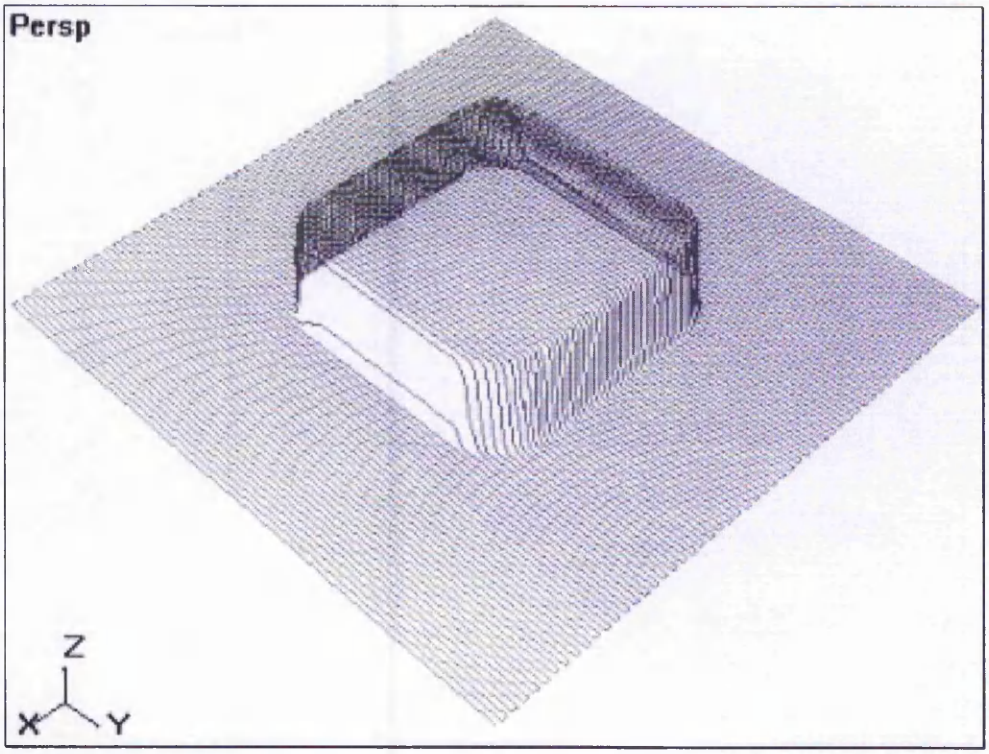

Fig. C-13: Compensated range image of Fig. C-9 based on edge detection algorithms.

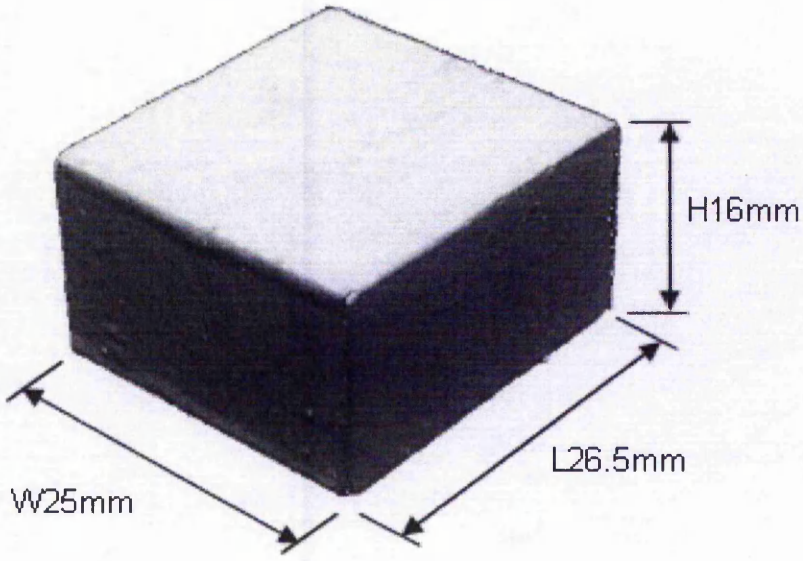

Fig. C-14: Rectangular block with sharper corners.

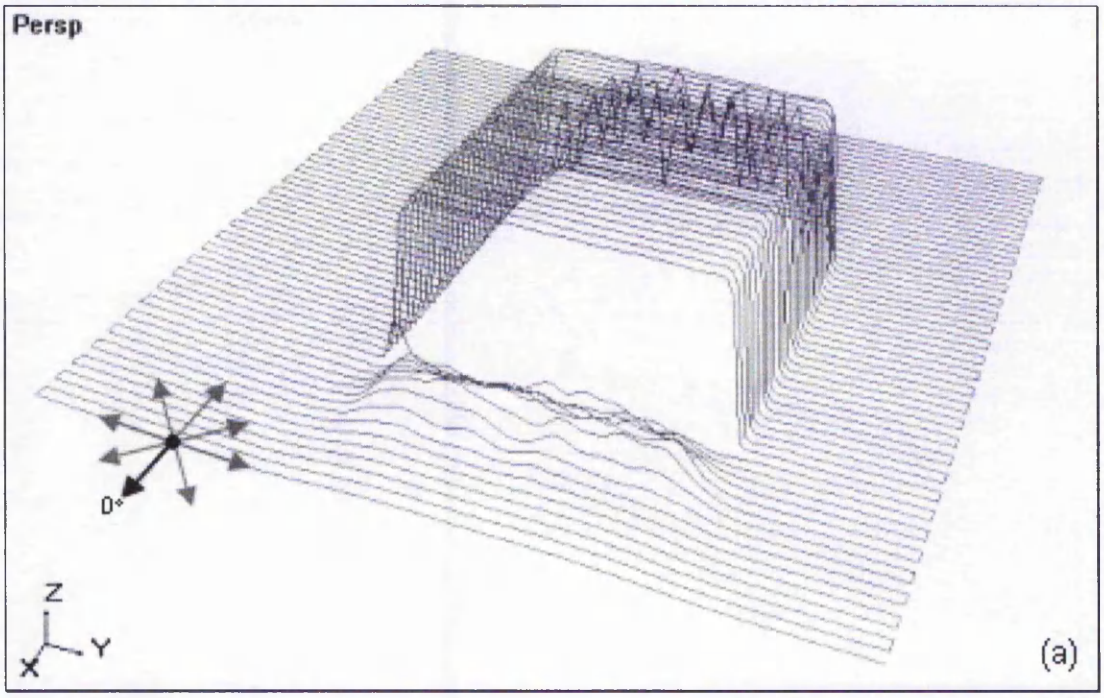

Fig. C-15: Range image of Fig. C-14 with orientation of sensor at (a) 0° ((b)-(h) on following pages).

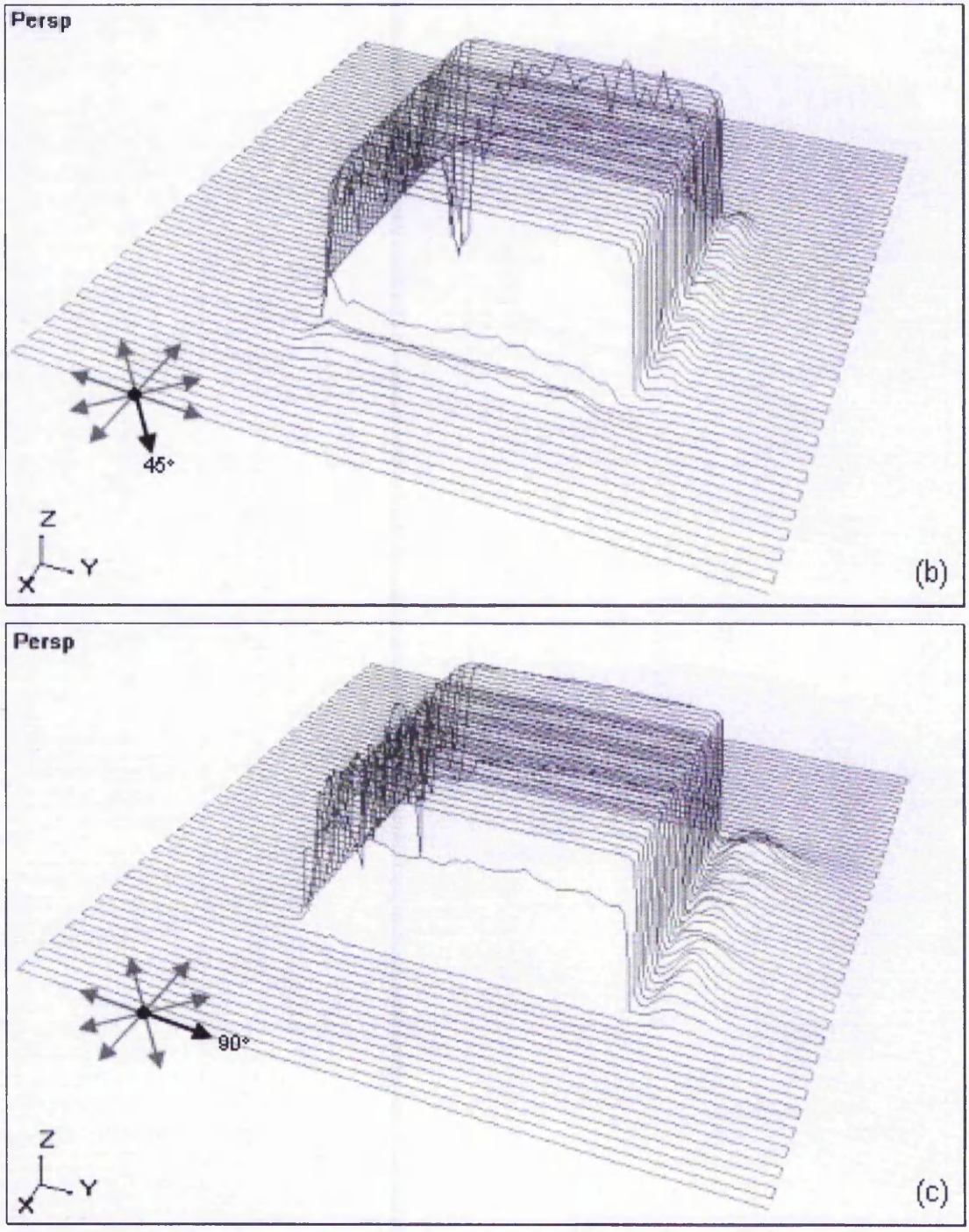

Fig. C-15: Range images of Fig. C-14 with orientations of sensor at (b) 45° and (c) 90° ((d)-(h) on following pages).

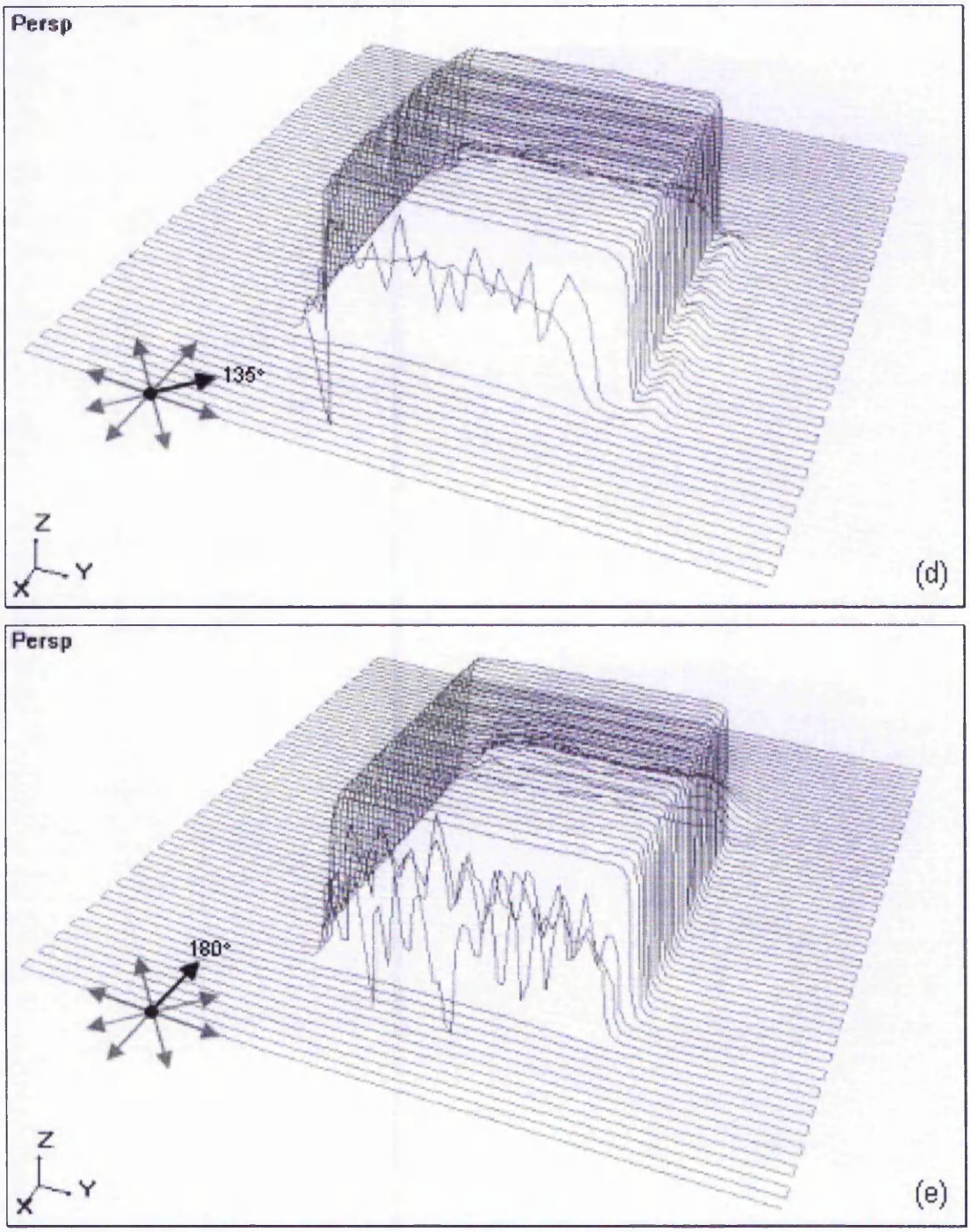

Fig. C-15: Range images of Fig. C-14 with orientations of sensor at (d) 135° and (e) 180° ((f)-(h) on following pages).

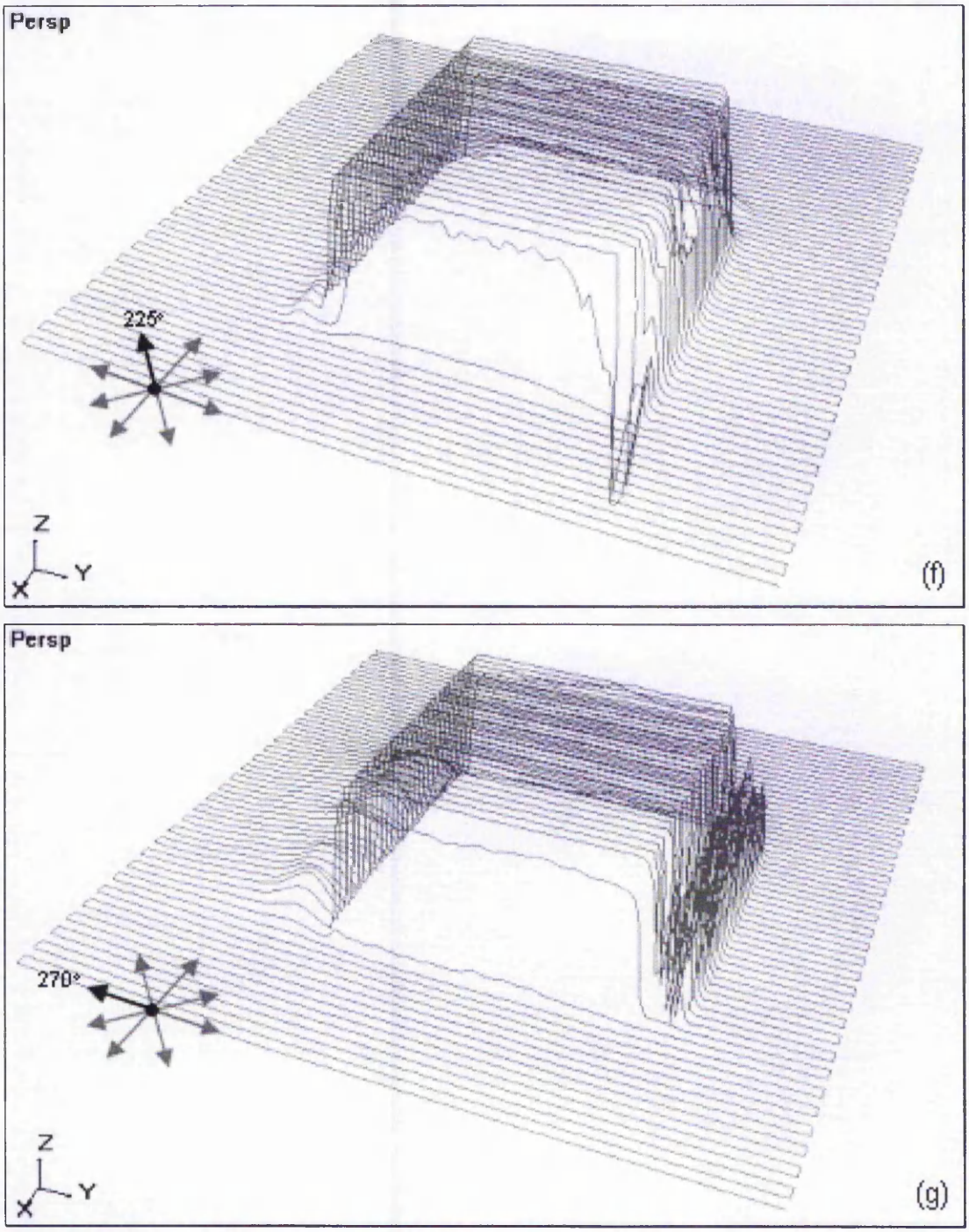

Fig. C-15: Range images of Fig. C-14 with orientations of sensor at (f) 225° and (g) 270° ((h) on following page).

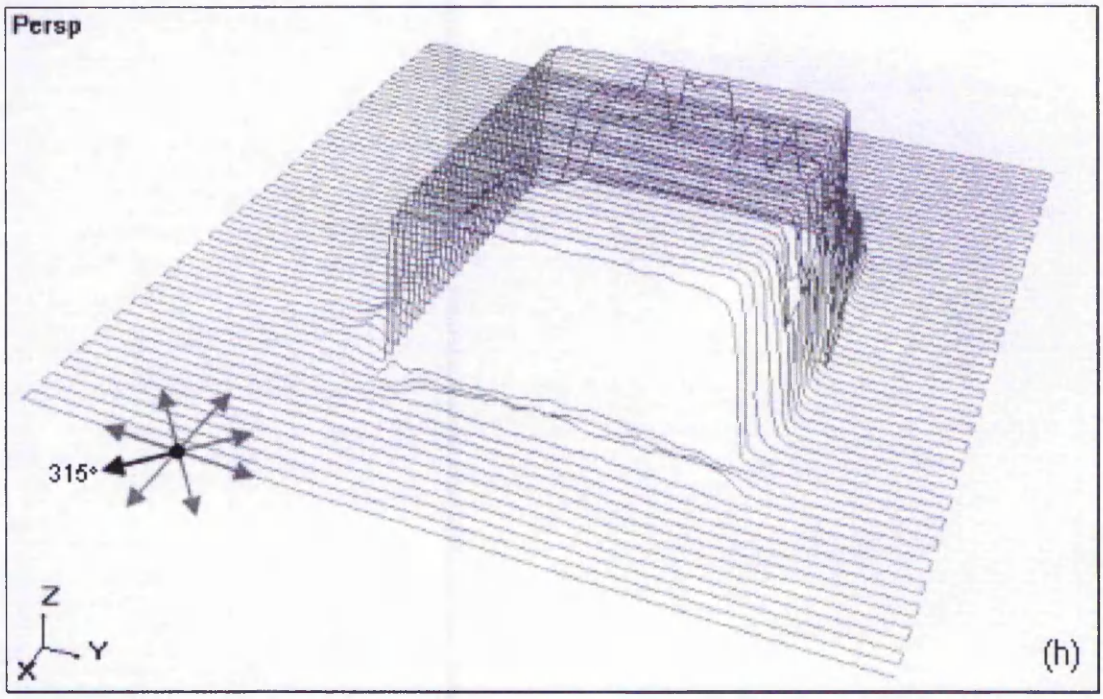

Fig. C-15: Range image of Fig. C-14 with orientation of sensor at (h) 315°.

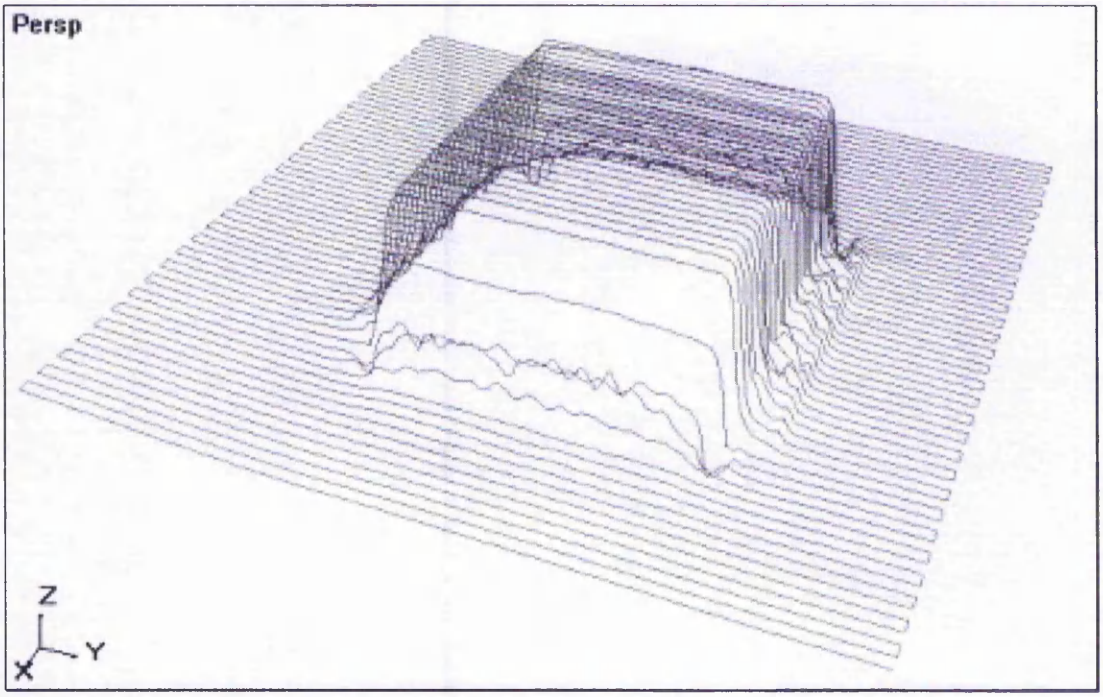

Fig. C-16: Averaging of eight range images of Fig. C-14.

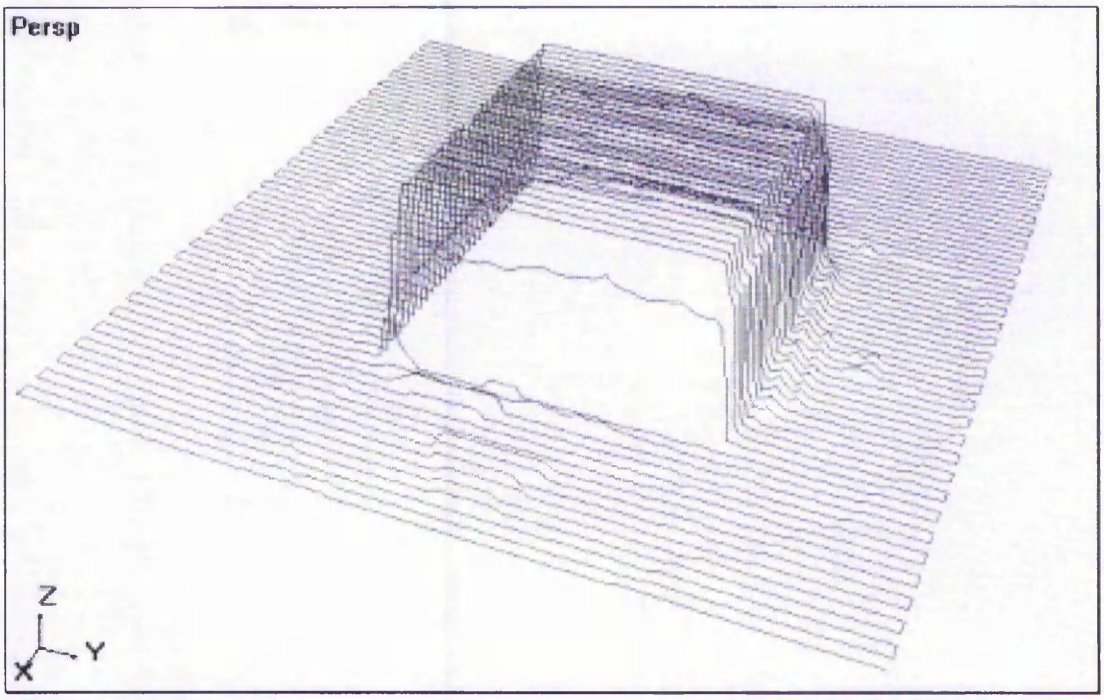

Fig. C-17: Selection of lowest *z*-values from multiple range images of Fig. C-14.

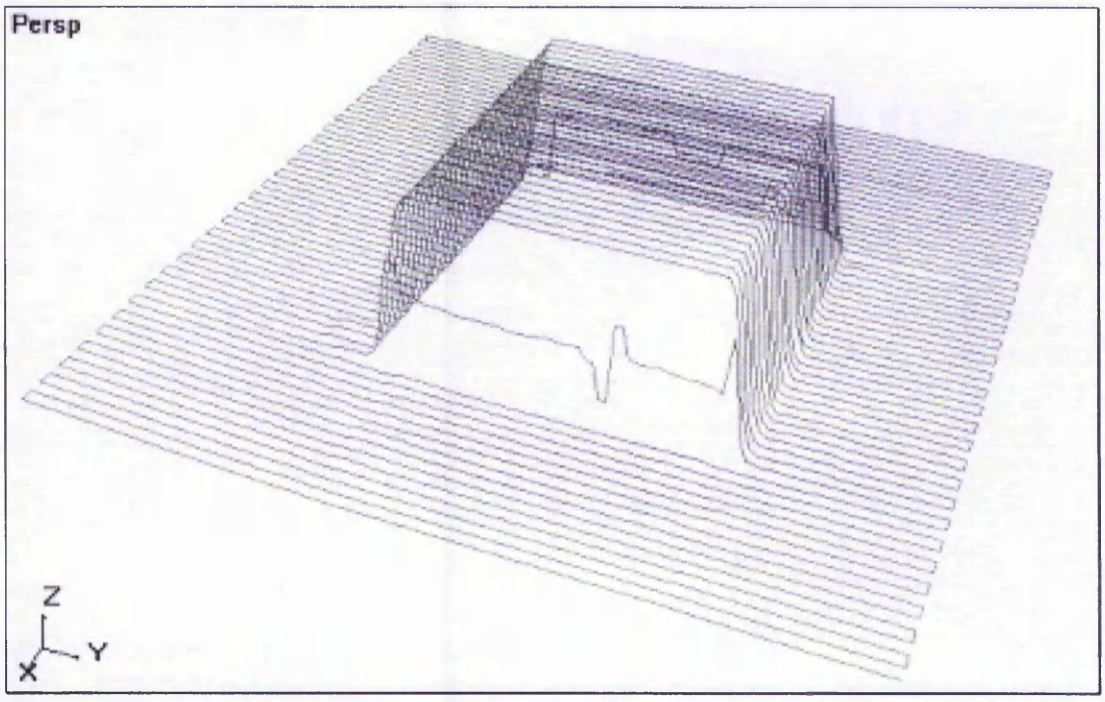

Fig. C-18: Compensated range image of Fig. C-14 based on edge detection algorithms.

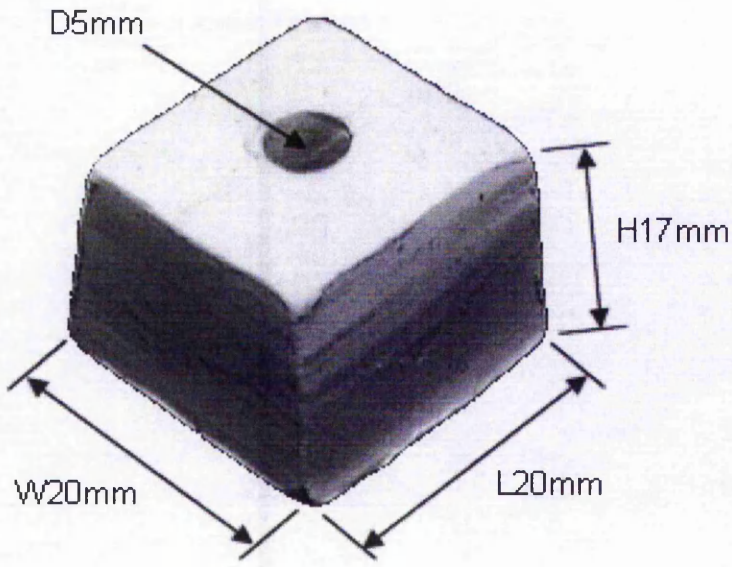

Fig. C-19: Block with square horizontal cross-section and 5mm-diameter cylindrical hole in the centre (sides not quite vertical).

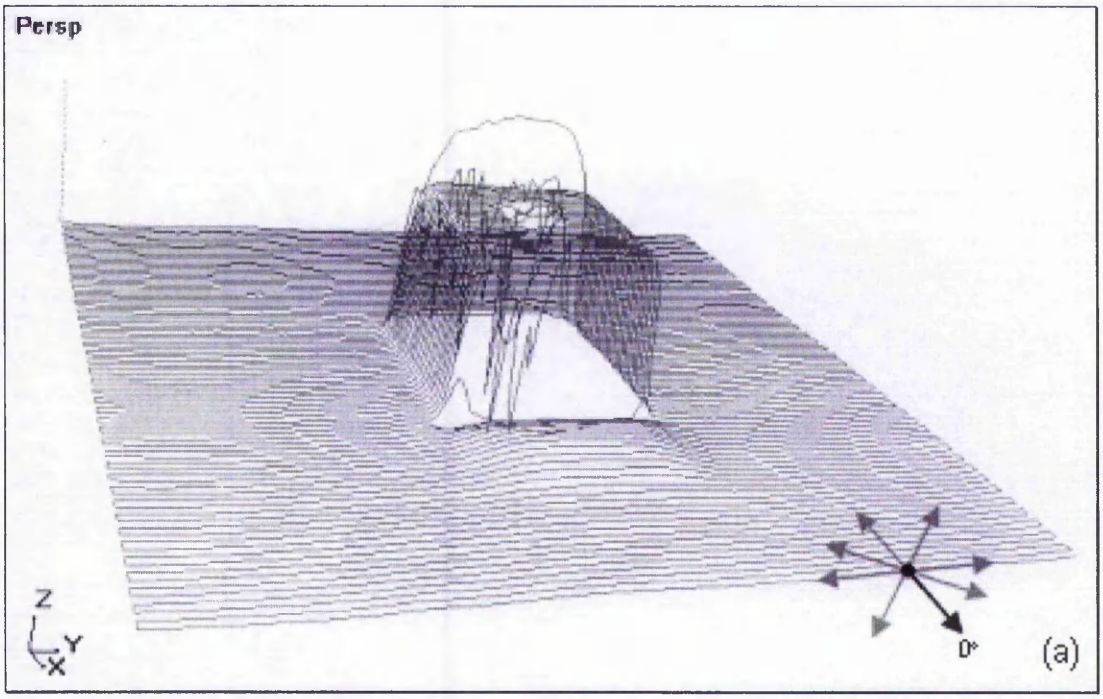

Fig. C-20: Range image of Fig. C-19 with orientation of sensor at (a) 0° ((b)-(h) on following pages).

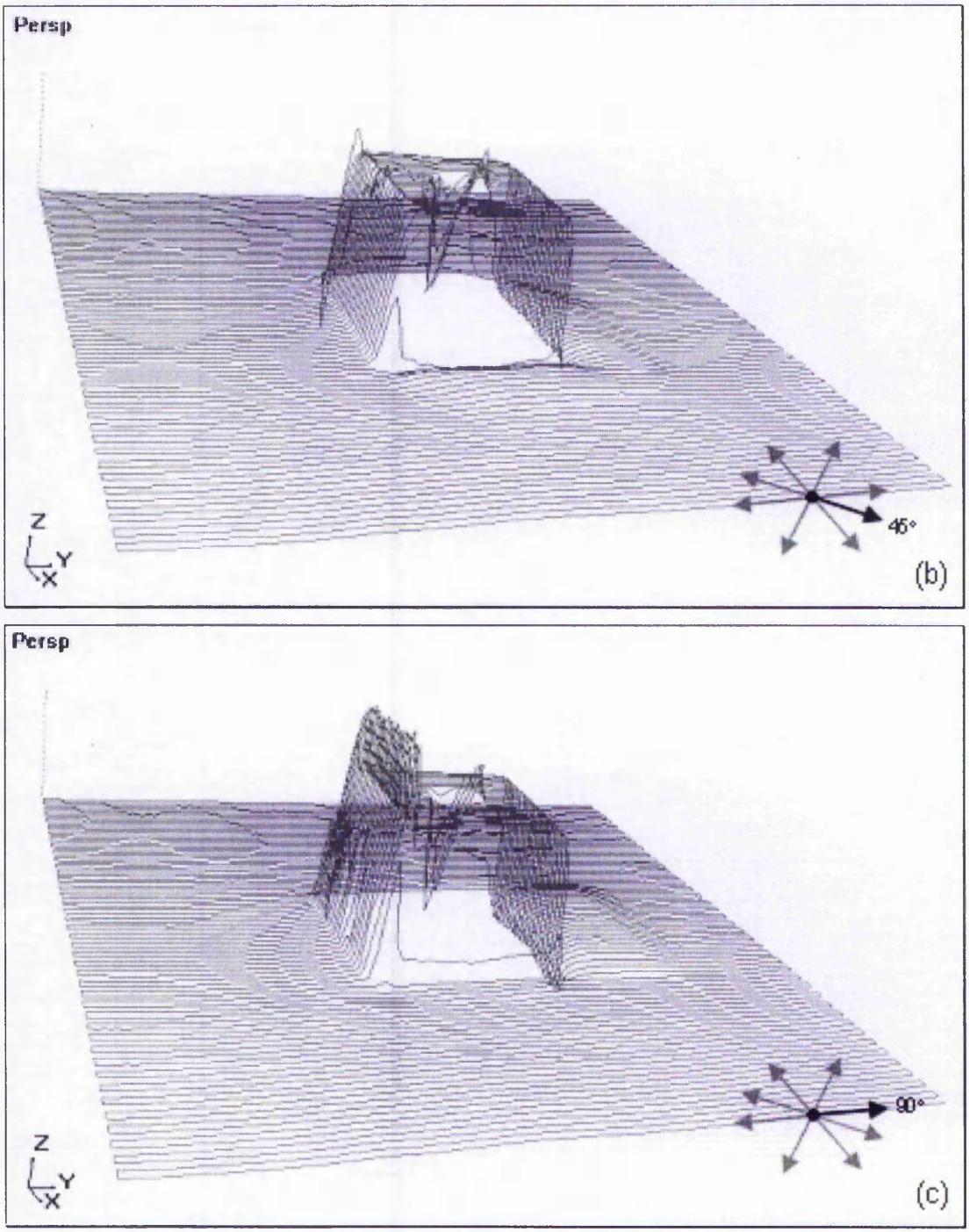

Fig. C-20: Range images of Fig. C-19 with orientations of sensor at (b) 45° and (c) 90° ((d)-(h) on following pages).

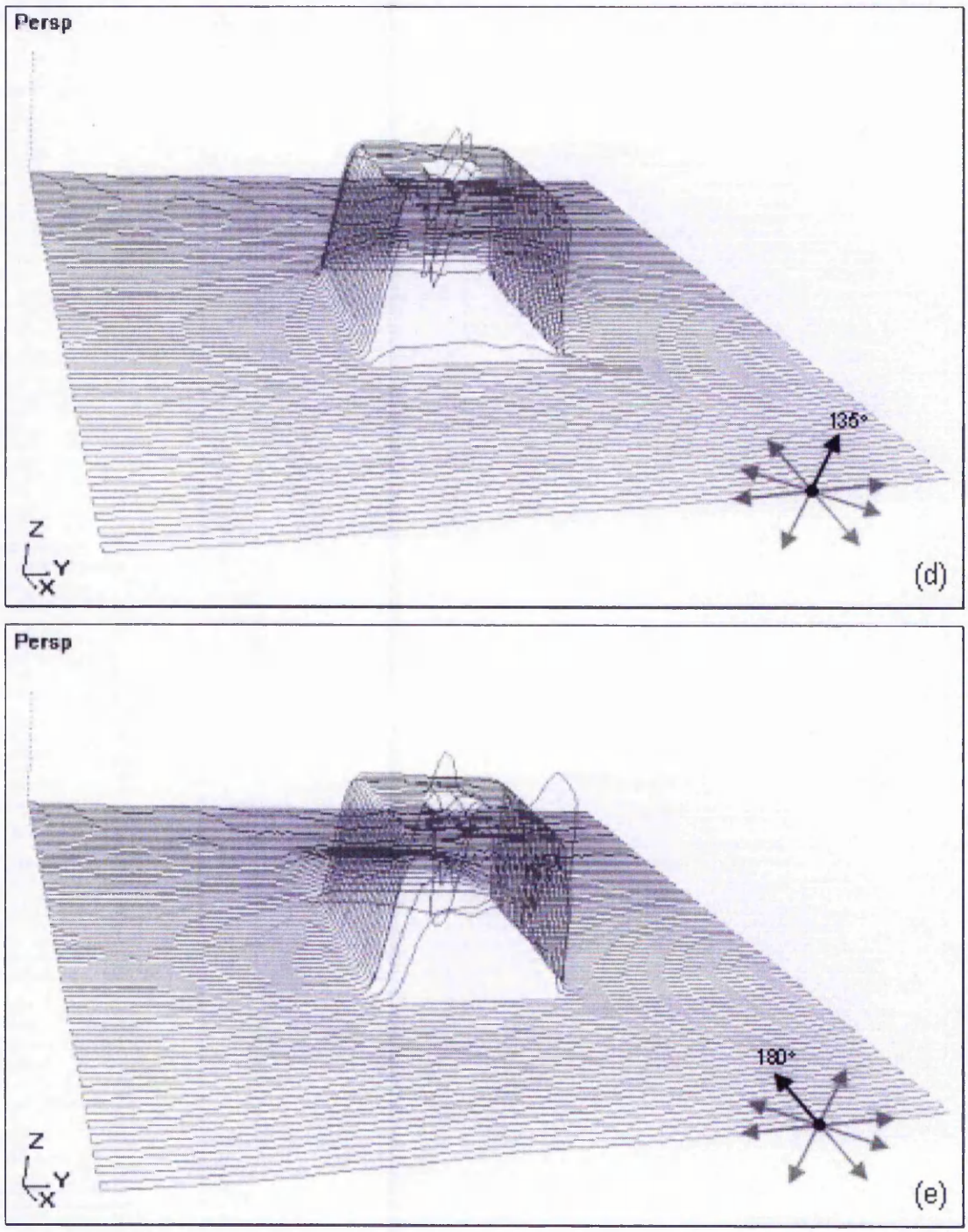

Fig. C-20: Range images of Fig. C-19 with orientations of sensor at (d) 135° and (e) 180° ((f)-(h) on following pages).

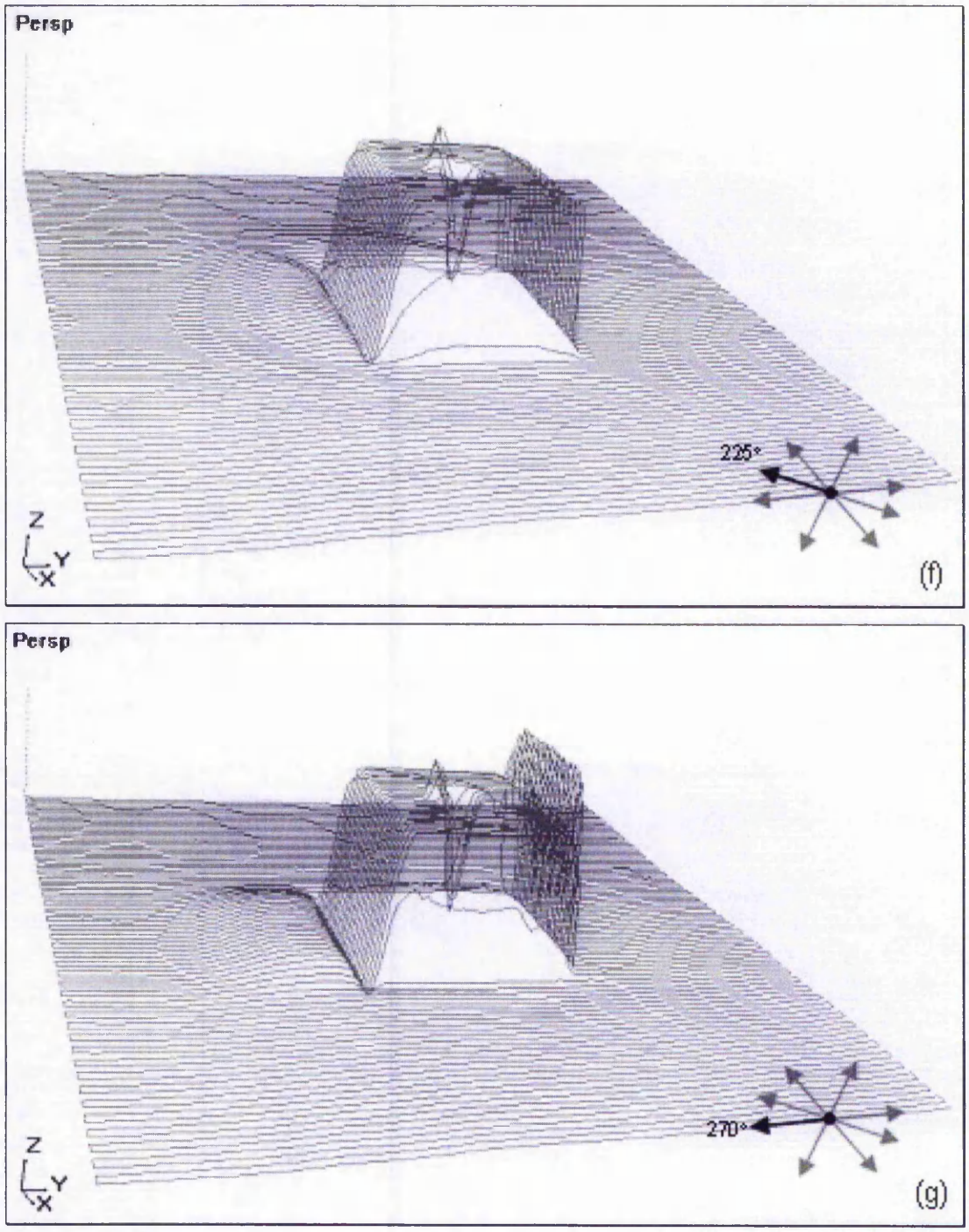

Fig. C-20: Range images of Fig. C-19 with orientations of sensor at (f) 225° and (g) 270° ((h) on following page).

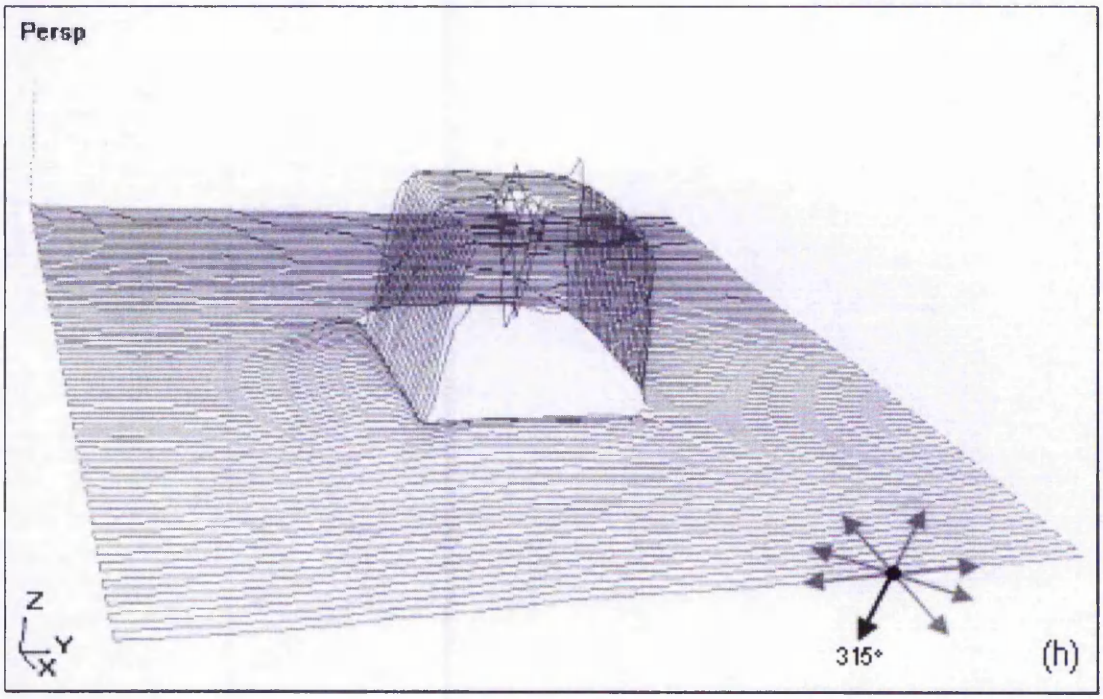

Fig. C-20: Range image of Fig. C-19 with orientation of sensor at (h) 315°.

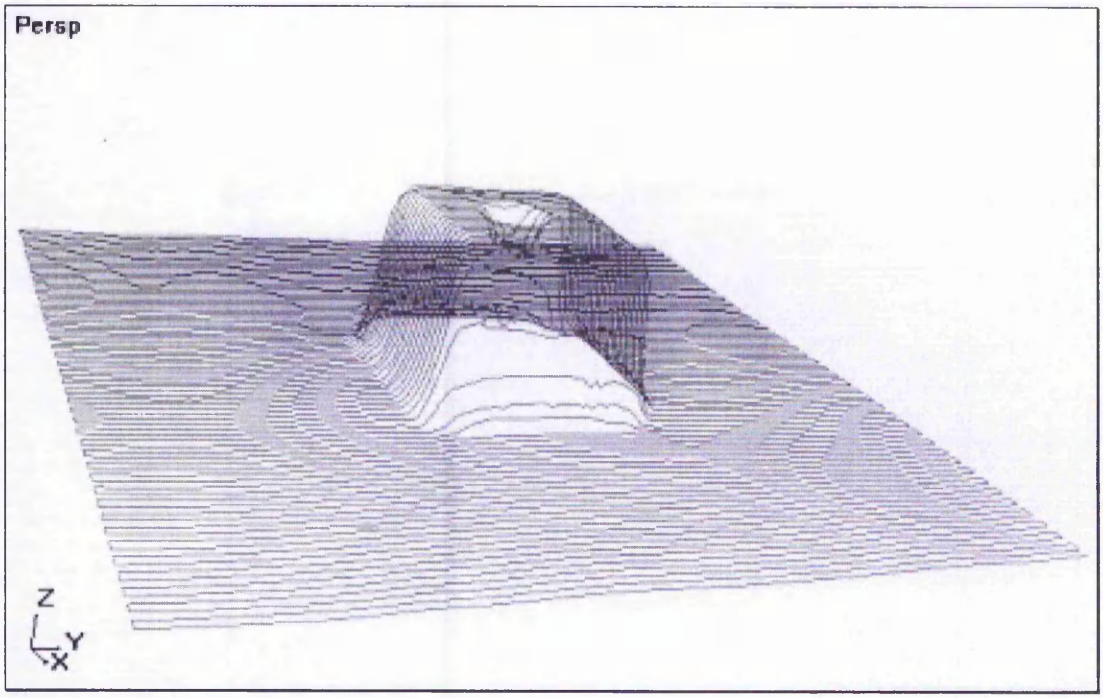

Fig. C-21: Averaging of eight range images of Fig. C-19.

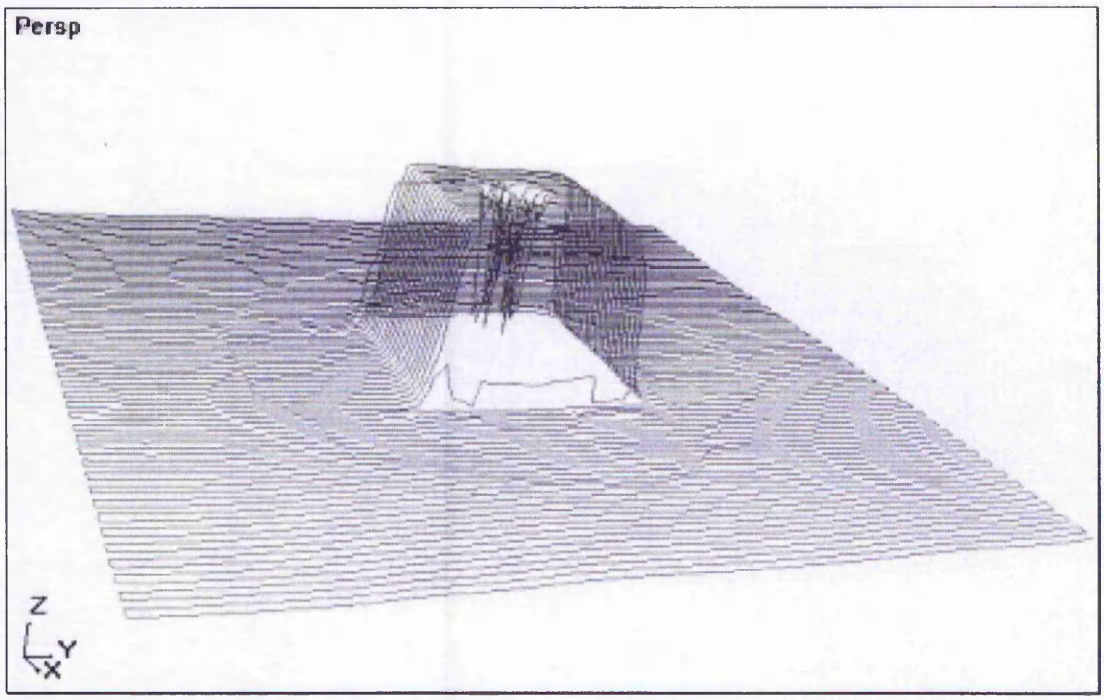

Fig. C-22: Selection of lowest *z*-values from multiple range images of Fig. C-19.

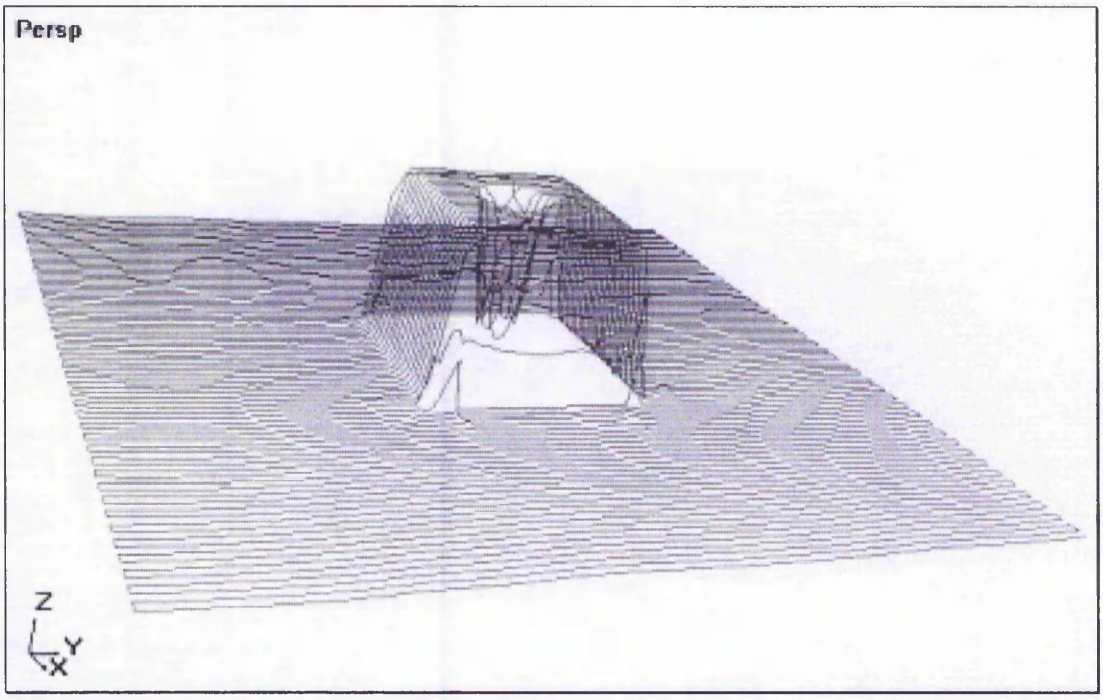

Fig. C-23: Compensated range image of Fig. C-19 based on edge detection algorithms.

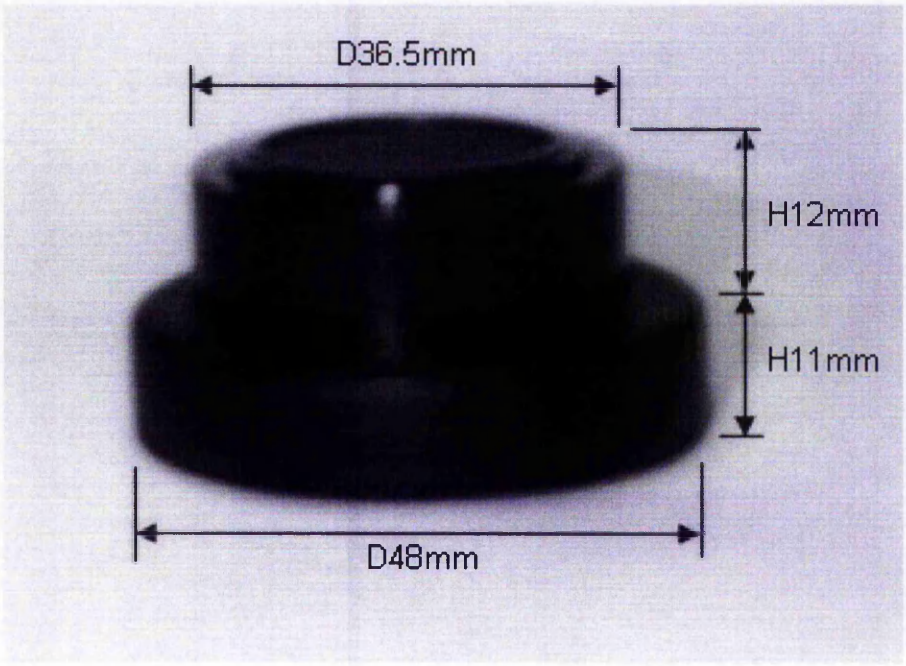

Fig. C-24: Stacked cylindrical camera caps.

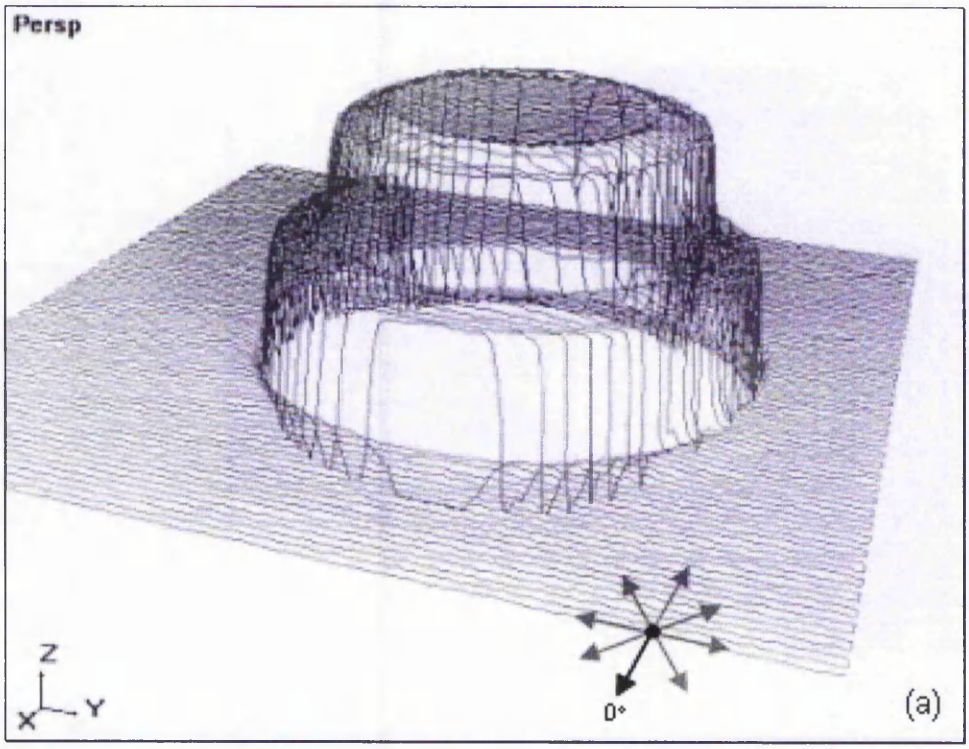

Fig. C-25: Range image of Fig. C-24 with orientation of sensor at (a) 0° ((b)-(h) on following pages).

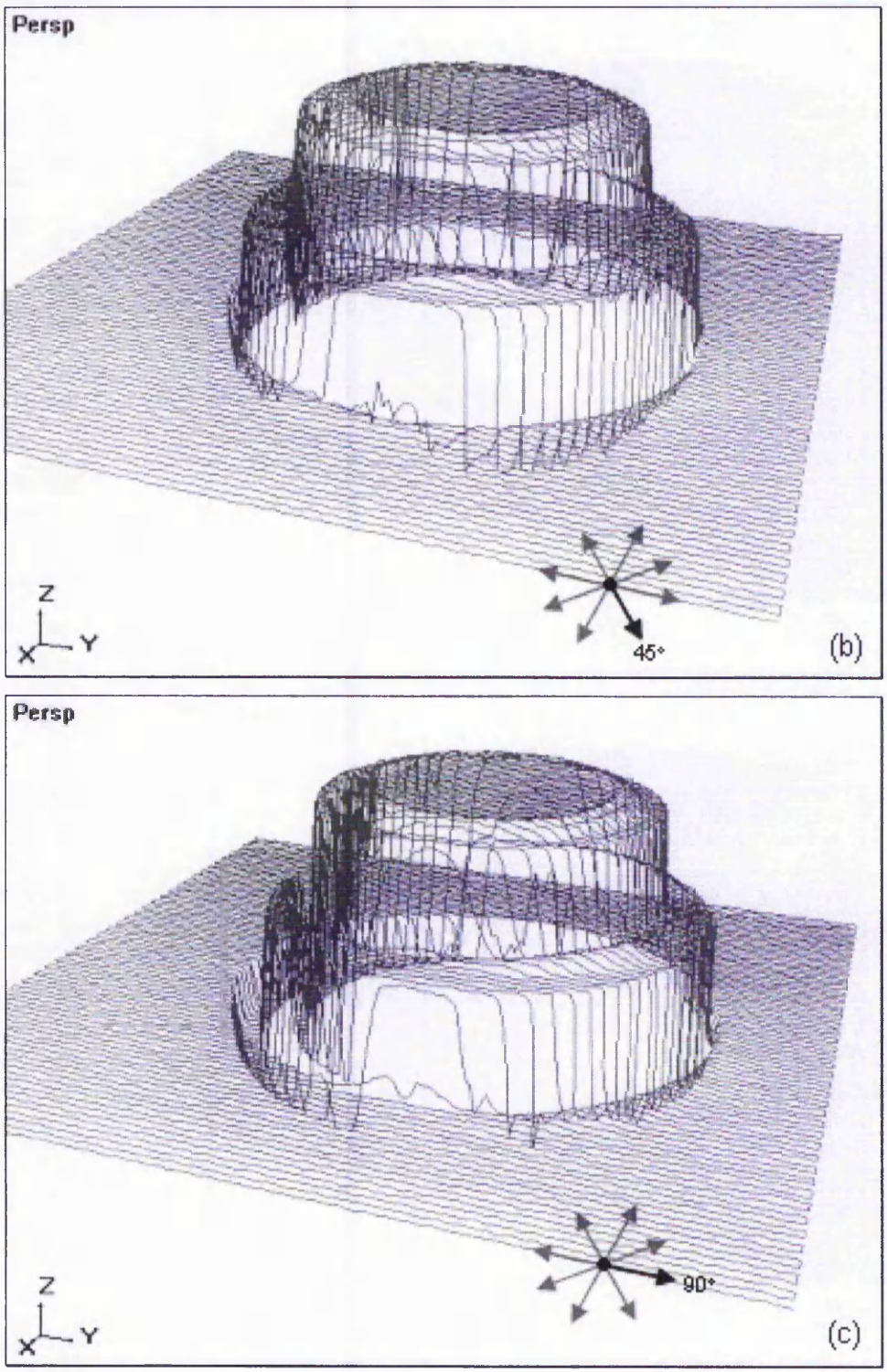

Fig. C-25: Range images of Fig. C-24 with orientations of sensor at (b) 45° and (c) 90° ((d)-(h) on following pages).

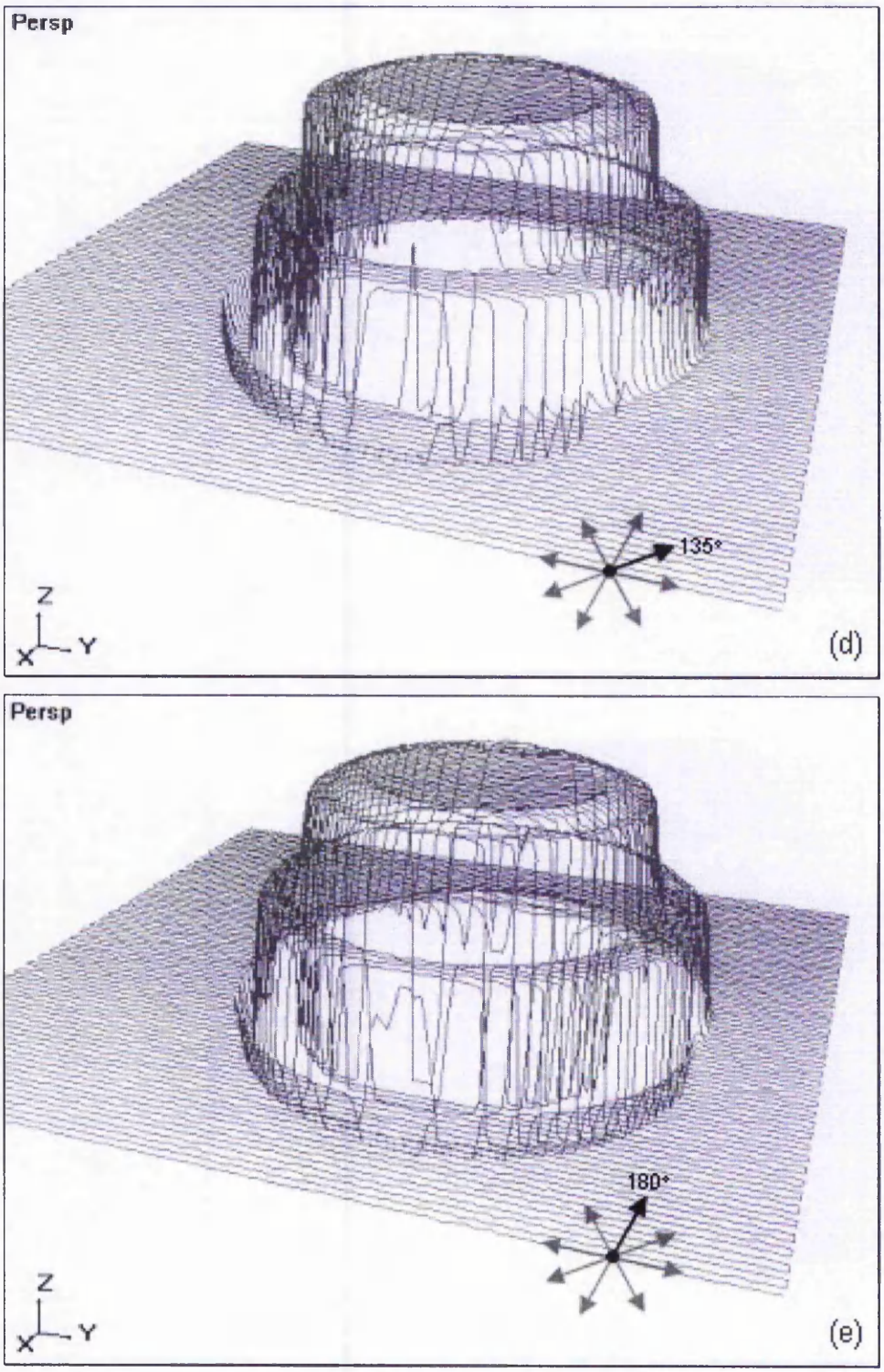

Fig. C-25: Range images of Fig. C-24 with orientations of sensor at (d) 135° and (e) 180° ((f)-(h) on following pages).

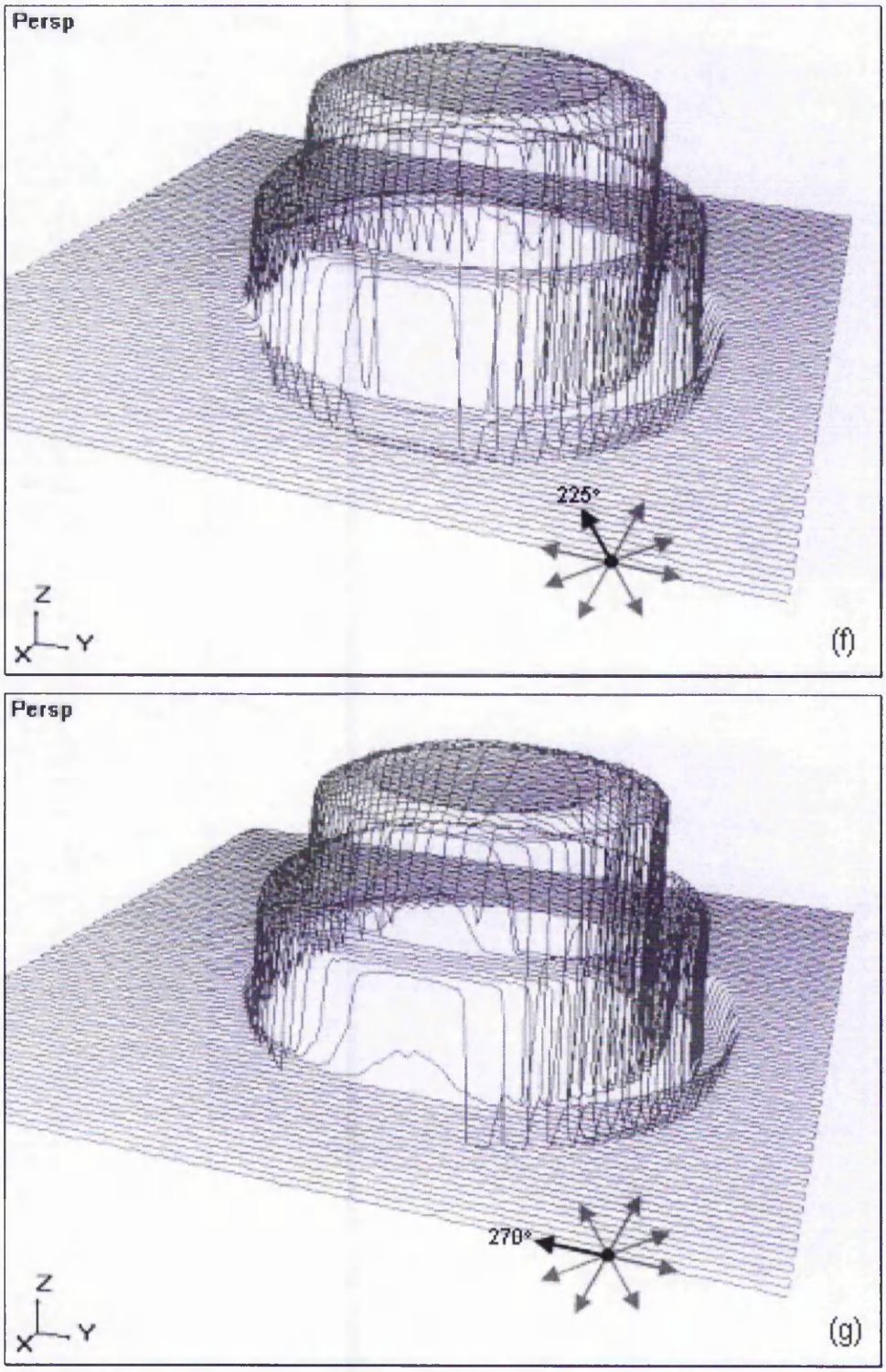

Fig. C-25: Range images of Fig. C-24 with orientations of sensor at (f) 225° and (g) 270° ((h) on following page).

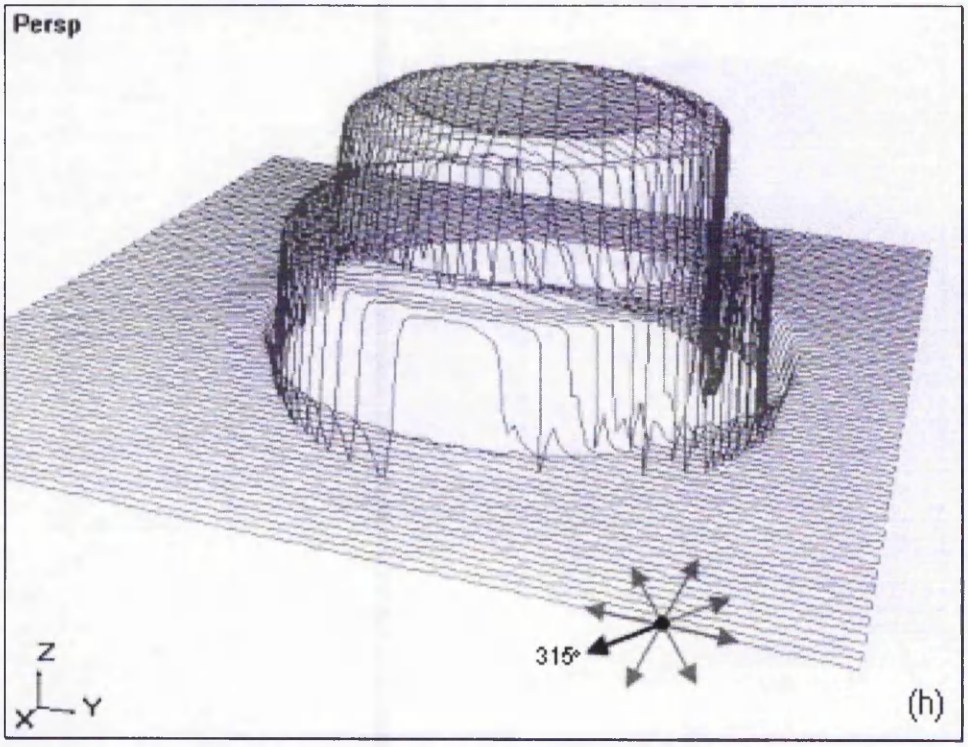

Fig. C-25: Range image of Fig. C-24 with orientation of sensor at (h) 315°.

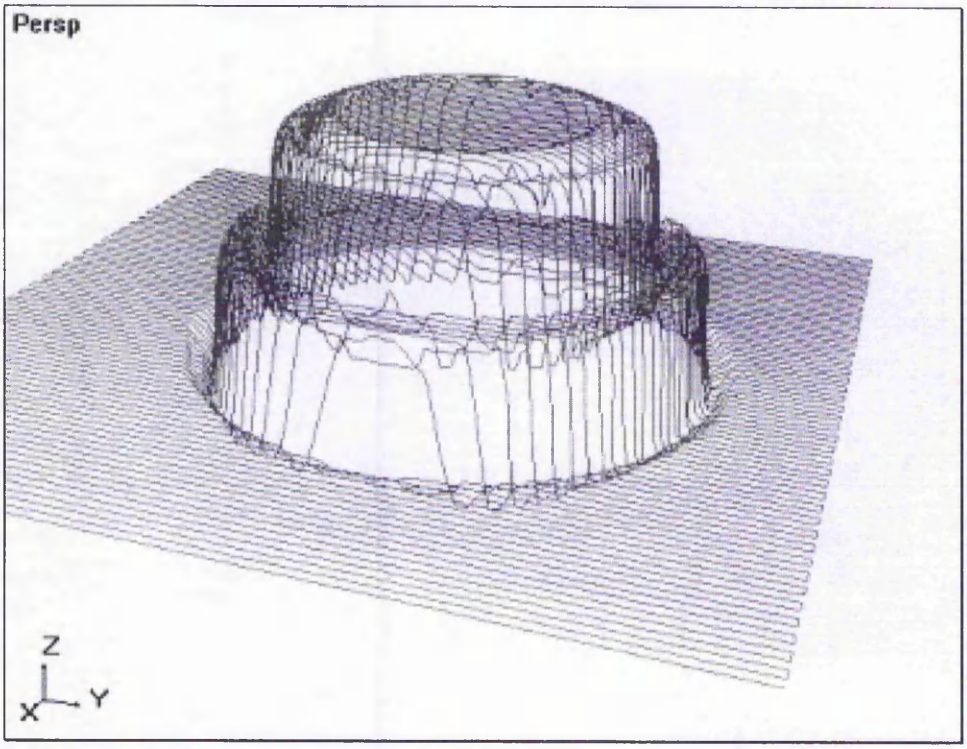

Fig. C-26: Averaging of eight range images of Fig. C-24.

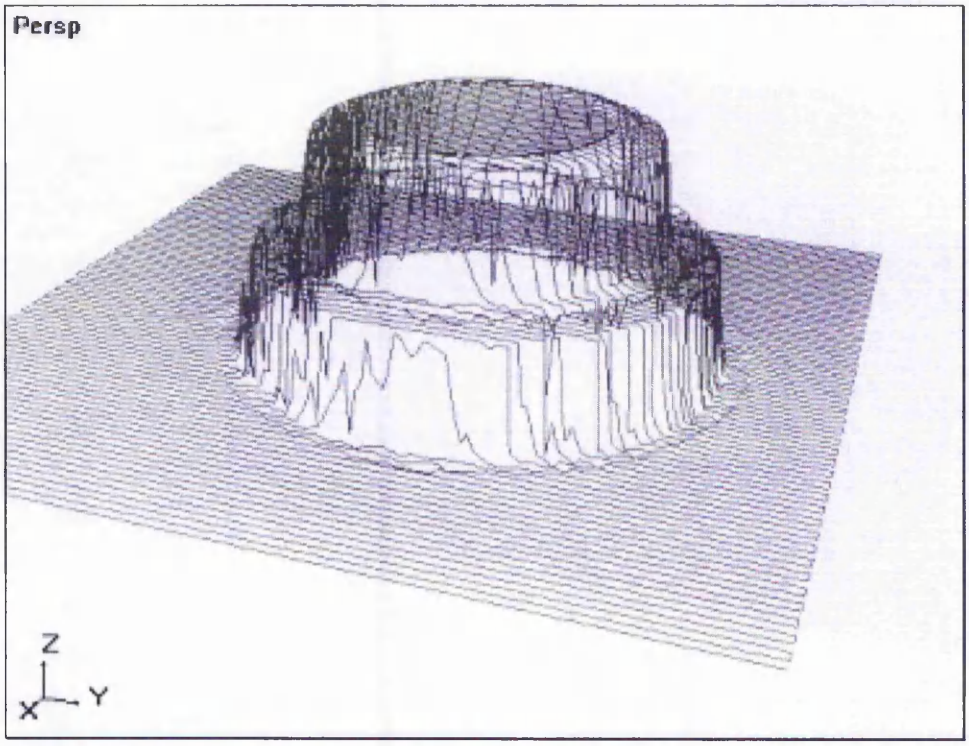

Fig. C-27: Selection of lowest *z*-values from multiple range images of Fig. C-24.

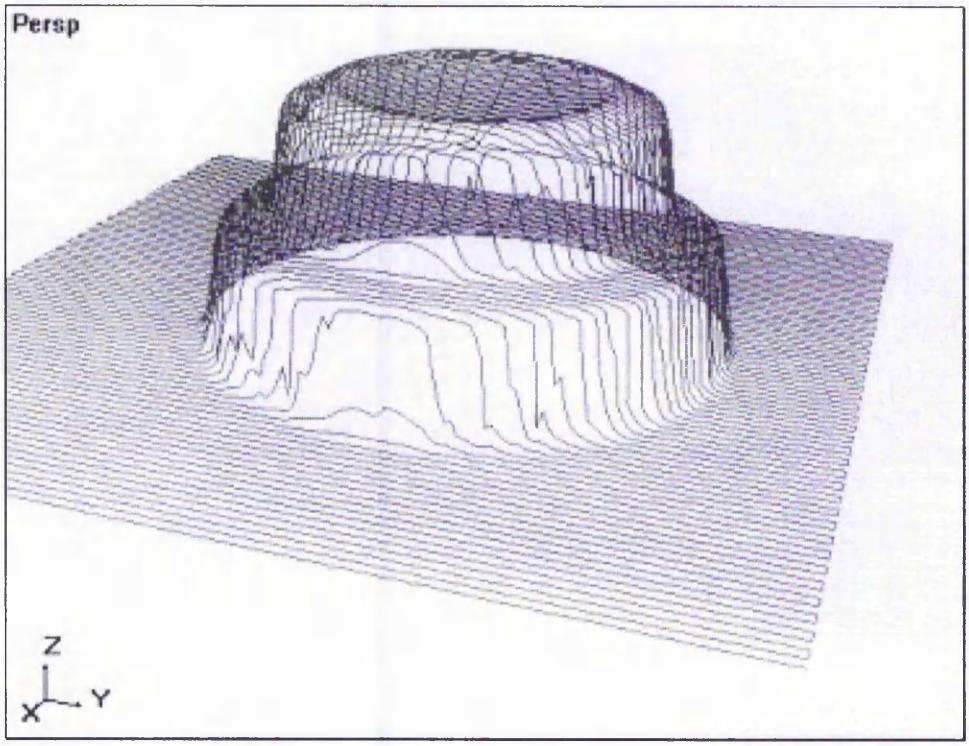

Fig. C-28: Compensated range image of Fig. C-24 based on edge detection algorithms.

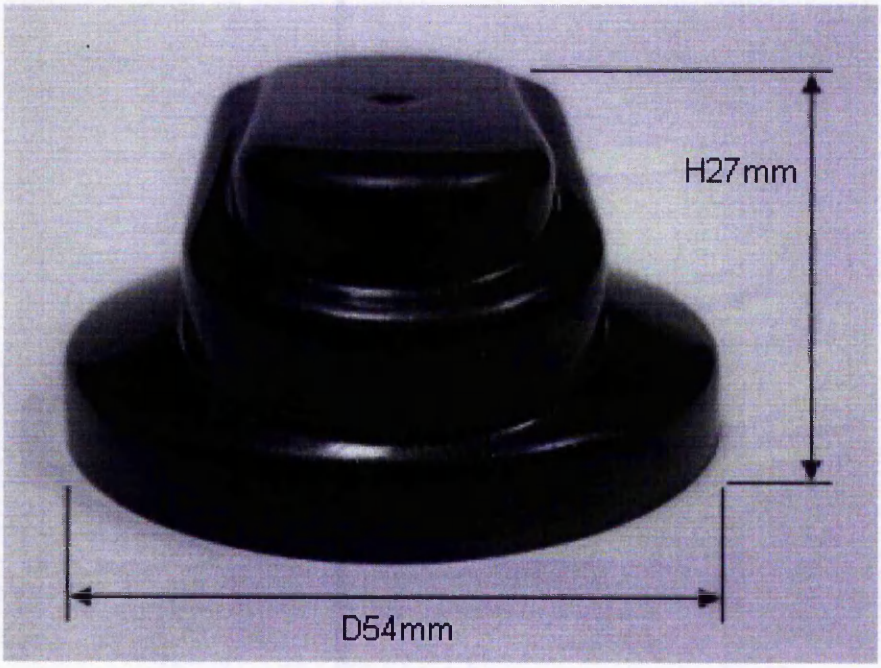

Fig. C-29: Technical object (height at 27mm and diameter of base at 54mm).

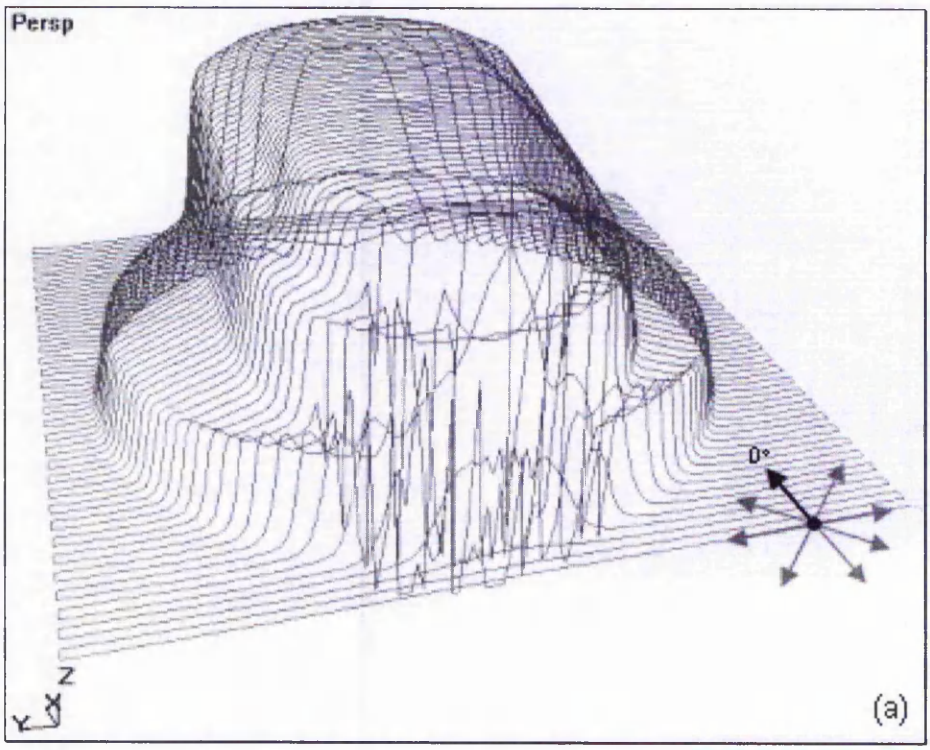

Fig. C-30: Range image of Fig. C-29 with orientation of sensor at (a) 0° ((b)-(h) on following pages).

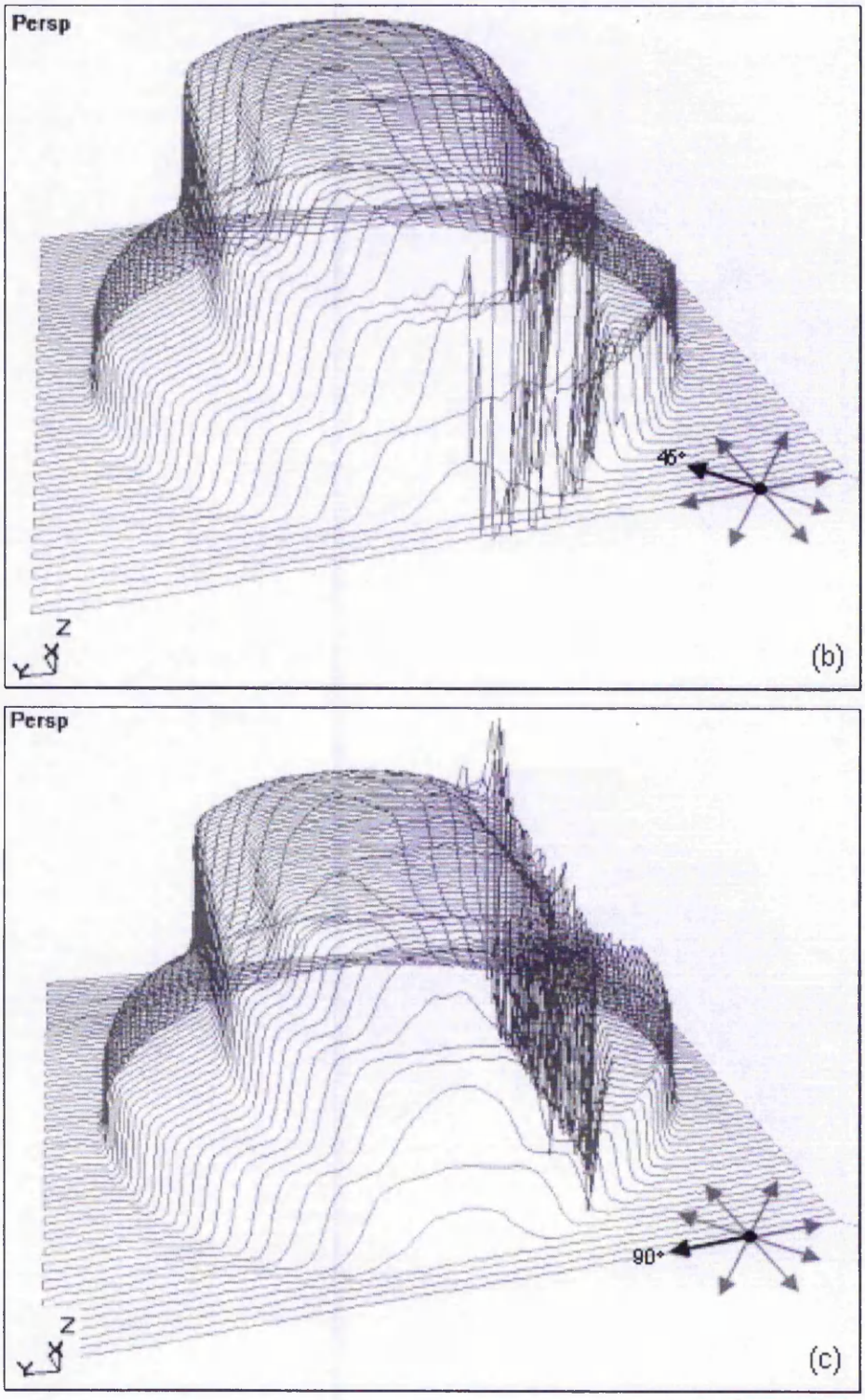

Fig. C-30: Range images of Fig. C-29 with orientations of sensor at (b) 45° and (c) 90° ((d)-(h) on following pages).

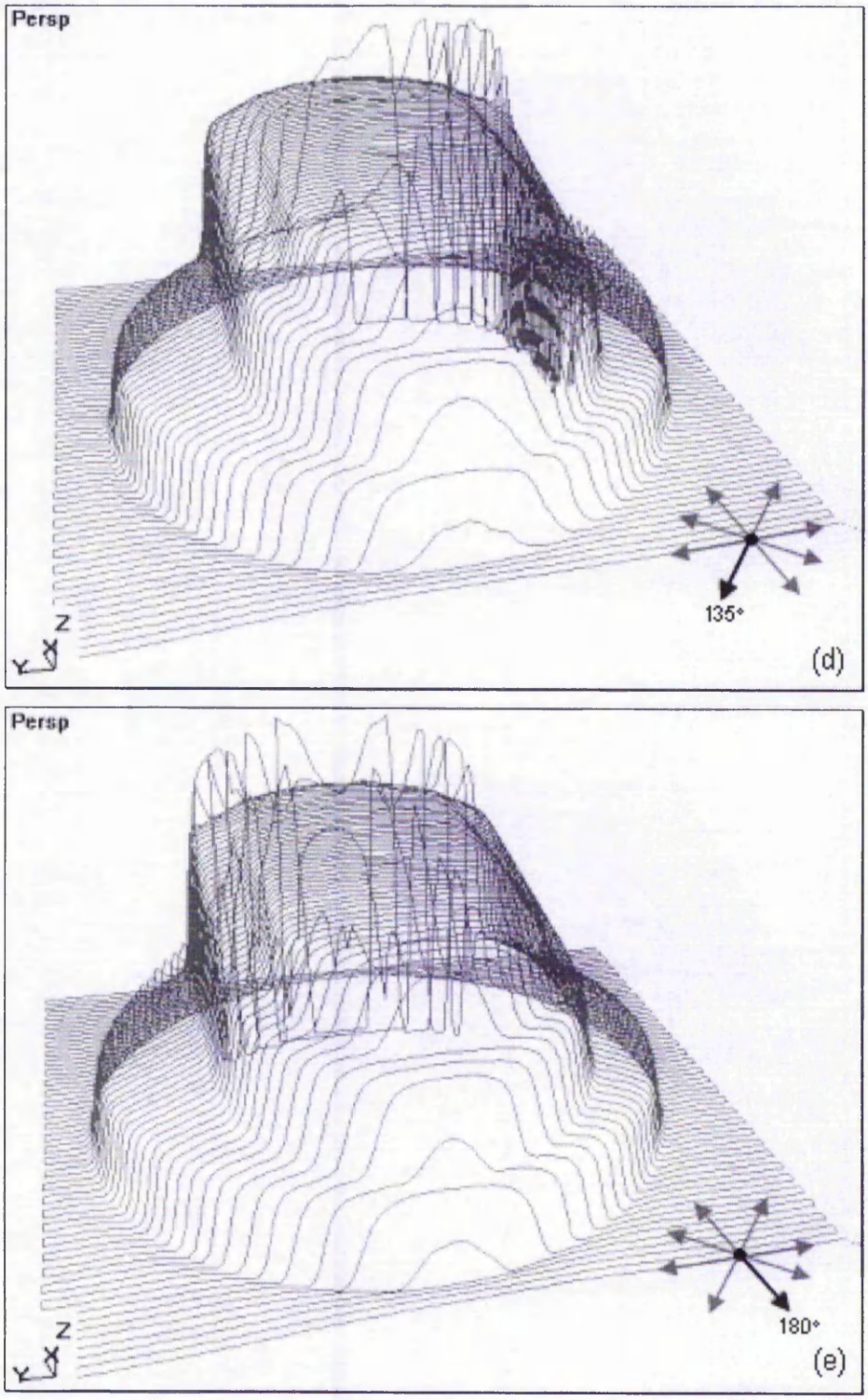

Fig. C-30: Range images of Fig. C-29 with orientations of sensor at (d) 135° and (e) 180° ((f)-(h) on following pages).

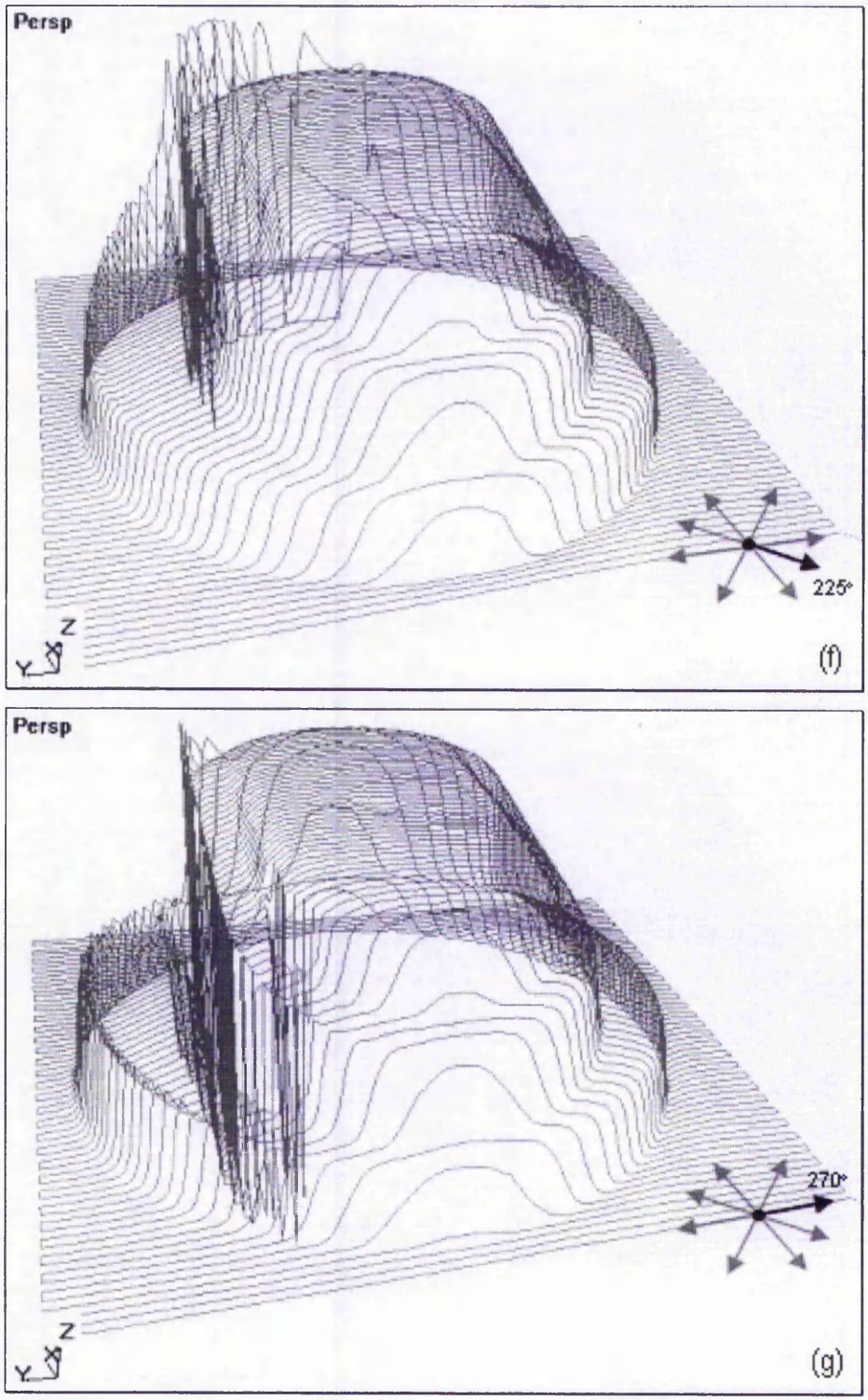

Fig. C-30: Range images of Fig. C-29 with orientations of sensor at (f) 225° and (g) 270° ((h) on following page).

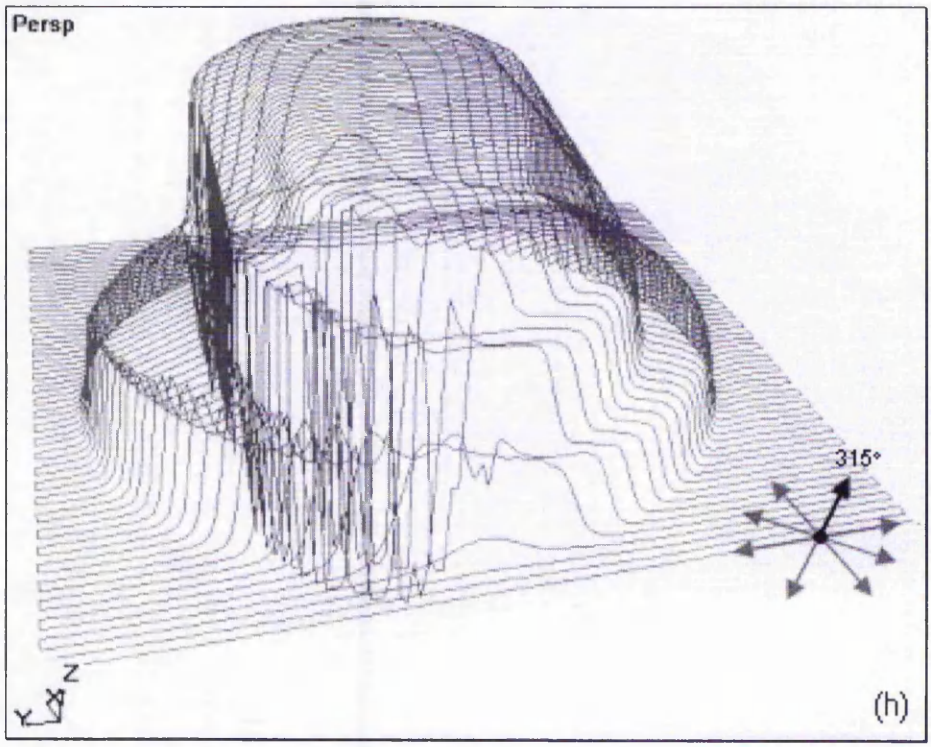

Fig. C-30: Range image of Fig. C-29 with orientation of sensor at (h) 315°.

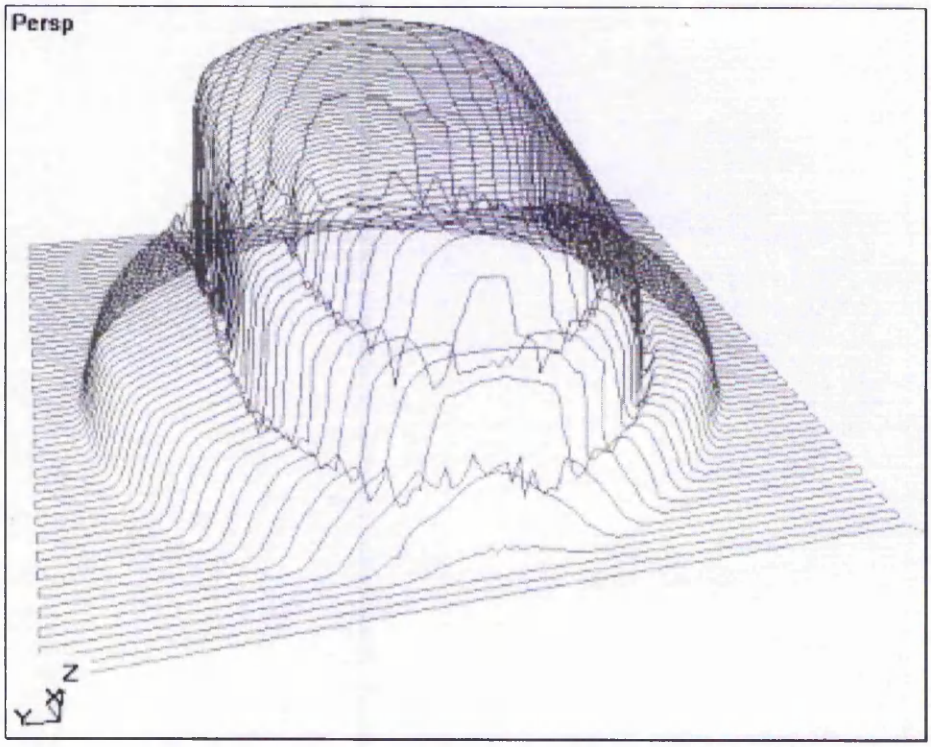

Fig. C-31: Averaging of eight range images of Fig. C-29.

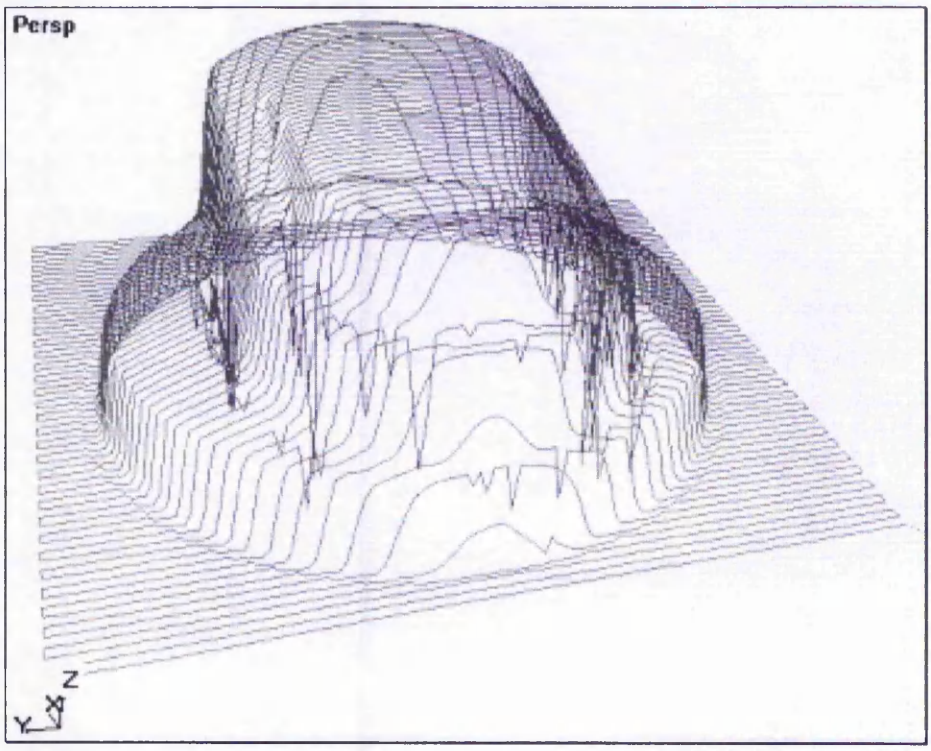

Fig. C-32: Selection of lowest *z*-values from multiple range images of Fig. C-29.

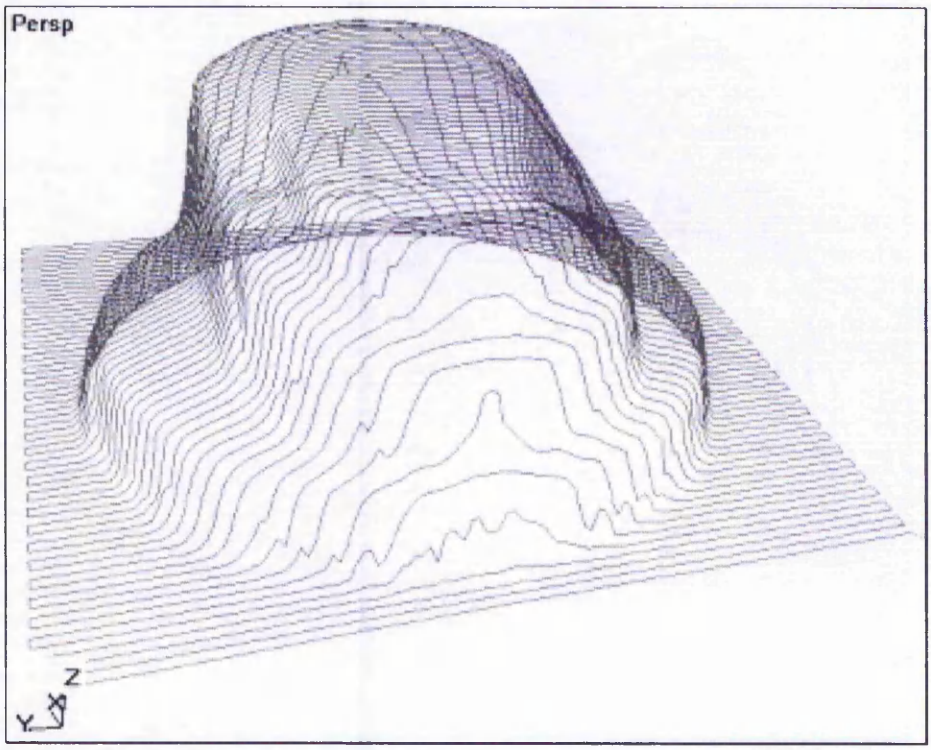

Fig. C-33: Compensated range image of Fig. C-29 based on edge detection algorithms.

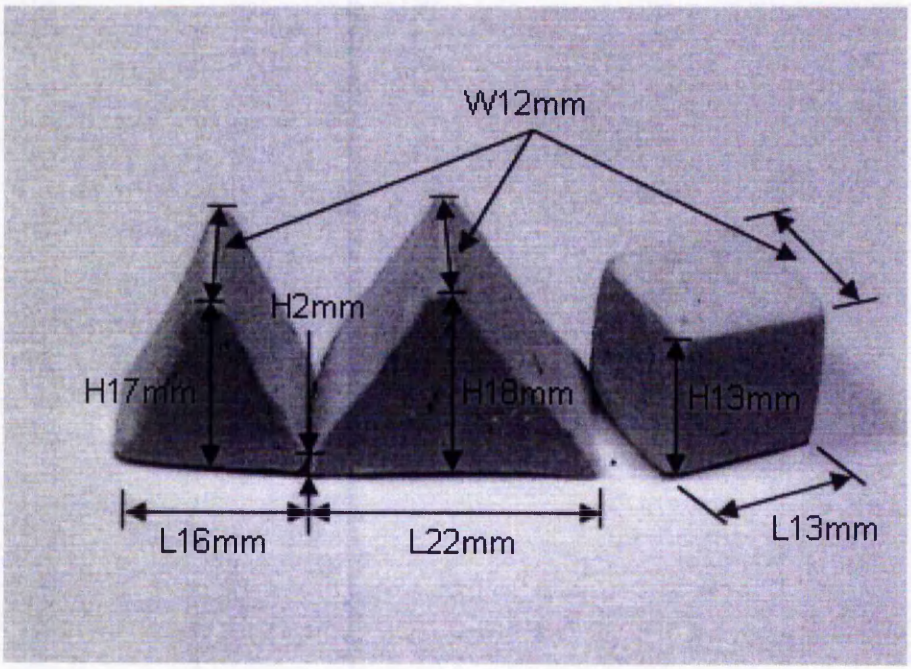

Fig. C-34: Double peaks and square object.

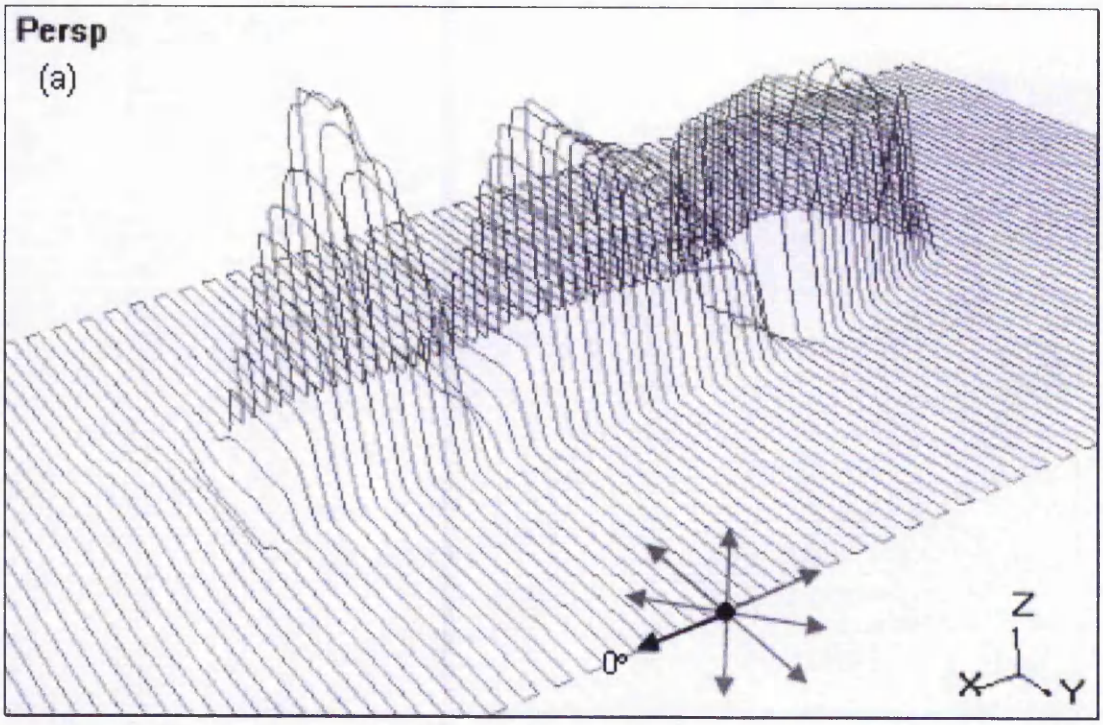

Fig. C-35: Range image of Fig. C-34 with orientation of sensor at (a) 0° ((b)-(h) on following pages).

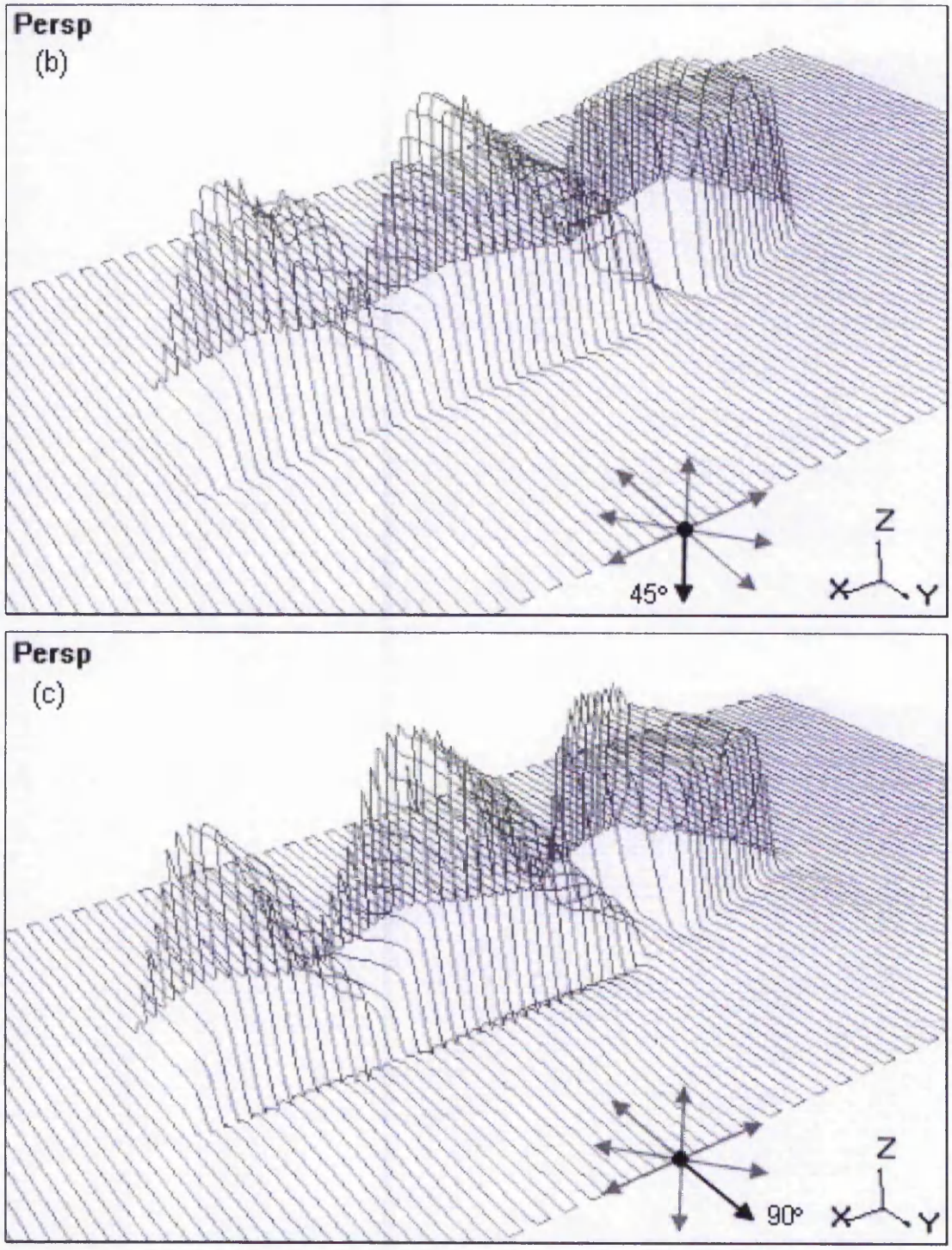

Fig. C-35: Range images of Fig. C-34 with orientations of sensor at (b) 45° and (c) 90° ((d)-(h) on following pages).

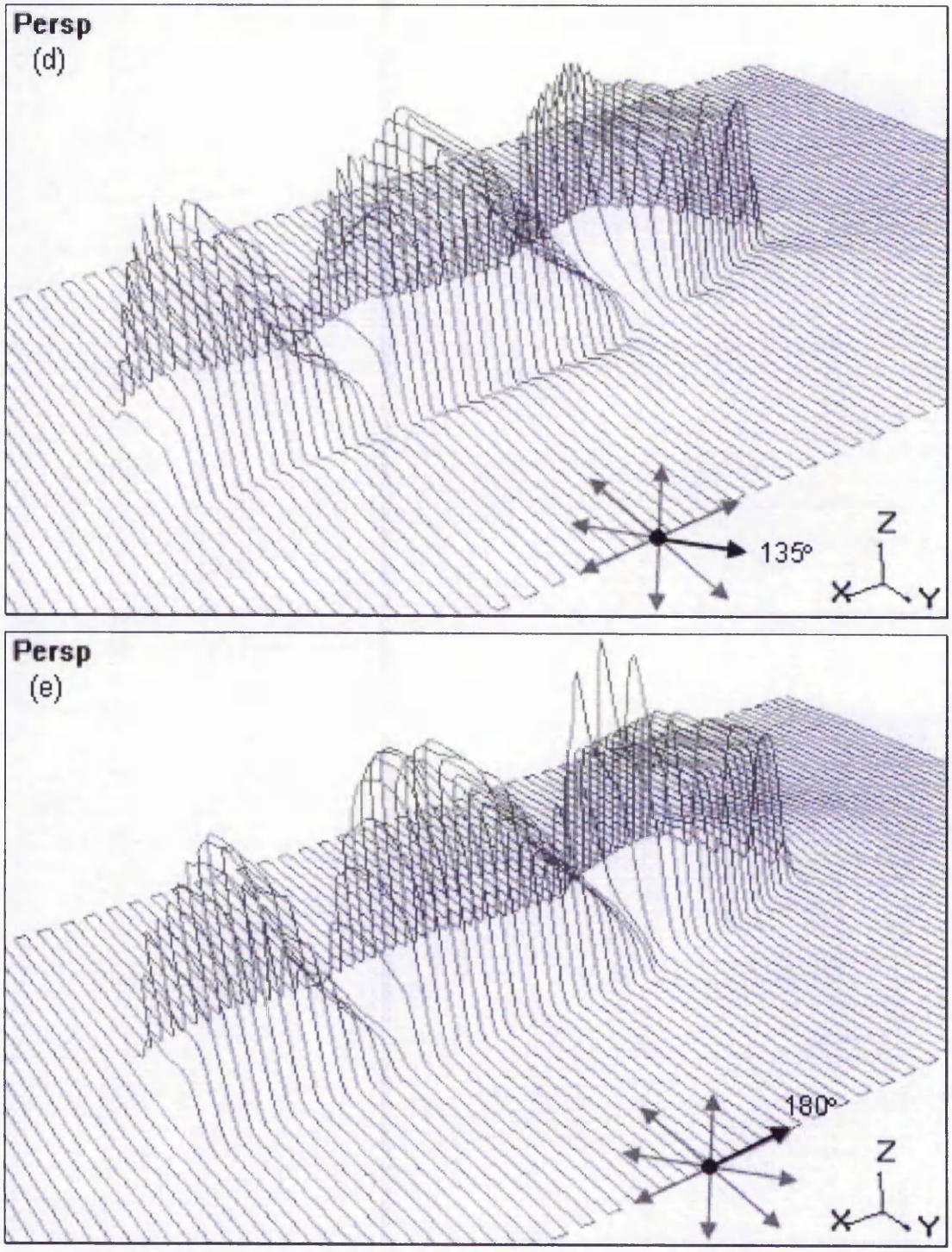

Fig. C-35: Range images of Fig. C-34 with orientations of sensor at (d) 135° and (e) 180° ((f)-(h) on following pages).

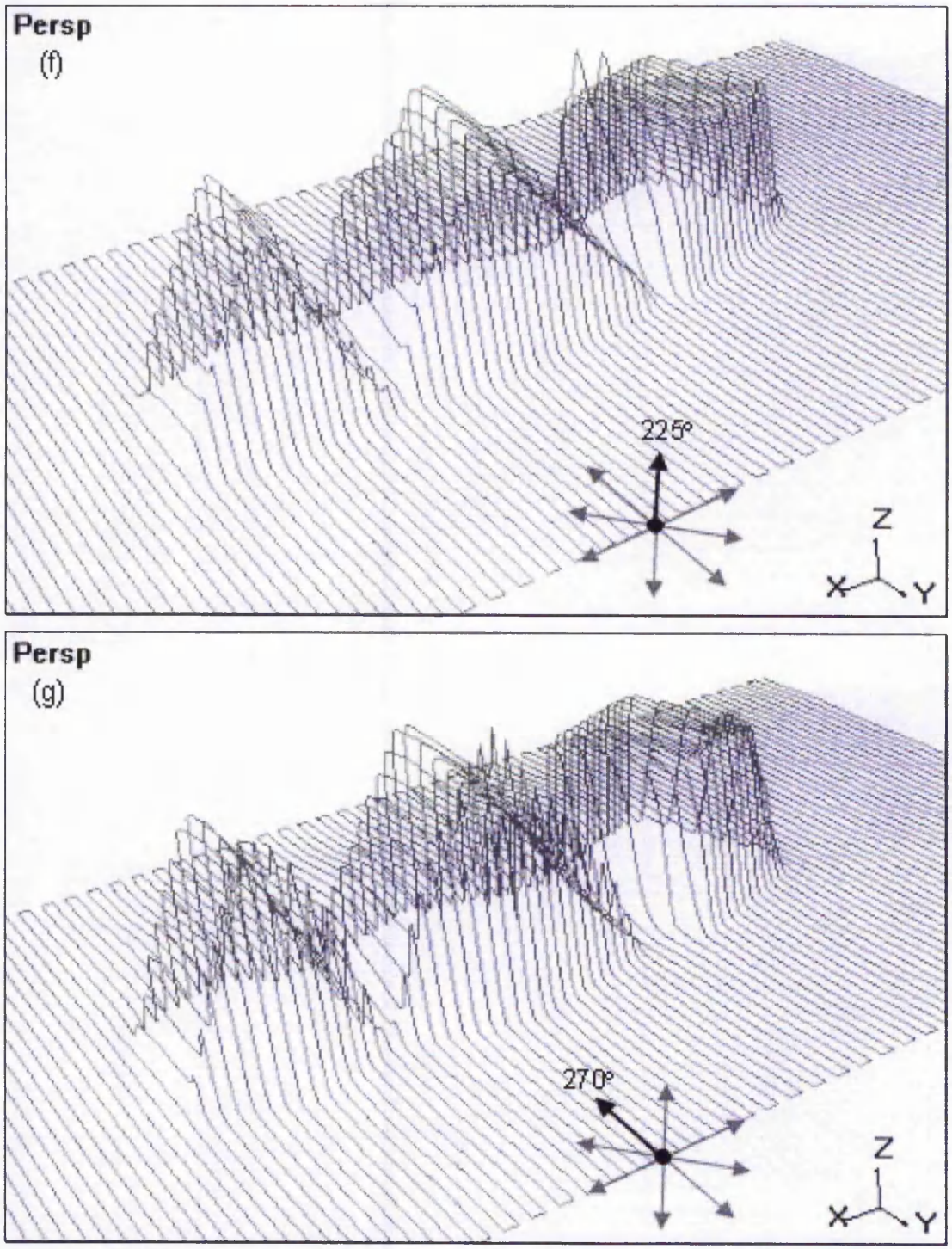

Fig. C-35: Range images of Fig. C-34 with orientations of sensor at (f) 225° and (g) 270° ((h) on following page).

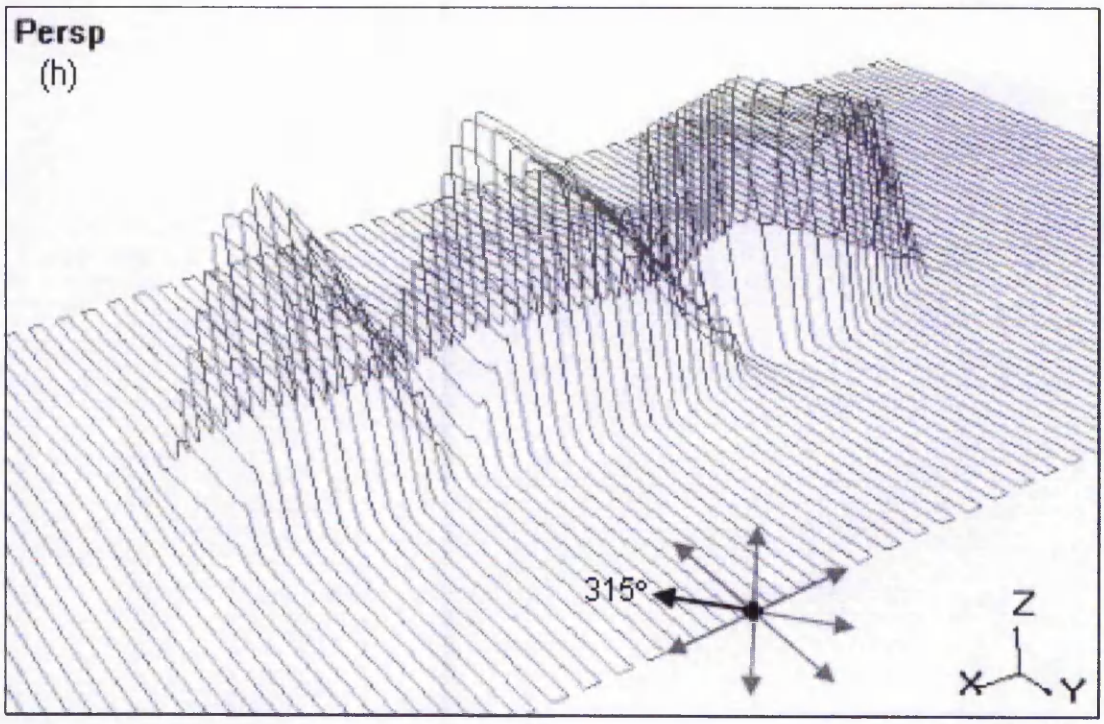

Fig. C-35: Range image of Fig. C-34 with orientation of sensor at (h) 315°.

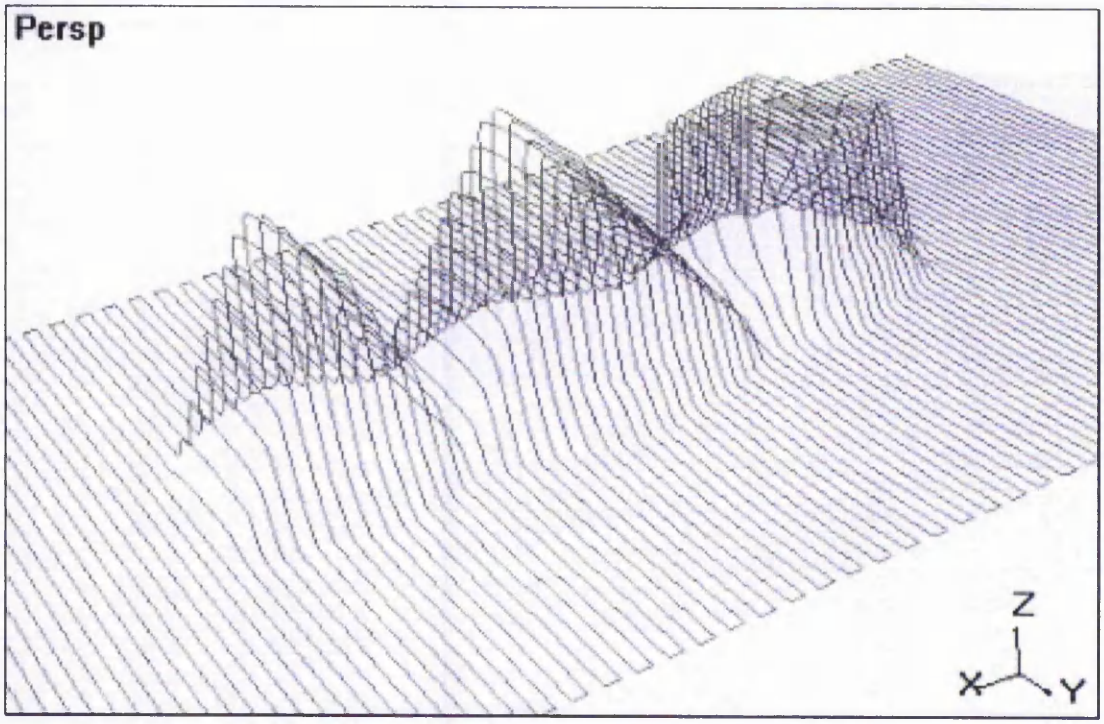

Fig. C-36: Averaging of eight range images of Fig. C-34.

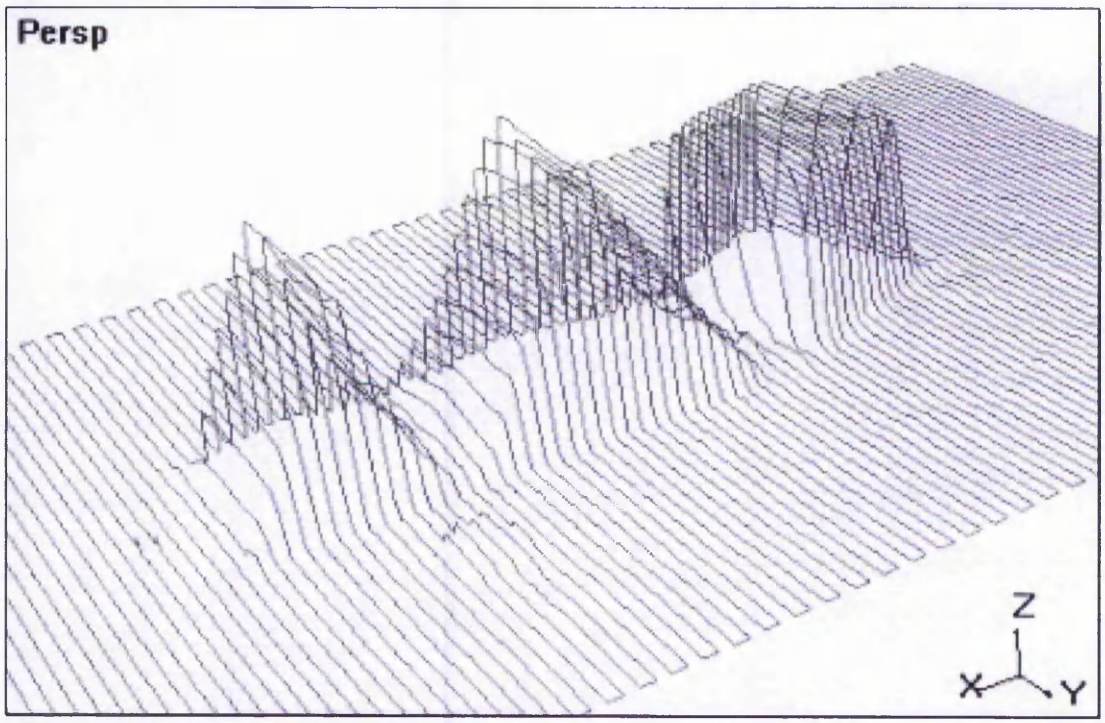

Fig. C-37: Selection of lowest *z*-values from multiple range images of Fig. C-34.

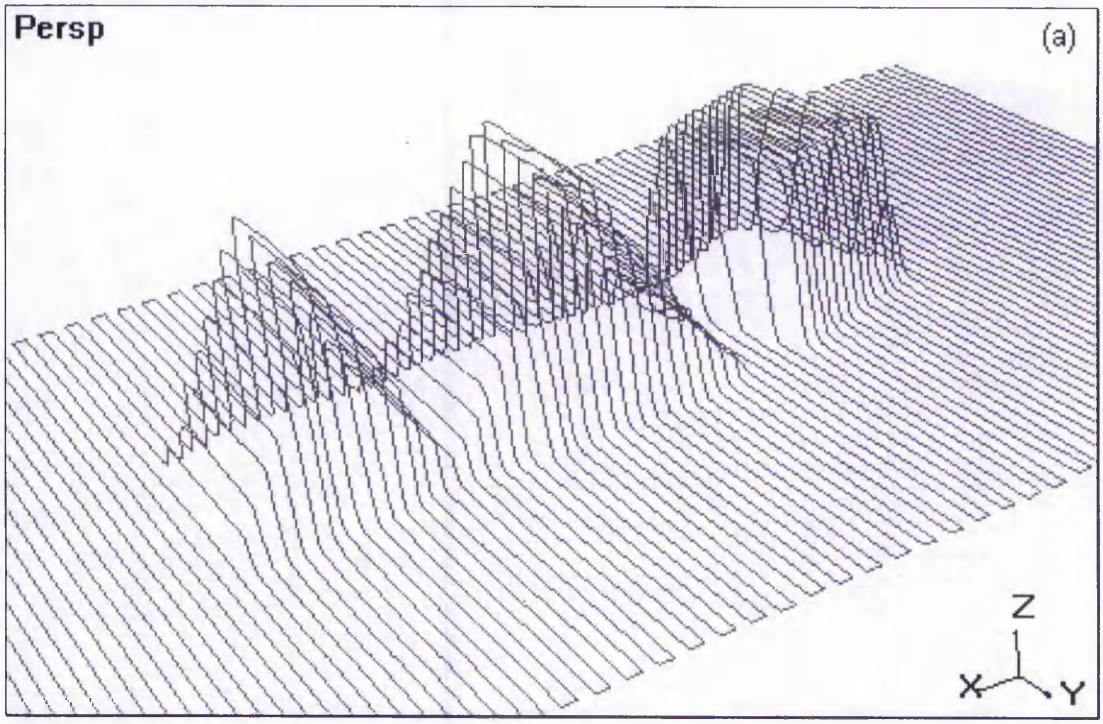

Fig. C-38: Compensated range image of Fig. C-34 based on edge detection algorithms with (a) perspective view ((b) and (c) on following page).

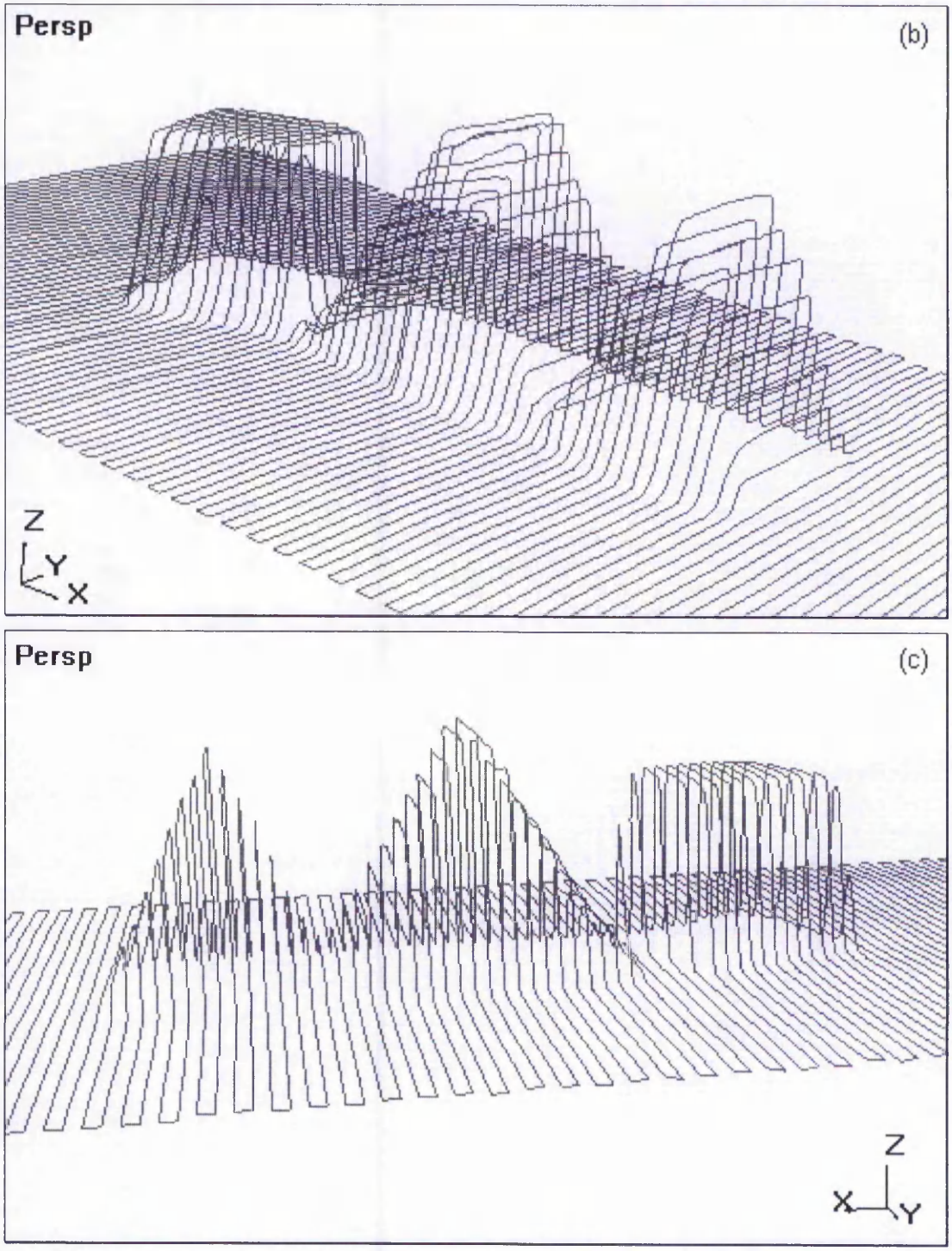

Fig. C-38: Compensated range images of Fig. C-34 based on edge detection algorithms with (b) another perspective view and (c) view from front.

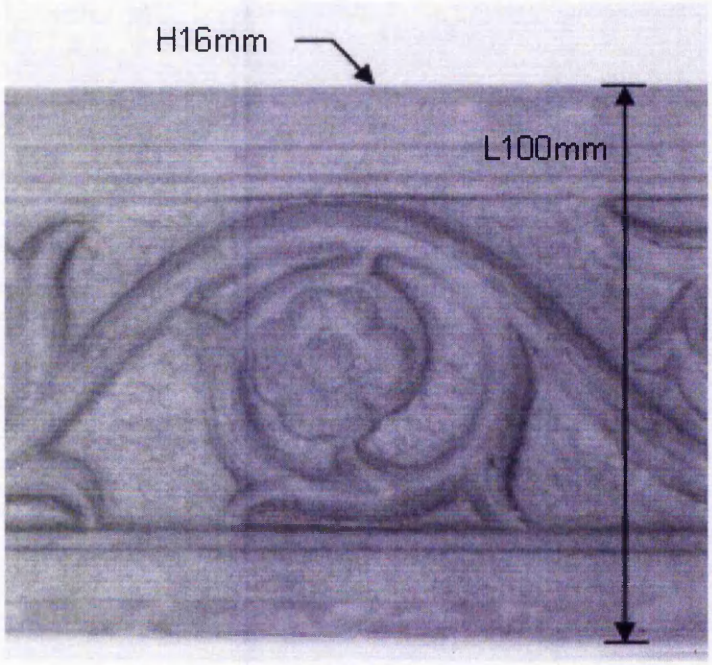

Fig. C-39: Tile object (height at 16mm).

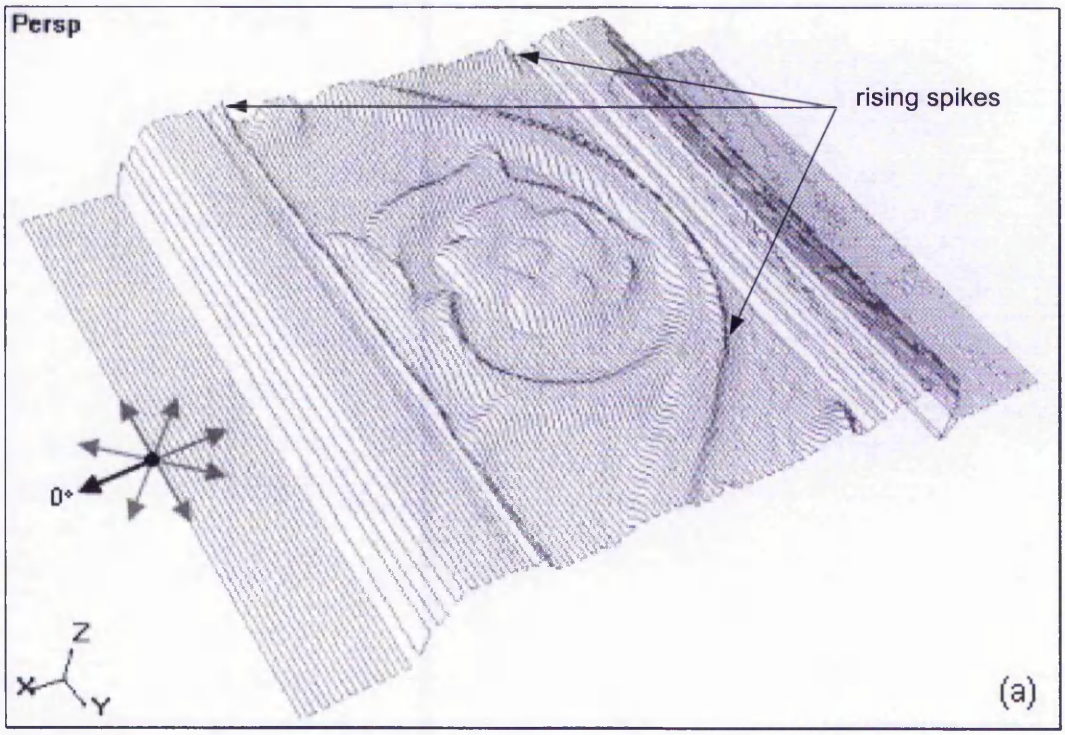

Fig. C-40: Range image of Fig. C-39 with orientation of sensor at (a) 0° ((b)-(h) on following pages).

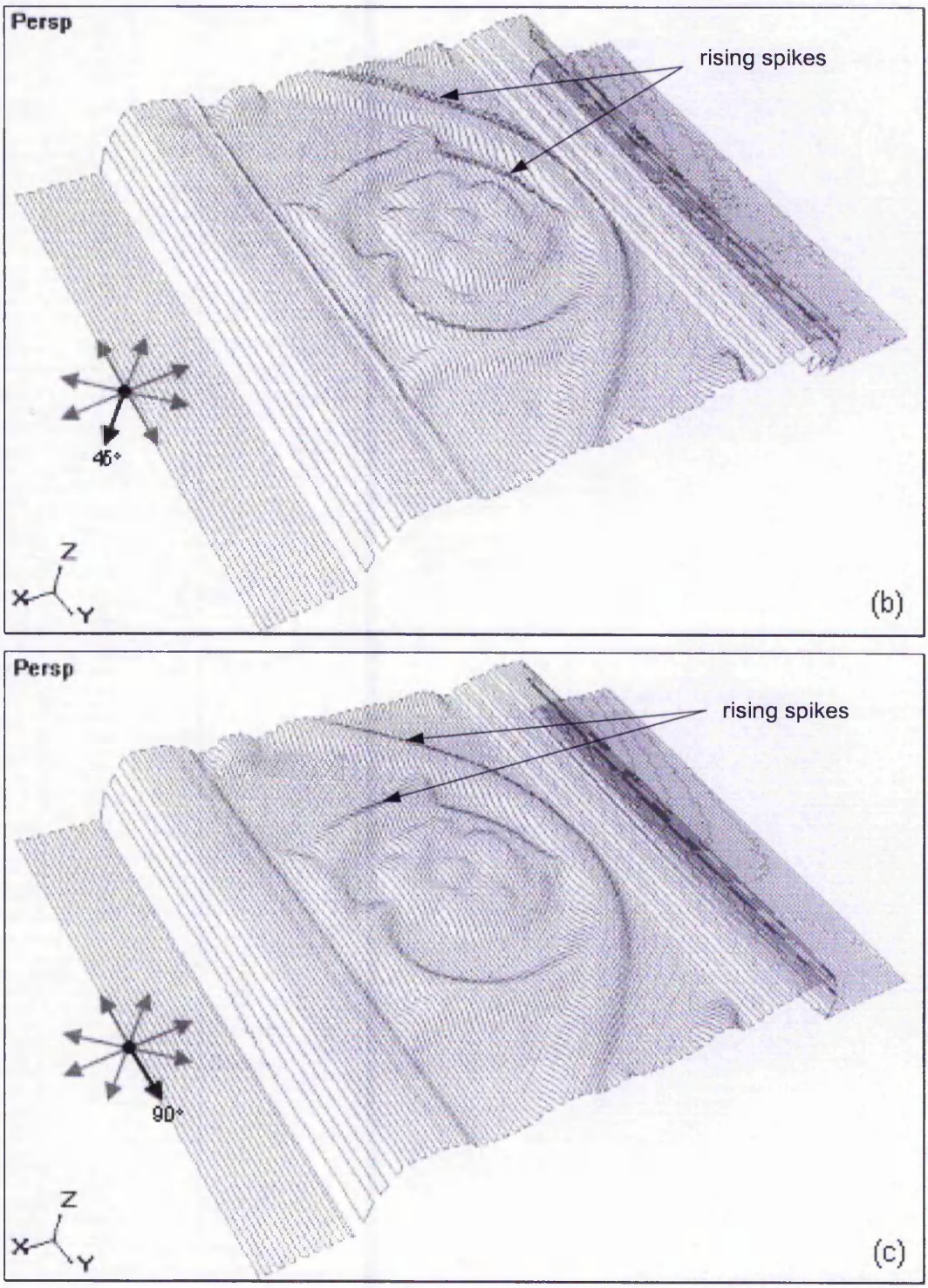

Fig. C-40: Range images of Fig. C-39 with orientations of sensor at (b) 45° and (c) 90° ((d)-(h) on following pages).

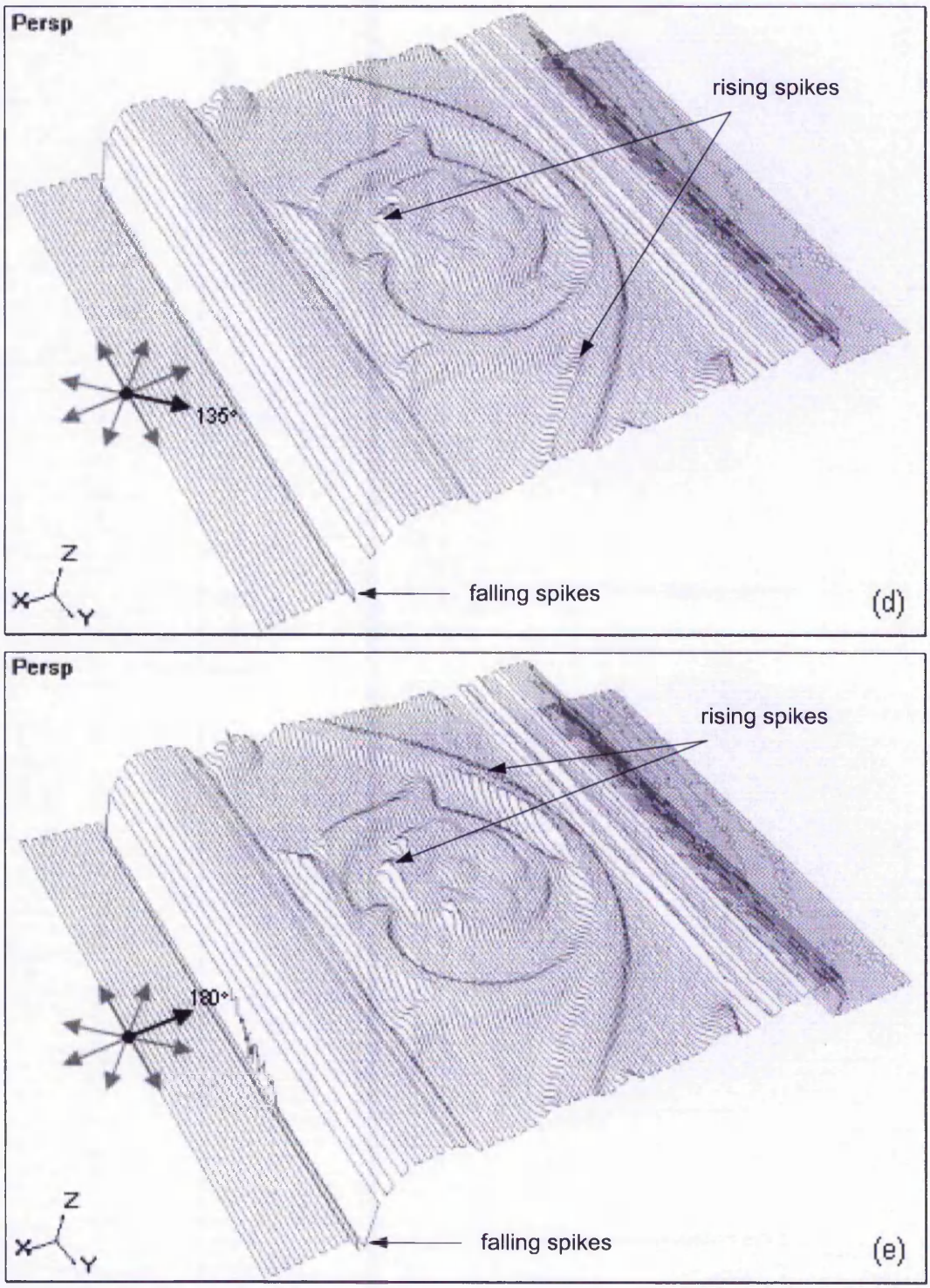

Fig. C-40: Range images of Fig. C-39 with orientations of sensor at (d) 135° and (e) 180° ((f)-(h) on following pages).

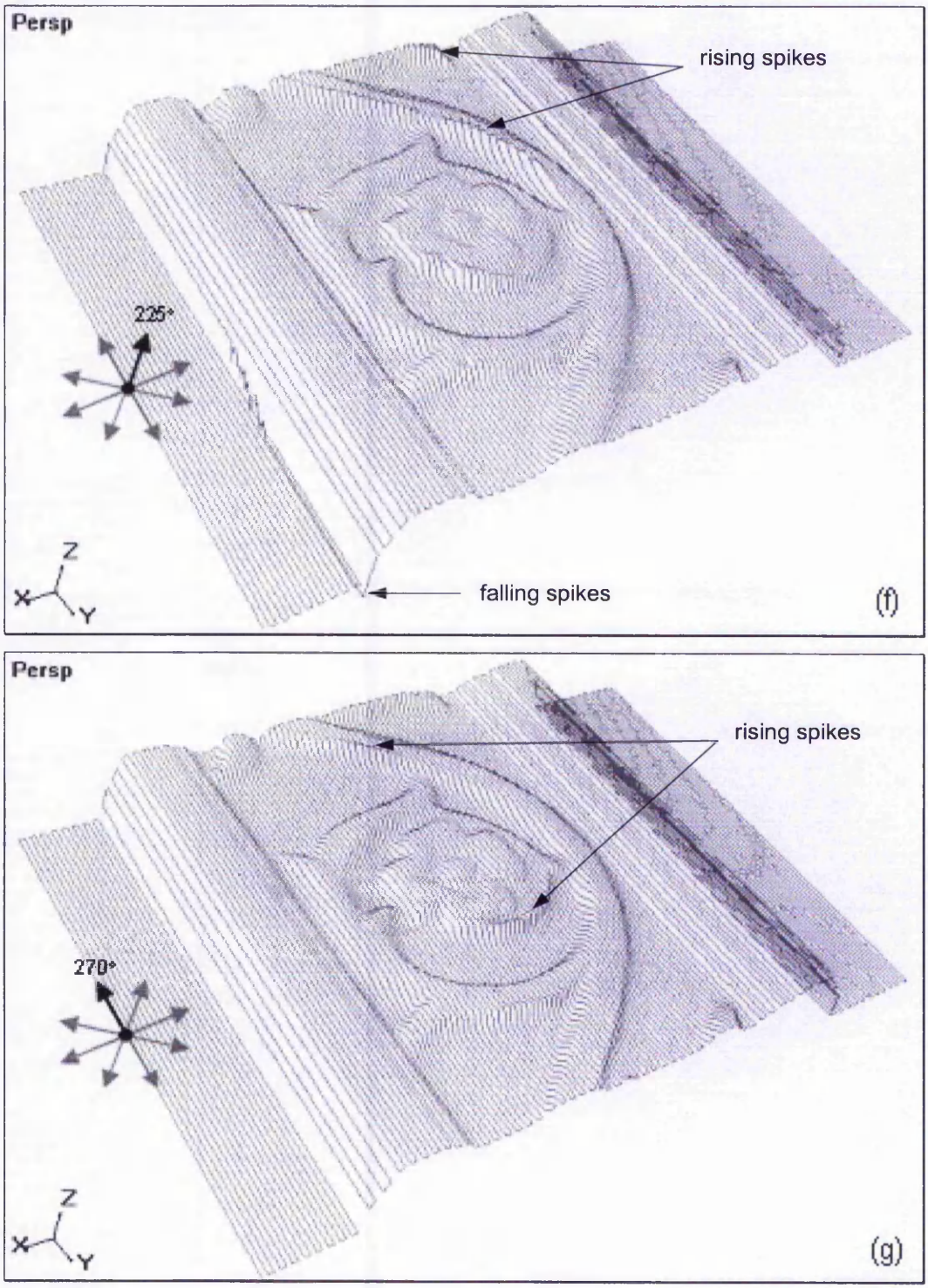

Fig. C-40: Range images of Fig. C-39 with orientations of sensor at (f) 225° and (g) 270° ((h) on following page).

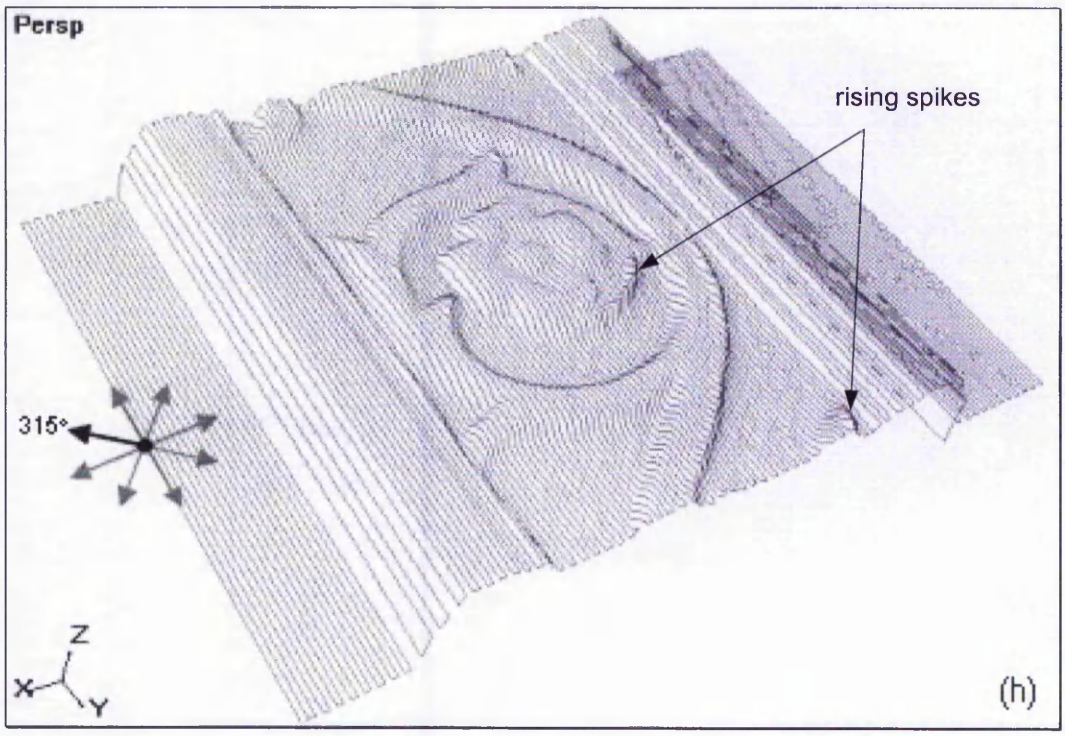

Fig. C-40: Range image of Fig. C-39 with orientation of sensor at (h) 315°.

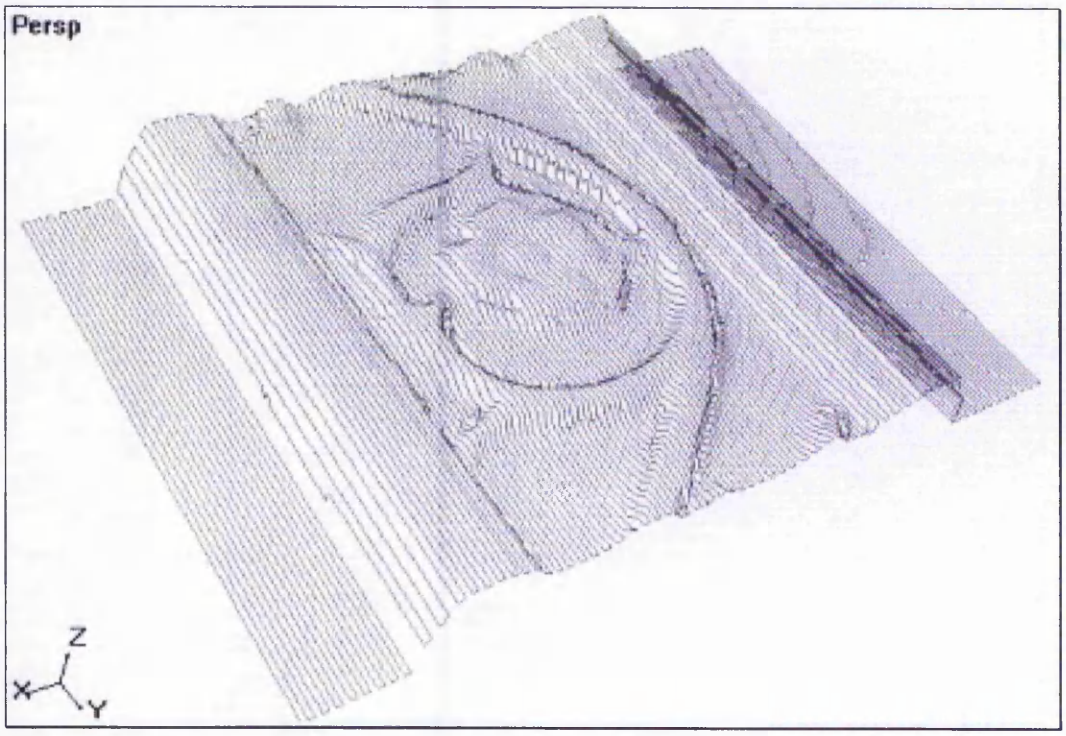

Fig. C-41: Averaging of eight range images of Fig. C-39.

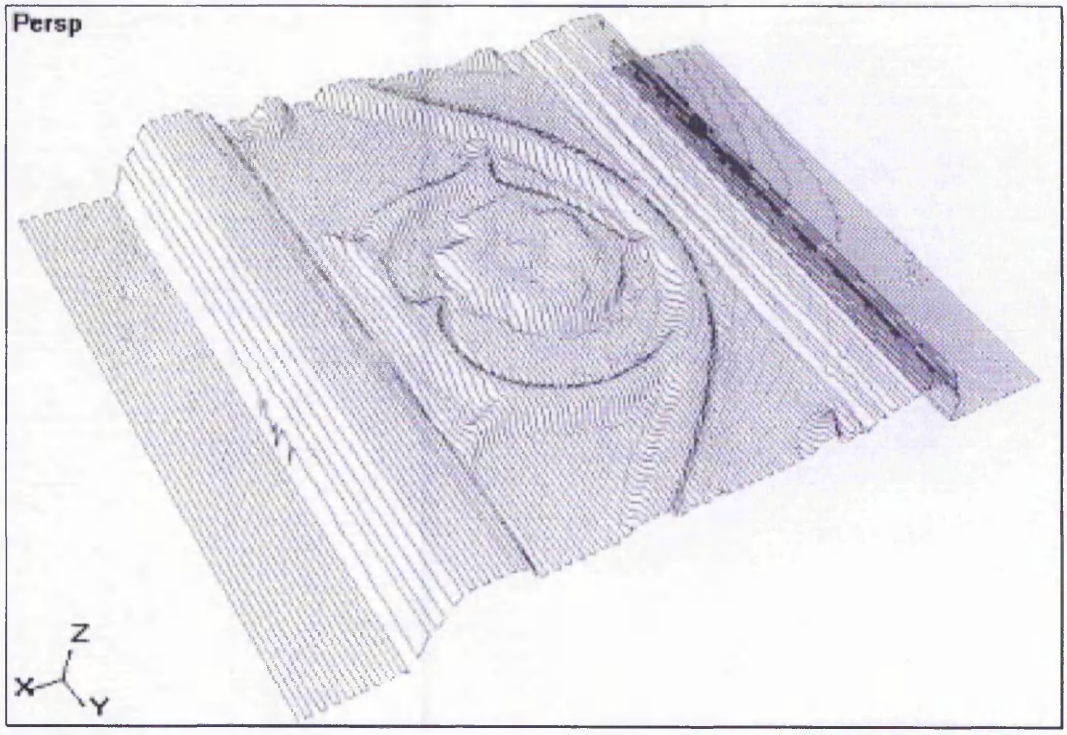

Fig. C-42: Selection of lowest *z*-values from multiple range images of Fig. C-39.

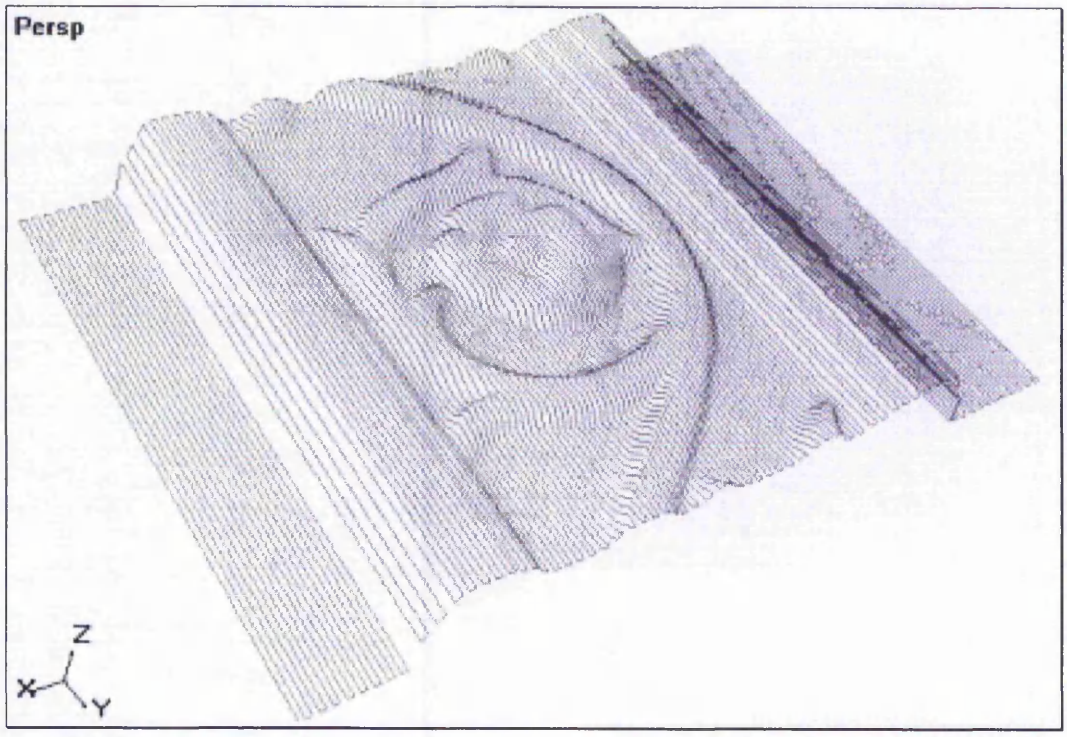

Fig. C-43: Compensated range image of Fig. C-39 based on edge detection algorithms.

Appendix D – Flowcharts of Compensation Algorithms

This section presents flowcharts for the three types of compensation algorithms used in the course of this research.

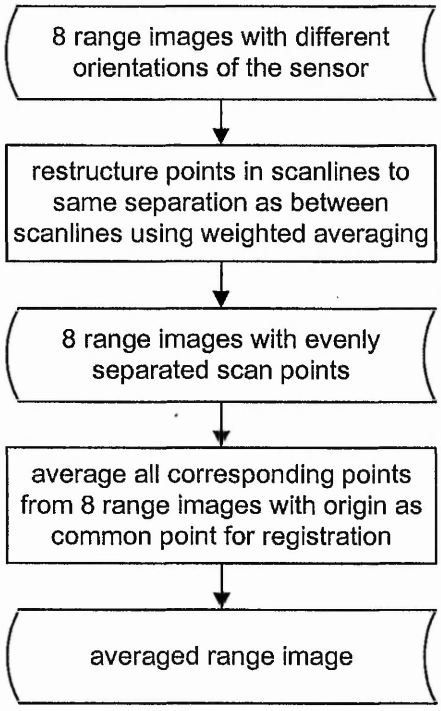

Fig. D-1: Flowchart for simple averaging algorithms.

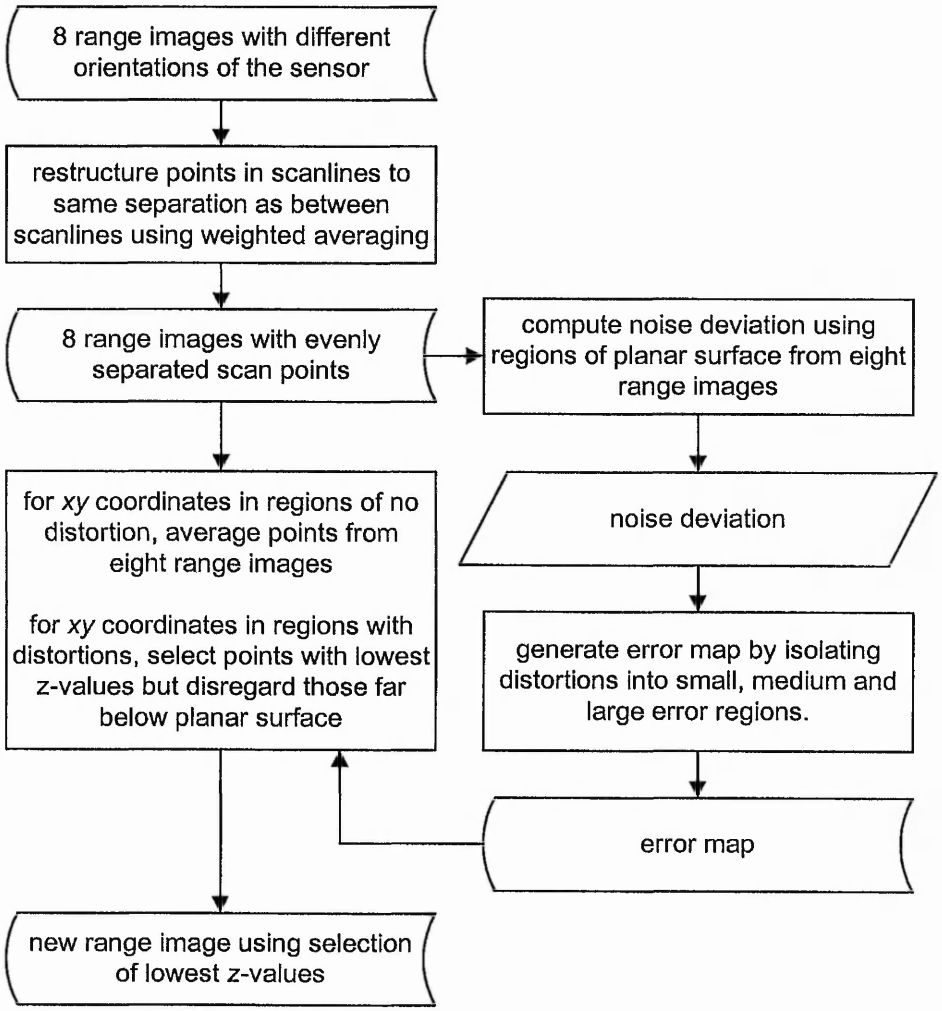

Fig. D-2: Flowchart for selection of lowest *z*-values algorithms.

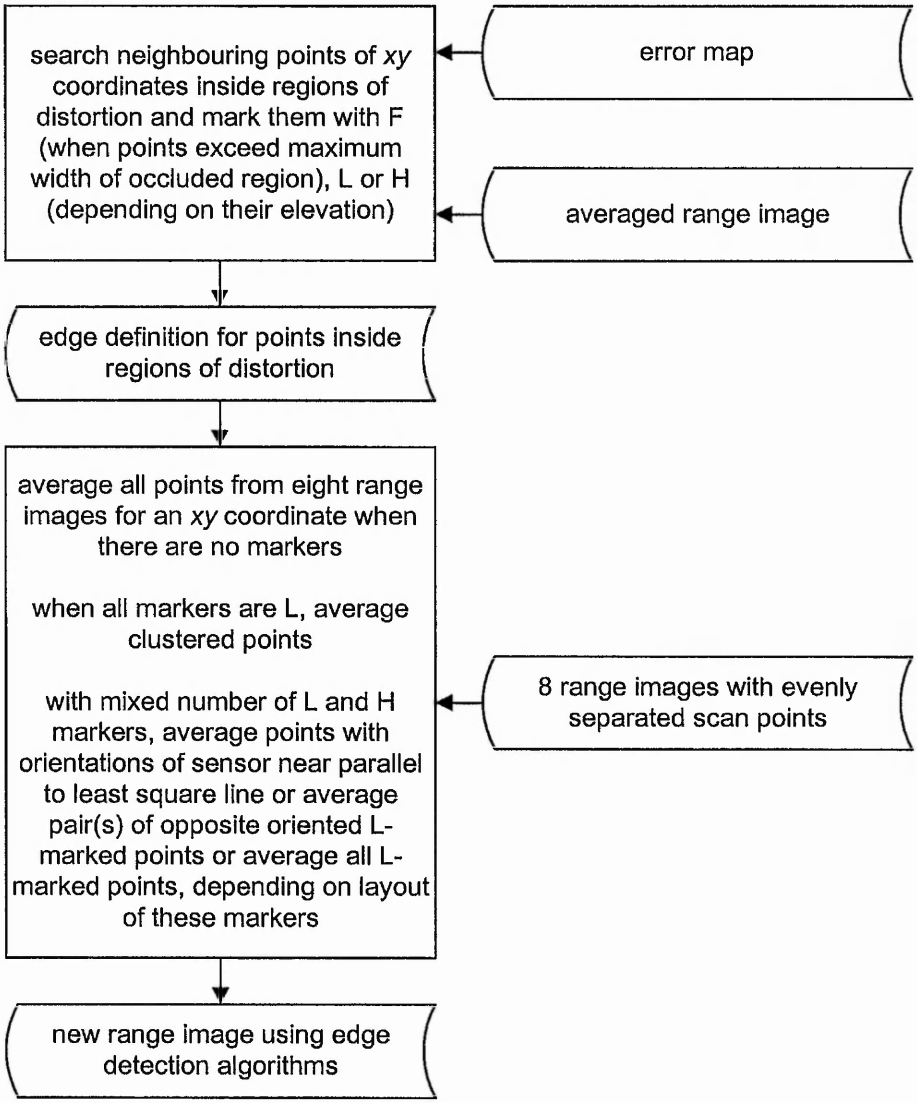

Fig. D-3: Flowchart for compensation using edge detection algorithms.

Appendix E – Published Scientific Papers

The Author had published two papers related to the research work:

1. Wong K. H, Poliakoff J. F. and Thomas P. D., *Automated Compensation for Distortion from a Single-Perspective Optical Triangulation Scanner*, Proceedings of 3rd Conference on Postgraduate Research in Electronics, Photonics, Communications and Software, Keele, UK, April 2001.
2. Wong K. H., Poliakoff J. F. and Thomas P. D., *Compensation Techniques For Distortions From A Single-Perspective Optical Triangulation Sensor*, Proceedings of 5th Conference on Optical 3-D Measurement Techniques, Vienna, Austria, October 2001.

AUTOMATED COMPENSATION FOR DISTORTIONS FROM A SINGLE PERSPECTIVE OPTICAL TRIANGULATION SCANNER

K. H. Wong, J. F. Poliakoff, P. D. Thomas

Introduction

The reverse engineering of a physical object often requires the production of a detailed digital representation of the object [1]. This can be used, after possible modification, to generate the path for a CNC machine to reproduce the object [2]. The digital representation, often known as a "range image", is obtained by measuring the position of a large number of points on the surface of the object. Methods for imaging the surface can be either tactile, which may involve possible damage to the object, or non-tactile, for example, using an optical process [3]. An inexpensive optical imaging method employs a single perspective triangulation sensor, which uses triangulation to measure the height of the spot from a laser beam shining vertically onto the surface of an object (see Fig. 1). The spot image is sampled by a position-sensitive photodetector adjacent to the laser.

Distortions in Range Images

Unfortunately, the range image obtained using such a simple optical sensor, as described in the previous section, often suffers from distortions [4]. Some of these are noise due to vibrations, which can be reduced by smoothing of the data. More serious distortions are caused by secondary reflections and diffusion of the laser light off a near vertical face of the object, giving rise to so called "bow waves" (see Fig. 2). Occlusion of the beam by another, differently oriented, near vertical face of the object also causes serious distortions, which are seen as "spikes" in the range image (see Fig. 2). These spikes can be categorized into "crest" and "trough", the precise nature of the distortions depending on the reflectivity of the object's surface.

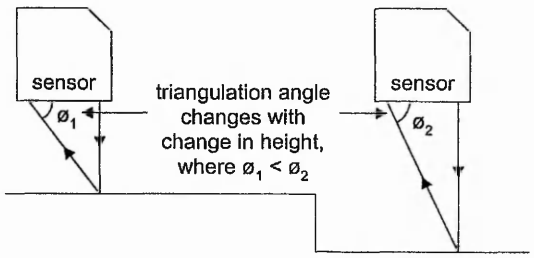

Fig. 1: The sensor uses the angle to determine height of the spot image.

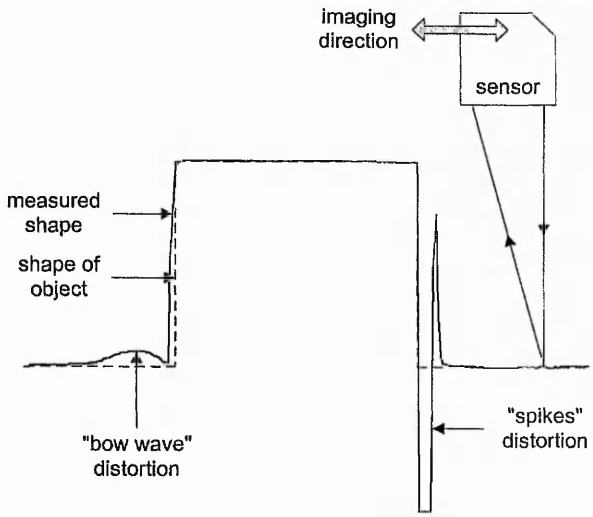

Fig. 2: Example of distortions obtained when imaging a rectangular object on a flat surface.

Thus changing the orientation of the sensor by 180° will reverse the position of the bow waves and spikes. On the other hand, changing it by 90° will prevent such distortions on this particular scanline (but they may occur elsewhere). This work focuses on algorithms to compensate for such distortions by combining data from a number of range images taken with different orientations of the sensor.

Results

Our investigations have shown that both the local geometry of the object and the orientation of the sensor device are critical in determining the nature of the distortions produced. Therefore taking the average of a number of range images with different sensor orientations will tend to reduce the distortions. However much more effective compensation can be achieved by using the geometry of the object to determine where distortions are expected for each particular range image.

Conclusion

Distortions from an inexpensive single-perspective optical triangulation scanner can be compensated by acquiring a number of range images with different orientations of the sensor. Then the range images can be combined using algorithms based on the geometry of the object.

References

[1] Vàrady T., Martin R. R. and Cox J., *Reverse Engineering of Geometric Models – An Introduction*, Journal of Computer-Aided Design, vol. 29, no. 4, pp. 255-268, 1997.

[2] Hoschek J., Dietz U. and Wilke W., *A Geometric Concept of Reverse Engineering of Shape: Approximation and Feature Lines*, Proceedings of International Conference on Mathematical Methods for Curves and Surfaces, pp. 253-262, Lillehammer, Norway, July 1997.

[3] Schönfeld H., Häusler G. and Karbacher S., *Reverse Engineering using Optical 3-D Sensors*, Proceedings of SPIE, vol. 3313, pp. 115-125, 1998.

[4] Carocci M., Lazzari S., Rodella R. and Sansoni G., *3-D Range Optical Sensor: Analysis of the Measurement Errors and Development of Procedures for their Compensation*, Proceedings of SPIE, vol. 3313, pp. 178-188, 1998.

COMPENSATION TECHNIQUES FOR DISTORTIONS FROM A SINGLE-PERSPECTIVE OPTICAL TRIANGULATION SENSOR

K. H. Wong, J. F. Poliakoff. P. D. Thomas

Department of Computing, The Nottingham Trent University, Burton St., Nottingham, England, NG1 4BU.

Abstract. In reverse engineering, a 3-D image of an object can be obtained by using an inexpensive single-perspective optical triangulation sensor. Unfortunately significant distortions can occur which compare unfavourably with those from the more expensive circular perspective triangulation sensor. Empirical studies have provided an understanding of the mechanisms by which such distortions occur. It has been found that the geometry of the object and the orientation of the sensor relative to the object, but *not* the scanning direction, are critical in determining the nature of the distortions. New geometry-based algorithms are presented here for the first time, which compensate for these distortions by combining a number of scans taken with different orientations of the sensor.

Key words: reverse engineering, 3-D imaging, single-perspective optical triangulation sensor, CNC machining, point cloud, range image, distortion.

1 Introduction

The reverse engineering of a physical object often requires the production of a detailed digital representation of that object [1]. This representation can be used, after possible modification, to generate the path for a CNC machine to reproduce the object [2]. The digital representation, often known as a point cloud or "range image", is obtained by measuring the position of a large number of points on the surface of the object. Methods for imaging the surface can be either tactile, which may involve possible damage to the object, or non-tactile, for example using an optical process [3]. An inexpensive optical imaging method employs a single perspective triangulation sensor, which involves triangulation to measure the height of the spot from a laser beam shining vertically onto the surface of an object. The spot image is sampled by a position-sensitive photodetector adjacent to the laser.

Unfortunately, the range image obtained using a simple optical sensor of this type often suffers from distortions [4]. Some of these are noise due to vibrations, which can be reduced by smoothing of the data. More serious distortions are observed in the vicinity of some near-vertical faces of the object, as can be seen along the right side of the range image of a face mask in Figure 1, where a "crest" appears in the perspective view (a) and a "trough" can be seen projecting below the level of the base in the side view (b). We have termed both the crest and the trough "spike" distortion. In Section 2 we examine in detail the nature of such artefacts and explain how they are related to the geometry of the object and the orientation of the sensor. Then, in Section 3, we present new compensation algorithms based on the surface geometry of the object.

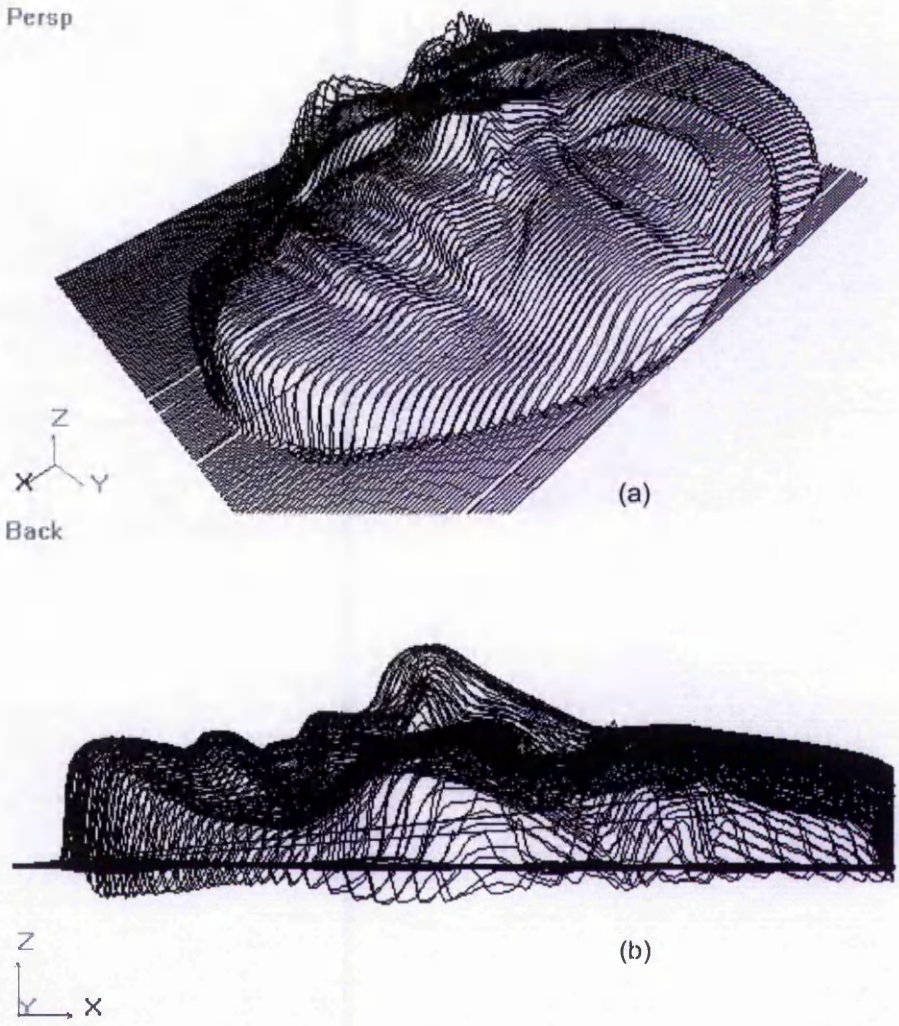

Figure 1. An example of distortions in a range image: (a) perspective view and (b) side view. The distortions can be seen most easily along the right side of the face, as a crest in (a) and a trough in (b).

2 Distortions in Range Images

The single perspective triangulation sensor uses a laser beam, which is projected vertically onto a surface. The height of the spot formed on the surface can then be found by measuring the angle of the light returning from the spot, as shown in Figure 2. The angle is measured by focusing the light onto a position-sensitive photodetector adjacent to the laser emitter. The calculation of the height is based on the fact that the spot is vertically below the laser emitter. By scanning over the surface and recording the horizontal position, (x, y), of the sensor together with the height, z, of the light spot on the surface below it, a range image is obtained. In our experiments we have used a Matsushita NAIS ANR1182 laser analogue sensor (range 80mm ± 20mm).

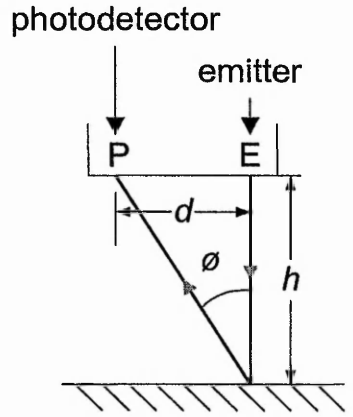

Figure 2. Diagram showing the measurement of height by triangulation using the formula $h = d/\tan\phi$.

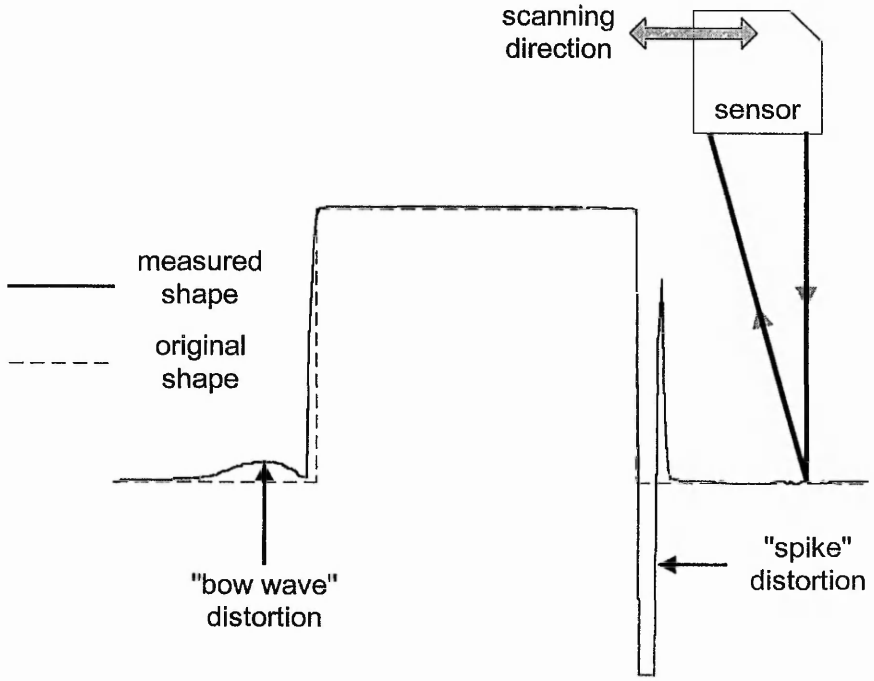

Figure 3. The distortions obtained in a single scan of a simple rectangular object about 23 mm. High. (The sensor is not to scale.)

In order to understand better the nature of the distortions, a simple rectangular block was placed on a horizontal base and scanned. Figure 3 shows one scan line from the resulting range image, which crossed the block itself. The largest distortions are on the right-hand side of the block, where there are large "spikes" both above and below the level of the base. This corresponds to the crest seen in Figure 1. The precise nature of the spike effect depends mainly on the reflectivity of the surface but can also be affected by small local irregularities. In addition, on the left-hand side of the block in

Figure 3 there is another distortion of the horizontal base, that we have termed a "bow wave", the size of which tends to increase as reflectivity of the surface increases. Figure 4(a) illustrates the resulting range image in a schematic diagram. Another range image, Figure 4(b), was then taken with nothing changed except the direction of scanning, which was approximately perpendicular to that of the first one. It can be seen that this time there were no significant distortions in the scan lines crossing the block. However, there were significant distortions in the scan lines crossing the base left and right of the block. Although the individual scan lines look different, the resulting surface is the same in the two cases. This shows that the nature of the distortions in the range image does *not* depend on the direction of scanning [5]. However, as we describe below, the orientation of the sensor is critical in determining the nature of the distortions.

We have investigated the causes of the serious distortions described above and have found that they can occur adjacent to a near-vertical face. This is because the distortions are caused by reflection and diffusion of the light from the spot when a near-vertical face is present. As can be seen from Figure 4, only two of the four vertical faces have distortions adjacent to them. Thus, these effects also depend on the orientation of the emitter and the photodetector of the sensor in relation to the face.

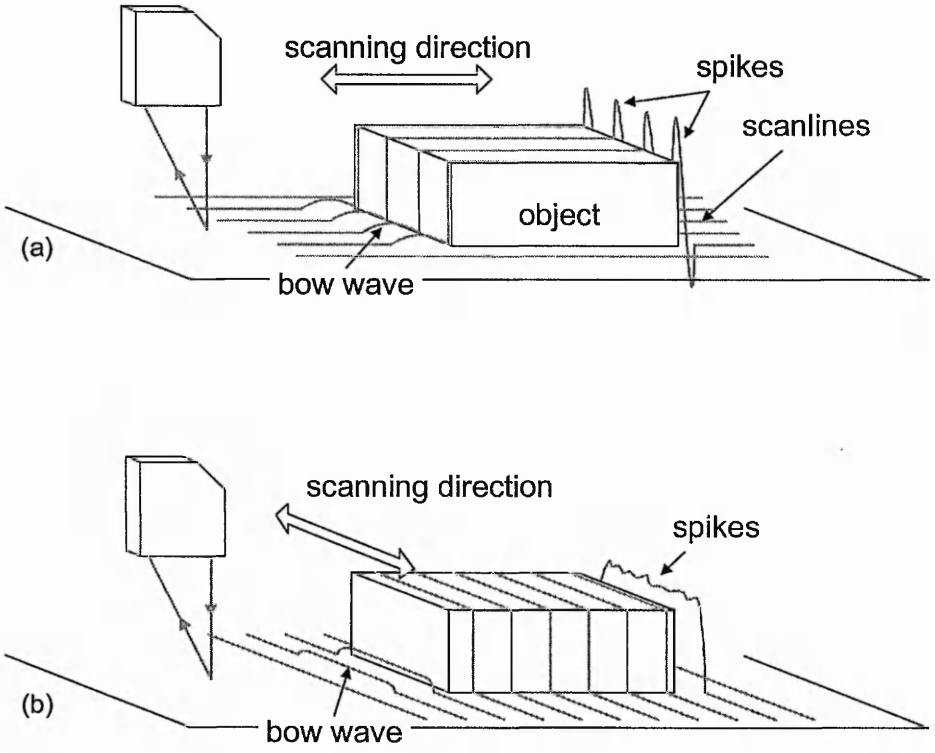

Figure 4. Schematic diagram to show how the nature of the distortion depends on sensor orientation and not on the direction of scanning. In (a) the sensor orientation is parallel to the direction of scanning and in (b) it is perpendicular to it.

Figure 5 shows the arrangement of the emitter and the photodetector of the sensor in relation to the block when bow wave distortions occur; the photodetector is facing *towards* the side of the block. The light from the primary spot on the horizontal

surface is reflected to form a more diffuse spot on the side of the block. Two spots are thus detected by the sensor, the second at a false height above the true height, because the calculation of height is based on the assumption that the spot is vertically below the emitter. Averaging by the sensor results in a "phantom spot" between the two but closer to the true height, as it has greater intensity. The phantom spot tends to decrease in height as surface reflectivity decreases, because the secondary spot then has lower intensity.

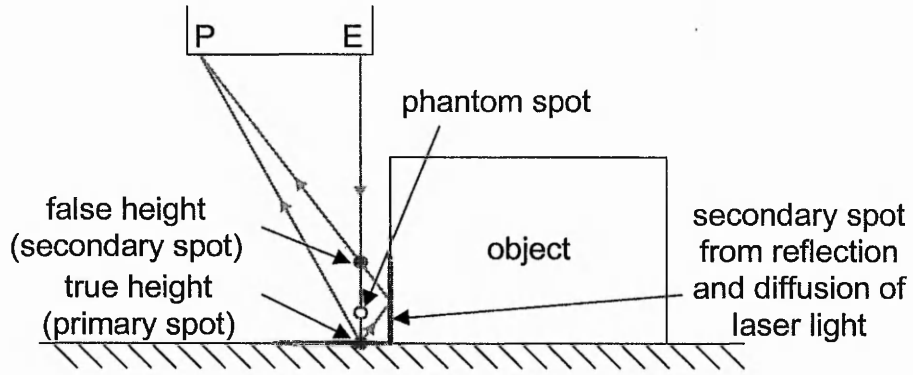

Figure 5. Diagram showing the generation of bow wave distortion. Averaging of the angles from the primary and secondary spots yields a "phantom spot". The phantom spot is closer to the true height, because the secondary spot has lower intensity than the primary spot.

The arrangement of the sensor in relation to the block when spikes occur is shown in Figure 6, with the photodetector facing *away from* the side of the block. The primary spot is now occluded from the photodetector by the edge of the block, Figure 6(a), and, when reflectivity is low, may result in an error value below the level of the base, if no light is detected. This is seen as a downward spike or trough. For a surface of higher reflectivity, Figure 6(b), some dispersed light reflected from the secondary spot on the side of the block will be detected beyond the occluded region. Again, because the calculation assumes that the spot is below the emitter, a "phantom spot" is detected above the true height and the result is an upward spike or crest.

In the other two cases, corresponding to the remaining two sides of the block, no significant distortions occur. This is because the photodetector is facing *parallel* to the edge of the block (when viewed from above). Therefore reflected and diffused light from the primary and secondary spots is unlikely to be detected, since they are outside the field of view of the photodetector.

Our investigations have thus shown that the nature of the distortions depends on the orientation of the sensor in relation to the geometry of the object. When the sensor is oriented approximately *parallel* to the direction of a near-vertical face (when viewed from above) there are only very small distortions. However, when the orientation of the sensor is roughly *perpendicular* to the near-vertical face, then there will be significant distortions adjacent to the face, with bow waves or spikes, depending on whether the photodetector is facing, respectively, towards the face or away from it.

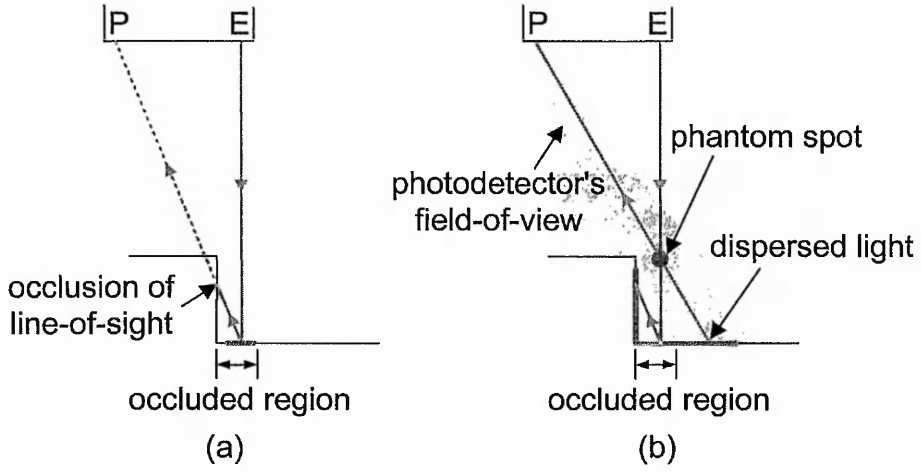

Figure 6. Diagram showing the generation of spike distortion. Spike distortion occurs when the line of sight is occluded and the primary spot cannot be detected. In (a) a downward spike occurs when no light is detected, resulting in an error reading below the level of the base. However, if the photodetector receives a trace of dispersed light (b), a "phantom spot" is detected, causing an upward spike.

One strategy to prevent such bow wave and spike distortions is to perform a rough scan of the object to enable near-vertical faces to be detected. Then a detailed scan can be planned in such a way that the sensor is oriented appropriately adjacent to every near-vertical face. This requires a preliminary scan followed by a number of separate partial scans, which then need to be registered. Our approach, on the other hand, is to obtain standard multiple scans of the object, changing only the orientation of the sensor. Then the resulting range images can be combined using algorithms based on the geometry of the object, as we describe in the following section.

3 Algorithms to Compensate for Distortions

We have developed algorithms to combine multiple range images of an object, which take into account the geometry of the object. All the range images are initially registered and aligned as required. For the simple object consisting of the rectangular block on a base, as in Figures 3 and 4, two scans would be sufficient, if the sensor were oriented as illustrated in Figure 7. However, merely rotating this simple object through 45° and repeating the two scans would result in considerable distortions. In this particular case four scans may be sufficient to remove the distortions. We have found that, in general up to eight different scans with the sensor spaced evenly at 45° intervals, may be needed.

The first stage of the process is to detect "error regions" for the set of range images. These error regions consist of those points within the scanned region of the x-y plane where there is significant variation between the height values, z, obtained from the different range images. If the variation at any point (x, y) is above a certain small tolerance (to allow for noise), the point is classified as an error point. Outside the error regions the heights from all the range images can be averaged to obtain a partial image.

However, the problem is to decide, at points inside an error region, which of the values are distorted and should be ignored.

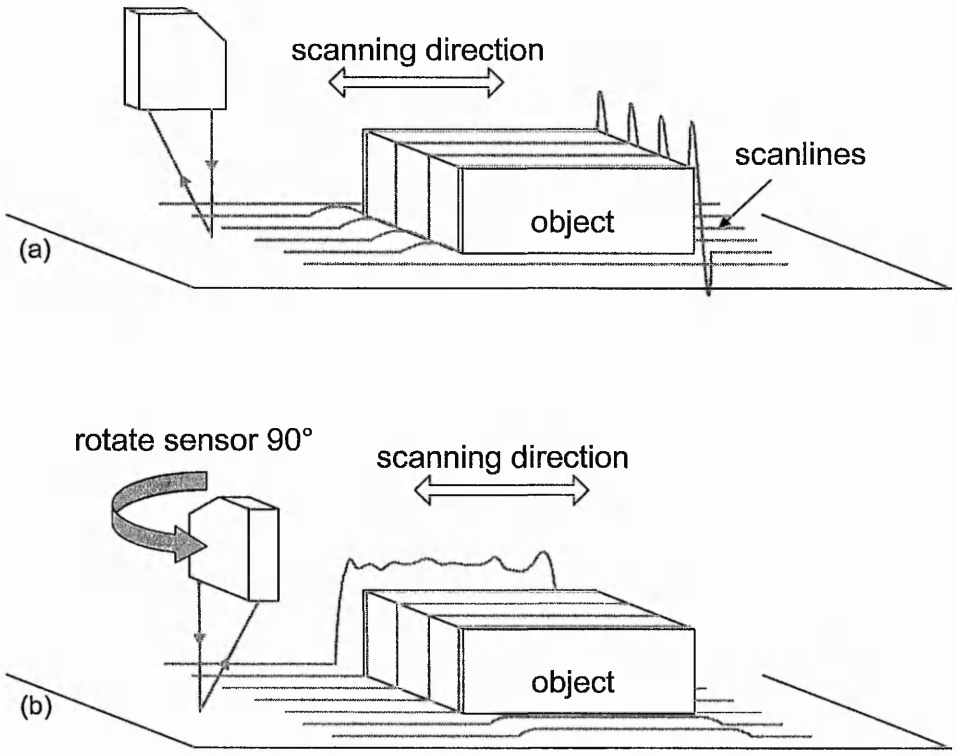

Figure 7. Schematic diagram illustrating the collection of two images of an object by rotating the sensor. In the case of two images the object is scanned (a) and then the sensor is rotated by 90° before the second scan (b).

In order to make use of the geometry of the object, an estimated or "rough" range image has to be used, because no prior information is available about the object. Such a rough range image is obtained by taking a partial image, as described above, but using a much larger tolerance. Thus points are removed where there are large spikes, for which the overall average will be very unreliable, but bow waves will be tolerated. Therefore the regions where no height is available in the rough image will be smaller than the error regions, whereas the remaining points will have at most small distortions. This rough range image is used to detect near-vertical faces object adjacent to each error region. Then those range images for which the sensor orientation is most likely to cause distortions can be ignored when calculating the compensated value.

4 Results

The compensation algorithms have been tested using an object with horizontal cross-section consisting of a square with rounded corners. Figure 8(a) shows two of the scanned images taken with the sensor oriented at 0° and 90° to the scanning direction. Both upward and downward spikes are easily visible behind the object (to right and left respectively) and a bow wave is just visible on the side opposite the spikes in each case.

Altogether eight scans have been combined to produce the range image shown in Figure 9. It can be seen that no significant distortions are present after compensation.

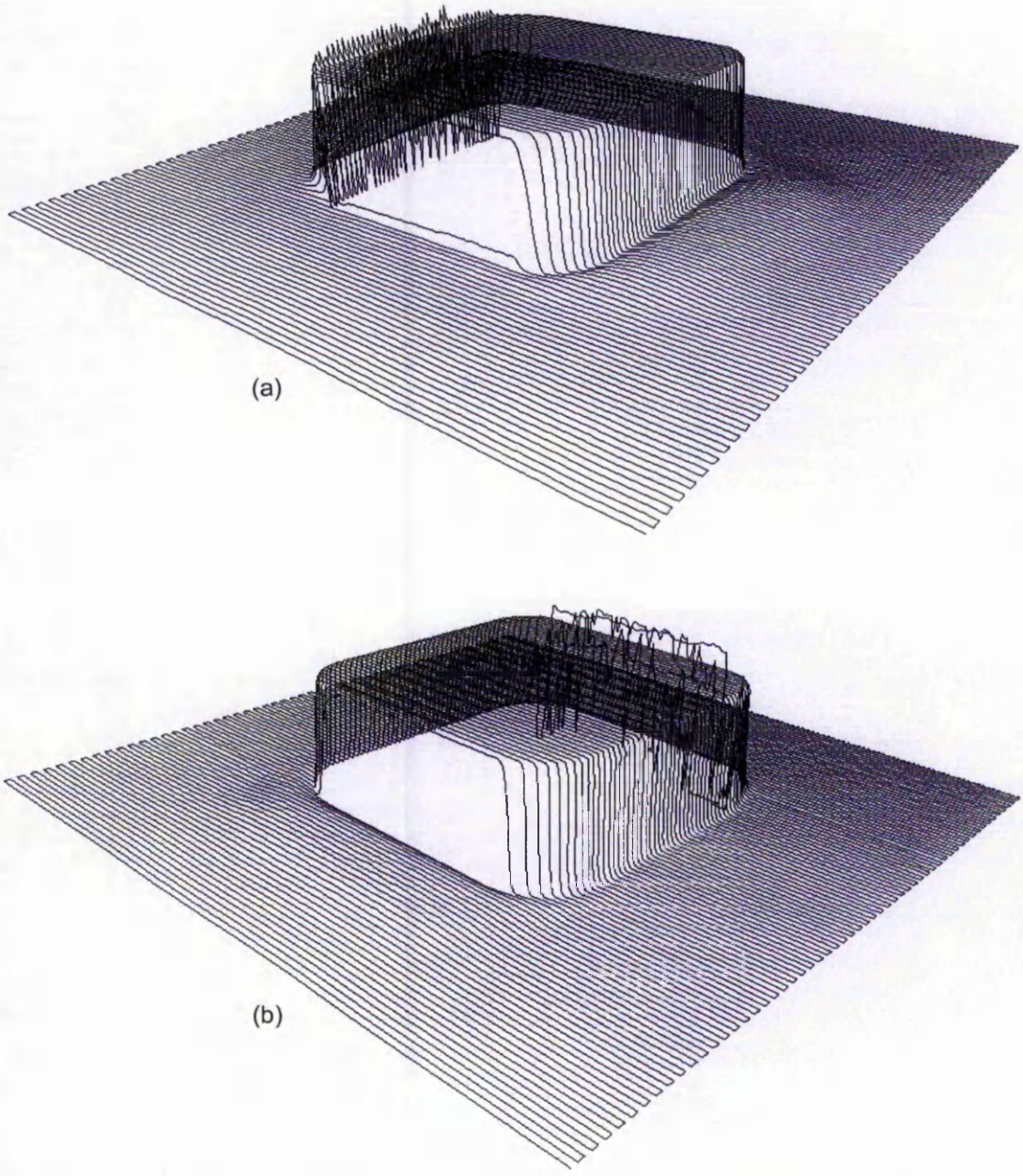

Figure 8. Two of a total of 8 single range images obtained from scanning a simple object: (a) with sensor orientation at 0°; and (b) with sensor orientation at 270° (the object has height approx. 23 mm and horizontal cross-section consisting of a square with rounded corners). A bow wave can be seen on the side opposite the spikes in each case.

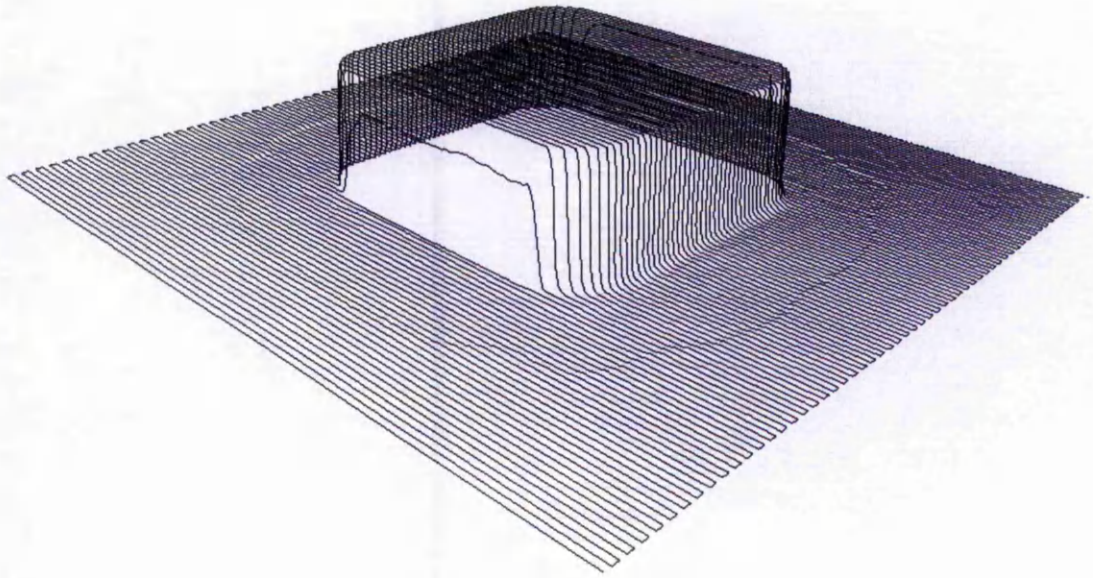

Figure 9. The range image obtained after compensation with the new algorithms for the object from Figure 8 (using 8 range images with sensor orientations at 0°, 45°, 90°, 135°, 180°, 225°, 270° and 315°).

5 Conclusions

Both object geometry and sensor orientation are critical in determining the nature of the distortions from a single perspective triangulation sensor. Our new geometry-based algorithms can compensate for such distortions by combining data from a number of range images taken with different orientations of the sensor. Preliminary results show successful compensation for simple objects but further investigation is needed.

6 Acknowledgements

We are grateful to Axiomatic Technology Limited for loan of equipment and software. We also thank Nottingham Trent University for supporting this work.

References

[1] Vàrady T., Martin R. R. and Cox J., *Reverse Engineering of Geometric Models - An Introduction*, Computer-Aided Design, 1997, vol. 29, no. 4: 255-268.

[2] Hoschek J., Dietz U. and Wilke W., *A Geometric Concept of Reverse Engineering of Shape: Approximation and Feature Lines*, Proceedings of International Conference on Mathematical Methods for Curves and Surfaces, Lillehammer, Norway, 1997. 253-262.

[3] Schönfeld H., Häusler G. and Karbacher S., *Reverse Engineering using Optical 3-D Sensors*, Proceedings of SPIE, 1998, vol. 3313: 115-125.

[4] Carocci M., Lazzari S., Rodella R. and Sansoni G., *3-D Range Optical Sensor: Analysis of the Measurement Errors and Development of Procedures for their Compensation*, Proceedings of SPIE, 1998, vol. 3313: 178-188.

[5] Wong, K. H., Poliakoff, J. F., Thomas, P. D., *Automated Compensation for Distortions from a Single-Perspective Optical Triangulation Scanner*, Third Conference on Postgraduate Research in Electronics, Photonics, Communications and Software (PREP2001), Keele, England, 2001. 89-90.